ULTRAFAST DYNAMICS OF SINGLE QUANTUM DOTS

ALISTAIR BRASH

Ultrafast studies of single quantum dots and their coupling to acoustic phonons and nanocavities

Thesis submitted for the degree of Doctor of Philosophy

Department of Physics and Astronomy
The University of Sheffield
June 2016

I have a friend who's an artist and has sometimes taken a view which I don't agree with very well. He'll hold up a flower and say "look how beautiful it is," and I'll agree. Then he says "I as an artist can see how beautiful this is but you as a scientist take this all apart and it becomes a dull thing," and I think that he's kind of nutty. First of all, the beauty that he sees is available to other people and to me too, I believe...

I can appreciate the beauty of a flower. At the same time, I see much more about the flower than he sees. I could imagine the cells in there, the complicated actions inside, which also have a beauty. I mean it's not just beauty at this dimension, at one centimeter; there's also beauty at smaller dimensions, the inner structure, also the processes. The fact that the colors in the flower evolved in order to attract insects to pollinate it is interesting; it means that insects can see the color. It adds a question: does this aesthetic sense also exist in the lower forms? Why is it aesthetic? All kinds of interesting questions which the science knowledge only adds to the excitement, the mystery and the awe of a flower. It only adds. I don't understand how it subtracts. — Richard Feynman

In loving memory of Arthur & Enid Brown and Jack & Lottie Brash.

1918 – 2013

ABSTRACT

In this thesis the results of experiments on the optical properties of single InGaAs quantum dots are presented. Using a range of ultrafast spectroscopy techniques the dynamics of single charge carriers confined within these quantum dots are probed. Both the coherent and incoherent driving regimes are explored with a view to applications for quantum information processing. Three key results are described in detail in this thesis. Firstly, by performing resonant coherent driving it is shown that reduction of the quantum dot neutral exciton fine-structure splitting enables fast and high-fidelity initialization of long-lived hole spin quantum bits. Secondly, by detuning the laser from the ground state - neutral exciton transition it is possible to both excite and de-excite exciton population through incoherent driving via the acoustic phonon bath. Finally, by considering quantum dots coupled to optical microcavities it is shown that the driving strength of both resonant coherent and quasi-resonant phonon-assisted excitation may be strongly modulated.

PUBLICATIONS

Some of the results and figures presented here have appeared previously in the following publications:

[1] J. H. Quilter, A. J. Brash, F. Liu, M. Glässl, A. M. Barth, V. M. Axt, A. J. Ramsay, M. S. Skolnick, and A. M. Fox. 'Phonon-Assisted Population Inversion of a Single InGaAs/GaAs Quantum Dot by Pulsed Laser Excitation.' *Phys. Rev. Lett.* 114 (13 Mar. 2015), p. 137401. DOI: 10.1103/PhysRevLett.114.137401.

[2] A. J. Brash, L. M. P. P. Martins, F. Liu, J. H. Quilter, A. J. Ramsay, M. S. Skolnick, and A. M. Fox. 'High-fidelity initialization of long-lived quantum dot hole spin qubits by reduced fine-structure splitting.' *Phys. Rev. B* 92 (12 Sept. 2015), p. 121301. DOI: 10.1103/PhysRevB.92.121301.

[3] F. Liu, L. M. P. Martins, A. J. Brash, A. M. Barth, J. H. Quilter, V. M. Axt, M. S. Skolnick, and A. M. Fox. 'Ultrafast depopulation of a quantum dot by LA-phonon-assisted stimulated emission.' *Phys. Rev. B* 93 (16 Apr. 2016), p. 161407. DOI: 10.1103/PhysRevB.93.161407.

[4] A. J. Brash, L. M. P. P. Martins, A. M. Barth, F. Liu, J. H. Quilter, M. Glässl, V. M. Axt, A. J. Ramsay, M. S. Skolnick, and A. M. Fox. 'Dynamic vibronic coupling in InGaAs quantum dots [Invited].' *J. Opt. Soc. Am. B* 33.7 (July 2016), pp. C115–C122. DOI: 10.1364/JOSAB.33.00C115.

*I think I can safely say that nobody
understands quantum mechanics*

— Richard Feynman

ACKNOWLEDGMENTS

Finally, I would like to thank my friends and family who have supported me throughout my studies. In particular, my loving girlfriend Lisa who has been there for me through thick and thin.

Thank-you everyone!

CONTENTS

ACRONYMS

AC   Alternating Current

AO   Achromatic Objective

AFM   Atomic Force Microscopy

Ag   Silver

Al   Aluminium

AlAs   Aluminium Arsenide

AlGaAs   Aluminium Gallium Arsenide

ARP   Adibatic Raman Passage

Au   Gold

Be   Beryllium

BQP   Bounded Error Quantum Polynomial Time

BS   Beam-Splitter

CCD   Charge-Coupled Device

cQED   Cavity Quantum Electrodynamics

CW   Continuous-Wave

DBR   Distributed Bragg Reflector

DC   Direct Current

DVC   Dynamic Vibronic Coupling

EBL   Electron Beam Lithography

EID   Excitation Induced Dephasing

FSS   Fine-Structure Splitting

FWHM   Full-Width Half Maximum

GaAs   Gallium Arsenide

He   Helium

HF   Hyrofluoric Acid

HH   Heavy Hole

HPF   High Pass Filter

HWP   Half-Wave Plate

ICP   Inductively Coupled Plasma

InAs   Indium Arsenide

InGaAs Indium Gallium Arsenide

KLM   Kerr Lens Mode Locking

LA   Longitudinal Acoustic

LAPSE   Longitudinal-Acoustic Phonon Stimulated Emission

LH   Light Hole

LO   Longitudinal Optical

LP   Linear Polarizer

MBE   Molecular Beam Epitaxy

MO   Microscope Objective

NA   Numerical Aperture

ND   Neutral Density

NIR   Near Infra-Red

NMR   Nuclear Magnetic Resonance

NV   Nitrogen Vacancy

OD   Optical Density

OPSL   Optically-Pumped Semiconductor Laser

OSE   Optical Stark Effect

PBS	Polarizing Beam-splitter
PC	Photocurrent
PhC	Photonic Crystal
PCC	Photonic Crystal Cavity
PDC	Parametric Down Conversion
μPL	Micro-Photoluminescence
PM	Power Meter
PID	Proportional-Integral-Derivative
PS	Pulse-Shaper
QCSE	Quantum-Confined Stark Effect
QD	Quantum Dot
QDM	Quantum Dot Molecule
QIP	Quantum Information Processing
QKD	Quantum Key Distribution
QM	Quantum Mechanics
QWP	Quarter-Wave Plate
RF	Resonance Fluorescence
SAQD	Self-Assembled Quantum Dot
SEM	Scanning Electron Microscope
Si	Silicon
SK	Stranski-Krastanov
SM	Single Mode
SO	Split-Off
STIRAP	Stimulated Raman Adibatic Passage
TEC	Thermo-Electric Cooler

Ti   Titanium

TIR   Total Internal Reflection

Ti:S   Ti:Sapphire

TTL   Trigger-Type Logic

UV   Ultraviolet

VWP   Variable Wave-Plate

WGM   Whispering Gallery Mode

ZPL   Zero Phonon Line

Part I

INTRODUCTION & REVIEW

In this part of the thesis the key concepts and motivations of Quantum Information Processing are introduced in chapter 1. Different candidates for implementing these concepts are then discussed and the semiconductor Quantum Dot scheme considered in this thesis is outlined. Finally, the key theory and literature in the field is reviewed in chapter 2 from background and fundamentals through to current state-of-the-art.

INTRODUCTION

Few physical theories have caused such a shift in our understanding of the world as Quantum Mechanics (QM). Originally motivated by a desire to better describe atomic structure and the behaviour of sub-atomic particles, the end result was a theory that challenges many of our longest standing preconceptions of the nature of reality and information. The principle of superposition of quantum states [1] exposes the non-determinstic nature of the theory, famously leading a sceptical Einstein to remark that *"God doesn't play dice with the world"* [2]. Despite the somewhat challenging philosophical implications, QM has withstood the test of time. Now, around a century after the inception of QM, scientific interest has turned to exploiting the properties of quantum systems to create "quantum technologies".

The Quantum Dots (QDs) studied in this thesis are excellent candidates for this. In particular, the work presented here is motivated by a desire to develop a QD-based architecture that exploits QM to process information. This is generally termed Quantum Information Processing (QIP) and can dramatically out-perform classical information processing for simulation of quantum systems (see subsection 1.1.3) and solving certain mathematical problems (see subsection 1.1.4). In section 1.1 of this chapter a brief review of the theory and applications of QIP is presented. The focus of section 1.2 is on the requirements for implementing an experimental QIP system whilst section 1.3 reviews a number of different approaches to this challenge. Finally, in section 1.4 the QD-based approach that motivates this thesis is outlined.

1.1 QUANTUM INFORMATION PROCESSING

QIP is the phrase used to describe the exploitation of exclusively quantum mechanical phenomena such as superposition [1] and entanglement [3, 4] to process data. In this section the theoretical found-

ations of QIP are reviewed along with the motivation and applications of the field.

1.1.1 *Quantum Bits*

In classical information the building block of all information is a bit, a variable taking one of only two values (0 or 1). In QIP this becomes a qubit [5] with a value instead defined by a probabilistic linear combination of 0 and 1 [6]:

$$|\psi\rangle = c_0 |0\rangle + c_1 |1\rangle, \tag{1.1}$$

where c_0 and c_1 are complex probability amplitudes obeying the normalisation condition $|c_0|^2 + |c_1|^2 = 1$. The full parameter space of the wavefunction (ψ) of a single pure qubit state may be visualised as the surface of the Bloch sphere [7] shown in Figure 1.1.
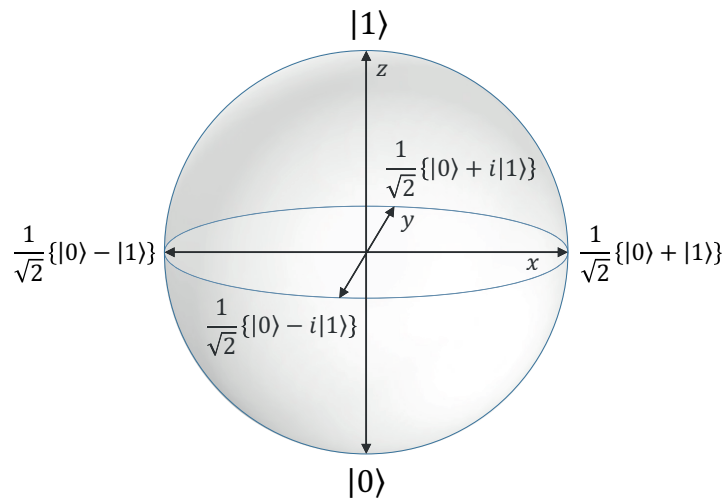
Figure 1.1: The Bloch sphere [7] - the surface represents all the possible states of a qubit. The z-axis shows the only classically allowed states $|0\rangle$ and $|1\rangle$, all other points on the surface are quantum mechanical superpositions.

1.1.2 *Qubit Registers*

The combined state of two noninteracting qubits with respective states $|\psi\rangle_A = c_0^A |0\rangle_A + c_1^A |1\rangle_A$ and $|\phi\rangle_B = c_0^B |0\rangle_B + c_1^B |1\rangle_B$ is defined by their tensor product:

$$\begin{aligned}
|\psi\rangle_A \otimes |\phi\rangle_B = {} & c_0^A c_0^B \,|0\rangle_A \,|0\rangle_B + c_0^A c_1^B \,|0\rangle_A \,|1\rangle_B \\
& + c_1^A c_0^B \,|1\rangle_A \,|0\rangle_B + c_1^A c_1^B \,|1\rangle_A \,|1\rangle_B \,.
\end{aligned} \tag{1.2}$$

However, the full Hilbert space of the composite system is defined by $H_A \otimes H_B$. This includes inseperable states where unlike Equation 1.2 the state of the composite system may not be written as a tensor product of states of the two systems. In this case, the criteria that the qubits do not interact has been relaxed and thus the qubits are *entangled*, for example the following state:

$$|\psi\rangle_{AB} = \frac{1}{\sqrt{2}} \left\{ |0\rangle_A \,|0\rangle_B + |1\rangle_A \,|1\rangle_B \right\} = \frac{1}{\sqrt{2}} \left\{ |00\rangle + |11\rangle \right\}, \tag{1.3}$$

which is one of the four Bell states [8] which exhibit the maximum degree of entanglement possible for 2 qubits.

These relations lead to some interesting results. Firstly, by considering Equation 1.2 for an n-qubit register, it becomes apparent that 2^n complex coefficients are required to completely describe the state of the system. Secondly, owing to entanglement the number of degrees of freedom of an n-qubit register is $2^{n+1} - 2$ rather than the $2n$ that would be expected without entanglement. The result is that the classical resources required to simulate a quantum system increase to the power of n and it is this that gives rise to the first compelling application of QIP.

1.1.3 *Quantum Simulation*

In subsection 1.1.2 it was shown that the resources required for classical simulation of quantum systems increase as a power law in the number of qubits (n). As many natural systems are fundamentally quantum in nature and involve large Hilbert spaces, an obvious application is to try to simulate these systems using QIP as first proposed by Feynman [9]. Current experimental state-of-the-art has seen trapped ions used to simulate the time dynamics of 6 interacting spins [10]. Whilst further scale-up is required to enter the classically

intractable region, this remains a very active area of research (see Ref. [11] for an excellent review) and is still a key motivation for QIP.

1.1.4   *Quantum Algorithms*

Beyond quantum simulation, QIP can also demonstrate a speed-up compared to classical information for certain calculations. Such problems are described by the Bounded Error Quantum Polynomial Time (BQP) [12] complexity class. Problems in this class may be solved by quantum algorithms in a time that scales polynomially with the "instance size" of the problem as opposed to exponentially for equivalent classical algorithms. In order to bring about improved performance, the properties of a qubit register described in subsection 1.1.2 are exploited. A common fallacy is that owing to the principles of entanglement and superposition, this is effectively massively parallel computing. However, all processing must end with a measurement which leads to a probabilistic collapse of the wavefunction to a single state. As such, an effective quantum algorithm engineers the maximal probability of measuring the correct outcome - that which contains the result of the computation.

Using this principle, algorithms have been defined for a number of BQP problems. Shor's Algorithm [13] for number factorising is probably the best known owing to its potential to break almost all public-key encryption systems currently in use. Other examples include Grover's Algorithm [14] for searching unordered lists and quantum equivalents of "random walk" problems [15]. Experimental demonstrations of algorithms are again still in their infancy though implementations of Shor's algorithm have shown factorization of 21 by a photonic QIP system [16].

1.2   DIVINCENZO CRITERIA

Since the advent of quantum information theory, a key challenge has been to develop a physical implementation of a qubit that is suitable for QIP. The requirements that a physical system must meet in order to be a viable candidate for QIP were formalized in the *DiVincenzo*

Criteria [17]. The criteria consist of 5 requirements for quantum computation plus a further two for networkability:

1. A scalable physical system with well characterized qubits

This requires a physical system matching the description of a qubit in subsection 1.1.1. The simplest case is that of a two-level quantum system although a two-dimensional subspace of a larger Hilbert space is a more typical case. In order for the qubit to be well characterized, the eigenstates of the system must be known and any couplings between the qubit subspace and other states must be accounted for. In order for the system to be scalable it must be practical to implement many such qubits whilst retaining the ability to address them individually.

2. The ability to initialise the state of the qubits to a simple fiducial state

In order to perform a reproducible computation, the initial state of the qubit register must be "initialised" each time to the same pure state, typically $|00...0\rangle$. Quantum error correction protocols also typically require a continuous supply of initialised qubits, imposing the requirement that initialisation is fast compared to the timescale of the computation.

3. Long relevant decoherence times, much longer than the gate operation time

Decoherence refers to degradation of the quantum state from a pure state to a mixed state due to interaction of the system with the environment. This gives the maximum time available for computation and hence the critical quantity is the ratio between the deoherence time and the gate operation time. An effective fault tolerant quantum computer requires around 10^4 gate operations within the coherence lifetime of the qubit [17].

4. A "universal" set of quantum gates

A "universal" set of quantum gates is a set of simple qubit operations that any computation may be decomposed into. Of note is the work of Barenco et al. [18] illustrating that any unitary n qubit gate may be expressed as a combination of only one-qubit gates and a single two-qubit gate.

5. A qubit-specific measurement capability

After completion of the computation it is necessary to measure the state of the qubit register. This generally takes the form of a projective measurement although this is not always possible. Again, the speed of the measurement relative to decoherence and the fidelity of the measurement are vital parameters.

6. The ability to interconvert stationary and flying qubits

In order to construct a quantum information processing network it is necessary to have both stationary qubits for long-lived memories and flying qubits for information transfer. In general, these two types of qubits have very different physical requirements leading to proposals with two or more different physical qubit implementations. In this case it becomes essential to convert efficiently and reliably between the different types of qubit.

7. The ability to faithfully transmit flying qubits between specified locations.

If any quantum network is to function reliably, the flying qubits must faithfully carry their encoded quantum state from point to point. Practically this means that decoherence should be minimal during transmission. This requirement is also essential for quantum communication protocols such as Quantum Key Distribution (QKD).

1.3 QUBIT CANDIDATES

1.3.1 *Photons*

A number of possible schemes exist for encoding a qubit state onto a single photon [19]. The simplest of these is to encode the qubit state on the polarization state of the photon. An alternative implementation, often used in "on-chip" processing is to encode the state using two different possible paths of the photon. Theoretical studies revealed that universal quantum computation with photons is possible using only beam splitters, phase shifters and single photon sources and detectors [20]. Owing to the very weak nature of both photon to photon and environmental interactions the qubit state is very robust
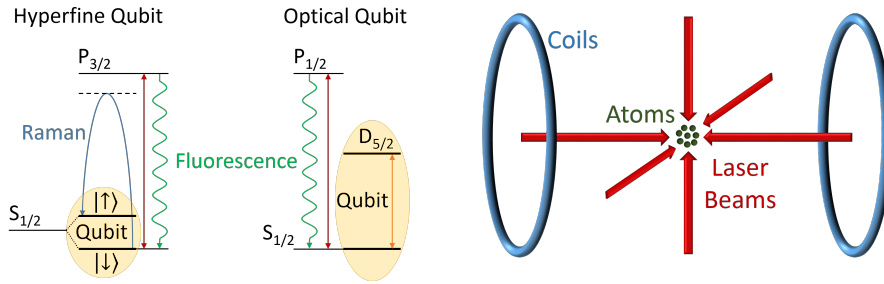
(a) Simplified energy levels of two common trapped ion qubit schemes. *Left:* Hyperfine qubit - the two qubit levels are hyperfine split spin states of the $S_{1/2}$ state. The qubit state may be manipulated by a Raman transition (blue arrow). *Right:* Optical qubit - the qubit levels comprise the $S_{1/2}$ state and the $D_{5/2}$ state. The qubit state is manipulated by direct driving of the transition (orange arrow). In both of these schemes pumping the additional $P_{n/2}$ level (red arrows) enables qubit readout by detecting state-dependent fluorescence (green arrows).

(b) A schematic of a typical magneto-optical trap for confinement of small numbers of atoms for QIP purposes. The coils provide initial confinement by electromagnetic fields whilst the 3-axis laser configuration produces a polarization gradient that leads to further reduction of the atoms kinetic energy [26]. This is often referred to as Sisyphus cooling.

Figure 1.2

against dephasing, with the primary error source being photon loss. In addition, photons may easily be guided between points in an on-chip geometry by confinement within waveguides [21]. This makes the photon an ideal flying qubit solution to the seventh DiVincenzo criterion. However, photon storage is very challenging and as such an alternative system is desirable for a stationary qubit implementation.

1.3.2 *Trapped Single Atoms / Ions*

Isolated single atoms [22, 23] or ions [24] in vacuum can provide qubit implementations with very weak decoherence owing to their excellent isolation from the environment [25]. A typical qubit is formed from a 2 level subspace of the atoms states, sometimes with further levels used as auxiliary levels (with care to avoid leakage of the qubit state to these levels) as illustrated in Figure 1.2a. These levels may be addressed with laser or microwave photons, allowing for manipulation of the qubit state.

The drawback to atomic and ionic qubits is that they are not inherently stationary. In one typical experimental geometry, a fountain of Rydberg atoms gives a continuous stream of individual atoms which are manipulated with microwaves [27]. A stationary approach is to use ion/atom traps whereby a cloud of ions [25] or atoms [28] are confined by electromagnetic fields and cooled and manipulated by lasers (see Figure 1.2b). This has worked well for laboratory experiments however attempts to miniaturize the traps have been impaired by anomalous heating effects [29, 30] leaving the scalability of the system in question.

1.3.3 *Crystal Impurity Centres*

Impurities in crystalline materials such as Nitrogen Vacancy (NV) centres in diamond [31, 32] or impurities in silicon [33, 34] can host an isolated electron [32] or nuclear spin [35] as illustrated in Figure 1.3a. This spin may be mapped to a single qubit state and manipulated by microwave or optical driving of transitions. Crystals may be prepared from isotopically pure nuclei which are spin zero [36] as shown in Figure 1.3a. This reduces the interaction between the qubit and the nuclear spins of the host material and allows for the longest coherence times of a solid state system [34]. Thus, these impurity centres are strong stationary qubit candidates.

Two significant drawbacks to NV centres are their strong coupling to phonons in the crystal [37, 38] and their random spatial formation. The strong phonon coupling leads to very broad luminescence spectra with as much as 90% of the photons emitted through the phonon sideband [39] (see Figure 1.3b), inhibiting efficient optical generation of entanglement between centres. Recent studies have overcome this by strongly enhancing emission into the ZPL by coupling to an optical cavity [40]. Meanwhile, implantation techniques have been developed as a means to deterministically position the centres [41].

1.3.4 *Atomic Nuclei Ensembles*

Nuclear Magnetic Resonance (NMR) techniques allow the manipulation of ensembles of nuclear spins by radio frequency pulses. As a

(a) Illustration of the atomic structure of a NV centre. The crystal vacancy (grey) is shown centrally and originates from the 3 bonds of the nitrogen atom (green) compared to the 4 of the carbons. In this illustration the sample has been isotopically purified to comprise almost entirely carbon-12 (red). In this situation a spin qubit may be formed either from the spin of a remaining carbon-13 nucelus (orange) or by loading a single electron (yellow) into the vacancy.

(b) Illustrative typical spectrum and energy level diagram of a single NV centre. As shown in the inset, strong phonon coupling enables radiative transitions (blue arrows) at lower energies than the ZPL emission (red arrow). As a result, the spectrum (black line shows total emission) shows a sharp line at the ZPL (red line) with a wide sideband comprising multiple broadened emissions from these radiative phonon transitions (other colours).

Figure 1.3

relatively mature system it has attracted interest for implementation of quantum algorithms in a range of materials [42]. However, the ensemble nature of the system has lead to questioning of the quantum nature of such measurements. Theoretical work indicates that these experiments are better viewed as a classical simulation of quantum computation as entanglement is not present [43]. It is also well-known that signal-to-noise considerations will prevent NMR systems from scaling up to larger numbers of qubits [44].

1.3.5 *Josephson Junctions*

Josephson junctions [45, 46] refer to a pair of superconductors joined by a linkage of lower conductivity. Combining these junctions into circuits allows for the creation of discrete energy levels. The non-linear inductance of the junction ensures that these energy levels are non-degenerate in energy which allows for the isolation of a single qubit sub-space. Depending on the parameters of the system, eigenstates may be formed in the basis of charge [47], phase [48], flux [49] or combinations of these [50].

The different implementations all share in common their macroscopic nature; whilst they behave as "artificial atoms" their qubit levels are quantum states of the *condensate* of carriers in the circuit as opposed to single particle states. This in combination with the non-dissipative nature of the superconducting junction means that the qubit states are remarkably robust against dephasing, with current state-of-the-art implementations having coherence times close to 100 μs [51] when integrated with waveguide cavities. Two drawbacks of the system are the relatively slow gate times for qubit operations [52] (~ 10 ns) and the need for ultra-low temperatures [48] (typically ~ 10 mK) to prevent thermal fluctuations exceeding the energy level spacing.

1.3.6 *Quantum Dots*

QDs are artifical structures in semiconductors whose dimensions are of the order of the de Broglie wavelength of charge carriers. This results in three-dimensional quantum confinement and gives rise to discrete energy levels for carriers within the dot. Because of this level structure, QDs are often termed artificial atoms. Quantum dots may be formed in many ways: epitaxial growth at the interface of lattice-mismatched solids [53], fluctuations in higher-dimensional structures such as quantum wells [54] or wires [55], colloidal nano-particles [56] or an electrostatic localizing potential in a 2D electron gas [57].

Being formed within a bulk semiconductor material gives QDs (excluding colloidal QDs) a number of advantages, beginning with their stationary nature. The semiconductor host also allows for integration with electrical circuits, enabling electrical control [58], tuning [59] and readout [60]. Furthermore, optical cavities [61] and waveguides [62] (e.g. photonic crystals) may be lithographically defined directly onto the semiconductor wafer allowing for enhanced light-matter interactions and efficient routing of photons between QDs.

However, the host material also presents drawbacks. Carriers confined within the QDs couple to phonons in the semiconductor lattice leading to pure dephasing [63, 64] although the resulting sideband is much smaller and weaker than NV centres [39, 65]. More significantly, the most common semiconductor materials (e.g. III-V materials such

as Gallium Arsenide (GaAs) or Indium Gallium Arsenide (InGaAs))
do not have spin-zero isotopes; hence nuclear spins present a strong
source of dephasing for qubits formed from QD confined carriers [66].

1.3.7 *Hybrid Systems*

The preceding sections serve to illustrate that at present all physical
implementations of QIP have both their strengths and drawbacks. As
a consequence, an emerging theme is that of *hybrid systems* whereby
multiple qubit implementations interact. Such systems would allow
the qubit system most suited to the particular task to be deployed. A
basic example of this concept is the transfer of information between
an optically active stationary qubit and a photon (e.g. for QDs [67–69]).
Processing of information may occur both through manipulation of
the stationary qubit and by passage of photons through optical logic
gates.

Beyond this, there is also interest in coupling different types of
stationary qubits, generally via photonic links. This is very much
an emerging field however early examples include coupling trapped
ions to QDs [70] and superconducting qubits to NV centres [71]. Whilst
there are significant obstacles to overcome, it is likely that future prac-
tical QIP schemes will be hybrids of some variety.

1.4 SEMICONDUCTOR QUANTUM OPTICAL CIRCUITS

The work contained in the experimental chapters of this thesis is mo-
tivated by the eventual goal of a complete QIP scheme integrated on-
chip on a III-V semiconductor wafer. Epitaxially grown InGaAs QDs
have the narrowest ZPLs of any type of QDs and so make both ex-
cellent stationary qubits and sources of flying photonic qubits (see
chapter 2). By integrating QDs within optical nanostructures such as
cavities or waveguides the photons may be efficiently routed around
the chip. Finally, superconducting nanowire detectors may also be in-
tegrated to enable efficient detection of single photons for quantum
state readout. A rendering of a concept device incorporating all of
these principles is illustrated in Figure 1.4. This concept is the subject
of the EPSRC (UK) programme grant EP/J007544/1 and provides the
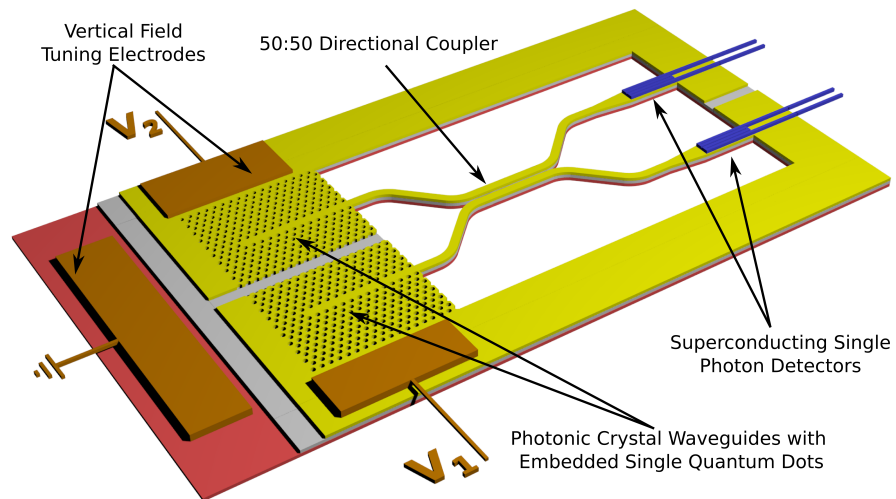
Figure 1.4: An illustration of a potential simple semiconductor quantum circuit device. Single photons are produced by a pair of InGaAs QDs embedded within photonic crystal waveguides to maximise their extraction efficiency. Application of independent electric fields to the tuning electrodes allows the energies of the two QDs to be matched. These single photons then interfere at a 50:50 beam-splitter formed by suspended ridge waveguides. Finally, the output photons are detected by superconducting detectors embedded at the end of the waveguides. Such a device would enable the demonstration of Hong-ou-Mandel interference between single photons, a fundamental result in linear quantum optics. Image courtesy of Rikki Coles, reproduced with permission.

motivation for the studies performed in this thesis. A comprehensive review of literature relevant to this scheme and the work presented in this thesis is given in chapter 2.

REVIEW

2.1 SELF-ASSEMBLY OF QUANTUM DOTS

In this section a brief review of the formation of QDs is presented, focusing on self-assembly through Stranski-Krastanov (SK) growth in III-V semiconductors. Strategies to locate and deterministically position individual QDs are also discussed.

2.1.1 *Quantum Wells, Wires & Dots*
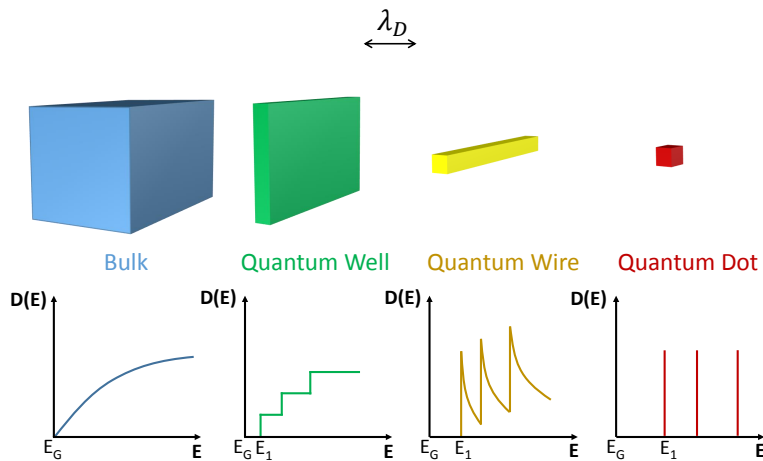
Figure 2.1: Comparison of the properties of bulk material and quantum wells, wires and dots. Characteristic changes in the density of states ($D(E)$) are observed with increasing number of confined dimensions.

Quantum wells, wires and dots are structures that act respectively as 1, 2 and 3-dimensional potential wells. As a confining potential becomes smaller than the characteristic de Broigle wavelength (λ_D), particles exhibit quantum confined behaviour. This is characterised by changes in the density of states ($D(E)$) with increasing number of confined dimensions as illustrated in Figure 2.1. For a quantum dot, discrete energy levels are formed, characterised by spaced delta-function peaks in $D(E)$. It is this level structure that gives rise to the
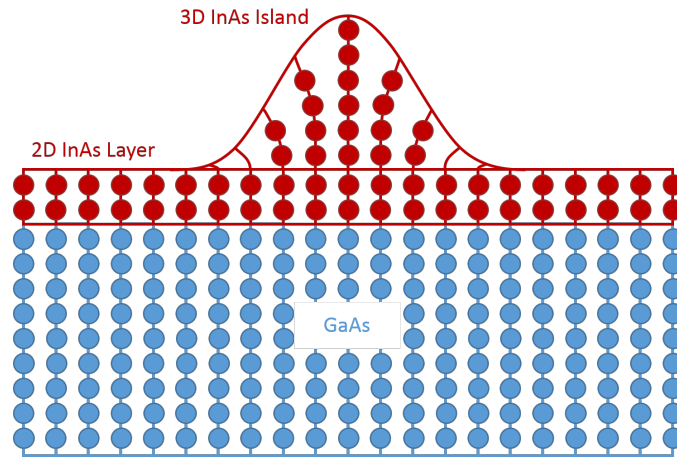
Figure 2.2: Illustration of the structure of an InAs/GaAs SAQD.

description of QDs as artificial atoms and also provides the levels required to implement a qubit.

2.1.2 *Formation & Self-Assembly*

The earliest observation of what is now termed a QD [72] was made in a glass matrix in the early 1980s [73]. As discussed in subsection 1.3.6, there are now numerous means of forming QDs. In this thesis "bottom-up" growth is considered as QDs grown by this method exhibit the highest optical qualities. This is supported by the observation of ZPL linewidths around $1\,\mu eV$ [74], essential for the production of highly indistinguishable photons and efficient quantum interference as required for QIP.

Epitaxial growth[1] of SAQDs [75–77] exploits the lattice mismatch between a substrate and growth material (e.g. GaAs/InAs). The growth material is typically deposited by Molecular Beam Epitaxy (MBE). At ultra-high vacuum, constituent elements are separately sublimed and subsequently condense on the substrate wafer where they react to form the crystalline growth layer. The lattice mismatch with respect to the substrate leads to a build-up of strain within the growth layer. After the growth of a thin 2D *"wetting layer"* [78–80] the strain increases to the point where formation of 3D coherently strained is-

---

1 Epitaxy refers to deposition with a fixed crystolographic orientation relative to the substrate.

lands is energetically favourable to further 2D layers [78]. This is known as SK growth [81–83] as illustrated in Figure 2.2.

By burying the dots (*"overgrowth"*) 3D carrier confinement is obtained and a quantum dot is formed. Such dots are termed *"self-assembled"* owing to the stochastic nature of the process. More detailed information on the self-assembly of QDs is widely available in the literature [83–85].

A consequence of the stochastic growth mechanism is that there is typically a distribution in the size (and thus energies) of SAQDs. Changes to the growth conditions (e.g. temperature, deposition rates) present a means to modify both the energies and the density of QDs that form. For QIP applications it is desirable to address individual QDs and thus growth conditions are typically tailored towards low-density growth.

2.1.3   *Positioning & Site Control*

A further requirement for any practical QIP scheme involving SAQDs is to interface multiple QDs acting either as single photon sources or spin qubits. Hence, it is necessary to acurately determine the position of individual QDs and preferable to be able to deterministically control the positions at which SAQDs form. In the following sub-sections several approaches to this problem are reviewed.

Dot Registration

Dot registration refers to methods which allows the position of QDs to be accurately determined and registered. Whilst this does not offer control over the positioning of dots, it allows dots of appropriate properties to be located. Nano-optics such as cavities and waveguides may then be fabricated around the dots. Previously such fabrication has relied upon a probabilistic approach [61] to obtaining the required coupling which is highly inefficient as it often takes many samples to find one with a suitably coupled dot. It is also clear that this approach is unsuitable for producing more complex quantum optical circuits potentially involving multiple dots.

Some schemes have located dots using Atomic Force Microscopy (AFM) to find the areas of strain that lead to QD nucleation with a

typical fabrication accuracy of the dot within ± 30 nm of the center of an optical microcavity [86, 87]. However, all-optical schemes have also shown considerable success and offer simpler implementation.

A common optical approach is to locate dots via. cryogenic Micro-Photoluminescence (μPL) spectra (or indeed recently cathodolumin-escence in-situ in an Electron Beam Lithography (EBL) setup [88]). Multiple luminescence scans are performed in the x-y plane to build up an intensity map of the QD emission. By fitting Gaussian intensity profiles along the x & y axes the position of the dot may be located to much higher precision than the diameter of the excitation laser [89–91]. Alignment markers either pre-patterned in gold [90, 91] or in-situ etched in photo-resist [89] allow the QD to be subsequently relocated.

EBL fabrication around the dot is then possible to a typical accuracy of ± 30 nm [90]. This has enabled the deterministic fabrication of Photonic Crystal Cavities (PCCs) [90] and micropillar cavities [92] coupled to a single target QD.

Site Control by Surface/Sample Modification

One approach to obtaining semi-deterministic growth of QDs is to locally modify the surface properties in order to give preferential growth within these regions. Typically these schemes involve surface lithography in order to pattern the substrate followed by deposition of various growth layers depending upon the scheme used. Calculation of the strain distribution shows that InAs islands nucleate at sites where the surface stress is highest such as the edges of litho-graphically defined features [79]. Such an approach has been used to grow regular arrays of InAs quantum dots localised to lithographic-ally defined mesas [93, 94] or pits [95, 96]. However, in early work it proved difficult both to isolate individual QDs and to prevent strong inhomogeneous broadening resulting from the surface modifications.

A significant recent breakthrough has been the use of a buried ox-ide stressor layer [97]. This layer manipulates the strain fields at the surface and causes selective nucleation during the growth process. The benefit of this approach is that the growth surface remains defect-free, preventing inhomogeneous broadening. Resolution-limited line-widths of 40 μeV [97] have been observed though at present this re-mains significantly larger than non site-controlled QDs.

An alternative approach is pyramidal quantum dot growth [98–100] whereby a different mechanism to conventional SK growth is used. QDs form within epitaxially grown pyramids whose location is defined by pre-deposited gold nanostructures. The linewidths of these QDs are again inferior to non-site controlled growth. Additionally, their protruding pyramidal structure and requirement for growth in the (111) crystal orientation² may present significant obstacles to integrating QDs of this type with nano-optics such as cavities and waveguides.

QDs Within Site Controlled Nanowires

Another approach is to incorporate QDs within site-controlled nanowires. Nanowires may be formed by epitaxial growth methods with their nucleation sites defined by surface modifications [101–104], similar to the surface modification methods previously described. QDs may be incorporated by deposition of a thin layer of a different semiconductor during the growth of the wire to produce 3D confinement [105–107]. However, these QDs also often suffer from large inhomogeneous broadening due to the proximity of the surface of the wire with typical linewidths an order of magnitude greater than conventional QDs [107]. Furthermore, integrating such QDs with nano-optics is an unresolved challenge.

2.2 ELECTRONIC STRUCTURE OF QUANTUM DOTS

In this section a brief outline of the band and orbital structure of carriers confined in SAQDs is presented. Following this, the excitonic complexes that these carriers may form are discussed and the main energy levels and transitions relevant to this thesis are reviewed.

2.2.1 Band Structure

In bulk III-V semiconductor materials the conduction band originates from s orbitals of the constituent atoms [108] whilst the valence band is primarily p-type in character with a contribution from d orbitals [109]. As a result, electrons confined within a SAQD have an atomic

---

2 Conventional SK growth of QDs is typically performed in the (001) orientation.

$$J = \frac{1}{2}, J_z = \pm\frac{1}{2}$$

$$J = \frac{3}{2}\begin{cases} J_z = \pm\frac{3}{2} \\ \\ J_z = \pm\frac{1}{2} \end{cases}$$

$$J = \frac{1}{2}, J_z = \pm\frac{1}{2}$$
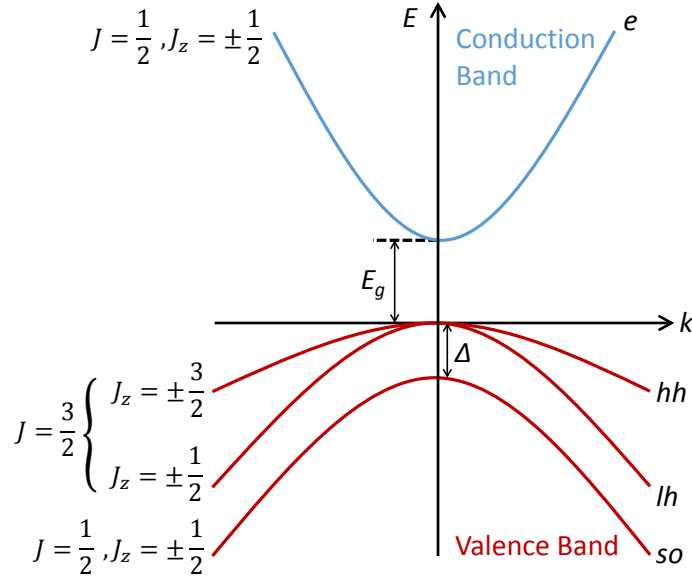
Figure 2.3: Illustration of the typical band structure of a III-V semiconductor material. The conduction band (blue) contains a single band which is split from the valence band by the bandgap (E_g). The valence band (red) contains three bands, the Heavy Hole (HH), Light Hole (LH) and Split-Off (SO) bands. The SO band is split from the other bands by the spin-orbit splitting (Δ). At $k = 0$ (Γ point) the HH and LH bands are degenerate however they split with increasing k.

s-type wavefunction with zero orbital angular momentum ($\mathbf{L} = 0$). The total angular momentum ($\mathbf{J}$) is given by Equation 2.1:

$$\mathbf{J} = \mathbf{L} + \mathbf{S} \qquad (2.1)$$

where $\mathbf{S}$ is the spin angular momentum, defined as $|\mathbf{S}| = s_z^e = 1/2$ for the electron. Hence the total angular momentum of the electron is given by $J = s_z^e = 1/2$. Two projections of the spin are possible along the z-axis ($m_{s,z}^e = \pm 1/2$) corresponding to the spin up / down ($\uparrow/\downarrow$) states of the electron.

The dominant p-type nature of the hole wavefunction gives an orbital angular momentum for holes of $|\mathbf{L}| = l^h = 1$ resulting in a more complex picture [110, 111]. The eigenvalues of J are given by $|l - s|$ and $|l + s|$. Thus as $l^h = 1$ these eigenvalues are $J = 3/2$ and $J = 1/2$. Each of these states may contain any half-integer J_z value between J and $-J$. Hence the $J = 3/2$ band may contain $J_z = \pm 3/2, \pm 1/2$ whilst the $J = 1/2$ band may contain only $J_z = \pm 1/2$ and is split-off to lower

energy by the *spin-orbit splitting* (Δ) which is around 0.1 to 0.5 eV for typical III-V semiconductors [112]. In turn, holes in the $J = {}^3/_2$ band with $J_z = m_{j,z}^{hh} = \pm 3/2$ are referred to as Heavy Holes (HHs) whilst those with $J_z = m_{j,z}^{lh} = \pm 1/2$ are referred to as Light Holes (LHs). The HH and LH bands are degenerate at the Γ point of a bulk semiconductor (see Figure 2.3). However, in a SAQD the broken symmetry of the system, different quantum confinement energies and the strain present lead to a splitting on the order of 30-300 meV [112–114] with the LH band at higher energy.

2.2.2 *In-Plane Orbitals*

As discussed in subsection 2.1.1, the electronic structure of a QD is very different to that of bulk material. In the case of InGaAs QDs (Figure 2.4a), the band gap of InGaAs is lower than that of GaAs (see Figure 2.4b) which leads to 3D confinement and the discrete density of states illustrated in Figure 2.1. The strain arising from the lattice mismatch between the two materials (see subsection 2.1.2) leads to modifications of the confinement potential [84, 115]. A further influence is that in the (001) orientation typical of InGaAs SAQDs, the anisotropy of the crystal means piezoelectric fields may also modify the potential [116]. However, for typical SK growth this may be neglected [116]. The end result of these modifications is that the confinement potential of a SAQD may be well approximated by a parabolic confinement potential resulting in the same energy spectrum as the 2D harmonic oscillator [117–119].

The height of SAQDs is generally much smaller than the diameter of their base (see Figure 2.4a) [78] leading to stronger confinement of carriers along the vertical axis. As a consequence, the energy spacing of vertically confined levels is much larger than than those in the growth plane allowing higher vertical states to be neglected. The in-plane orbital angular momentum of carriers leads to an orbital structure of circularly symmetric harmonic wavefunctions [113, 119]. These orbitals are analagous to the spherically symmetrical orbitals found in atomic physics (*s, p, d, f...*) though they are two-dimensional as they only describe in-plane angular momentum.
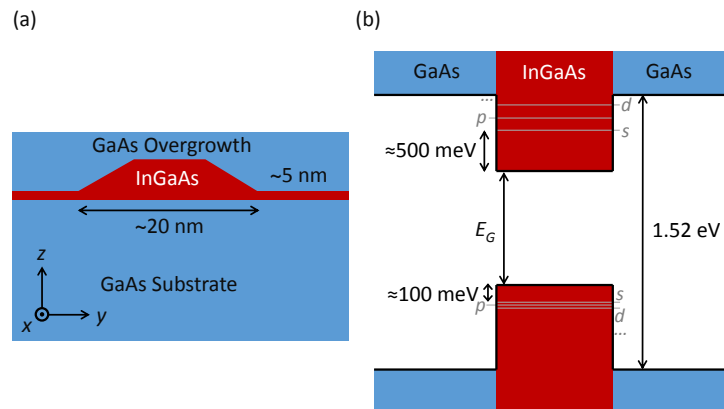
Figure 2.4: (a) Schematic of a truncated pyramid InGaAs SAQD showing typical dimensions. The InGaAs QD is formed on top of a 2D wetting layer before being burried by GaAs overgrowth leading to 3D confinement. (b) Illustration of the band gaps of InGaAs and GaAs at 4.2 K (liquid Helium temperature) - carriers in the InGaAs QD are confined owing to the smaller band gap. The band gap of InGaAs depends strongly on the ratio of Indium to Gallium with increased Indium incorporation reducing the band gap [120]. Typical values for the conduction and valence band offsets of InGaAs SAQDs are shown [79].

A consequence of this is that the *s, p, d...* shells of SAQDs may only accomodate 1, 2, 3... electron (or hole) opposing spin pairs respectively (see Figure 2.5) [113, 121] whilst the equivalent 3D atomic shells may contain 1, 3, 5... of such electron pairs. Selection rules only allow valence band electrons to be promoted to the same conduction band shell (excluding a weakly allowed $s \to d$ transition) [113, 121] although this may be relaxed by shell mixing in asymmetric QDs [113, 121].

2.2.3 *Neutral Excitons*

When an electron is promoted to the conduction band of a semiconductor, Coulomb attraction between this electron and the resulting hole in the valence band can bind the two. This bound electron-hole pair may be described as a quasiparticle - an *exciton*. In a typical InGaAs SAQD, the confinement (see Figure 2.4 and Figure 2.5 for typical energy scales) is comparable to the electron-hole Coulomb interaction (~ 30 meV [122]). Hence, the Coulomb interaction is treated as a peturbation to the energies of the single particles - this is termed the exciton binding energy. As discussed in subsection 2.2.1, both the LH and SO bands are split to significantly higher energies in SAQDs and thus generally only excitons containing Heavy Holes (HHs) are considered. It is worth noting however that LH excitons have been observed in elastically-stressed unstrained QDs [123] and that both asymmetric QDs [124] and QDs in an in-plane magnetic field have exhibited significant HH-LH mixing.

An electron-hole pair both in their respective *s*-shells combine to form the ground-state exciton. The possible z-axis spin projections (S_z) of this quasiparticle are given by Equation 2.2:

$$S_z = m_{j,z}^{hh} + m_{s,z}^{e} = \pm 3/2 \pm 1/2 = -2, -1, 1, 2 \qquad (2.2)$$

Absorption/emission of a single circularly-polarized photon may only impart a change in angular momentum of ± 1 [125]. Hence $S_z = \pm 1$ "bright excitons" (typically notated as X^0) with circular polarization ($|\uparrow\Downarrow\rangle$ and $|\downarrow\Uparrow\rangle$) are optically allowed whilst $S_z = \pm 2$ "dark excitons" are optically forbidden and cannot be directly observed in lumines-
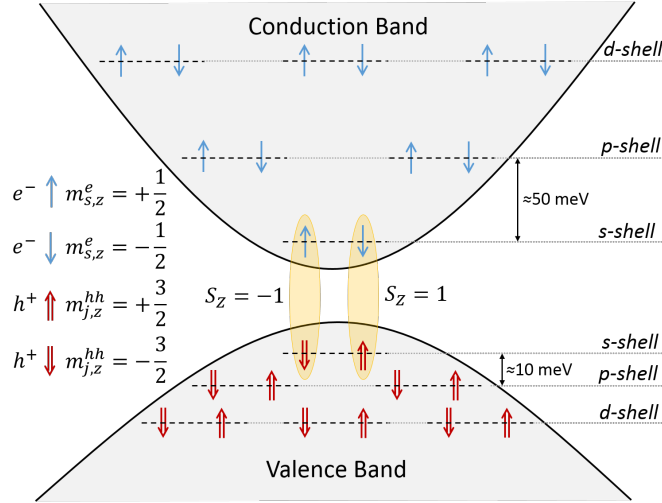
Figure 2.5: Level structure of a QD with s, p, and d shells filled with carriers. Each shell may contain respectively one, two or three pairs of electrons / Heavy Holes (HHs) with opposite spins. The energy spacing of the conduction band states is signficantly larger than those in the valence band, typical scales for InGaAs SAQDs are shown [79]. The $S_z = \pm 1$ s-shell bright exciton states have opposite electron/hole spins and are highlighted in yellow. The $S_z = \pm 2$ dark excitons correspond to same-spin pairs. The LH and SO bands are ignored for the purposes of this figure.

cence measurements. In Figure 2.5 the level structure of a QD whose s, p, and d shells are filled with carriers is shown. The s-shell bright excitons are highlighted in yellow.

2.2.4 Exciton Fine Structure

An "ideal" QD exhibits radial symmetry in the growth (x-y) plane. However, the self-assembly process typically leads to QDs with some degree of asymmetry. In this case the two bright exciton states become coupled by the electron-hole exchange interaction [126], leading to a precession between the $S_z = \pm 1$ states with angular frequency δ [127]. As a result, the eigenstates of the exciton now become linearly polarized as defined in Equation 2.3:

$$
\begin{aligned}
|X_x\rangle &= \frac{1}{\sqrt{2}}\{|\downarrow\Uparrow\rangle + |\uparrow\Downarrow\rangle\} \\
|X_y\rangle &= \frac{1}{\sqrt{2}}\{|\downarrow\Uparrow\rangle - |\uparrow\Downarrow\rangle\}
\end{aligned}
\tag{2.3}
$$

Symmetric QD   Asymmetric QD

$$|X_x\rangle = \frac{1}{\sqrt{2}}\{|\downarrow\Uparrow\rangle + |\uparrow\Downarrow\rangle\}$$

$$|X_y\rangle = \frac{1}{\sqrt{2}}\{|\downarrow\Uparrow\rangle - |\uparrow\Downarrow\rangle\}$$
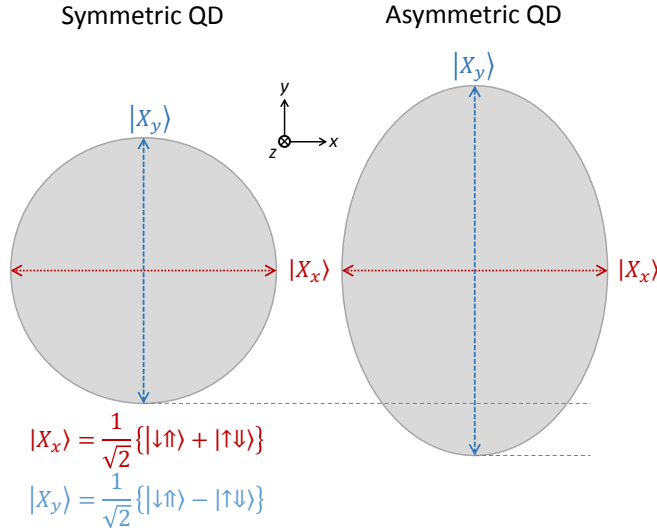
Figure 2.6: Growth plane $(x - y)$ illustration of the influence of asymmetry on a QD. As the QD becomes elongated along one axis the eigenstates become linear with an energy splitting $\hbar\delta$.

The magnitude of the Fine-Structure Splitting (FSS) between the two eigenstates is determined by the degree of elongation of the QD as illustrated in Figure 2.6.

As the splitting originates from the growth process [128] and is detrimental for a number of QIP applications [129–131], modified growth protocols have been developed to attempt to deterministically grow symmetric QDs [100, 132, 133]. Studies have also seen reduction of the FSS by post-growth thermal annealing [134–137]. Whilst such methods have reduced the variance of the FSS, it is not currently possible to deterministically grow fully symmetric QDs. As such, in-situ methods for tuning FSS are widely studied, using strain [138, 139], magnetic [140] and laser [141, 142] fields as well as both lateral [143–145] and vertical [146, 147] Direct Current (DC) electric fields.

2.2.5 *Biexcitons*

As shown in Figure 2.5, the s-shells of both the conduction and valance bands can be occupied by two carriers with opposite spins. Therefore it is possible for both of the $S_z = \pm 1$ neutral excitons to exist simultaneously, forming a *biexciton* (generally notated either XX or $2X$). Much in the same manner as the formation of excitons, Cou-
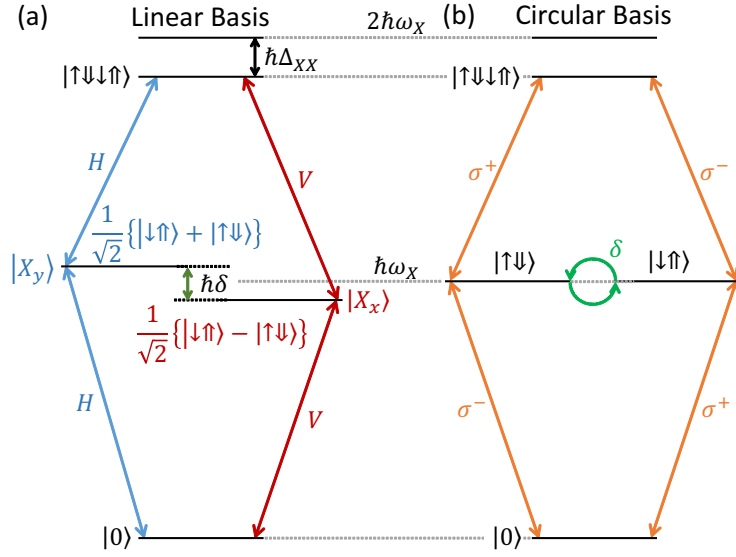
Figure 2.7: Illustrative energy level diagram of the *s*-shell neutral exciton & biexciton: (a) In the basis of linearly-polarized optical transitions the two eigenstates $|X_x\rangle$ and $|X_y\rangle$ are split by the FSS ($\hbar\delta$). (b) For circularly-polarized excitation with a linewidth $> \hbar\delta$ the FSS instead causes precession between the two states, indicated by the green arrows. The exciton transition energy is given by $\hbar\omega_X$ whilst the biexciton binding energy is given by $\hbar\Delta_{XX}$. For clarity, the splittings in the diagram are not to scale as $\hbar\delta \ll \hbar\Delta_{XX} \ll \hbar\omega_X$.

lomb interactions between the two excitons result in a binding energy ($E_{XX} = \hbar\Delta_{XX}$) that reduces the transition energy to less than the energy of 2 excitons. The resulting energy level structure is illustrated in Figure 2.7, the so-called biexciton cascade. Figure 2.7(a) shows the energy levels in the basis of linear excitation. The eigenstates of the system are linear and split by the FSS energy $\hbar\delta$. For circular excitation as shown in Figure 2.7(b), single exciton spin states are excited and the energy splitting is zero. However, as the eigenstates of the system are linear, the exciton spin precesses with a frequency δ.

A particular application of the biexciton cascade is as a source of entangled photon pairs. These are emitted when the biexciton relaxes to the ground state via the exciton state [129, 130, 148]. For this application low FSS is critical as otherwise the two H/V decay paths have different energies, leading to reduced entanglement.
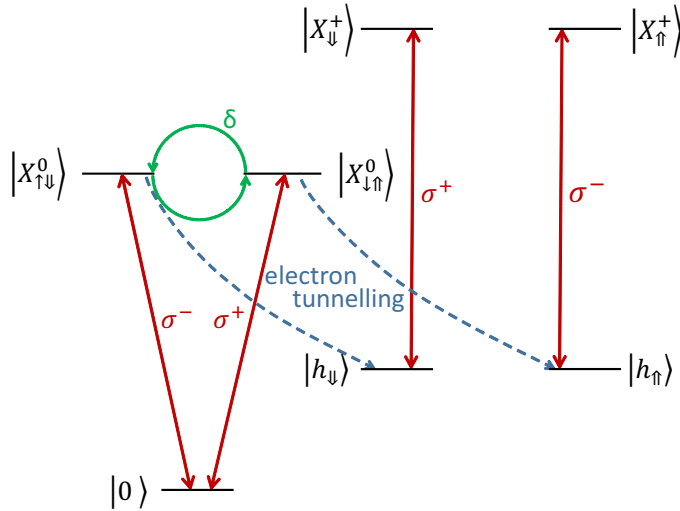
Figure 2.8: Schematic illustrating the initialisation of a single hole by exciton ionization. On the left are the exciton energy levels in the circular basis as in Figure 2.7. After electron tunnelling only a single hole remains. Excitation of this hole with circularly polarized light leads to the creation of a positively charged trion as illustrated on the right. In the case of a single electron the level structure is identical except the trion now has negative charge.

2.2.6 *Single Carriers & Trions*

Single carriers (electrons or holes) may also be confined and manipulated within QDs. Typically this is motivated by the much longer coherence times that are possible compared to excitons (see subsection 2.4.1). The process is significantly more complicated though as a single carrier cannot be photoexcited like an exciton. Typical strategies to isolate single carriers employ QDs embedded within diode structures either to ionize a photoexcited exciton [127, 149–152] or to deterministically charge the QDs [153–158]. It is also possible to add a dopant layer during sample growth; by tuning the doping concentration, it is possible to produce a mean carrier occupation of 1 in the QDs at equilibrium [159, 160]. Figure 2.8 illustrates the principle of hole spin initialisation by exciton ionisation. An exciton is created by circularly polarised light before undergoing ionisation by electron tunnelling to leave behind a single hole with spin inherited from the exciton. This process is studied in detail in chapter 4.

Once a single carrier has been isolated, the energy level structure (see Figure 2.8) is similar to that of the ground state - exciton system.

Photoexcitation of the single carrier adds an additional electron-hole pair to the system, leading to the formation of a charged exciton referred to as a *trion*. A single electron leads to a negatively charged trion (e.g. $|X^-\rangle = |\uparrow\Uparrow\downarrow\rangle$) whilst a single hole leads to a positively charged trion (e.g. $|X^+\rangle = |\Uparrow\uparrow\Downarrow\rangle$). As shown in Figure 2.8, these trion transitions have orthogonal circular polarization which forms the basis for various spin-readout schemes as each carrier spin state is coupled only to one trion.

2.3   QDS IN EXTERNAL FIELDS

In this section the influence of external electric and magnetic fields on the QD energy levels is detailed. Both static and alternating electric fields are considered in addition to magnetic fields oriented either within or out of the sample plane.

2.3.1   *Electric Fields*

Quantum-Confined Stark Effect

In SAQDs the material composition of the QD is not uniform owing to varying degrees of gallium incoroporation into the InAs QD layer. Studies have shown that for typical SK growth of InGaAs SAQDs, the electron & hole wavefunctions are vertically aligned [161, 162]. However, the hole wavefunction is localized in the region of high indium content towards the top of the QD with the electron towards the bottom [161, 162]. A consequence of this is that SAQDs typically possess a strong permanent electric dipole moment (p).

When a DC electric field is applied to the QD, the electron and hole confinement energies are modified by the Quantum-Confined Stark Effect (QCSE). Phenomenologically, with increasing electric field the electron and hole wavefunctions become further separated, reducing the Coulomb attraction and leading to a red-shift of the exciton energy. The energy shift of a transition ($\triangle E_{Stark}$) due to an applied DC electric field strength (F) varies quadratically and is given by Equation 2.4 [161, 162]:

$$\triangle E_{QCSE} = pF + \beta F^2, \tag{2.4}$$
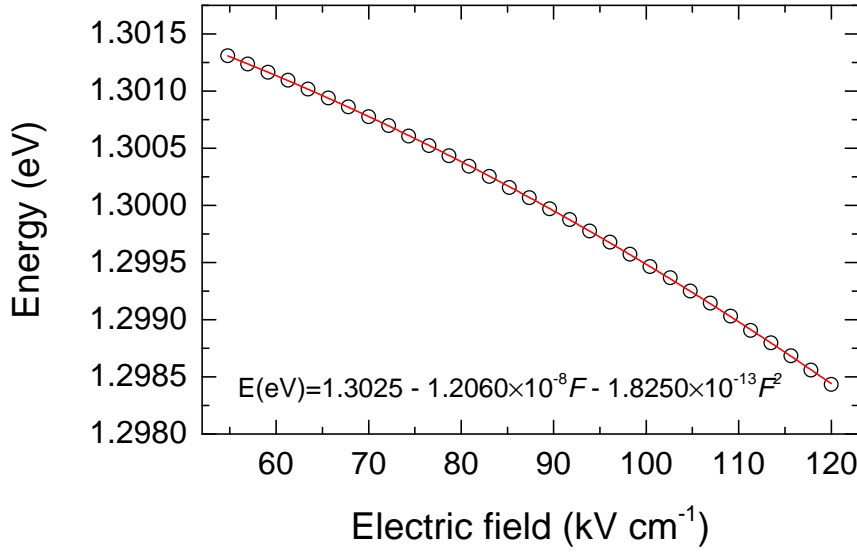
Figure 2.9: Measurement of the exciton energy vs. applied DC electric field for a QD in the photocurrent sample (see subsection 3.4.1). A clear quadratic redshift of the exciton energy is seen with increasing electric field. The red line is a fit of Equation 2.4 which allows the values of p and β to be determined. The data was measured by taking photocurrent spectra at different biases and fitting the peak energies.

where β is the electric polarizability in the direction of the DC field. Owing to the physical origin of the shift, it is possible to use the DC Stark shift to determine the electron and hole separation [162]. The primary application of the QCSE, however, is to tune the exciton energies of QDs for applications such as coupling to an optical cavity (as demonstrated in chapter 6) or tuning two separate QDs into resonance. This tuning of energy along with extraction of the values of p and β is illustrated in Figure 2.9.

As the QD dipole is oriented along the growth (z) axis, the largest energy shifts due to the QCSE are observed for devices which have a vertical electric field. This is usually achieved by the incorporation of doped layers which produce a diode structure in the QD wafer [153–155, 161, 163]. A smaller effect may be produced by application of a lateral electric field. However, the primary application of such devices is to tune the FSS by compensating asymmetry in the confinement potential as previously discussed [143–145].
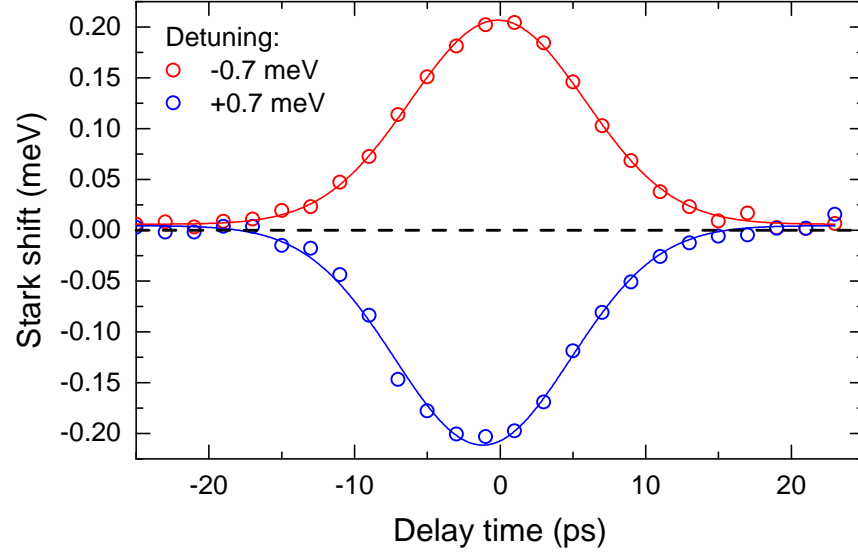
Figure 2.10: Measurement of the optical Stark shift of a QD exciton trans-
ition. The laser pulse has pulse area $\Theta = 5.25\pi$ and is de-
tuned by $\pm 0.7\,\text{meV}$ (blue/red data) from the exciton transition
which is co-polarised with the laser. The data was measured by
performing time-resolved pump-probe photocurrent measure-
ments similar to those described in subsection 5.4.1.

Optical Stark Effect

Stark shifts of QD transitions are not limited only to DC electric fields.
Application of an Alternating Current (AC) electric field also leads
to a shift that depends both on the frequency and strength of the
electric field. In QDs this is generally induced by an additional laser
field of angular frequency ω_l and is referred to as the Optical Stark
Effect (OSE). The shift is described by Equation 2.5 [164]:

$$\Delta E_{OSE}\left(t\right) = \frac{\hbar}{2}\left(\Delta - \sqrt{\Delta^2 + |\Omega_R\left(t\right)|^2}\right)$$

$$\Omega_R\left(t\right) = \frac{\mu E_l\left(t\right)}{\hbar}, \tag{2.5}$$

where $\Delta = \omega_0 - \omega_l$ is the detuning of the laser from the transition
(which has angular frequency ω_0), $\Omega_R\left(t\right)$ is the Rabi splitting, μ is
the transition dipole moment and $E_l\left(t\right)\cos\left(\omega_l t\right)$ describes the elec-
tric field of the laser. Figure 2.10 shows the optical Stark shift of the
neutral exciton induced by a strong laser pulse which is detuned by
$\pm 0.7\,\text{meV}$. The sign of the energy shift is swapped by the sign of the
detuning. The solid lines are Gaussian fits to the data, indicating that
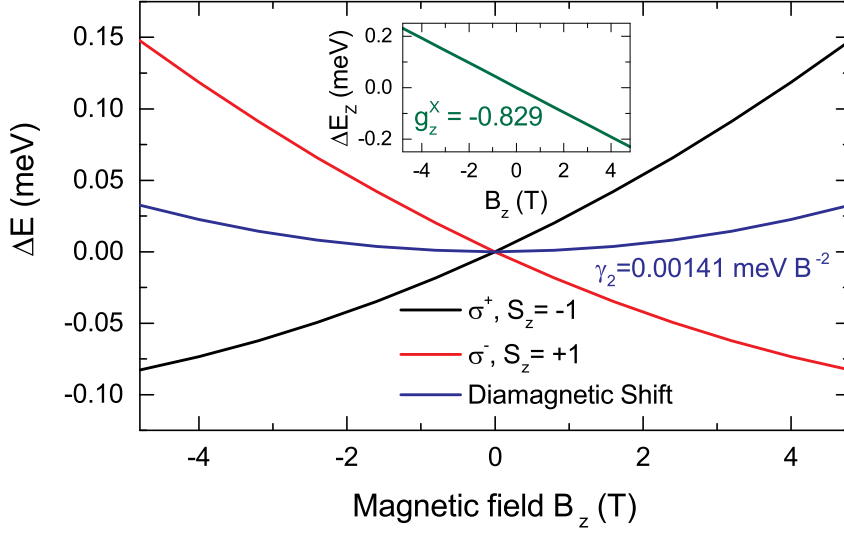
Figure 2.11: Illustration of the influence of an external magnetic field on the energies of the neutral exciton spin-states. The σ^+ / $S_z = -1$ and σ^- / $S_z = +1$ states are shown by the black and red lines respectively, whilst the blue line shows the magnitude of the diamagnetic shift which can be extracted from a fit of Equation 2.7. The green line in the inset shows the variation of the Zeeman splitting ($E_{\sigma^-} - E_{\sigma^+}$) with magnetic field; g^X may be extracted by fitting Equation 2.6. The lines plotted here were calculated from experimental measurements of γ_1 and γ_2 in an out-of-plane magnetic field.

the shift follows the Gaussian envelope of the laser electric field as would be expected from the $\Omega_R(t)$ term in Equation 2.5.

A significant property of the OSE is that the shift is sensitive to polarization, meaning that transitions orthogonally polarized to the laser are not shifted. This has been exploited to cancel FSS by shifting only one eigenstate in order to restore the energy degeneracy [141, 142]. This approach is employed to improve the fidelity of hole spin initialisation in section 4.7.

2.3.2   Magnetic Fields

As a magnetic field (B) is applied to the QD, the electron and hole levels become increasingly *Zeeman* split owing to the opposing signs of m_j for the two s-shell carriers. The magnitude of this splitting is determined by Equation 2.6:

$$E_Z^i = g^i \mu_B B, \tag{2.6}$$

where g^i is the Landeé g-factor for the carrier or exciton complex denoted by the index i (e electron, h hole, X neutral exciton) and μ_B is the Bohr magneton. As the value of g^i contains an implicit factor of m_j, the measured hole g-factor evaluated according to Equation 2.6 includes an additional factor of 3 compared to the electron, allowing the hole ($m_j = \pm 3/2$) to be regarded as having a *pseudospin* of $\pm 1/2$.

This allows the definition of the exciton g-factor as $g^X = g^h - g^e$. In addition, for the neutral exciton a weak quadratic *diamagnetic shift* is also observed [165–168]. This shifts the exciton emission to higher energy irrespective of spin, unlike the g-factor. Thus the total energy shift of an exciton in a magnetic field may be described by Equation 2.7:

$$\Delta E = \gamma_1 B + \gamma_2 B^2, \tag{2.7}$$

where γ_2 is the diamagnetic coefficient and $\gamma_1 = \frac{S_z g^X \mu_B}{2}$.

Two fundamentally different sets of behaviour are observed depending upon if the magnetic field is orientated within or out of the sample plane. These are outlined in the following subsections.

Faraday (Out-of-Plane) Geometry

A *Faraday* geometry magnetic field is a magnetic field that is oriented along the growth (z) axis of the QD (i.e. out of plane). Measurements of the exciton g-factor in such a field have found a typical range of $-3 \lesssim g_z^X \lesssim -1$ for InGaAs SAQDs [169, 170]. It should be noted, however, that g-factors are sensitive to QD size, shape, strain and material composition [170] and hence variation between samples is common. Measurements of the magnitude of the individual carrier g-factors for a single InGaAs SAQD have found $\left|g_z^h\right| = 0.53$ and $\left|g_z^e\right| = 0.60$ for a Faraday magnetic field [171].

For an asymmetric QD ($\delta > 0$), the initially linear eigenstates (see Figure 2.7) become the circular eigenstates $|\uparrow\Downarrow\rangle$ and $|\downarrow\Uparrow\rangle$ once $E_{Z_z}^X > \hbar\delta$. This can provide a means to cancel the fine-structure precession with demonstrated applications such as entangled photon pair production [129] and high fidelity spin initialisation by exciton ionization [172] (see also section 4.5).
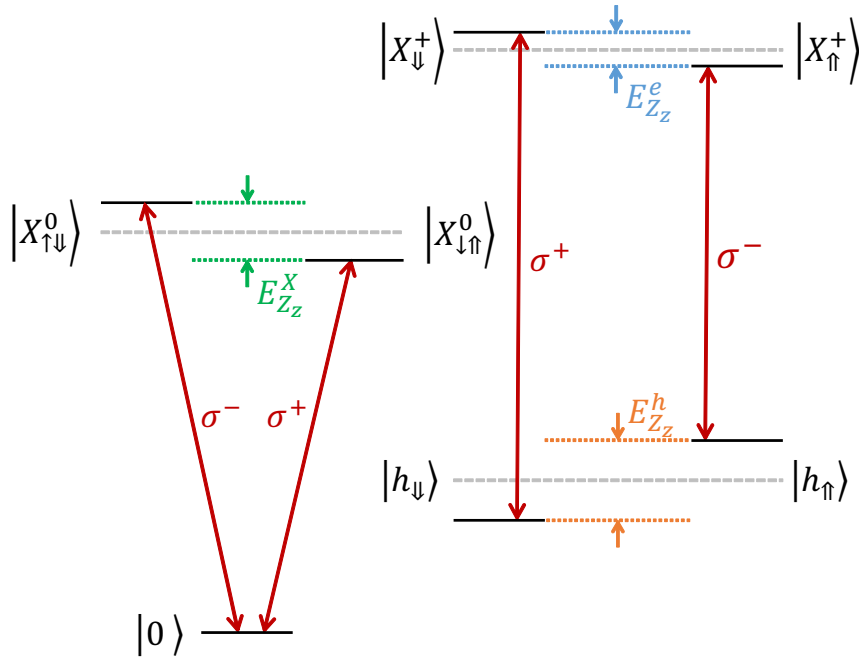
Figure 2.12: Energy level schematic of the neutral exciton and hole-trion transitions in a Faraday (out-of-plane) magnetic field. The hole levels are split by the hole Zeeman splitting ($E_{Z_z}^h$) whilst the trion levels are split by the electron Zeeman splitting ($E_{Z_z}^e$) as they contain two holes of opposite spin with a single electron. The exciton levels are split by the exciton Zeeman splitting ($E_{Z_z}^X$) which contains both electron and hole contributions. These splittings grow with increasing external magnetic field (B_z) according to Equation 2.6.
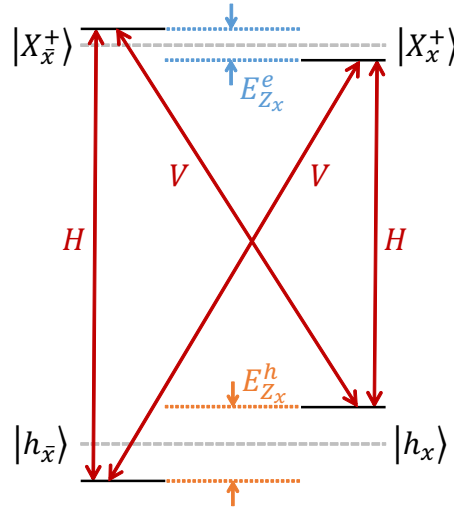
Figure 2.13: Hole-trion energy levels in a Voigt geometry magnetic field directed along the x-axis. States are labelled as either parallel (x) or anti-parallel ($\bar{x}$) to the magnetic field.

Another class of applications for an out-of-plane magnetic field is to energetically split single carrier levels. This enables detection of the spin state of the carrier by spectrally resolving the hole-trion transitions. Significantly, unlike an in-plane magnetic field, the "diagonal" transitions between a trion and a carrier of the opposite spin are only very weakly allowed (around 450 times weaker than the "vertical" transitions [173]) due to HH-LH mixing [173] and the hyperfine interaction with nuclear spins [174]. This enables single-shot readout of the carrier spin by repumping the trion transitions with a Continuous-Wave (CW) laser and performing spectrally-selective detection [173]. A similar approach may also be used to initialise single carrier spins [156].

Voigt (In-Plane) Geometry

A *Voigt* geometry magnetic field is orientated within the sample (x-y) plane, perpendicular to the growth axis. Depending on the degree of asymmetry of the QD confinement, the bright ($S_z = \pm 1$) and dark ($S_z = \pm 2$) exciton states may become mixed in such a field [169]. As such, the bright/dark exciton eigenstates are no longer clearly defined and it is simpler to consider single carrier states. The g-factors of both electrons [171, 175, 176] and holes [171] are known to be anisotropic for InGaAs SAQDs with the hole exhibiting significantly

stronger anisotropy. For a specific InGaAs SAQD, in-plane g-factor magnitudes of $\left|g_x^h\right| = 0.08$ and $\left|g_y^h\right| = 0.23$ have been measured for the hole whilst for the electron the magnitudes were $\left|g_x^e\right| = 0.54$ and $\left|g_y^e\right| = 0.52$ [171].

Figure 2.13 illustrates the eigenstates of the hole-trion system in a Voigt geometry field. The hole and trion states are defined in terms of their orientation with respect to the magnetic field and are split by the hole and electron Zeeman energies respectively. The hole-trion transitions are co-linearly polarized with a pair of cross-polarized diagonal transitions coupling the hole states to the orthogonal trion state. The spin up and spin down states ($\left|h_{\Uparrow/\Downarrow}\right\rangle$) are now superpositions of these eigenstates and thus carrier spins precess about the in-plane field with angular frequency $\omega_Z = E_Z/\hbar$. In terms of the Bloch sphere this implements a coherent rotation about the field axis and thus is widely used for coherent control of single carrier spins (see section 2.6).

2.4 QD - ENVIRONMENT INTERACTIONS

As SAQDs are formed from a macroscopic number of nuclei within a semiconductor lattice, it is necessary to consider interactions between carriers confined in the QD and the host material. This section presents a brief review of interactions between QD-confined carriers and the nuclear spins, electrical environment and lattice phonons of the host material.

2.4.1 *Dephasing*

To understand these interactions, it is first necessary to define their influence on the quantum state of the carriers in the QD. Generally these interactions degrade the quantum state, causing the initially pure state to become mixed. This can be visualised on the Bloch sphere (Figure 1.1) as the Bloch vector (a Cartesian representation of a state vector) moving inwards from the surface and is termed dephasing. Phenomenologically there are two kinds of dephasing processes which evolve the state in different ways. Considering a Bloch vector $\underline{s} = (s_x, s_y, s_z)$, the dephasing may be represented as follows [177]:

$$\dot{s_z} = -\frac{[s_z + 1]}{T_1} \tag{2.8}$$

$$\dot{s}_{x,y} = -\frac{s_{x,y}}{T_2} = -\left[\frac{1}{2T_1} + \frac{1}{T_2^*}\right]s_{x,y} \tag{2.9}$$

These processes are referred to as *longitudinal* (T_1) & *transverse* (T_2) dephasing. T_1 processes involve relaxation of population from the excited state which results in a change of the z-component of the Bloch vector described by equation Equation 2.8. Examples of T_1 processes include radiative recombination of excitons [122, 178] and tunnelling of carriers from the QD [179]. The timescale on which the qubit remains coherent is determined by transverse dephasing and characterised by the coherence time T_2. This is determined by 2.9 with contributions both from T_1 processes (as they are incoherent) and *pure dephasing* which is characterised by a timescale T_2^*. Pure dephasing alters only the coherence of the state without any change in the level populations, thus only the x & y components of the Bloch vector are modified. For confined carriers, examples of T_2^* processes are the hyperfine coupling to the inhomogeneous Overhauser field of the nuclear spins [180], the deformation potential potential coupling between electrons and acoustic phonons [63, 64] and fluctuations in the electric field acting on the hole g-factor [181–183]. In Figure 2.14 the effects of T_1 and T_2^* dephasing are illustrated on the *x-z* plane of the Bloch sphere.

In the low temperature limit, single excitons confined in SAQDs have been observed to have lifetime-limited coherence [178, 184, 185], i.e. $T_2 = 2T_1$ where T_1 is typically 400 to 800 ps owing to radiative recombination [122, 178]. By contrast, single carrier spins do not undergo radiative recombination, leading to T_1 values in the range of 0.2 - 20 ms [149, 186] for single spins confined in SAQDs. At these timescales, significant pure dephasing occurs during the spin lifetime and the coherence time is dominated by the T_2^* term in 2.9. For InGaAs SAQDs, electron spin coherence times (T_2^*) of the order of $1 - 2$ ns are typically measured [187, 188] with values of around 10 ns measured for holes [158, 179, 181, 182]. However, there are means by which pure dephasing can be supressed (see subsection 2.4.5), allowing coherence times to be extended to the μs regime [181, 188]..
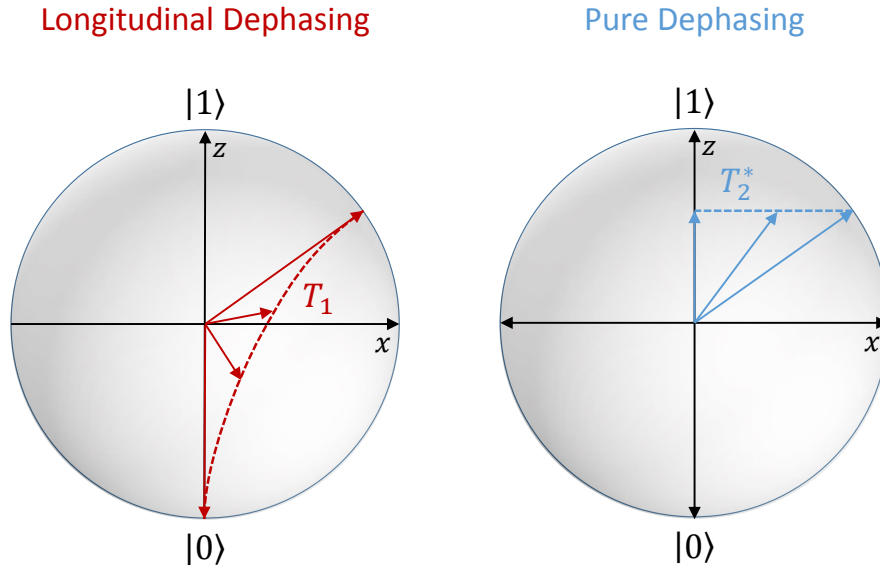
Figure 2.14: Left: T_1 dephasing in the Bloch sphere representation. The red arrows represent the Bloch vector at various points in time whilst the dashed red line is the trajectory of the tip of the vector. Right: T_2^* dephasing (blue arrows / line) of the same initial state.

2.4.2 *Nuclear Spins*

Owing to the finite size of a SAQD, the QD itself comprises around 10^6 nuclei. As discussed in section 1.3, the III-V materials of SAQDs do not have spin-zero isotopes so the approach of isotopic purification [36] to reduce nuclear spin effects [34] is not possible here. Instead, the nuclear spins and the QD interact via. the hyperfine interaction [189] which is usually described by effective magnetic fields. Carriers in the QD interact with the large number of nuclear spins in the bath and experience an effective field termed the Overhauser field [190, 191]. A single nuclear spin also experiences a hyperfine interaction from the confined carrier with the corresponding effective field known as the Knight field [190–192].

The random Overhauser field in InGaAs SAQDs has been found to have a mean magnitude of around 30 mT [183, 193, 194] at zero external magnetic field. Significantly though, the field is not static, hyperfine interactions [189] involving nuclear spins (see Ref. [66] for a review) cause the spin bath to fluctuate in time with a measured

standard deviation of 14 mT [193]. The fluctuation time is typically much longer that the carrier lifetime [183], thus the field can be considered quasi-static on the lifetime of any single carrier [195]. The influence of the nuclear spin dynamics is thus primarily that when repeating a measurement many times, the QD carriers experience different magnetic fields and hence different precession frequencies, leading to T_2^* dephasing [188]. This time-dependent field also causes broadening of the QD linewidth if the measurement is slow relative to the nuclear spin dynamics [183, 196].

2.4.3   *Electrical Environment*

As discussed in subsection 2.3.1, QD energy levels are very sensitive to external electric fields through the Stark effect. In terms of the QD environment, fields may arise from charges trapped in localization centres in the semiconductor material [197], again leading to broadening of the QD linewidth [198]. Furthermore, the g-factor (see subsection 2.3.2) of QD-confined carriers exhibits an electric field dependence [199–202]. This means that in the in-plane magnetic field typically used for coherent control of spins (see section 2.6), a time-varying electric field will cause T_2^* dephasing by differing precession rates [181, 182], similar to the case of nuclear spins.

2.4.4   *Phonons*

The presence of a lattice-structured host material in solid-state qubit systems provides the ideal environment for phonons. InGaAs QDs couple to both Longitudinal Acoustic (LA) and Longitudinal Optical (LO) phonons [203–205]. LO phonon scattering in GaAs is characterised by an energy scale of around 36 meV. For InGaAs QDs this leads to observation of weak "phonon replica" peaks at the corresponding negative detuning [205]. These peaks form sharp lines owing to the discrete distribution of LO phonon energies. In addition, quasi-resononat driving at a positive detuning of a multiple of the LO phonon energy is also possible [206–208]. The scattering process corresponds to T_1 dephasing as it results in a loss of population. LO phonons may also contribute to pure dephasing. However, theoretical

studies have found that this influence is negligible at low temperatures as the LO phonon energy $> k_B T$ [209].

By contrast, LA phonons exhibit a continuous distribution with energies in the few meV regime. Again, features corresponding to this may be observed in both emission [210] and absorption [211] spectra. In this case, owing to the continuous distribution of phonon energies, these spectral features take the form of smooth side-bands. Beyond simple phonon scattering as a form of T_1 dephasing, LA phonons also contribute to pure dephasing [63, 64, 204] by providing an incoherent relaxation channel when the QD is optically driven (see chapter 5).

Unsurprisingly, the phonon dynamics depend strongly upon temperature. Strong linewidth broadening [185, 205, 212, 213], redshifting [213, 214] of the QD levels and stronger dephasing [63, 64, 204] has been observed with increasing temperature. As such, QD experiments are typically performed at low temperatures ($\sim 4 - 20\,\mathrm{K}$) to minimise these effects. At these low temperatures and low driving strengths, phonon induced dephasing is generally weak compared to spin or charge noise effects [181–183] and is often neglected. However, in the presence of strong optical driving [63, 64, 215] or an optical cavity [86, 208, 216–218] phonon interactions may play a significant role in determining the dynamics of the entire system. This regime is explored in detail in chapter 5.

2.4.5 *Controlling Dephasing*

A general approach to reducing the influence of inhomogeneous dephasing (T_2^*) is to use spin echo techniques [219] to "refocus" the precessing states. This has been demonstrated for single electrons in InGaAs SAQDs with a corresponding increase in T_2^* of around 10^3 [188]. However, application of the multiple optical pulses required is experimentally difficult and also a potential source of dephasing itself.

As such, it is interesting to consider the possibility of suppressing these dephasing sources directly. General consensus is currently that electron dephasing is dominated by hyperfine nuclear spin interactions [188]. A non-invasive means of suppressing nuclear spin dephasing is to pump the spin bath into a polarized state, reducing

the fluctuations [220]. However, total polarization of nuclear spins remains elusive experimentally. Direct investigation of the nuclear spin bath has shown that the strain present in InGaAs SAQDs slows the fluctuations [221], presenting a potential sample engineering route to reduced dephasing.

Owing to a primarily *p*-type orbital structure, the hole hyperfine constant is found to be around 10% of that of the electron [109]. As a result, charge noise is instead attributed as the general dominant source of hole dephasing [181, 182, 222]. The primary source of this noise appears to be charges trapped at the capping layer interface [183, 197] which presents the possibility of reducing fluctuations by sample engineering. In addition, an optical method of passively suppressing hole spin dephasing has been recently proposed where the OSE opposes any change in Zeeman splitting induced by charge fluctuations [223].

2.5   OPTICAL MICROCAVITIES

The interactions between a quantum emitter and a reflective cavity give rise to the field of Cavity Quantum Electrodynamics (cQED). The cavity confines the light to the vicinity of the emitter, enhancing the light-matter interaction strength. The field of cQED has been widely studied, particularly in atomic physics where it has allowed experimental verification of some famous predictions of QM [224]. In the semiconductor QD architecture considered in this thesis it is possible to engineer cavities far smaller than those used in atomic experiments by lithographic processing of the sample wafer. Termed microcavities, when fabricated around a single QD these structures produce a very compact cQED system on a single chip.

Semiconductor optical microcavities coupled to single QDs have been used to demonstrate a number of useful effects such as brighter and more indistinguishable single photon sources [225, 226], enhancement of weaker emission channels such as LA phonon-assisted emission [86, 208, 216, 218] and ultrafast optical switching [227–229]. In this section the basic theory of cQED is outlined and the main types of semiconductor optical microcavity are reviewed.
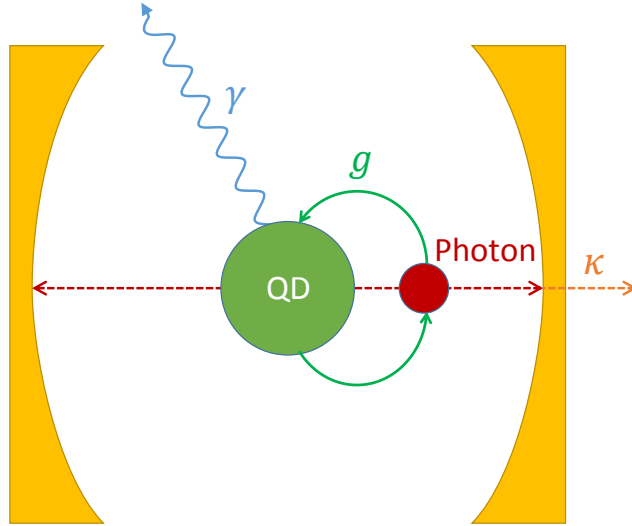
Figure 2.15: Schematic illustrating the key parameters of a coupled cavity-QD system. The strength of the interaction between the cavity photons and the QD is defined by the coherent coupling strength g. The rate of leakage from the cavity mode is defined as κ whilst γ is a rate incorporating both decay and dephasing of the QD state.

2.5.1 Theory

It is first necessary to define the properties of the cavity that will determine the behaviour of the coupled system. The performance of an optical cavity is defined by two parameters [230]; the first of these is the mode volume (V_m) which is defined by equation 2.10 [231, 232]:

$$V_m = \frac{\int d^3r \epsilon(r) |E(r)|^2}{max\left(\epsilon(r) |E(r)|^2\right)}. \tag{2.10}$$

Here ϵ is the relative permittivity and E is the amplitude of the electric field. The second parameter is the cavity quality factor Q which is defined in equation 2.11:

$$Q = \frac{\omega_0}{\triangle \omega}. \tag{2.11}$$

In this case ω_0 and $\triangle \omega$ are respectively the cavity resonance frequency and linewidth. The rate at which the field leaks from the cavity (κ) is defined as $\Delta\omega = 2\kappa$; hence larger Q factors indicate a longer cavity confinement time.

The strength of the QD-cavity interaction is defined in equation 2.12 by the coherent coupling strength g:

$$g = \frac{1}{\hbar} \sqrt{\frac{\hbar \omega}{2 V_m}} \mu, \qquad (2.12)$$

where μ is the dipole moment of the QD and it is assumed that the QD is placed at the maxima of $\epsilon(r) |E(r)|^2$. These parameters are illustrated in Figure 2.15.

2.5.2 *Weak, Strong & Ultrastrong Coupling*

It is now important to define the different regimes of operation for the cavity-QD system as this dramatically influences the observed behaviour.

Weak Coupling

In the weak coupling regime the interaction of the QD and the cavity is dominated by incoherent decay processes such as cavity losses (κ) or QD decay and dephasing (γ). Hence the definition of weak coupling is:

$$g \ll \kappa, \gamma. \qquad (2.13)$$

The key characteristic of this regime is the Purcell effect [231] where the rate of spontaneous emission is either enhanced or suppressed by the cavity depending on the cavity-QD detuning. This phenomenon is well-observed in QDs [233–235] and has been widely applied in the production of highly efficient single [62] and entangled [236] photon sources. If the cavity is resonant with a QD in the centre of the cavity mode, the Purcell factor (F_P) is defined as:

$$F_P = \frac{3}{4\pi^2} \left(\frac{\lambda_c}{n} \right)^3 \left(\frac{Q}{V_m} \right) \qquad (2.14)$$

where λ_c is the cavity wavelength and n is the refractive index of the cavity material.

Strong Coupling

In the strong coupling regime the interaction is dominated by the coherent interaction between the QD and the cavity field:

$$g \gg \kappa, \gamma. \tag{2.15}$$

The strong coupling regime is characterised by vacuum Rabi oscillations [237] whereby population coherently oscillates between the QD and the cavity field. In the spectral domain this is characterised by peaks corresponding to hybrid light-matter states (polaritons) which have a splitting of $\Omega_R = 2g$. The figure of merit for a strongly coupled system is the ratio $Q/\sqrt{V_m}$. Higher Q values reduce the cavity loss rate κ and smaller mode volumes (V_m) increase the coupling strength g.

Ultrastrong Coupling

It is worth briefly noting that beyond strong coupling lies the *ultrastrong* coupling regime [238, 239] where the coupling strength approaches or exceeds the resonant frequency of the cavity:

$$g \lll \omega_c. \tag{2.16}$$

Ultrastrong coupling has recently been observed experimentally in a number of systems [240, 241] including quantum wells [242] however QD systems are unlikely to enter this regime as their dipole moment is smaller. As such, the ultrastrong regime is included here only for completeness.

2.5.3   *Types of Cavities*

A number of different physical implementations of optical microcavities that can couple to SAQDs have been demonstrated. The first type of these are cavities using Photonic Crystal (PhC) structures, Photonic Crystal Cavities (PCCs). PhCs [243, 244] are formed by patterning a periodic structure from two materials of differing refractive index. This creates a structure analogous to a semiconductor crystal lattice, posessing a band gap for light in a manner equivalent to the electronic band gap of semiconductors. This gap originates from destructive interference of light owing to the periodic refractive index difference.

By manipulating the periodicity, the photonic band gap may be tuned. If an emitter is placed in a defect in the crystal, the propagation of photons with energies falling within the band gap will be heavily suppressed, forming a cavity.

In the III-V materials system used in this thesis, PCCs are formed by EBL etching of air holes in the semiconductor material. As this method only produces a 2D PCC, the sample beneath the cavity is also etched away to produce an air-clad slab with confinement in this axis arising from Total Internal Reflection (TIR) at the slab-air interfaces. Three common types of PCCs are illustrated in Figure 2.16(a-c), the H1 and L3 cavities where 1 and 3 holes are respectively omitted from a PhC slab and a nanobeam cavity where 1D PhC confinement is added to an etched slab waveguide with 2D TIR confinement. An attraction of photonic crystal structures is that it is relatively easy to engineer in-plane emission for circuit-style devices by addition of waveguides.

Microdisk cavities (shown in Figure 2.16(d)) are formed from a disk of etched semiconductor material attached to the wafer by a thin pedestal. Optical confinement is from TIR in all three directions, allowing the structure to support high-Q Whispering Gallery Modes (WGMs). A drawback of microdisk cavities is that the emission direction is not well-defined, this may be overcome by fabricating waveguides close to the disk but at the cost of reduced Q-factor. Finally, micropillar cavities (Figure 2.16(e)) consist of an etched cylinder protruding from the sample with TIR providing 2D confinement. The wafer is grown such that Distributed Bragg Reflector (DBR) mirror layers (e.g. alternating Aluminium Arsenide (AlAs)/GaAs) are present above and below the emitter, providing the final dimension of confinement. The emission of the pillar is well-defined along the pillar axis which permits efficient optical excitation and collection. However, the downside is that this does not easily apply to a circuit-style device where in-plane emission is required.

Table 2.1 shows typical values of the mode volume (V_m) and Q-factor for five of the most common types of semiconductor optical microcavity. The parameter Q/V_m is also calculated as this represents a figure of merit for the strength of interaction between a cavity and a QD. The key conclusion from Table 2.1 is that the significantly lower mode volume of the PhC type cavities gives them a much stronger coupling to the QD for an equal Q-factor. This, combined with the
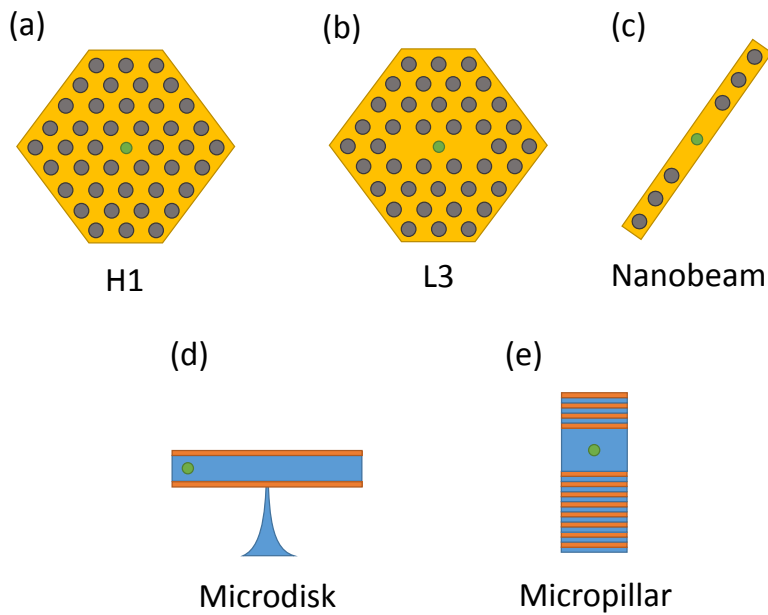
Figure 2.16: Schematics of some of the main types of optical microcavity. QDs are shown (not to scale) at the centre of the cavity modes by green dots. The PCCs (a-c) all comprise a suspended membrane surrounded by air. (a) An H1 PCC is formed by omitting a single air hole from the lattice. (b) L3 PCCs omit three air holes in a line. (c) A nanobeam PCC is formed by omitted air-holes in a suspended ridge waveguide. (d) A microdisk cavity consists of an etched disk of semiconductor material supported by a thin pedestal. (e) A micropillar cavity comprises a cylindrical pillar with DBR layers (often AlAs/GaAs) at the top and bottom.

	Type	$V_m\,(\lambda/n)^3$	Q	$Q/V_m\,(\lambda/n)^{-3}$
H1	PhC	0.39 [245]	17,000 [245]	44,000
L3	PhC	~1 [90]	25,000 [246]	25,000
Nanobeam	PhC	0.38 [247]	25,000 [247]	66,000
Microdisk	WGM	8 [248]	12,000 [248]	1,500
Micropillar	DBR	16 [249]	12,000 [226]	750

Table 2.1: Table of state-of-the-art mode volumes (V_m) and Q-factors for a number of common semiconductor optical microcavity implementations.

in-plane geometry makes PCCs the most attractive platform for the circuit architecture proposed in section 1.4. In chapter 6 the low mode volume of an H1 PCC is exploited to strongly enhance the driving strength experienced by a coupled QD.

2.6   COHERENT CONTROL OF QD SPINS

In order to meet the 4th DiVincenzo requirement of "a universal set of quantum gates", it is necessary to demonstrate full control of the spin state of the chosen qubit level. In practice this requires rotations around at least 2 axes of the Bloch sphere to cover the surface of the sphere. In this section the fundamentals of coherent optical driving of a QD are reviewed along with their applications to coherently controlling a single spin.

2.6.1   *Rabi Splitting of Dressed States*

By considering the QD-laser interaction in the dressed states picture [250] it can be derived that the addressed levels (with undressed transition energy $E_0 = \hbar\omega_0$) split into two levels with energies given by:

$$E_0 + E_\pm = \hbar\omega_0 + \frac{\hbar}{2}\left(-\Delta \pm \Lambda(t)\right), \tag{2.17}$$

where the level splitting $\Lambda(t)$ is an effective Rabi frequency defined as:

$$\Lambda(t) = \sqrt{\Omega_R(t)^2 + \Delta^2}. \tag{2.18}$$
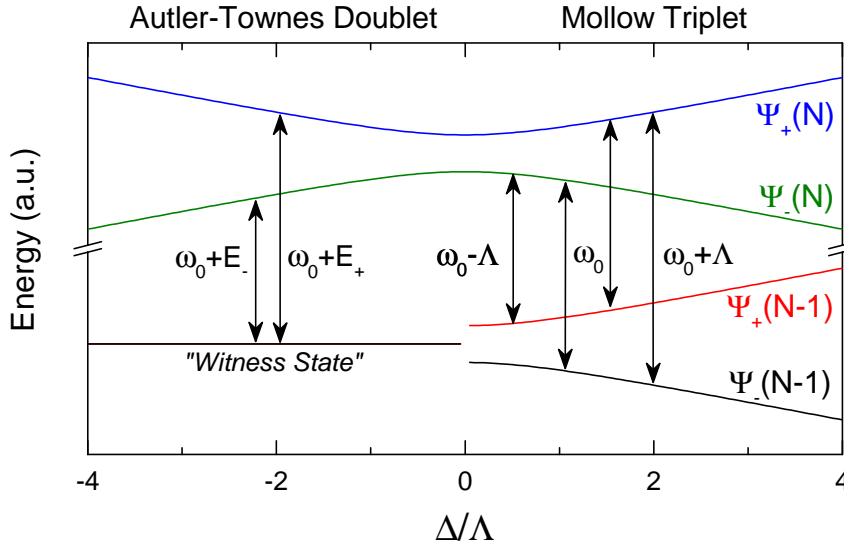
Figure 2.17: An illustration of the Rabi-split energy level spectra produced by the Autler-Townes doublet (left) and Mollow triplet (right) dressed states schemes. Dressed states of the *Nth* level are indicated as $\Psi_{\pm}(N)$, $\hbar\omega_0$ is the undressed transition energy and $\hbar\Lambda$ & $E_{\pm}$ are as defined in Equation 2.17. Increasing splitting with detuning (Δ) is observed.

This splitting is a function of both the laser Rabi frequency and detuning from the transition resonance and hence is referred to as Rabi splitting. This splitting gives rise to two common spectral signatures of coherent driving of a two-level system. In the case of the Autler-Townes doublet [251] a strong pump laser dresses a transition (e.g. $|X\rangle \rightarrow |XX\rangle$) whilst a weak probe monitors a transition to one of these states (e.g. $|0\rangle \rightarrow |X\rangle$). This gives two transitions to the "witness state" and hence a doublet. The second case is a Mollow triplet [252] whereby the probe monitors the same transition as the pump. Splitting of both levels gives four levels, two of which are degenerate thus a triplet spectrum is observed. This is illustrated in Figure 2.17.

Both phenomena have been experimentally observed a number of times. The Autler-Townes doublet is generally observed in transmission or PL spectra and has been observed for both the $|0\rangle \rightarrow |X\rangle$ [253] and $|X\rangle \rightarrow |XX\rangle$ [141, 253] transitions. The Mollow triplet was first observed in the CW-transmission spectra of the $|0\rangle \rightarrow |X\rangle$ transition [254]. More recent experiments have utilised resonance fluorescence techniques [255].
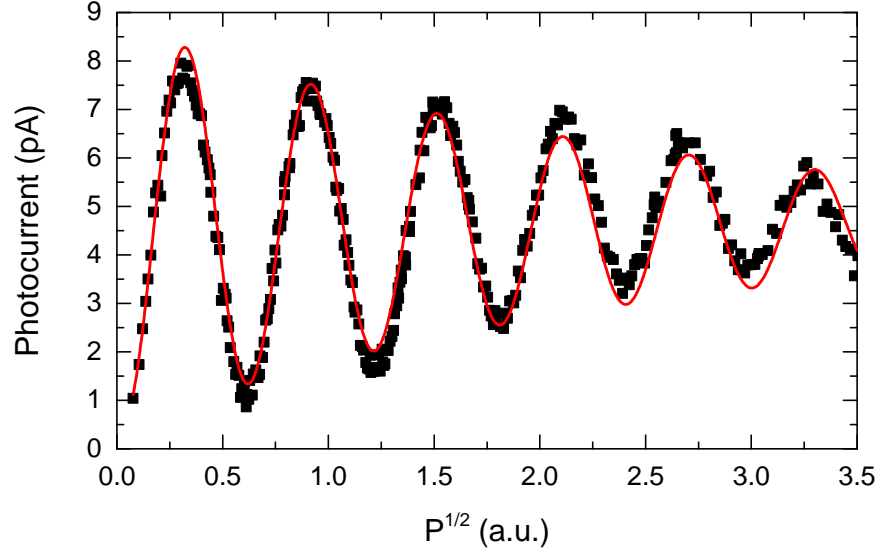
Figure 2.18: Rabi rotation of the neutral exciton transition of a single InAs/GaAs quantum dot. The photocurrent (final exciton population) oscillates according to the pulse area Θ (which is proportional to the square root of the applied laser power). The red line shows a damped sinusoidal fit to the data which reasonably approximates the behaviour of the acoustic phonon damped system [63, 64].

2.6.2   *Rabi Oscillations & Rotations*

The true significance of these Rabi splitting effects is revealed by considering the time domain picture. Flagg et. al [255] observed time-domain oscillations in the $g^{(2)}$ (second-order correlation) function [256] under resonant excitation of the $|0\rangle \rightarrow |X\rangle$ transition. These oscillations have a Rabi frequency proportional to the square root of the driving laser power and a Fourier transform to the spectral domain reproduces the Mollow triplet. As $g^{(2)}$ is proportional to the upper state occupation, these results indicate that the exciton population is modulated by the laser:

$$g^{(2)}(\tau) \propto n_x(\tau) \sim \sin^2(\frac{\Omega_R \tau}{2}). \qquad (2.19)$$

This phenomenon is referred to as Rabi oscillation and in the Bloch sphere takes the form of a rotation of angular frequency Ω_R about the x-axis. This result becomes significantly more interesting when considering single laser pulses with temporal length much less than the coherence time of the transition. In this case, the population oscil-

lates during the passage of the laser until the pulse completes, allowing the final occupancy to be controlled by varying either Ω_R or the pulse duration. In the case of control with ultrafast lasers, varying the pulse length is difficult and thus the final occupancy is manipulated by changing the pulse energy and hence Ω_R. The strength of the laser pulse is defined by the pulse area, Θ:

$$\Theta = \int_{-\infty}^{+\infty} \Omega_R(t)\,dt\,. \tag{2.20}$$

A single laser pulse will in fact rotate the state vector about the x-axis by an angle equal to Θ. This is termed a Rabi rotation and has been observed experimentally a number of times [60, 257–263]. A typical Rabi rotation is shown in Figure 2.18 where 7 oscillatory periods are clearly visible. The intensity damping observed arises due to acoustic phonon interactions [63, 64] and is termed Excitation Induced Dephasing (EID).

2.6.3 Ramsey Interference

Ramsey interference uses the principle of wavepacket interference to produce a rotation about an arbitrary axis in the x-y plane. A pair of phase-locked laser pulses are produced with a small temporal separation by an actively stabilised interferometer [264, 265]. By varying the relative phase between these pulses, a rotation about the axis $(\cos(\phi), \sin(\phi), 0)$ results. The relative pulse phase is given by $\phi = \omega\tau$, where τ is the delay between pulses and ω is the carrier frequency of the control laser.

More explicitly, in a typical scheme a pair of $\pi/2$ pulses are used. Depending upon the value of ϕ the two rotations either constructively (maxima at $\phi = 2n\pi$) or destructively (minima at $\phi = (2n+1)\pi$) interfere with the result being fringes in the population of the excited state plotted against τ. Between the two pulses the exciton state also undergoes dephasing as discussed in subsection 2.4.1, resulting in a reduction of the amplitude of the fringes. Indeed, the amplitude decay of these fringes is the most common method of measuring T_2^* [179, 181, 266]. An example of unstabilised Ramsay interference is presented in section 5.6.

2.6.4 *AC-Stark Shift*

Rotation around the z-axis of the Bloch sphere can be achieved by the AC-Stark shift (see subsection 2.3.1). In the dressed states picture previously discussed, the eigenenergies of the system are [177]:

$$\lambda_{\pm} = \frac{1}{2}\sqrt{\Delta^2 + |\Omega_R|^2},$$ (2.21)

where Δ is the detuning and Ω_R the Rabi frequency of the transition. A laser pulse detuned far from resonance ($\Delta \gg \Omega_R$) shifts the frequency of the optical transition by $\Delta\omega$:

$$\Delta\omega = \frac{1}{2}\left(\Delta - \sqrt{\Delta^2 + |\Omega_R|^2}\right) \approx -\frac{\Omega_R^2}{4}.$$ (2.22)

As the laser is far detuned, the level populations are almost unchanged and no x-axis rotation occurs. However, a z-axis rotation occurs due to this frequency shift; the rotation angle ϕ_z is given by:

$$\phi_z = \int \lambda_-(t)\, dt,$$ (2.23)

where $\lambda_-(t)$ is the eigenfrequency from equation 2.21 evolving with time due to the action of the laser pulse. Application of this method to quantum dots has demonstrated z-axis rotations of greater than π [164].

2.6.5 *Coherent Control of Single Electron Spins*

Coherent control of a single electron spin is based upon the electron-trion system previously discussed in subsection 2.3.2. Whilst there are a number of potential approaches to coherent control in this geometry, the first experimental realisation was carried out by Press et al. [266]. In an in-plane magnetic field, the energy levels may be considered as a pair of independent Λ systems incorporating the two electron spin states and one of the trion states each (see Figure 2.13). Under circular excitation, the probability amplitudes from the two systems add. By utilising a large detuning $\Delta \gg \Omega_H, \Omega_V$, unwanted population in excited states is minimised and the upper states may be adiabatically

eliminated. Hence a single broadband circularly-polarised pulse will produce coherent Rabi rotations via Stimulated Raman Adibatic Passage (STIRAP). The process may also be described by the AC Stark shift as discussed in section 2.6.4.

These rotations constitute z-axis rotations on the Bloch sphere. The authors implemented x-axis rotations by Larmor precession of the spin about the applied magnetic field (see subsection 2.3.2) in order to demonstrate full control of the spin state. These were characterised by Ramsey interference. Rotations of single electron spins by Larmor precession [267] and AC Stark shift [268, 269] have also been demonstrated in interface GaAs QDs.

2.6.6 *Coherent Control of Single Hole Spins*

Optical coherent control of a single hole spin may be obtained using similar methods to those outlined for the electron. In the work of both Greilich [182] and De Greve [181] et al., an AC Stark shift scheme was used. This is a direct equivalent to the scheme used for the electron discussed in section 2.6.5 with x-axis rotations again implemented by Larmor precession. In addition, Greilich et al. successfully demonstrated control of a two hole-spin state for two interacting dots.

An alternative approach was employed by Godden et al. [179] where z-axis rotations are implemented by the "geometric phase" [270] approach. In this case, exciting with circularly polarised light that is broad compared to the Zeeman splittings simplifies the hole-trion system to a pair of independent two level systems that may be selected by orthogonal circular polarisations. On the timescale of picosecond laser pulses, the energy levels may be regarded as stationary as the Rabi period of hole-hole or trion-trion transitions is several orders of magnitude greater. Applying a σ^+ polarised laser pulse on resonance drives a Rabi rotation between the spin-down hole state and the corresponding trion state [270]:

$$
\begin{aligned}
|\psi\rangle &= h_\Uparrow |\Uparrow\rangle + h_\Downarrow |\Downarrow\rangle \\
&\rightarrow h_\Uparrow |\Uparrow\rangle + h_\Downarrow \left[\cos\left(\frac{\Theta}{2}\right) |\Downarrow\rangle + i \sin\left(\frac{\Theta}{2}\right) |\Downarrow\Uparrow\downarrow\rangle \right].
\end{aligned}
\tag{2.24}
$$

Hence in the case of a pulse area $\Theta = 2\pi$ and assuming weak trion dephasing the wavefunction returns to the hole spin sub-space with the spin-down state having gained a phase shift of π relative to the spin-up state. Varying the angle of rotation is implemented by detuning the control laser pulse [179, 270], the rotation angle is given by [270]:

$$\phi_z = 2 \arctan\left(\frac{\beta_z}{\Delta}\right),\tag{2.25}$$

where β_z is the pulse bandwidth and Δ the detuning from resonance with the hole-trion transition. This implements a z-axis rotation with x-axis rotations again performed by Larmor precession. The scheme may also be extended to perform rotations about an arbitrary axis which eliminates the need for Larmor precession, potentially reducing the gate time [270].

2.7 QIP WITH QUANTUM DOTS

In this section a brief review of the QIP applications of QDs is presented. Applications of QDs both as stationary spin qubits and sources of flying photonic qubits are considered. In addition, other light matter interactions that could enable useful processes such as switching and logic gates are outlined.

2.7.1 *Spin Qubits*

Single Spins

As discussed in section 2.6, coherent control of single excitons, electrons and holes in SAQDs with ultrafast optical pulses is an established technique. However, studies continue into alternative methods of manipulating single spins. One such example is the demonstration of coherent control using rotations about the Overhauser field rather than applying an external field [195]. Another interesting proposal is the possibility of electrically controlled spin rotations in a static magnetic field [271]. The electric field mediated change in sign of the g-factor that this requires has been observed [199] but full control is yet to be demonstrated. An additional possibility is the direct manip-

ulation of the spin state by microwave excited electron spin resonance [272].

It is also worth noting that full coherent control of the dark exciton spin state is possible using ultrafast optical pulses [273]. The weak optical coupling of the dark exciton necessitates a more complex control scheme utilising optically allowed intermediate states but also provides long qubit lifetimes and coherence times.

Multiple Spins

Formation of two or more SAQDs in proximity can form a Quantum Dot Molecule (QDM). Individual separately confined spins may then interact through tunnelling. These spins may be controlled using similar ultrafast techniques to those previously discussed [182]. The tunnel coupling also presents the possibility to produce and coherently manipulate entangled two-qubit states [274]. The scalability of this approach to higher qubit numbers remains an open question.

An alternative approach also utilising QDMs is to prepare the two spins in a coherent superposition, a "singlet-triplet state". This has been realised for a pair of electron spins [275] with a key advantage being that such a qubit is significantly less susceptible to dephasing.

Distant Spins - Towards Spin Networks

Moving beyond proximal QDs requires interfacing remote spins. This directly relates to the networkability DiVincenzo criteria discussed in section 1.2. Owing to the optically active nature of QDs, photons present an obvious candidate to transmit information between them. The spin state of a photoexcited exciton directly corresponds to the polarization state of the laser pulse used to create it [276], a direct mapping between the Poincare and Bloch spheres. Equivalently, entanglement has been observed between QD spins and emitted photons [67–69]. These results illustrate the potential for conversion between photonic and spin qubits.

Transfer of a quantum state from a photonic qubit to a spin qubit has been demonstrated by quantum teleportation [277]. Subsequently, entanglement of two hole spins that were separated by 5 meters has been achieved [278]. This is realised by a projective measurement on the emitted photons and is a key step towards scaling to larger sys-

tems of interacting spins. The system generates 2300 entangled pairs per. second, much higher than results with atomic [279] or NV centre [280] qubits. There is significant scope for future improvements by increasing the coherence time or reducing the initialisation time of the spins. This result presents a key step towards networks of larger spins and is particularly interesting for realizing quantum repeaters [281] which are used in some QIP schemes to facilitate the generation of entanglement over very long distances.

2.7.2 *Photon Sources*

One of the earliest proposed applications of single QDs has been to use the emission of a single transition as a source of single photons [148, 282, 283] or to extend the scheme to the biexciton cascade to produce entangled pairs [129, 130, 148]. Current studies are focused on improving the performance of such sources and also extending them to the production of larger strings of entangled photons that are useful for QIP.

Single Photon Sources

Single photons are generated by radiative recombination of QD carriers, generally from $|X\rangle \to |0\rangle$, although single photon emission from charged trions has also been observed. A pair of key parameters for QIP is the indistinguishability (wave-packet overlap) and purity (absence of multiphoton emission) of the photons. Indistinguishability is of course negatively impacted by fluctuations such as those discussed in section 2.4, whilst purity can be reduced by excitation of the biexciton or uncertainty in the radiative lifetime.

The key to improving these parameters beyond early demonstrations [282, 283] has been the use of resonant excitation [196, 225, 226, 284] as opposed to *p*-shell or above-band excitation which introduce charge noise [285] and timing jitter [286] due to their reliance on relaxation from higher energy states. Careful optimisation of sample and driving parameters to minimise spin noise has also demonstrated improvements [196].

In addition, placing QDs in optical microcavities [225, 226] has been shown to be an effective way to increase the source brightness (when

continuously driven), purity, collection efficiency and also to suppress phonon scattering [226]. Current state-of-the-art has demonstrated both indistinguishabilities and purities in excess of 99% [226].

A downside to resonant excitation, however, is that the laser pump and single photon emission may only be separated by polarization. In current work many of the photons emitted share the laser polarization [226] and as such the process is inherently lossy. This, along with the prospect of broad tuning of the emission provides motivation for quasi-resonant pumping of single photon sources. In a recent experimental realisation, phonon relaxation spectrally splits the laser pump and single photon emission, enabling broad tuning [218]. The studies presented in chapter 5 and section 6.5 also present a means of quasi-resonantly pumping the exciton through the acoustic phonon sideband with potential single photon source applications. It remains to be seen however if the performance of such a source can match a fully-resonant scheme.

A recently theoretically proposed alternative to phonon schemes is to use stimulated emission from the biexciton to a virtual level defined by a cavity [287]. The transition from this virtual level back to the crystal ground state results in the emission of a single photon. Significantly, as the process is stimulated, the polarization, energy and emission time of the photon may be controlled by the pump laser. Furthermore, as the emission is through a virtual level, the emission energy can be chosen to be off-resonant from both the biexciton pump and the stimulating laser, allowing easy spectral filtering of the single photon emission.

Entangled Pair Sources

Radiative recombination of the biexciton leads to emission of a pair of polarisation-entangled photons [148]; however, FSS (see subsection 2.2.5) causes the two paths to be distinguishable, reducing the degree of entanglement. An initial approach to overcome the problem was to spectrally filter the emission to erase the wavelength information [130]. Subsequent work has involved tuning the energy levels to eliminate FSS by methods such as the OSE [142] or the combination of electric field and mechanical strain [139]. Cavity enhanced pair emission has also been observed by placing a dot in a nanopillar cavity

exhibiting a pair of non-degenerate modes that are tuned to match the biexciton cascade [236].

Similarly to the single photon case, the use of resonant excitation has recently led to a significant increase in the quality of these sources. By driving the $|0\rangle \rightarrow |XX\rangle$ two-photon transition [288] of a QD with vanishing FSS, purities exceeding 99% have been obtained with an entanglement fidelity of 81% [289]. The performance of this scheme exceeds any previous although it is reliant upon a QD with vanishing FSS which is difficult to obtain. In addition, the finite radiative lifetime of the exciton state provides time for dephasing between the emission of the two photons, limiting the fidelity of the state. It should be noted that contrary to the case of resonantly driven single photon sources, the pump is not resonant with the emission owing to the biexciton binding energy.

Several recent theoretical works have investigated the dynamics of the biexciton cascade in a cavity [290–292]. When the cavity resonance is tuned to half the biexciton binding energy, the two-photon emission ($|XX\rangle \rightarrow |0\rangle$) probability can be strongly enhanced. As this decay occurs by emission of 2 photons into the cavity mode without any intermediate X^0 state, the photons are identical and entangled which could yield close to ideal entangled pairs even in the presence of FSS. This process has been observed in experimental work with non-resonant excitation [293] though the photon statistics were not measured. Changing the parameters in this scheme (such as cavity detuning) also has the possibility to generate other interesting two-photon states [292].

Multi-Photon States

Cluster states [294] are multi-photon states of entangled qubits. They form the basis of many measurement-based QIP schemes and experimental methods of producing them are of great interest. A QD-based scheme has been theoretically proposed [295] where Larmor precession is used to implement spin rotations (as in coherent control schemes) with optical excitation used to transfer the spin state to a photon. This proposal is interesting because the only current source of photonic entangled cluster states is Parametric Down Conversion (PDC) [296, 297] which is an inherently probabilistic process.

As a result, for PDC current state-of-the-art is 6 photons states [298] with significant progress beyond this unlikely owing to the probabilistic nature of the process. The quantum dot approach has the potential to deterministically generate far longer strings [295] and could even be extended to 2D cluster states via a double-dot structure [299]. Such a source would be a near-universal source for measurement-based photonic quantum computing.

Very recently a three-photon cluster state has been demonstrated using the dark exciton as a spin qubit [300]. In this work, precession between two non-degenerate eigenstates of the dark exciton is used instead of Larmor precession but the principles remain broadly similar. Reduction of the excited state radiative lifetime (perhaps through cavity enhancement) and increasing the collection efficiency present two key routes to demonstrating longer clusters.

Recent theoretical work has suggested that a cavity-QD system in the strong coupling regime could also provide a source of bundles of a well-defined number of photons [301].

2.7.3 *Cavity-Enhanced Light-Matter Interactions*

All-Optical Switching

One application for a strongly coupled cavity-QD system is to act as an ultra-fast switch with optical control of the dot able to turn the cavity from transparent to opaque [302, 303]. Recently such schemes have been demonstrated [227–229] with a detuned pump pulse modifying the coupling between a QD and a PCC. As a result, the scattered and transmitted amplitudes of probe pulse are modulated. Thus, the presence of the pump pulse effectively switches the transmission of the probe pulse. Switching times as low as 50 ps have been observed [229], a future direction is to try and reduce the photon number required for the switching. Of particular interest is the suggestion that such a scheme could extend into the single photon limit [229] although other analysis suggests that this may not be possible [227]. Recent work [304] with a QD in a PhC waveguide has demonstrated modification of the transmission of a waveguide by a QD in a similar manner to the cavity experiments previously discussed.

Electro-Optical Modulation

Another application of cavity-coupled QDs is to use a rapid bias modulation to Stark shift the QD in and out of resonance with the cavity in order to implement a fast optical switch. The switching occurs due to the strong difference in the reflectivity spectra between the coupled and uncoupled cases. Such devices have been studied theoretically [305] and are predicted to have very low switching energies and switching frequencies of the order of 10 GHz which would be state-of-the-art. Current experimental implementations [306, 307] have reached a switching frequency of 150 MHz [307]. Improved sample fabrication is likely to provide a path to better performance.

Spin-Photon Interactions

The enhanced light-matter interaction in strongly-coupled cavity-QD systems presents the possibility for direct interactions between spins and photons. A controlled-NOT logic gate between a polarisation encoded photonic qubit and an exciton spin has been demonstrated [308]. The presence or absence of an exciton in a state orthogonal to the photonic qubit causes the photons to either experience the bare or coupled cavity spectrum. In the bare case the polarization is flipped on reflection whilst it is unchanged in the coupled case, implementing the conditional flip. In this case the polarization flip is conditional on the presence or absence of an exciton. For QIP, the key goal is logical interactions between polarization and spin.

A possible route toward such interactions is the effect of Faraday rotation, a magneto-optical effect in which magnetic fields cause a phase shift between the two circular components of light. Alternatively, in the linear basis this may be viewed as a rotation of the polarization. A weak rotation of a around 15 µrad was observed for a single SAQD [309]. Addition of an optical microcavity to strengthen the light-matter interaction saw a significant improvement to a phase shift of aorund 0.1 rad from a single hole [310] or electron [311] spin.

In subsequent work, a phase shift exceeding π has been measured from a single electron spin [312] strongly coupled to a PCC. The scheme is similar to Ref. [308] whereby the presence or absence of one spin state determines the cavity reflectivity spectrum. The complementary effect was also observed whereby reflection of a single

photon rotates the spin of the electron. The observation of a π phase shift is significant as it fulfils the requirement of numerous QIP proposals to exploit such a phase shift. Potential applications include entanglement distribution [313, 314] and non-demolition measurements [315, 316]. The implementation in Ref. [312] is again primarily limited by the relatively short coherence time ($T_2^* \simeq 1$ ns) and long spin initialisation time (~ 1 ns).

Coherent Control

Full coherent control of an electron spin weakly coupled to a microcavity has been demonstrated [317]. In this work a single electron transition was coupled to the cavity and thus the cavity serves only to Purcell enhance this transition. Theoretical work [318] has proposed a more complex scheme whereby two transitions of the electron-trion system are coupled to two non-degenerate cavity modes. This scheme has the potential to increase initialisation fidelity and reduce the gate times for spin manipulation [318]. In addition, in a strongly-coupled system, coherent control of vacuum Rabi oscillations has been demonstrated [319]. In this work cavity-enhanced OSE from ultrafast pulses is used to shift the emitter in and out of resonance with the cavity, effectively switching on and off the coherent energy transfer between the QD exciton and the cavity photonic mode.

Part II

EXPERIMENTAL INVESTIGATIONS

In this part of the thesis experimental results of ultrafast studies of Quantum Dot phenomena are presented. First, the details of the experimental apparatus, techniques and samples are outlined in chapter 3. The following three chapters each focus on a different area of study; chapter 4 explores the high fidelity initialization of hole spin qubits, chapter 5 studies a *dynamic vibronic coupling* between excitons and acoustic phonons whilst chapter 6 investigates ultrafast processes in QDs weakly-coupled to photonic crystal cavities.

3

EXPERIMENTAL METHODS

_____

3.1 INTRODUCTION

In this chapter the experimental methods used to obtain the results presented in this thesis will be outlined. The primary purpose of the experimental setup is to perform pulsed resonant coherent excitation of single QDs. The configuration presented here allows a single QD to be excited by a pair of laser pulses with tunable bandwidth and centre energy. The intensities and polarizations of the two pulses and additionally the delay time between them can also be specified. The setup also allows an additional CW laser to be applied to the sample with control over polarization and intensity. The optical setup is highly mechanically stable to prevent noise in the measurements.

The sample is held in a liquid helium bath cryostat to provide the low temperatures required for coherent QD experiments. The cryostat facilitates positioning of the sample relative to the laser and again exhibits excellent mechanical stability. The samples studied here are carefully engineered to facilitate electrical tuning of the QD levels by the QCSE and also to allow the resolution of single QD lines. Finally, the dynamics of the QD under study may be detected either electrically by ultra-low noise photocurrent measurements or optically by high sensitivity resonance fluorescence detection.

3.2 EXCITATION LASERS

3.2.1 *Pulsed Resonant Excitation: Coherent Mira 900F*

In all experiments performed in this thesis that utilise pulsed excitation, the laser source is a Coherent Mira 900F [320] Ti:Sapphire (Ti:S) pumped by a Coherent Verdi G10 [321] Optically-Pumped Semiconductor Laser (OPSL). The Verdi G10 produces 10 W of power at 532 nm which is used to pump the Ti:S crystal of the Mira 900F. Kerr Lens

Mode Locking (KLM) [322] is utilised to produce transform-limited Gaussian pulses with Full-Width Half Maximum (FWHM) duration $\Delta t \approx 80$ ps and $\Delta \lambda \approx 16.2$ nm. The pulse repetition rate is 76.2 MHz giving a corresponding pulse separation of 13.2 ns. The central wavelength of the pulses for the Mira may be tuned between $700 - 1000$ nm. For these experiments, the value chosen ranges between 915 and 955 nm to best correspond to the typical wavelength of the neutral exciton transition for the sample under study. A glass slide immediately after the laser aperture (see Figure 3.1) samples the laser output into a laser spectrometer which allows the centre wavelength and bandwidth of the pulses to be monitored.

Under optimal conditions, the time-averaged power output when mode-locked at 955 nm is 865 mW, corresponding to a pulse energy of around 11.4 nJ. As water vapour exhibits significant absorption in the Near Infra-Red (NIR), the laser is purged using dry nitrogen gas to ensure emission stability. Furthermore, both the diodes of the Verdi and the Ti:S crystal of the Mira are maintained at 17°C by a closed-loop deionized-water chiller to prevent thermal damage and stabilise the output.

The pulses undergo significant shaping before reaching the sample, details of this are discussed in subsection 3.3.1.

3.2.2 *Continuous-Wave Resonant Excitation: Toptica DL Pro*

In certain experiments it is necessary to utilise a narrow linewidth CW laser operating either resonant with a QD transition or close to resonance. Examples of these are the high-resolution Photocurrent (PC) spectroscopy technique described in subsection 4.4.2 or the OSE measurements contained in section 4.7. For these experiments, a Toptica DLC DL Pro [323] single-mode laser is used. This comprises a semiconductor diode laser within a high-finesse tunable external grating cavity. Tuning the cavity allows selection of a single narrow mode from the spectrally broad diode emission with typical linewidths of < 1 MHz. The diode specified has a tuning range between 910 and 985 nm and a typical power output of approximately 50 mW. Active feedback electronics stabilise the cavity whilst a Thermo-Electric Cooler (TEC) stabilises the diode temperature to ensure stable output.
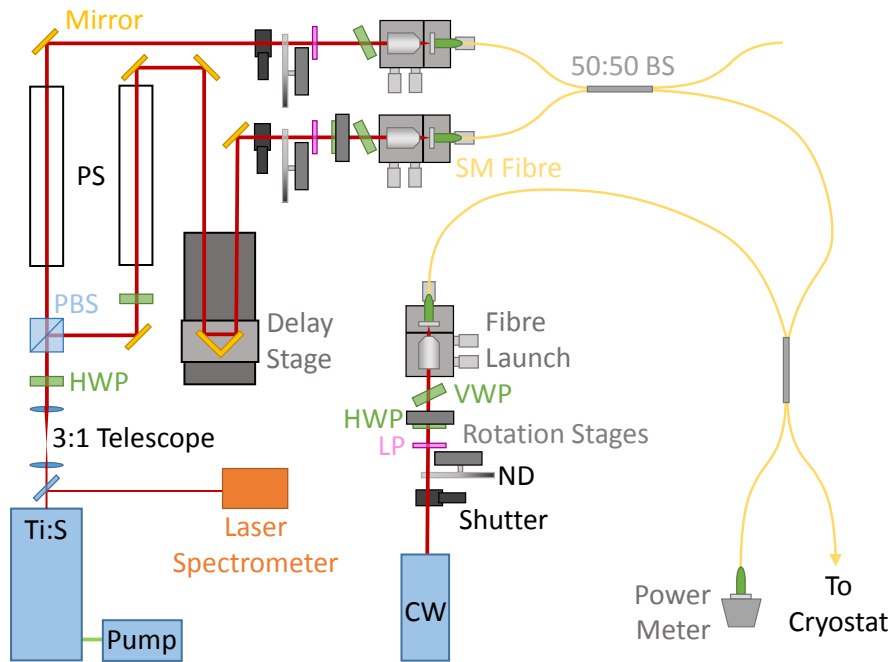
Figure 3.1: Schematic of the optical setup used for the measurements de-
scribed in this thesis. All of the items shown in this diagram are
mounted on an optical table that is actively isolated from the rest
of the room by pneumatic legs. List of acronyms: Beam-Splitter
(BS), Half-Wave Plate (HWP), Linear Polarizer (LP), Neutral
Density (ND), Polarizing Beam-splitter (PBS), Pulse-Shaper (PS),
Single Mode (SM)

3.2.3 *Continuous-Wave Non-Resonant Exciation: Thorlabs LDM21*

For characterisation measurements it is advantageous to use non-
resonant excitation to excite the QD ensemble incoherently rather
than resonant excitation of a single transition. For these experiments
various TO can mount diode lasers can be used. These are mounted
in a Thorlabs LDM21 mount which is driven by a Thorlabs TLD001
driver. A monitor photodiode in the laser is used to stabilise the laser
power output whilst a Thorlabs TTC001 temperature controller sta-
bilises the diode temperature using a TEC in the mount. Two diodes
are used, a Thorlabs LD808-SA60 producing 60 mW at 808 nm and
a Thorlabs HL63142DG producing 100 mW at 637 nm. Both of these
are above the band-gap of the InGaAs QD samples.
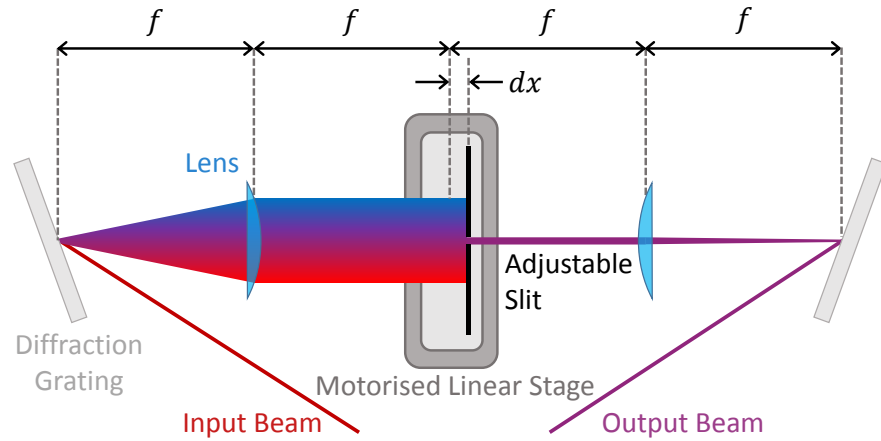
Figure 3.2: Schematic of a Pulse-Shaper (PS) of the type used in the experimental setup.

3.3   OPTICS

In this section the optical setup prior to the cryostat is outlined. This comprises all of the optics between the lasers and the single single-mode fibre that routes the excitation to the top of the cryostat, these are illustrated in Figure 3.1. Additional optics are present on top of the cryostat however the configuration of these depends strongly upon the detection method and as such they are discussed in section 3.6.

After sampling the output to a laser spectrometer, the beam is expanded by a factor of 3 using a variable optical beam expander (Thorlabs BE02-05-B) in order to sample more lines of the PS diffraction gratings. A PBS is used in combination with a HWP to split the laser power into two separate paths with the intensity of each determined by the HWP angle. On the reflected path, a HWP is used to rotate the linear polarization back to the axis of the PS diffraction gratings to maximise the power transmitted through the Pulse-Shaper (PS). For simplicity, in Figure 3.1 the Pulse-Shapers (PSs) are represented by black outlined rectangles and are discussed in full detail in subsection 3.3.1.

3.3.1   *Pulse Shaping*

As the output of the laser is spectrally very broad ($\Delta E > 20\,\mathrm{meV}$), it is necessary to shape the pulses to a much narrower spectral profile

in order to address individual QD transitions. A schematic of a Pulse-Shaper (PS) of the type used in this setup is shown in Figure 3.2. Two 1200 lines mm^{-1} diffraction gratings are arranged along an optical axis in a subtractive double configuration such that the dispersion of the first grating is cancelled by the second. The gratings are aligned so that at the centre energy of the laser pulses, the first order passes directly along the optical axis. Two lenses of focal length $f = 500$ mm are placed on the axis separated by $2f$ (forming a 1:1 telescope) and a distance of f from the nearest diffraction grating (see Figure 3.2). In this configuration, without a slit the spectral, spatial and angular properties of the output are theoretically identical to the input.

As the spectral components are spatially spread at the focal plane, a slit may be introduced to shape the pulse by allowing only certain components to pass. The width of the slit is adjustable by a micrometer drive, allowing for the pulse width to be continuously varied from a diffraction limited value of ~ 0.1 meV upwards. The centre energy of the pulses may be tuned through the entire spectral width of the unshaped pulses by translating the slit using a motorized linear stage (Newport MFA-CC). The slit is displaced from the focal plane by a small displacement $dx \approx 1$ cm. This displacement ensures that the output has a Gaussian spectral profile rather than the top-hat profile that arises at $dx = 0$. Further general details of the principles of femtosecond optical pulse shaping are contained in Refs. [324, 325].

Calibration of Pulse Shapers

In order to characterize and calibrate the output of the pulse shapers, spectra of the output were measured directly with a 0.75m spectrometer (Princeton Acton SP2750) and a back illuminated deep-depletion Charge-Coupled Device (CCD) detector (Princeton PyLoN 400BR). The spectrometer and CCD setup was in turn calibrated using a Neon Argon spectral lamp. Figure 3.3(a) shows the spectrum of an unshaped pulse (black lines) overlaid with the spectrum obtained for various different slit positions of the pulse shaper (coloured lines). The intensities of the shaped pulses approximately follow the envelope of the unshaped pulse.

In Figure 3.3(b) a close-up of an individual shaped pulse is shown. A Gaussian fit (red line) confirms the Gaussian lineshape and also al-
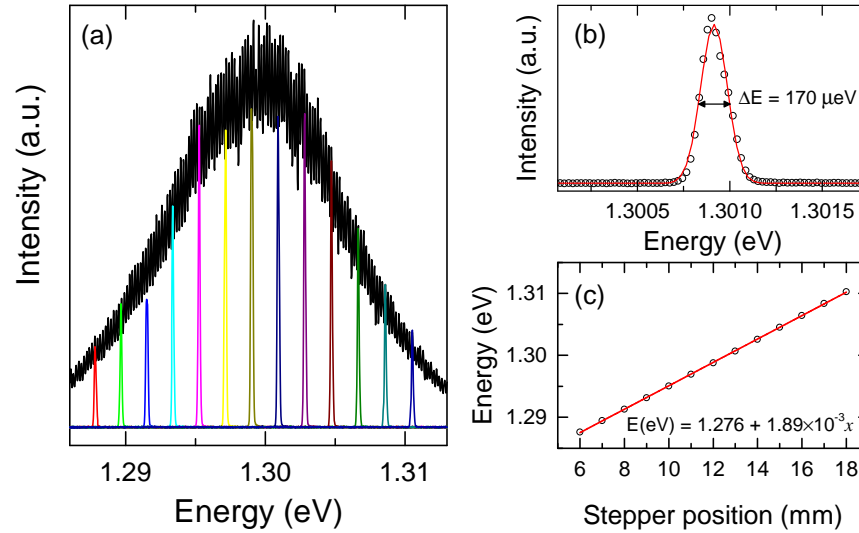
Figure 3.3: (a) Spectra of the input pulse (black line) and pulse-shaper output for different slit positions (coloured lines). (b) Close-up spectrum of the pulse shaper output. The red line is a Gaussian fit to the spectrum showing that the FWHM of the pulse is 170 μeV for this slit width. (c) Plot of pulse shaper slit position vs. centre energy of the output peak. A linear relationship (red line) is observed as expected.

lows the FWHM to be determined for the present slit width (170 μeV here). By plotting the centre energy of the peaks in Figure 3.3(a) against the slit position it is possible to calibrate the energy of the pulses as shown in Figure 3.3(c). A linear calibration (red line) is obtained as would be expected for the linear dispersion of the diffraction grating.

3.3.2 *Optical Delay*

In order to extract time dynamics from pump-probe experiments, it is necessary to be able to control the delay between the two pulses. This is achieved by mounting a hollow retro-reflector to a motorized linear stage (Newport M-IMS 300) in the optical path of the probe pulse. The stage has a travel of 300 mm; hence at maximum displacement an additional 600 mm is added to the optical path corresponding to a delay of 2 ns. For these experiments, the optical path lengths of the two arms are carefully matched such that the two pulses arrive simultaneously at a stage position of 76.2 mm. This calibration is obtained by observing the stage position at which quantum interference between

the two pulses is maximised when both are resonant with the QD $0 \rightarrow X$ transition. The chosen *time-zero* position allows the time-order of the two pulses to be reversed which can be useful for interrogating time dynamics around $t = 0$ whilst still allowing for delay times of greater than 1 ns.

3.3.3 *Intensity & Polarization Control*

Control of the intensity and polarization of each laser beam is achieved by a series of optics immediately before the beams are coupled into optical fibres. Before these optics, individual electrical shutters (Thorlabs MFF101) enable individual beams to be blocked or unblocked as required for a particular experiment. These shutters may be operated either by manual button press or by external Trigger-Type Logic (TTL) signals.

Intensity Control

A circular graduated ND filter is mounted on a motorised rotation stage (Newport PR50-PP). The Optical Density (OD) ranges between 0 and 4 depending on the position of the filter, giving a dynamic range of 10^4 in power. This high dynamic range is essential for power-dependence measurements and also enables the power to be stabilised when scanning the PS wavelength or delay stage position.

Polarization Control

Control of the polarization begins with a linear film polariser (Thorlabs LPVIS050) which is co-polarized with the laser; this ensures a pure input state. In the case of the probe beam and the CW laser a HWP mounted in a motorised rotation stage (Newport PR50-PP) allows the linear polarization angle to be arbitrarily rotated. This allows the probe polarization to be readily changed between co- and cross-polarized with respect to the pump as utilised for the fidelity measurements in chapter 4. This also enables the CW laser polarization to be orientated with respect to the sample crystal axes as employed in the OSE measurements of section 4.7.

Optical fibres exhibit a stress-induced birefringence which leads to an arbitrary shift in the polarization of light passing through them

[326]. As this shift is stress-induced, the fibres are securely fixed in place to ensure that the stress remains constant. To compensate for the polarization shift induced by the fibres, Variable Wave-Plates (VWPs) of the Berek type are used prior to the fibres. Adjusting both the rotation and the tilt of the wave-plate relative to the optical axis allows for full compensation.

3.3.4   *Fibre Optics*

The excitation beams are transmitted from the optical table to the cryostat in single-mode optical fibres (Thorlabs SM800) equipped with ferrule connectors. To couple the beams into the fibres, Microscope Objectives (MOs) (Olympus Plan achromat $10\times$) are mounted on high-precision x, y, z translation stages (Elliot Scientific Gold series xyz flexure stage) allowing the focused laser spot to be aligned precisely with the fibre core. The fibre has a mode field diameter of 5.6 µm; the MO is chosen to have a Numerical Aperture (NA) of 0.25 and a working distance of 10.6 mm which matches the focused size of the laser beam with the mode field diameter to ensure efficient coupling.

Wherever possible angle polished connectors are used to minimise back-reflection of power which can cause destabilising interference in the laser cavity. Fibre Beam-Splitters (BSs) with a 50:50 splitting ratio are used to combine the laser beams into a single fibre for transmission to the cryostat. The spare output of the final BS provides a convenient place to monitor the excitation power using a power meter (Coherent FieldMaster GS). In experiments where not all excitation paths are utilised, the relevant fibre BSs may be removed to increase the maximum power that can be transmitted to the sample.

3.4   SAMPLES

3.4.1   *Photocurrent Sample*

For the photocurrent measurements contained within chapter 4 and chapter 5, a sample fabricated from a cleaved piece of the VN382 wafer is used. This wafer was grown by H. Y. Liu and M. Hopkinson at the National Centre for III-V Technologies in Sheffield. The
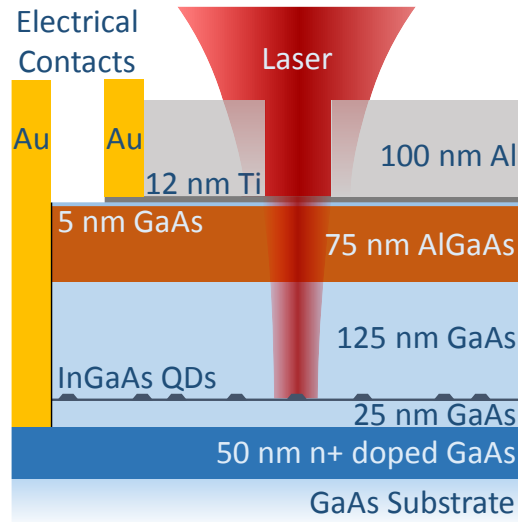
Figure 3.4: Illustration of the sample structure of the photocurrent sample fabricated on the VN382 wafer. The sample comprises a low-density layer of InGaAs SAQDs in an *n-i*-Schottky diode which is formed between an n^+ doped GaAs layer and a Ti top contact. The diode may be connected to an external circuit by Au contacts. An Al shadow mask with lithographically defined apertures ensures that the laser only excites a very small number of QDs.

structure consists of a layer of self-assembled InGaAs QDs (nominal in-plane QD density 30-60 μm^{-2}) grown on a GaAs substrate. A 50 nm layer of n^+ doped GaAs (nominal Silicon (Si) density 4×10^{18} cm^{-3}) is incorporated below the QD layer whilst a 75 nm Aluminium Gallium Arsenide (AlGaAs) layer lies above the QD layer[1]. The full layer structure is illustrated in Figure 3.4 where the wafer ends at the top 5 nm GaAs spacer layer.

Schottky Diodes

Photocurrent (PC) measurements require application of a reverse bias DC electric field to promote carriers to tunnel from the QDs. In order to apply this electric field, *n-i*-Schottky diodes were fabricated onto the cleaved wafer. An array of Ohmic and Schottky contacts are defined by Ultraviolet (UV) photolithography and then fabricated by thermal evaporation of metals onto the lithographically defined features. For this sample, the processing was performed by the previous PhD student John Quilter at the EPSRC National Centre for III-V Tech-

---

1 This layer would act as a hole tunnelling barrier if it was closer to the sample. It is included purely for historical growth reasons.
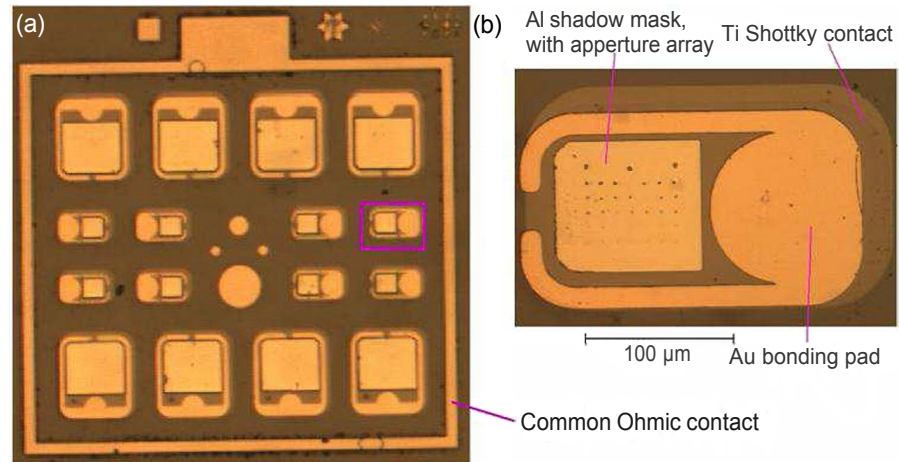
Figure 3.5: (a) Micrograph of the surface of the fabricated sample. The large image shows a single completed chip, as defined by the bordering Ohmic contact. The circular features in the centre are Au markers. (b) Close-up showing a single small mesa, including the Al shadow mask and aperture array. The apertures decrease in size from the top with each row having the same diameter. Image courtesy of John Quilter and reproduced with permission.

nologies in Sheffield. The end result is shown in Figure 3.5(a) with an array of 16 diodes, 8 large and 8 small. The electrical properties of the diodes are discussed in detail in subsection 3.6.1.

Apertures

If the electrical properties of the fabricated diodes are satisfactory, the next step is to fabricate apertures on the diode surface. These are significantly smaller than the diffraction-limited laser spot and thus reduce the number of QDs excited by the laser to ensure that single QDs may be resolved. Owing to this small size, EBL is used to define an array of apertures with diameters ranging between 200 nm and 1 µm. The apertures are formed by deposition of 100 nm of Al which is chosen to avoid diffusion into the GaAs which would reduce the electrical quality of the diodes. This processing was again performed by John Quilter at the EPSRC National Centre for III-V Technologies in Sheffield. A micrograph of a finished array of apertures is shown in Figure 3.5(b).

Sample Mounting

The sample must be mounted on a set of x-y-z piezo stages within the cryostat to allow it to be accurately positioned with respect to the
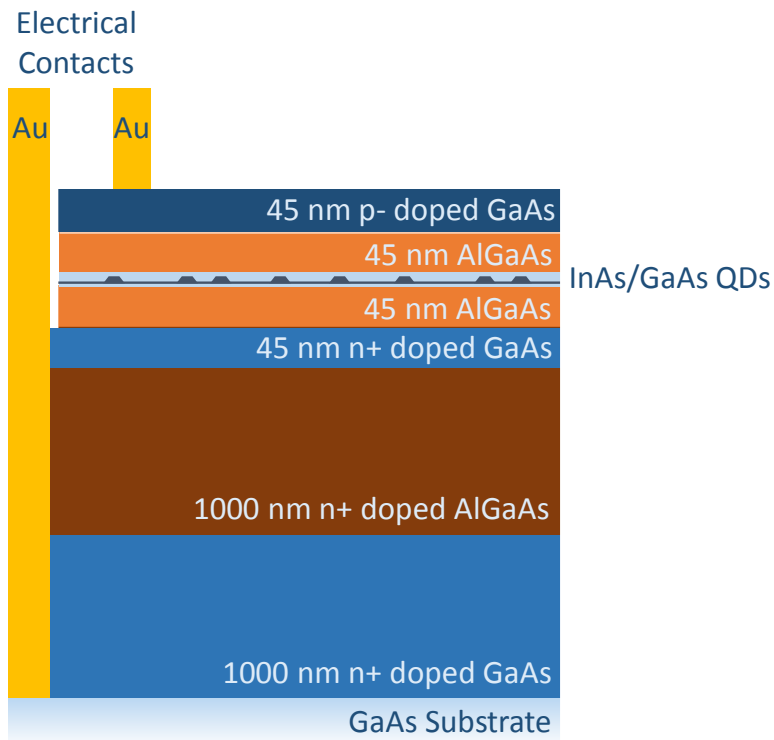
Figure 3.6: Schematic of the sample structure of the H1 cavity sample fabricated on the VN2668 wafer. The sample consists of a layer of InGaAs QDs incorporated in a *p-i-n* diode structure formed by doped GaAs layers above and below the sample. The diode is connected to an external circuit by Au contacts.

focused laser beam. In addition, the mounting must be mechanically stable, non-magnetic and allow the measurement circuit to be reliably connected to the diodes on the sample. To achieve this, the sample is mounted to a non-magnetic, leadless chip carrier with Silver (Ag) paint. Thin Au wires are then bonded between the chip carrier and the Ohmic and Schottky contacts on the sample. The chip carrier is electrically insulated from the cryostat by a ceramic tile and brass screws are used both to hold the carrier in place and to make electrical contact for the measurement circuit. The ceramic tile is then mounted with non-magnetic brass screws to the sample holder (see section 3.5).

3.4.2 *H1 Cavity Sample*

For the resonance fluorescence measurements described in chapter 6, a sample fabricated from a cleaved piece of the VN2668 wafer is used.
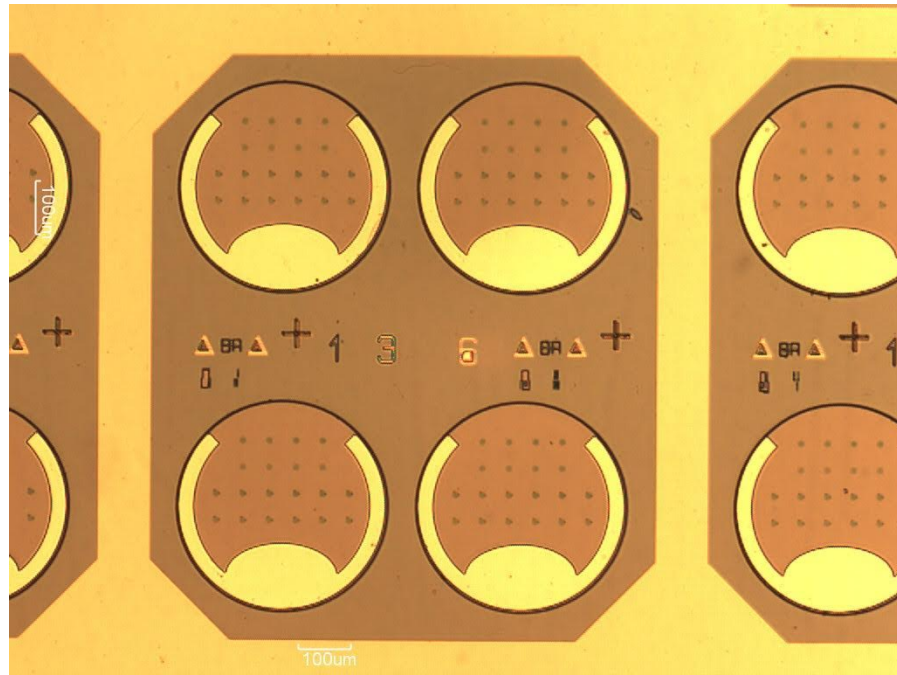
Figure 3.7: Micrograph of the fabricated sample surface. Four complete mesas each corresponding to a single *p-i-n* diode are visible in the centre of the image. The smaller features within each diode are PhCs. Image courtesy of Christopher Bentham and reproduced with permission.

This wafer was grown by E. Clarke at the EPSRC National Centre for III-V Technologies in Sheffield. The structure is illustrated in Figure 3.6 and consists of a layer of self-assembled InGaAs QDs grown on a GaAs substrate. Tunnelling barriers comprising 45 nm of undoped AlGaAs are incorporated both above and below the QD layer to maximise the electric field that may be applied without carrier tunnelling occurring [327]. This ensures that a large QCSE tuning range is possible. Above the top barrier there is a 45 nm p^+ doped GaAs layer (nominal Beryllium (Be) density 2×10^{19} cm^{-3}) whilst below the lower barrier is a 45 nm n^+ doped GaAs layer (nominal Si density 2×10^{18} cm^{-3}) followed by a sacrificial layer of 1 μm of n^+ doped AlGaAs and a contacting layer of 1 μm n^+ doped GaAs.

p-i-n Diodes

For the measurements presented in chapter 6, it is desirable to be able to tune the QD-cavity detuning. To achieve this, *p-i-n* diodes are fabricated on the sample in order to tune the QD energies by the QCSE. An array of Au *p*-type contacts and a common *n*-type contact are fab-
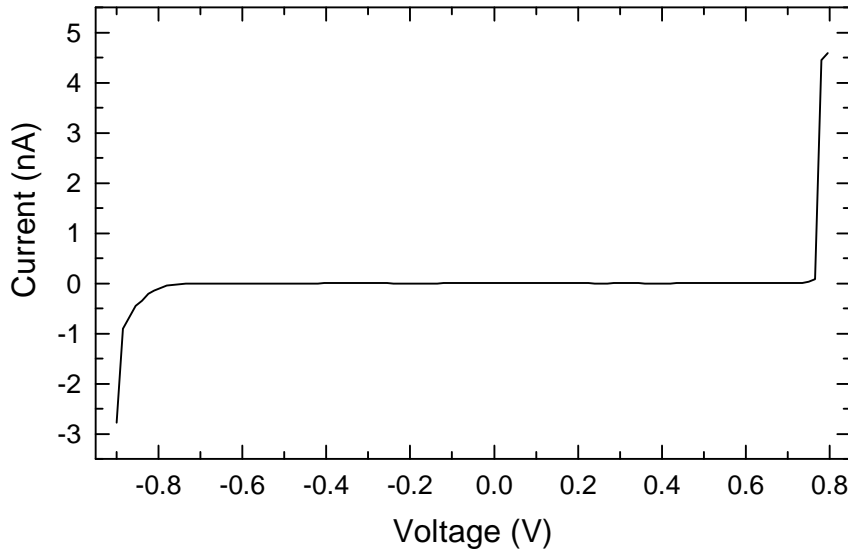
Figure 3.8: I-V curve of the diode studied in chapter 6 at $T = 4.2 \, \text{K}$ without illumination. Positive voltage denotes forward bias whilst negative voltage is reverse bias.

ricated using the same process of UV photolithography and metal deposition described previously for the Photocurrent (PC) sample in subsection 3.4.1. Figure 3.7 shows a micrograph of the fabricated sample surface with 4 complete diodes visible in the centre. An example low temperature I-V curve of a diode in the sample is shown in Figure 3.8. This processing was performed by Ben Royal and Christopher Bentham at the EPSRC National Centre for III-V Technologies in Sheffield.

H1 Photonic Crystal Cavities

The Photonic Crystal Cavities (PCCs) in this sample are defined by EBL and then etched by Inductively Coupled Plasma (ICP) etching. The sacrificial AlGaAs layer (the brown layer in Figure 3.6) is then etched away by immersion in 40% Hyrofluoric Acid (HF) solution to leave a suspended PhC membrane 200 nm thick. The H1 PCC design incorporates displaced and reduced radius holes for the first ring around the cavity to improve the cavity performance [245]. An additional small shift of the pair of holes above and below the cavity was introduced to lift the degeneracy of the cavity modes which have orthogonal linear polarizations. The PCC is fabricated aligned with
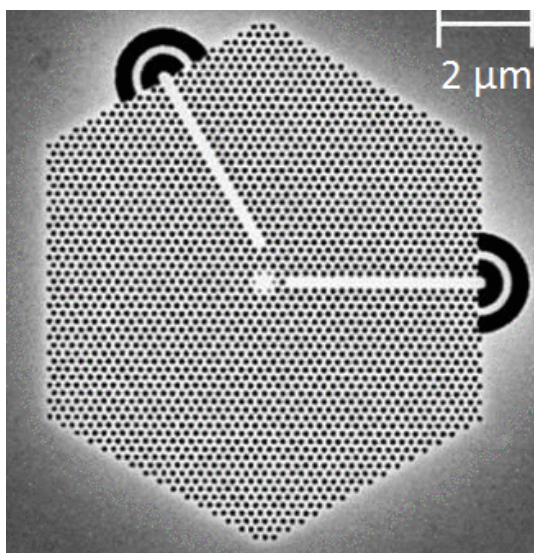
Figure 3.9: SEM image of a single fabricated H1 cavity with waveguides. Image courtesy of Ben Royal and reproduced with permission.

the crystal axes of the sample meaning that each cavity mode should couple to one eigenstate of the QD exciton.

W1 defect waveguides are positioned to couple to one cavity mode each [328]. These waveguides allow selective excitation of and collection from the two cavity modes and have previously been employed to demonstrate exciton spin readout [328] and single photon routing [329]. The waveguides are not used in the initial studies presented in chapter 6 but have a number of potential applications in further studies. Full details of the design, optimisation and fabrication of these structures may be found in Refs. [328, 329] The fabrication of the PCCs was performed by Ben Royal at the EPSRC National Centre for III-V Technologies in Sheffield.

Sample Mounting

The sample is mounted on a TO-5 header to provide the necessary electrical connections. Thin Au wires are bonded between the header and the p-type and n-type contacts on the sample. The TO-5 header is mounted to the top of the piezo stack using a purpose-made metal holder to ensure that the sample position is mechanically stable.

3.5   CRYOSTAT

To maintain the low temperatures required for QD experiments (see subsection 2.4.4), a helium bath cryostat (Attocube AttoLiquid) was used. The sample (mounted to the piezo stack) is attached to the end of an insert comprising a cage structure (Thorlabs) which permits optical access and also the mounting of the sample objective lens. This is in turn inserted into a cylindrical tube which is pumped to a high vacuum before approximately $10\,\mathrm{cm}^3$ of Helium (He) gas is added to enable thermal exchange. A glass window in the top of the tube permits optical access.

The cryostat consists of a reservoir of approximately 50 litres of liquid He into which the sample tube is inserted. An optical breadboard is mounted to the top of the tube to allow optics to be mounted between the excitation fibre and the sample. Vacuum insulation of the reservoir limits heating of the reservoir, allowing a stable base temperature of $4.20 \pm 0.05\,\mathrm{K}$ to be maintained for around 7 days between liquid He refills. The reservoir is also suspended from the external cryostat casing by vibration dampers to ensure the mechanical stability of the setup and in turn the alignment of the excitation to the sample.

3.5.1   *Temperature Control*

In some experiments (see section 5.5) it is interesting to vary the temperature that the sample experiences. For this purpose, a resistive heater and a thin-film resistive temperature sensor (Lake Shore Cernox) are incorporated into the sample mount (see Figure 3.10). The current delivered to the heater is regulated by a computer-controlled power supply (Aim TTi PI303). Using real-time data from the temperature sensor a Proportional-Integral-Derivative (PID) feedback algorithm is implemented allowing stable temperatures between 4.2 and 70 K to be maintained to within $\pm 1\,\mathrm{mK}$.

3.5.2 *Magnetic Field*

In order to apply a magnetic field to the sample, a 5 T superconduct-
ing magnet is located in the lower section of the He reservoir of the
cryostat. The field is aligned in the vertical direction and centred upon
the sample insert. The field is controlled by a power supply (Lake
Shore Model 625) that regulates the current in the magnet. The power
supply may be computer controlled, permitting automatic magnetic
field dependent measurements. Changing the current direction re-
verses the field direction, giving a full field range of -5 to 5 T. When
the sample is mounted directly to the piezo stack, the magnetic field
is orientated out of the sample plane (Faraday geometry). Mounting
the sample on a right-angled aluminium bracket allows an in-plane
(Voigt geometry) field to be applied.

3.6 DETECTION

In this thesis two different detection methods are used. In chapter 4
and chapter 5 a photocurrent detection technique is used with the
sample described in subsection 3.4.1 whilst in chapter 6 Resonance
Fluorescence (RF) detection is used with the sample described in sub-
section 3.4.2. This section outlines the basics of each technique and
the apparatus used to perform the measurements.

3.6.1 *Photocurrent*

Optics

The cryostat and corresponding optics are shown in Figure 3.10. The
laser beam exits the fibre and is re-collimated by an objective lens. A
92:8 pelicle BS is mounted on a flip-mount. The BS sends light to the
camera, allowing the sample surface to be imaged in reflection for
alignment of the sample relative to the laser using the piezo stages.
The pelicle BS is flipped out of the beam-path during experiments
to maximise the power transmitted to the sample. A QWP sets the
laser polarization to circular. Close to the sample an aspheric lens
(Edmund Optics) with focal length 4.51 mm focuses the light onto
the sample surface. The lens diameter is 6.33 mm with a numerical
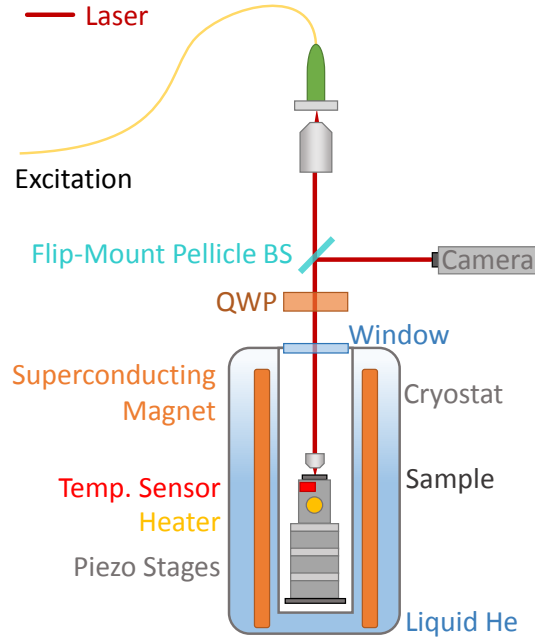
Figure 3.10: Cryostat optics and setup for photocurrent measurements. List of acronyms: Beam-Splitter (BS) Helium (He) Quarter-Wave Plate (QWP)

aperture of 0.55, resulting in a focused spot FWHM of around 1.8 μm at a wavelength of 950 nm.

Principles of Photocurrent Detection

The principle of photocurrent detection is to electrically detect carriers as they tunnel from the QD [60]. As such, it is necessary to ensure that the carriers tunnel from the QD much faster than the rate of radiative recombination (typical timescale 400 - 800 ps [122, 178]. This is achieved by applying a reverse bias (V_A) to the sample as illustrated in Figure 3.11. The excitation laser photo-excites carriers in the QD which subsequently tunnel to either the Ohmic (n^+ GaAs) or the Ti Schottky contact. A suitably sensitive measurement circuit is able to measure the photocurrent that arises from this.

The electric field (F) applied to the sample is given by Equation 3.1 [163]:

$$F = \frac{(V_A - V_{Bi})}{W_i},$$

(3.1)

where V_A is the applied bias, V_{Bi} is the built-in voltage of the diode
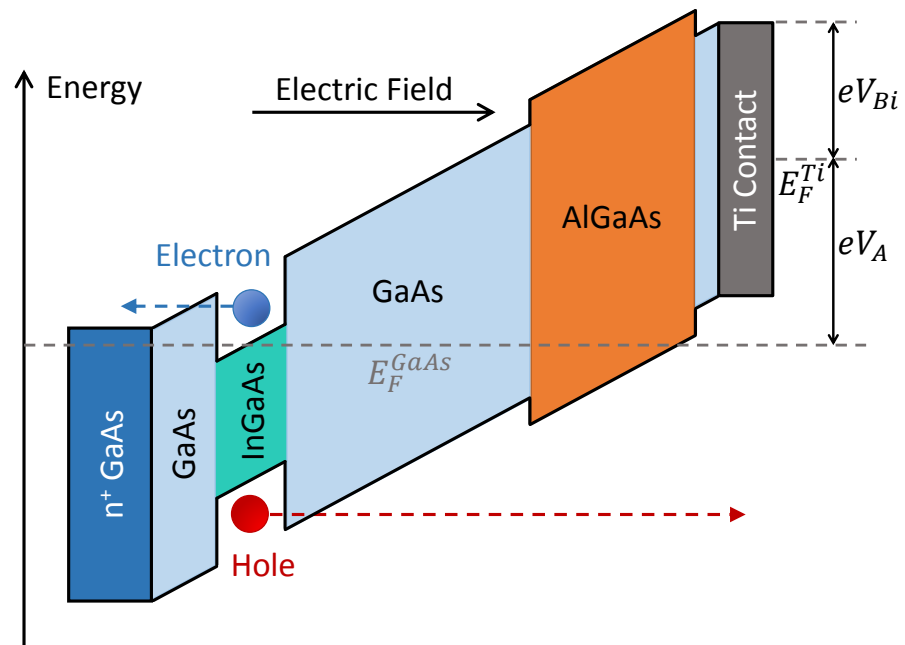
Figure 3.11: Schematic band structure diagram of the photocurrent sample (see subsection 3.4.1). The Fermi levels of the Ti (E_F^{Ti}) and the GaAs (E_F^{GaAs}) are different, leading to a built-in voltage (V_{Bi}) in the device. Application of a reverse bias voltage (V_A) increases E_F^{Ti} relative to E_F^{GaAs}, tilting the bands further. This increases the rate of electron (blue) and hole (red) tunnelling (dashed arrows) from the QD which may be measured as a photocurrent.
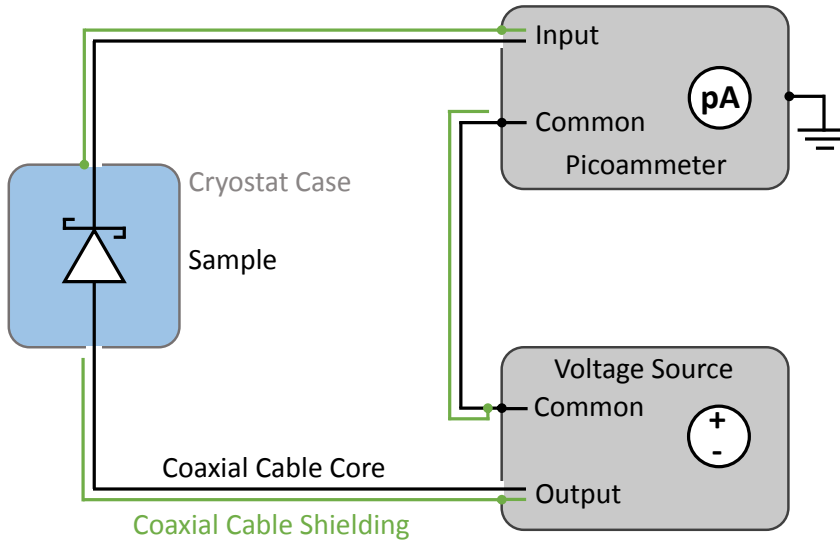
Figure 3.12: Schematic of the photocurrent measurement circuit. Coaxial cables are used throughout.

(see Figure 3.11) and W_i is the width of the intrinsic region. V_{Bi} is taken to be 0.76 V (half the band gap of GaAs) whilst W_i is taken to be the separation of the Ohmic and Schottky contacts which is 230 nm for this sample (see subsection 3.4.1). A photocurrent signal is observed in the range $-1.2 \leq V_A \leq -0.5$ V which corresponds to $-54.8 \leq E \leq -93.9 \, \text{kV cm}^{-1}$. At lower fields it is possible for carriers to tunnel from the contacts to the QD which is typically exploited to deterministically charge QDs with single carriers [154]. In the bias range utilised for the photocurrent measurements, the QD remains uncharged until illuminated by the laser.

Measurement Circuit

The currents arising from photocurrent are extremely small. The theoretical maximum photocurrent from a single exciton can be determined by:

$$I_{PC} = e\Gamma_{rep} \tag{3.2}$$

where e is the electron charge and Γ_{rep} is the laser repetition rate. Using the repetition rate of the Ti:S (76.2 MHz) gives a value of $I_{PC} =$
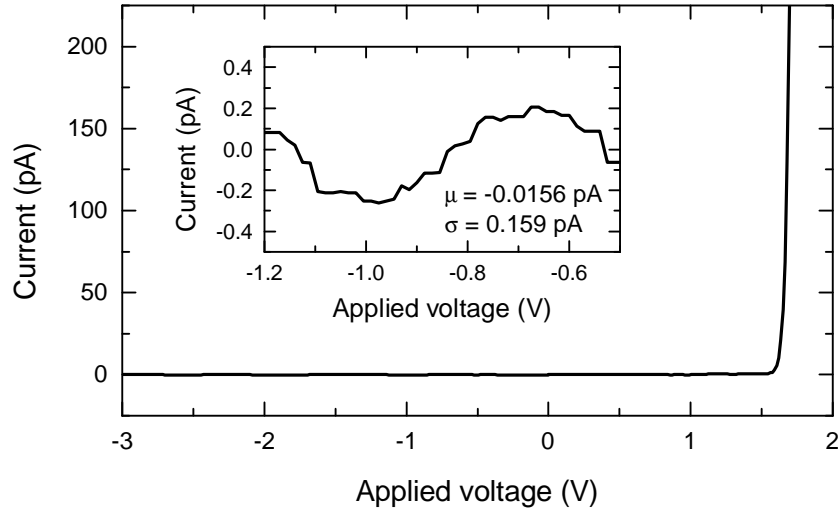
Figure 3.13: IV curves of the sample taken without illumination at a temperature of 4.2 K. As defined in Equation 3.1, negative voltages correspond to reverse bias and positive voltages to forward bias. The inset shows a close-up of the behaviour of the dark current in the region where photocurrent is observed.

12.2 pA. As such, in order to accurately measure the exciton population the measurement setup most not only be sensitive to sub-picoamp currents but any noise must also be significantly less than the expected signal.

In Figure 3.12 a schematic of the measurement circuit is shown. A voltage source (Keithley 230) biases the sample whilst a picoammeter (Keithley 6485) with 10 fA resolution and 20 fA typical noise [330] measures the resulting current. Co-axial cables are used with the outer layer (green lines) connected only to ground to serve as shielding to prevent noise from external electromagnetic interference. In addition, care is taken to ensure that the entire circuit is grounded only to a single common ground at the picoammeter. This prevents ground loops which are a major noise source as they can allow noise currents to arise from electromagnetic induction.

Electrical Properties of Sample

The low photocurrents that are to be measured also require excellent electrical performance from the sample. In particular, the leakage current should be as low as possible and any fluctuations should be much smaller than the QD signal. In order to characterise the elec-

trical properties of the diodes, IV curves are measured for the diodes. An example low temperature (4.2 K) dark IV measurement is presented in Figure 3.13. Towards forward bias (positive voltage) the diode turns on at around -1.6 V whilst in reverse bias (negative voltage) the leakage current is very small and close to constant. The inset shows a close-up of the voltages where photocurrent is observed, very small fluctuations are observed indicating the excellent electrical properties of the diode. The mean dark current in this region is found to be -15.6 fA with a standard deviation of 159 fA. This enables measurement of photocurrent spectra across a range of reverse biases with a high signal to noise ratio.

Background Signals & Detection Efficiency

When the sample is illuminated by the laser, a power-dependent background signal is observed. This originates from incoherent absorption by other QDs within the laser spot. A typical raw power dependence measurement for a single QD in this sample is shown in Figure 3.14(a). A linear fit gives a gradient of $1.163 \pm 0.005 \, \mathrm{pA}^{-1} \, \mathrm{\mu W}^{-1}$ which is typical for this sample. By subtracting this background, the coherent response of the QD can clearly be seen as a Rabi rotation (Figure 3.14(b)). Owing to the incoherent nature of the excitation, the gradient of this background does not change significantly with excitation wavelength and thus photocurrent spectra such as Figure 3.15 (where the excitation energy is scanned) show clear peaks from QD transitions against a flat background.

The background-subtracted photocurrent for excitation with a π-pulse is around 10.8 pA. Comparing this with Equation 3.2 shows that this value is 89% of the theoreretical maximum and thus the detection is highly efficient. The primary source of loss is radiative recombination of the exciton occuring before electron tunnelling (around 6-8% for typical parameters when minimised by application of a strong reverse bias [2]). When performing experiments at lower electric fields a reduced photocurrent is measured in accordance with this expectation. It should also be noted that the theoretical maximum assumes an exciton population of 1 is created by the laser pulse, in practice

---

2 This can be derived by solving a simple rate equation with electron tunneling rate $\Gamma_e = 50 \, \mathrm{ps}^{-1}$ and radiative recombination rate $\Gamma_R = 600 - 800 \, \mathrm{ps}^{-1}$. Further discussion of these rates can be found in chapter 4.
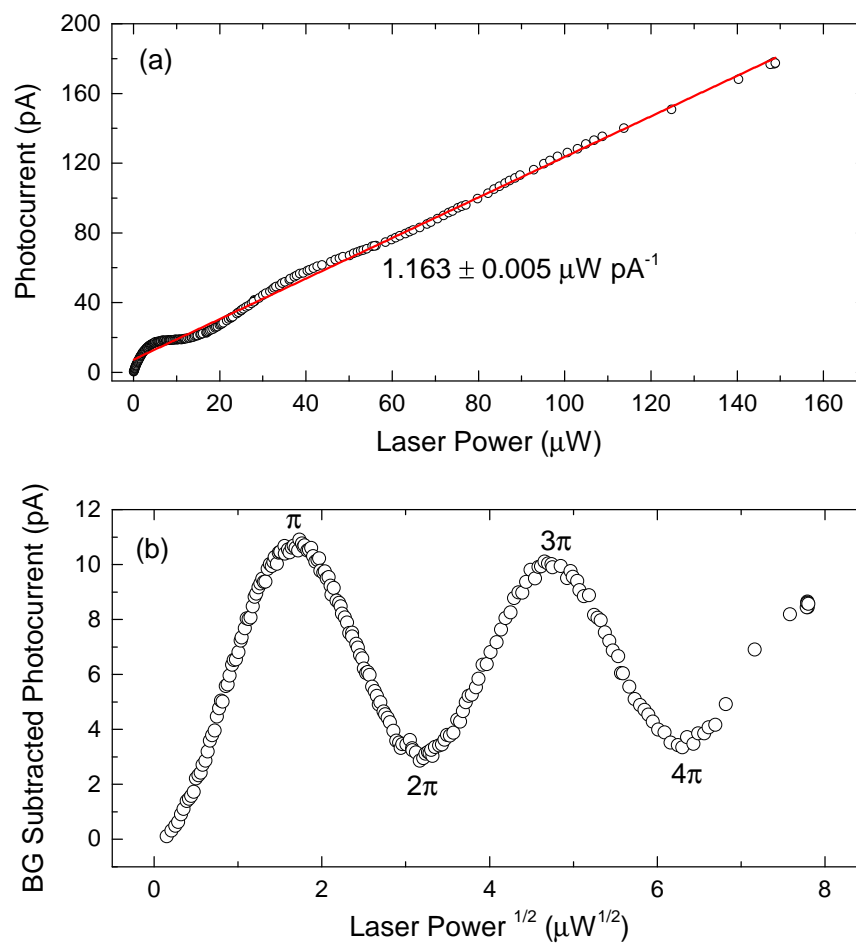
Figure 3.14: Typical Rabi rotation of a single QD exciton measured by photocurrent detection: (a) As the laser power is increased, characteristic oscillations are observed in the photocurrent with a linear background. (b) Subtracting the linear background and plotting the photocurrent against the square-root of laser power allows the oscillation (Rabi rotation) of the exciton population to be clearly resolved.
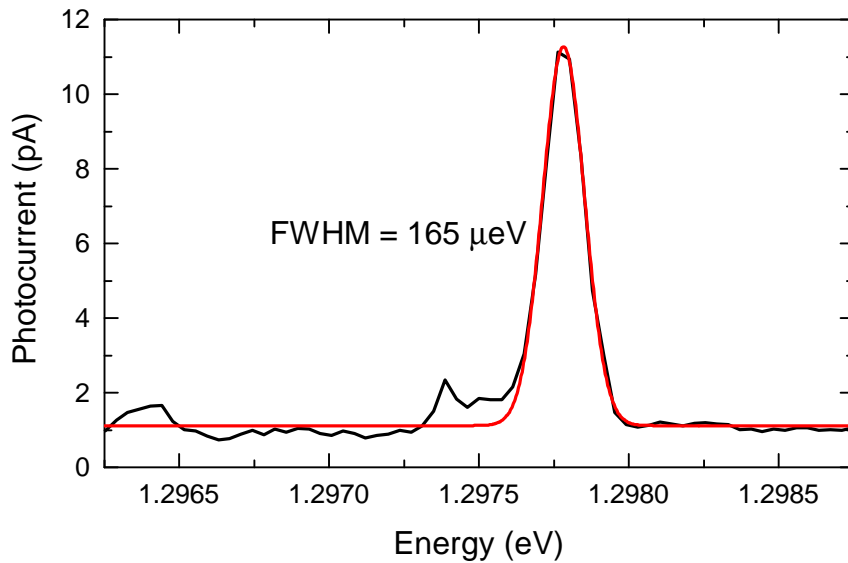
Figure 3.15: Typical single pulse spectrum of a single QD exciton measured by recording the photocurrent as the energy of a π-pulse is scanned. The red line is a Gaussian fit to the experimental data which reproduces the linewidth of the excitation laser. Occasional weak peaks in the background are observed, these correspond to excitation of other QDs that are poorly coupled to the laser (e.g. under the shadow mask).

this value is reduced by acoustic phonon damping [63, 64]. The conversion between photocurrent and exciton population is discussed in detail in subsection 5.3.2.

In a pump-probe measurement such as those presented in chapter 4 and chapter 5, the pump pulse contributes an additional background both from the incoherent absorption previously discussed and from coherent excitation of the pumped transition. Owing to the excellent power stability of the excitation, this background is also very stable as the probe energy is scanned to produce a spectrum (see Figure 4.2 for example). In some figures where single pulse and pump-probe measurements are compared the background levels of both signals are subtracted (see for example Figure 5.4). This is achieved by measuring the background when the probe pulse is detuned from any resonance and then subtracting this from the spectrum.
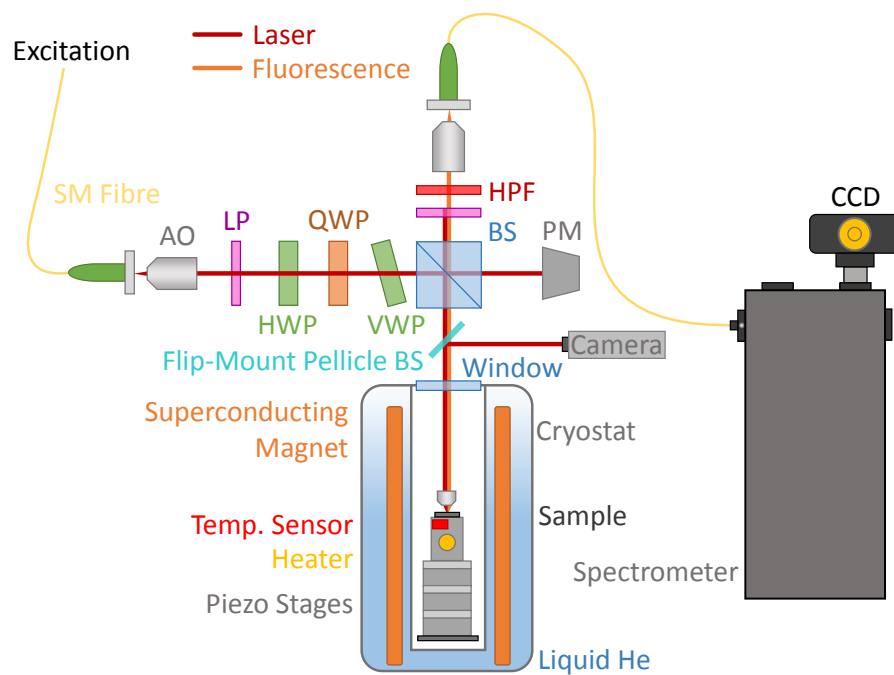
Figure 3.16: Cryostat optics and setup for resonance fluorescence measurements. A cross-polarized excitation detection setup is used to supress detection of the scattered laser light. List of acronyms: Achromatic Objective (AO), Beam-Splitter (BS), Charge-Coupled Device (CCD), High Pass Filter (HPF), Half-Wave Plate (HWP), Linear Polarizer (LP), Power Meter (PM), Quarter-Wave Plate (QWP), Single Mode (SM), Variable Wave-Plate (VWP)

3.6.2   *Resonance Fluorescence*

Optics

To perform RF measurements, the cryostat optics are modified considerably from the setup used for photocurrent measurements shown in Figure 3.10. The resonance fluorescence setup is illustrated in Figure 3.16. A 50:50 BS is placed to split the cryostat optical axis into separate excitation and detection paths. Adjustment of the relative positions and alignments of the fibres and objective lenses allows the excitation and collection paths to be aligned correctly. The Achromatic Objective (AO) used on the excitation path is a Thorlabs AC050-008-B-ML with an effective focal length of 7.5 mm, chosen to give good matching to the SM fibre mode.

A Linear Polarizer (LP) ensures a pure input state after the fibre whilst a series of waveplates (HWP, QWP and VWP (Berek type)) allow the excitation polarization to be accurately defined. Between leaving the BS and returning to it, the optical path and cryostat are identical to those described in Figure 3.10 with the exception that the QWP is removed as linear polarization is used in these experiments.

When the light returns from the cryostat, the vertical path from the BS contains a second LP which is cross-polarized with respect to the excitation laser. This heavily suppresses the scattered laser light, enabling the detection of RF from single QDs. A High Pass Filter (HPF) with a cut-off at 900 nm is also present. When non-resonant above-band excitation is used, the HPF prevents the laser from reaching the spectrometer. The light is coupled to a SM fibre using an aspheric lens (Thorlabs C110TMD-B) with a focal length of 6.24 mm and delivered to the spectrometer.

Detection

A 0.75 m single spectrometer (Princeton Acton SP2750) and back illuminated deep-depletion CCD detector (Princeton PyLoN 400BR) were used to detect the QD emission. The setup was calibrated using a Neon Argon spectral lamp to ensure high accuracy. One advantage of this approach over typical single-channel detection is that the detection is spectrally resolved. This allows processes involving two transitions such as the biexciton cascade to be resolved in a single meas-
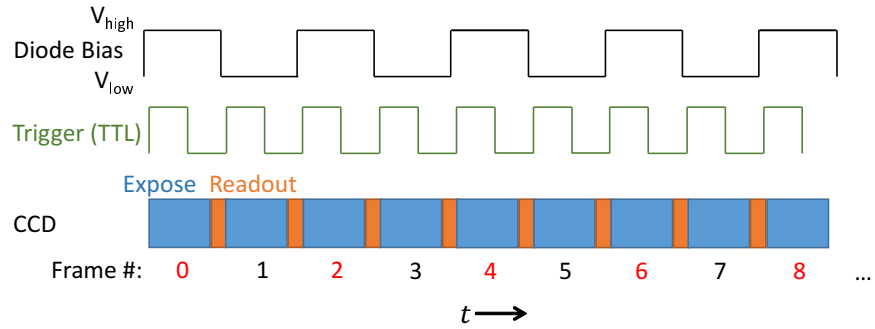
Figure 3.17: Schematic of the differential modulation scheme. A square wave of frequency f is applied to the sample diode. A phase-locked ($\phi = 0$) TTL signal with frequency $2f$ is sent to the CCD detector, triggering a new exposure (blue rectangles) on each rising edge. The frames are sent to two bins, one (red numbers) for even frames and the other (black numbers) for odd frames. The differential spectrum is obtained by subtracting the two bins.

urement. At low excitation powers the polarization suppression and spatial filtering from the SM fibres is sufficient to observe background-free RF (see subsection 6.4.1 for example).

Differential Resonance Fluorescence

At higher excitation powers, scattered laser light (resolvable due to the greater linewidth) begins to appear increasingly strongly in the spectra. This is unsurprising as owing to the phenomenon of Rabi rotation (see subsection 2.6.2), the QD signal will never exceed that observed for driving with a π-pulse whilst the scattered laser power continues to increase linearly. To overcome this, for higher power measurements a differential technique is used whereby the QD is shifted by the QCSE in and out of resonance with the laser. This is achieved by application of a square-wave bias to the sample with the off-resonance case always chosen to be to higher energy to prevent phonon-assisted excitation (see section 5.2). The CCD exposure is synchronised with the diode modulation using TTL, allowing alternate frames to be captured with the QD resonant and off-resonant with the laser. The modulation scheme is summarised in Figure 3.17. The modulation rate is typically set to around 22 Hz as a trade-off between suppressing noise fluctuations and maximising the signal to noise of the CCD exposure and readout processes.
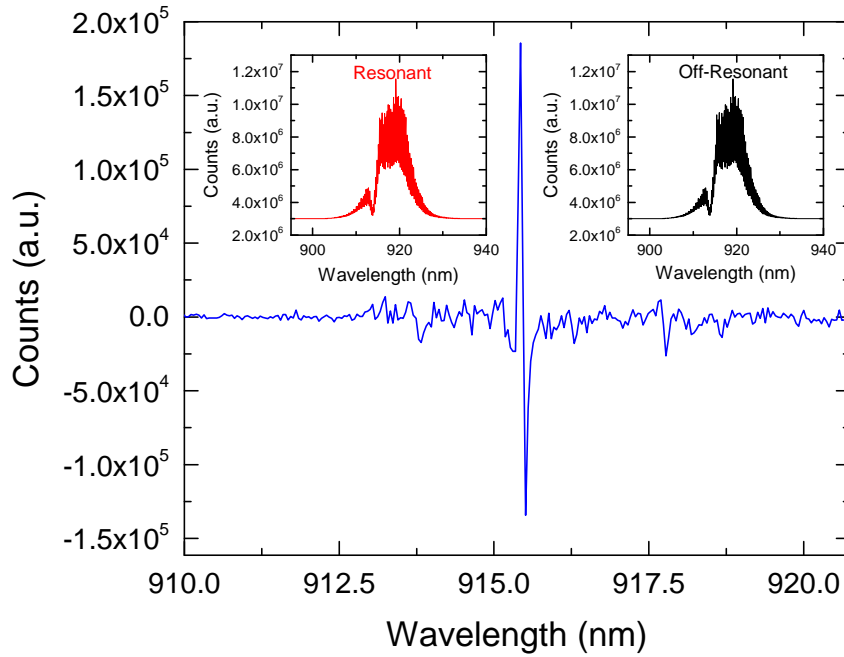
Figure 3.18: Differential resonance fluorescence spectrum of a single QD. In this measurement the unshaped laser was used ($\Delta\lambda \approx 16.2$ nm). The insets show the non-differential spectra for the cases where the QD is resonant (red) and off-resonant (black) with the cavity. The cavity is observed in both insets as a strong dip in reflectivity at around 915 nm. The blue line in the main figure shows the differential spectrum derived from the two insets; a narrow differential feature corresponding to the QD emission at the two biases is observed with the scattered laser light effectively suppressed.

Repetition of this process for many frames and then subtracting the off-resonant frames from the resonant frames allows recovery of the QD signal even in the presence of a much stronger scattered laser signal. An example of this is shown in Figure 3.18 where the blue line is the differential spectrum. Owing to the spectrally broad ($\Delta\lambda \approx 16.2$ nm) unshaped laser being used, the QD is excited at both biases leading to a differential feature in the spectrum. By comparison with the non-differential spectra (insets) it can be seen that this method allows recovery of a low-noise single QD signal even when the scattered laser is around two orders of magnitude stronger than the QD emission.

3.7   SUMMARY

The experimental setups outlined in this chapter present a means to resonantly excite single QDs with picosecond pulses whose centre energy, spectral width, polarization, pulse energy and inter-pulse delay may be readily controlled. This provides a versatile excitation setup for performing both single-pulse and pump-probe investigations of single QD dynamics. In addition, electric, magnetic and additional CW laser fields may be applied to the sample whilst the sample temperature may also be varied. Finally, two different means of accurately detecting single QD dynamics have been presented: electrical detection of photocurrent and optical detection of resonance fluorescence.

4

HIGH-FIDELITY INITIALISATION OF HOLE SPIN QUBITS

4.1 INTRODUCTION

Single hole spins confined in semiconductor QDs are an attractive stationary qubit candidate owing to their long coherence times [158, 179, 181], ultrafast optical coherent control [179, 181, 182] and potential for integration with circuit-style devices for QIP [67, 68, 331]. Initialisation of a qubit to a well-defined state is a critical part of any QIP protocol as it limits the fidelity of the entire process. An ideal initialisation scheme should be fast, operate on-demand and have high fidelities to permit error correction [17, 332] (see second DiVincenzo criterion in section 1.2), whilst long qubit lifetimes are desirable to maximize the number of possible gate operations (see third DiVincenzo criterion in section 1.2).

A range of single carrier spin initialisation schemes have previously been demonstrated for both single QDs and QDMs. These include optical pumping [156, 157, 333], coherent population trapping [158, 334] and the ionization of an exciton [127, 149–152]. Optical pumping methods have reached fidelities as high as 99.8% in an out-of plane magnetic field [156] with initialisation times of the order of μs. Faster (ns) initialisation with slightly lower fidelities has been observed in an in-plane magnetic field [157, 334]. However, practical fault-tolerant QIP implementations [17, 332] require initialisation that is fast compared to decoherence to ensure that the maximum number of gate operations may be performed within the qubit coherence time. Hence, it is desirable to further increase the initialisation speed.

When driven by ultrafast pulsed lasers, exciton ionization schemes can offer both picosecond initialisation times and on-demand operation. Unfortunately, the anisotropic exchange interaction [126, 128, 169] (see subsection 2.2.4) typically reduces fidelity by causing spin precession during the exciton lifetime [127, 172, 335]. Fast electron tunnelling minimizes this effect with fidelities of $\mathcal{F} > 96\%$ obtained

for ionization in QDMs [152] and $\mathcal{F} > 97\%$ for probabilistic (CW) initialisation of single QDs [336]. However, a negative consequence is the reduction of the hole qubit's lifetime to 300 ps [152] or 3 ns [336] respectively. This is significantly less than the hole's long extrinsic coherence time ($T_2^* \approx 10$ ns) [158, 179, 181, 182], reducing the coherence time (T_2) and the number of possible gate operations. Application of a strong out-of-plane magnetic field inhibits spin precession (see subsection 2.3.2) resulting in $\mathcal{F} > 99\%$ [172]; however out of plane fields are incompatible with present coherent control schemes [158, 179, 181, 195] which require in-plane spin quantization.

In this chapter fidelities exceeding 99% are demonstrated at zero magnetic field with on-demand, < 100 ps initialisation and a hole lifetime that can be as high as 25.2 ns. This is achieved by exciton ionization in a QD with near-zero Fine-Structure Splitting (FSS), rendering the anisotropic exchange interaction negligible relative to the exciton lifetime. To demonstrate that such a scheme is also applicable to typical QDs with finite FSS, the Optical Stark Effect (OSE) [164] is used to reduce the FSS [141, 142], resulting in increased fidelity. These key results were published as a Rapid Communication in Physical Review B [131].

4.2   SAMPLE DETAILS

These measurements were performed on the photocurrent sample discussed in subsection 3.4.1 based upon the VN382 wafer. 5 QDs were chosen for further study on the basis that they exhibited a range of different values of FSS ($E_{FSS} = \hbar\delta$) between 2.01 and 31.2 µeV. These QDs were located in either the C1 or C2 apertures of the sample and are referred to as dots A-E in order of increasing FSS as detailed in Table 4.1.

4.3   SPIN INITIALISATION BY EXCITON IONIZATION

4.3.1   *Principles of Operation*

The concept of hole spin initialisation by exciton ionization is outlined in Figure 4.1. A circularly-polarized laser pulse with π pulse

QD	FSS (μeV)
A	2.02 ± 0.20
B	7.10 ± 0.32
C	13.2 ± 0.72
D	21.6 ± 1.10
E	32.2 ± 0.71

Table 4.1: Measured values of FSS for the five QDs under study. See section 4.4 for measurement details.
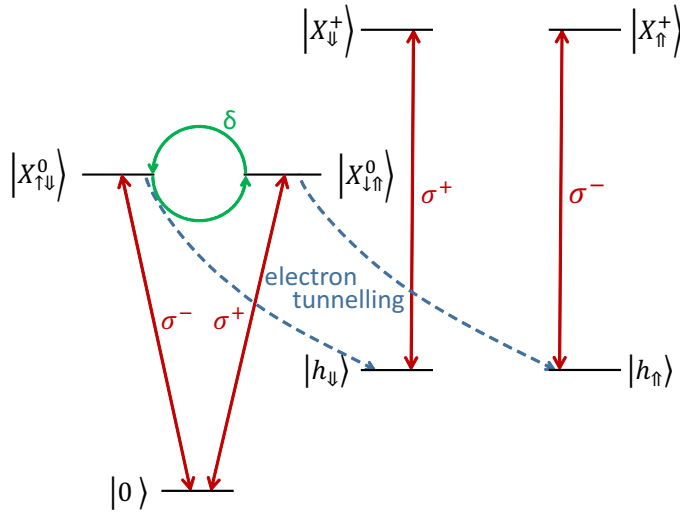
Figure 4.1: Energy levels in the circularly polarized basis at zero magnetic field where ($\downarrow$ / $\uparrow$) and ($\Downarrow$ / $\Uparrow$) represent electron and hole spins respectively. The neutral exciton (X^0) states are coupled by the FSS with angular precession frequency δ (green arrows) and decay by electron tunnelling at a rate Γ_e (blue dashed arrows) to leave single holes (h). The hole spin state can be read out by probing the $h \rightarrow X^+$ (positive trion) transitions using $\sigma^{+/-}$ polarized pulses.
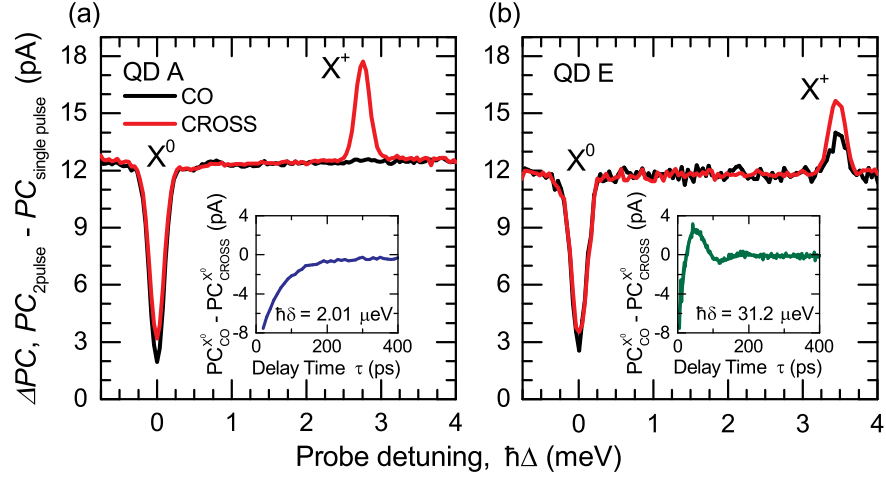
Figure 4.2: Two-colour pump-probe photocurrent spectra of QDs exhibiting (a) negligible (2.01 µeV) and (b) large (31.2 µeV) FSS. Spectra are measured at $E = -72$ kV cm^{-1} and $\tau = 100$ ps when only the hole is left in the QD. Black (red) lines corresponds to a co (cross)-polarized probe laser. Insets: The precession of the neutral exciton spin measured by time-resolved pump-probe spectroscopy [337] (see section 4.4). The exponential damping of the fine-structure beats corresponds to the exciton lifetime $(1/\Gamma_X)$.

area creates a neutral exciton (X^0) in the QD at time $t = 0$. Under a reverse bias DC electric field (F) the exciton population decays at a rate $\Gamma_X = \Gamma_r + \Gamma_e + \Gamma_h$ where Γ_r is the rate of radiative recombination and Γ_e and Γ_h are the electron and hole tunnelling rates respectively. Owing to the larger hole effective mass, the electron tunnelling rates exceed hole tunnelling rates by around two orders of magnitude $(\Gamma_e \gg \Gamma_h)$. At the electric fields studied here, radiative recombination rates are slow compared to electron tunnelling in devices of this structure [122, 178] and hence $\Gamma_X \simeq \Gamma_e$. The tunnelling of the electron leaves behind a single hole with spin conserved from the X^0; thus the initialisation time for the hole is equal to $1/\Gamma_e$. The anisotropic exchange interaction causes precession between the $X^0_{\uparrow\Downarrow}$ and $X^0_{\downarrow\Uparrow}$ states at angular frequency δ, reducing the polarization of the resultant hole spin.

To measure the initialised hole spin, a co (cross)-circularly polarized probe π pulse arrives after a delay (τ) with a detuning of Δ relative to the first pulse. By scanning the probe detuning, two-pulse spectra like those shown in Figure 4.2 are obtained where black (red) traces represent the co (cross)-polarized cases respectively. For presentation purposes, a single-pulse (probe only) spectrum is subtracted

from the two-pulse spectrum to remove any weak spectral features not arising from the pumped QD; the dip at $\Delta = 0$ corresponds to subtraction of the X^0 peak. At Δ equal to the positive trion (X^+) binding energy the $h \rightarrow X^+$ transitions shown in Figure 4.2 are probed. Peaks corresponding to these transitions are observed in the spectra and the hole spin state may be extracted from their relative amplitudes.

In Figure 4.2 the spectrum of QD A with a small FSS of 2.01 μeV is shown. The inset illustrates that exciton spin precession during electron tunnelling is negligible; as a result, the hole spin preparation is almost ideal with no trion peak observed for a co-polarized probe. By contrast, Figure 4.2 shows the case of QD E with a large FSS of 31.2 μeV. The exciton spin precession is seen clearly in the inset whilst prominent trion peaks in both spectra illustrate the reduced fidelity.

4.3.2 *Model*

In order to quantitatively analyse the fidelity of spin initialisation, it is necessary to begin by defining fidelity. A general definition is Equation 4.1 [338]:

$$\mathcal{F} = \langle \phi \,|\rho|\, \phi \rangle \tag{4.1}$$

where ρ is the density matrix of the prepared state and ϕ is the target state. In the case of spin initialisation, the target state is generally either spin up ($\Uparrow$) or spin down ($\Downarrow$).

As outlined in subsection 4.3.1, the fidelity of the hole spin initialisation is limited by the precession of the exciton spin during the exciton lifetime. In order to support experimental measurements and also predict parameter regimes that maximise fidelity, it is helpful to create an analytical model of the hole spin initialisation. The following derivation proceeds along the same lines as previous work by Godden et al. [172, 339]

As a starting point it is taken that the effect of the first (preparation) pulse is to create a spin-polarized neutral exciton in the QD. The FSS causes precession between the two spin states $X^0_{\downarrow\Uparrow}$ and $X^0_{\uparrow\Downarrow}$ with angular frequency δ. To calculate the dynamics of the system the Zeeman splitting ($\hbar\omega_z$) is also included yielding the 2×2 Hamiltonian:

$$H = \frac{\hbar}{2} \begin{bmatrix} \omega_z & \delta \\ \delta & -\omega_z \end{bmatrix}. \tag{4.2}$$

The eigenvectors $|\psi_\pm\rangle$ of this Hamiltonian are:

$$\begin{aligned} |\psi_+\rangle &= \sin(\theta) |{\downarrow}{\Uparrow}\rangle + \cos(\theta) |{\uparrow}{\Downarrow}\rangle \\ |\psi_-\rangle &= \cos(\theta) |{\downarrow}{\Uparrow}\rangle - \sin(\theta) |{\uparrow}{\Downarrow}\rangle, \end{aligned} \tag{4.3}$$

where θ is a mixing angle given by $\tan(2\theta) = -\delta/\omega_z$. The eigenvalues are:

$$\lambda = \pm \frac{\hbar}{2} \sqrt{\omega_z^2 + \delta^2}. \tag{4.4}$$

As previously discussed in [subsection 4.3.1](#), a $\sigma^{-/+}$ preparation pulse creates an exciton with spin $|{\uparrow}{\Downarrow}\rangle/|{\downarrow}{\Uparrow}\rangle$ respectively. These exciton spin states can be rewritten in terms of the eigenvectors:

$$\begin{aligned} |{\uparrow}{\Downarrow}\rangle &= \sin(\theta) |\psi_+\rangle + \cos(\theta) |\psi_-\rangle \\ |{\downarrow}{\Uparrow}\rangle &= \cos(\theta) |\psi_+\rangle - \sin(\theta) |\psi_-\rangle. \end{aligned} \tag{4.5}$$

At a time $t > 0$ these states evolve by accumulating a relative phase determined by the eigenenergy of the Hamiltonian. Considering the scenario of a σ^- polarized preparation pulse, the evolution of the exciton spin state with time may be written as:

$$\left|\psi_{{\uparrow}{\Downarrow}}(t)\right\rangle = \sin(\theta) |\psi_+\rangle e^{i\lambda t} + \cos(\theta) |\psi_-\rangle e^{-i\lambda t} \quad . \tag{4.6}$$

It is now possible to calculate the time-dependent probabilities ($P_{{\uparrow}{\Downarrow}}(t)$ & $P_{{\downarrow}{\Uparrow}}(t)$) of measuring either exciton state by projecting $\left|\psi_{{\uparrow}{\Downarrow}}(t)\right\rangle$ into the basis of exciton spins:

$$\begin{aligned} P_{{\downarrow}{\Uparrow}}(t) &= \left|\langle{\downarrow}{\Uparrow}|\, \psi_{{\uparrow}{\Downarrow}}(t)\rangle\right|^2 = \sin^2(2\theta) \sin^2(\lambda t) \tag{4.7} \\ P_{{\uparrow}{\Downarrow}}(t) &= \left|\langle{\uparrow}{\Downarrow}|\, \psi_{{\uparrow}{\Downarrow}}(t)\rangle\right|^2 = 1 - \sin^2(2\theta) \sin^2(\lambda t). \tag{4.8} \end{aligned}$$

At this point it is necessary to consider the time evolution of the neutral exciton population itself as well as that of the spin. The three sources of exciton population decay are radiative recombination (Γ_r), electron tunnelling (Γ_e) and hole tunnelling (Γ_h). These are illustrated
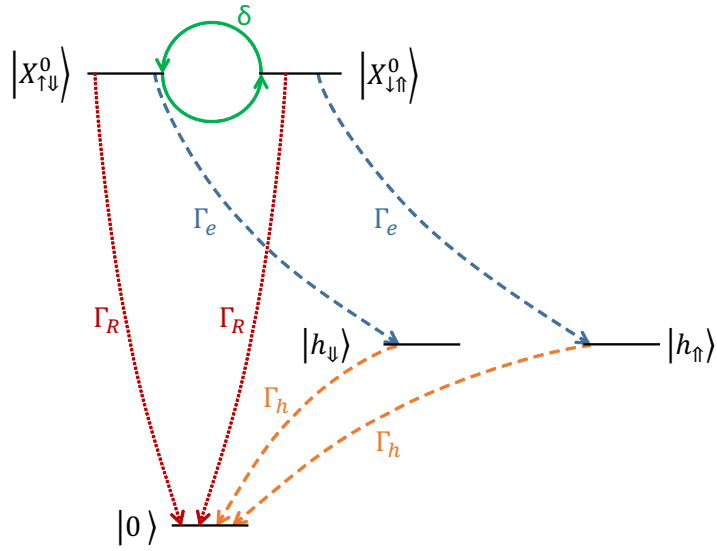
Figure 4.3: Energy level schematic showing the decay channels of the neutral exciton in the device studied. The two neutral exciton spin states are coupled by fine-structure precession of angular frequency δ. The exciton may decay either by radiative recombination to the ground state with a rate Γ_R or to a single hole by electron tunnelling with a rate Γ_e. Single electron states are disregarded as hole tunnelling (Γ_h) is much slower than Γ_e. The single hole states decay to the ground state by hole tunnelling at a rate Γ_h. Hole spin relaxation between spin states is neglected as the hole lifetime is much shorter than the timescale of hole spin relaxation [186].

in Figure 4.3. As discussed in subsection 4.3.1, this sample exhibits electron tunnelling that is much faster than either radiative recombination or hole tunnelling. As such, it is possible to assume that the decay rate of the exciton population (Γ_X) is dominated by electron tunnelling:

$$\Gamma_X = \Gamma_r + \Gamma_h + \Gamma_e \approx \Gamma_e. \tag{4.9}$$

Using this it is now possible to construct expressions for both the total neutral exciton population ($P_+(t)$) and the difference in population between the two neutral exciton spin states ($P_-(t)$):

$$P_+(t) = P_{\uparrow\Downarrow}(t) + P_{\downarrow\Uparrow}(t) = e^{-\Gamma_X t} \tag{4.10}$$

$$P_-(t) = P_{\uparrow\Downarrow}(t) - P_{\downarrow\Uparrow}(t) = \left[1 - \sin^2(2\theta)\sin^2(\lambda t)\right] e^{-\Gamma_X t}. \tag{4.11}$$

As the aim of this scheme is to prepare hole spins, the mapping of the exciton to the hole must be considered. Hole spin relaxation may be neglected as it is several orders of magnitude slower than hole tunnelling at the electric fields considered [186]. Therefore, it is possible to write expressions for the rate of change of the occupation of both hole spin states:

$$\dot{h}_{\Downarrow} = \Gamma_e P_{\uparrow\Downarrow}(t) - \Gamma_h h_{\Downarrow} \tag{4.12}$$

$$\dot{h}_{\Uparrow} = \Gamma_e P_{\downarrow\Uparrow}(t) - \Gamma_h h_{\Uparrow}. \tag{4.13}$$

Defining h_+, h_-, $\dot{h}_+ = \dot{h}_{\Uparrow} + \dot{h}_{\Downarrow}$ and $\dot{h}_- = \dot{h}_{\Uparrow} - \dot{h}_{\Downarrow}$ in a similar manner as to the exciton, it is now possible to write a pair of differential equations for the total and difference of the hole spin state populations:

$$\dot{h}_+ + \Gamma_h h_+ = \Gamma_e P_+ \tag{4.14}$$

$$\dot{h}_- + \Gamma_h h_- = \Gamma_e P_-. \tag{4.15}$$

Both Equation 4.14 and Equation 4.15 have the form:

$$\dot{y} + \alpha y = Q, \tag{4.16}$$

which has the general solution:

$$y = e^{-I} \left[\int_0^t Q e^I \, \mathrm{d}t + c \right],$$ (4.17)

where:

$$I = \int \alpha \, dt.$$ (4.18)

Thus it is possible to find h_+ and h_-. Defining the hole spin contrast (C):

$$C = \frac{h_-}{h_+},$$ (4.19)

it is then possible to derive the fidelity ($\mathcal{F}$) using the relation $C = 2\mathcal{F} - 1$. Finally, the limit $\Gamma_X t \gg 1$ is taken to eliminate the time dependence by considering the case where electron tunnelling is essentially complete. This results in Equation 4.20:

$$\mathcal{F} = \frac{C+1}{2} = 1 - \frac{1}{2} \left\{ \frac{\delta^2}{\delta^2 + \omega_z^2 + (\Gamma_X - \Gamma_h)^2} \right\}.$$ (4.20)

The key conclusion from Equation 4.20 is that the fidelity is determined by competition between electron tunnelling and fine-structure precession, in agreement with the qualitative discussion presented in subsection 4.3.1. Furthermore, it can be seen that the application of a large ($\left| g_z^X \mu_B B_z \right| \gg |\hbar \delta|$) Faraday magnetic field will result in $\mathcal{F} \rightarrow 1$ as fine-structure precession is inhibited by the transformation of the eigenstates from linear to circular as outlined in subsection 2.3.2.

4.3.3 Measuring Fidelity

In order to measure fidelity, it is necessary to define it in terms of experimentally measurable parameters. The photocurrent measured from the co-/cross-polarized trion transitions is proportional to the population of each of the hole spin states respectively. As such, the hole spin contrast (C - see Equation 4.19) may be redefined in terms of these photocurrents:

$$C = \frac{h_-}{h_+} = \frac{PC_{cross}^{X^+} - PC_{co}^{X^+}}{PC_{cross}^{X^+} + PC_{co}^{X^+}},$$ (4.21)
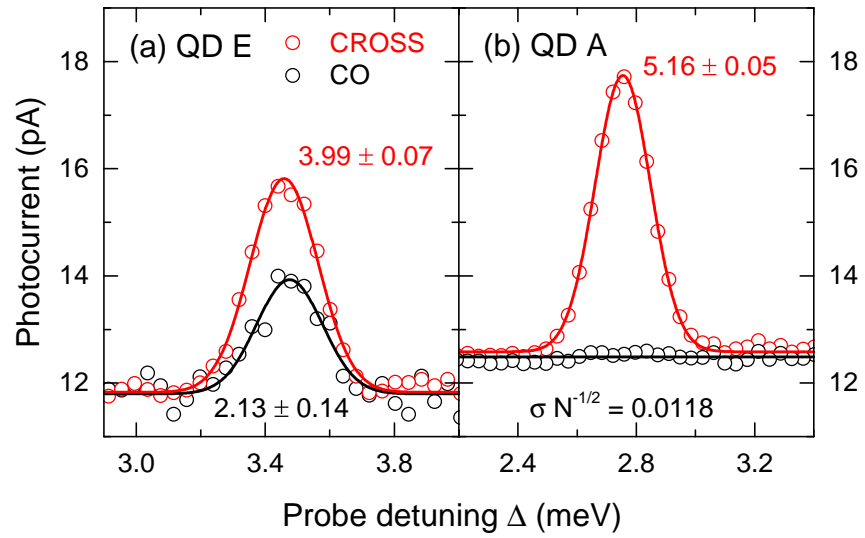
Figure 4.4: Close-up PC spectra of the positive trion peaks of (a) QD E with large FSS and (b) QD A with vanishingly small FSS. The data is the same as in Figure 4.2. The red points represent a probe pulse that is cross-polarized with the pump pulse whilst the black points are the co-polarized case (see Figure 4.1). With the exception of the black line in (b), solid lines are Gaussian fits to the data with numeric values being the extracted amplitudes. In the case of (b), the co-polarized peak is vanishingly small and the quantity $\sigma N^{-1/2}$ is evaluated instead with the line representing the mean value.

where $PC_{cross}^{X^+}$ and $PC_{co}^{X^+}$ are the amplitudes of the X^+ peaks in the co- and cross-polarized spectra respectively. Using the relation $\mathcal{F} = \frac{C+1}{2}$ results in Equation 4.22:

$$\mathcal{F} = \frac{PC_{cross}^{X^+}}{PC_{cross}^{X^+} + PC_{co}^{X^+}}. \tag{4.22}$$

The quantities $PC_{cross}^{X^+}$ and $PC_{co}^{X^+}$ are extracted from Gaussian fits to PC spectra like Figure 4.2. The fitting is illustrated in Figure 4.4(a) for QD E where the large amplitudes of both peaks illustrate that the fidelity is low owing to high FSS. This contrasts to Figure 4.4(b) where the fidelity is high owing to the vanishing FSS of QD A and a peak is observed only for cross-polarization.

For very high fidelities, it is no longer reliable or meaningful to fit a Gaussian peak to the co-polarized spectrum. In this case the variance of the photocurrent noise at the trion position is used to estimate the amplitude [339] and report a lower bound for the fidelity. The datapoints within the laser FWHM of the trion energy are sampled and the amplitude estimate (ϵ) can then be found by Equation 4.23:

$$\epsilon = \frac{\sigma}{\sqrt{N}}, \tag{4.23}$$

where N is the number of datapoints within the sample and σ is their standard deviation. The quantity ϵ then replaces $PC_{co}^{X^+}$ in Equation 4.22 to calculate the lower bound of $\mathcal{F}$. This case is illustrated in Figure 4.4(b) for QD A; evaluating Equation 4.22 for this data gives a fidelity lower-bound of $\mathcal{F} \geq 0.998$.

4.4 MEASUREMENT OF TUNNELLING RATES & FSS

In order to compare experimental results to the predictions of the model accurately it is necessary to know the values of Γ_e, Γ_h and δ with high precision. In this section two different experimental methods to measure these parameters are described.

4.4.1   *Time-Resolved Pump-Probe*

Γ_e, Γ_h and δ may be measured directly by time-resolved pump-probe measurements [337, 340]. In these measurements a circular-polarized pump pulse with $\Theta = \pi$ is resonant with the $|0\rangle \rightarrow |X\rangle$ transition at $t = 0$. After a delay of τ, a resonant probe π-pulse arrives either co- or cross-circularly polarized with respect to the pump pulse. The amplitudes of the neutral exciton photocurrent peaks measured for a co- or cross-circularly polarized probe are referred to as $PC_{co}^{X^0}$ and $PC_{cross}^{X^0}$ respectively. These quantities relate to the occupancy of the co/cross-polarized exciton states ($C_{X^0}/C_{\bar{X}^0}$) by the following relations:

$$PC_{cross}^{X^0} + PC_{co}^{X^0} \propto C_{X^0} + C_{\bar{X}^0} = e^{-\Gamma_X t} \tag{4.24}$$

$$PC_{cross}^{X^0} - PC_{co}^{X^0} \propto C_{X^0} - C_{\bar{X}^0} = e^{-\Gamma_X t} \sin(\delta t) \tag{4.25}$$

As can be seen from Equation 4.24, the quantity $PC_{cross}^{X^0} + PC_{co}^{X^0}$ decays proportional to the total exciton population. This is an exponential decay which is dominated by electron tunnelling as $\Gamma_X \approx \Gamma_e$. Meanwhile, Equation 4.25 illustrates that $PC_{cross}^{X^0} - PC_{co}^{X^0}$ is proportional to the difference between the population of the two exciton states. This results in a precession between the two states of angular frequency δ with the amplitude damped by the exciton lifetime. As such, fitting time-resolved measurements of these quantities allow the values of Γ_X ($\approx \Gamma_e$) and δ to be extracted. Fits to $PC_{cross}^{X^0} - PC_{co}^{X^0}$ for QD A and QD E are illustrated by the red dashed lines in Figure 4.5. The fine-structure oscillation is clearly visible for QD E whilst the vanishingly small FSS of QD A means that only the exponential decay of the exciton population is observed.

In a similar manner, performing time-resolved pump-probe measurements with the probe resonant with the $|h^+\rangle \longrightarrow |X^+\rangle$ transition allows the occupancy of the hole state to be interrogated:

$$PC_{cross}^{h^+} + PC_{co}^{h^+} \propto C_{h^+} + C_{\bar{h}^+} = e^{-\Gamma_h t} - e^{\Gamma_e t}. \tag{4.26}$$

As illustrated by Equation 4.26, the total hole population rises exponentially due to electron tunnelling whilst simultaneously experien-
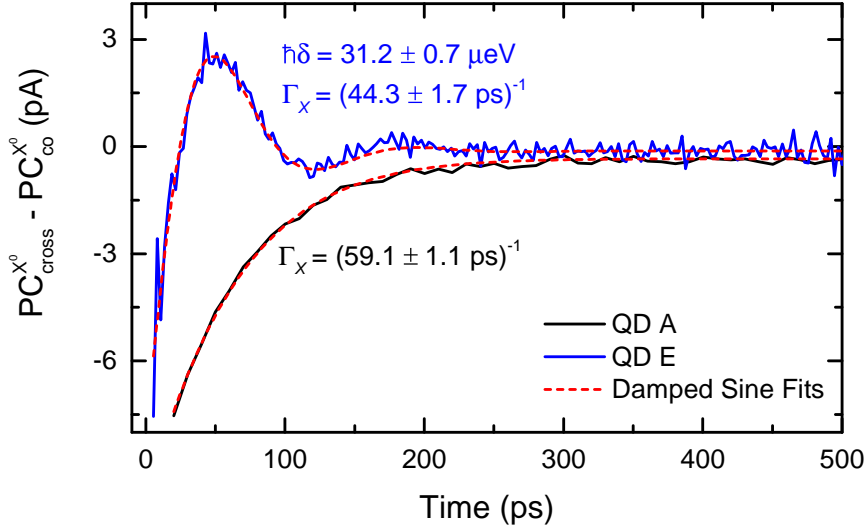
Figure 4.5: Example measurements of $PC^{X^0}_{cross} - PC^{X^0}_{co}$ vs. time for the QDs with the highest (QD E - green) and lowest (QD A - black) FSS. The electric field was was $-73.6\,\mathrm{kV\,cm^{-1}}$ for both measurements. Dashed lines show damped sine fits to the data, the clear oscillation of QD E allows both the values of δ and Γ_X to be extracted. In the case of QD A the fine-structure precession is much slower than Γ_X and the value of δ cannot be reliably determined.

cing a slower exponential decay due to hole tunnelling. Fitting time-resolved measurements of $PC^{h^+}_{cross} + PC^{h^+}_{co}$ thus allows the values of Γ_e and Γ_h to be determined.

An example of such a measurement is illustrated by the black circles in Figure 4.6 for QD A with the electron and hole tunnelling rates for this electric field extracted from the fit (green line). The fidelity of the prepared hole spin may also be evaluated from these measurements using Equation 4.22 and is shown by the red circles. The lack of any clear time dependence illustrates that fidelity is constant with time as would be expected in the case of negligible hole spin relaxation.

4.4.2 *High-Resolution Photocurrent Spectroscopy*

The time-resolved pump-probe method has a limited resolution for the measurement of FSS. The origin of this limit is the case when δ becomes sufficiently small that it approaches the magnitude of Γ_X. In this case, the oscillations in $PC^{X^0}_{cross} - PC^{X^0}_{co}$ are sufficiently damped
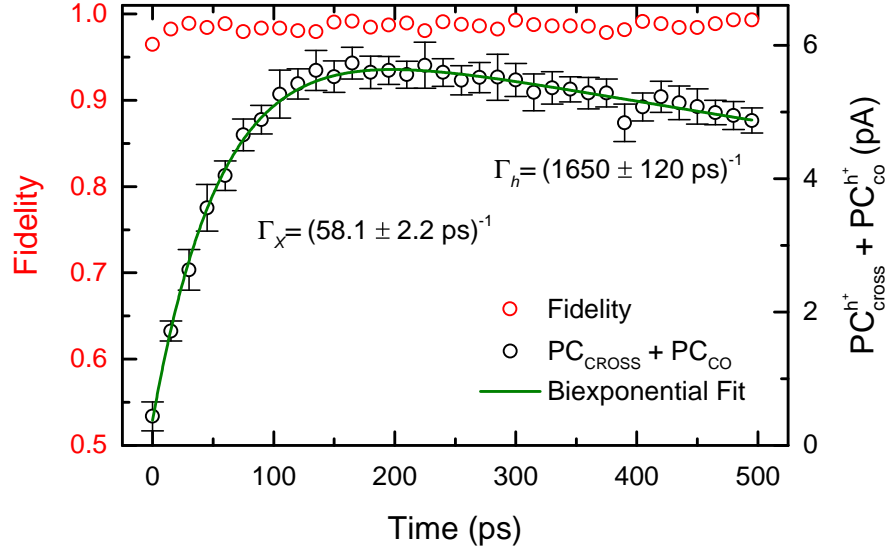
Figure 4.6: Plot of $PC_{cross}^{h^+} + PC_{co}^{h^+}$ (black circles) and F (red circles) vs. time for QD A at an electric field of $-73.6\,\mathrm{kV\,cm^{-1}}$. A bi-exponential fit (green line) to $PC_{cross}^{h^+} + PC_{co}^{h^+}$ allows Γ_e and Γ_h to be extracted.

that it is not possible to resolve them as in the black data for QD A in Figure 4.5. Thus, to measure the smallest values of the FSS a different approach is required. A narrow linewidth CW laser (FWHM $<$ 10 neV) operating at a fixed wavelength is used to perform high resolution photocurrent spectroscopy [163, 341, 342]. The $0 \rightarrow X_0$ transition is Stark-shifted through the laser line by changing the bias applied to the diode. In order to convert from applied bias to the energy of the exciton, a series of single pulse photocurrent spectra are measured at different bias voltages. Plotting the energy of the exciton peak vs. bias gives the expected quadratic dependence (Equation 2.4), an example of which is illustrated for QD C in Figure 4.7.

After conversion to exciton energy, the resulting spectrum has a Lorentzian lineshape with typical linewidth $\sim 40\,\mu\mathrm{eV}$ as illustrated in Figure 4.8(a). In an ideal case, the linewidth (ΔE) of the exciton should obey the uncertainty relation of Equation 4.27:

$$\Delta E = \frac{\hbar \Gamma_X}{2}, \qquad (4.27)$$

which is approximately $14\,\mu\mathrm{eV}$ at this value of Γ_X. The broadening relative to this limit is attributed to charge fluctuations in the electrostatic environment of the dot during the measurement which has been observed in similar devices [197].
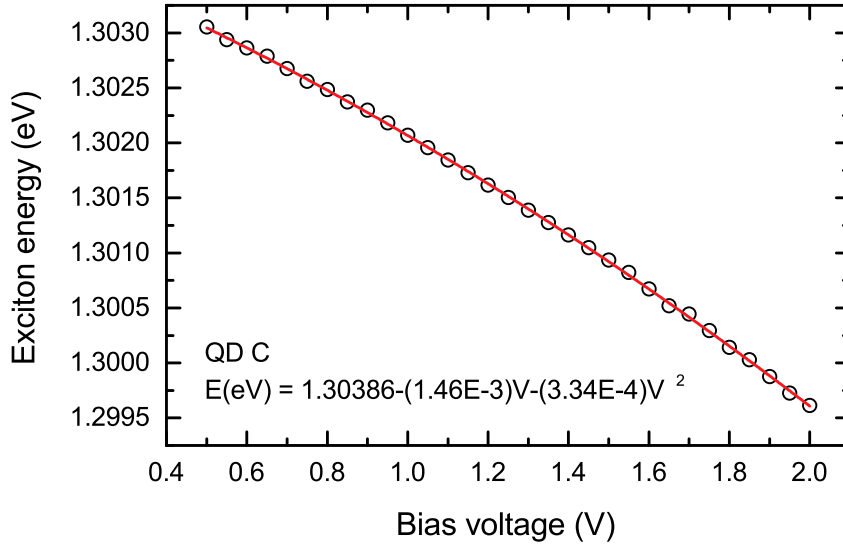
Figure 4.7: Example plot of exciton energy (extracted from single pulse pho-
tocurrent spectra) vs. bias voltage for QD C. The data agrees
well with a quadratic fit of the form of Equation 2.4 (red line) al-
lowing accurate conversion from bias voltage to energy for high
resolution photocurrent spectroscopy.
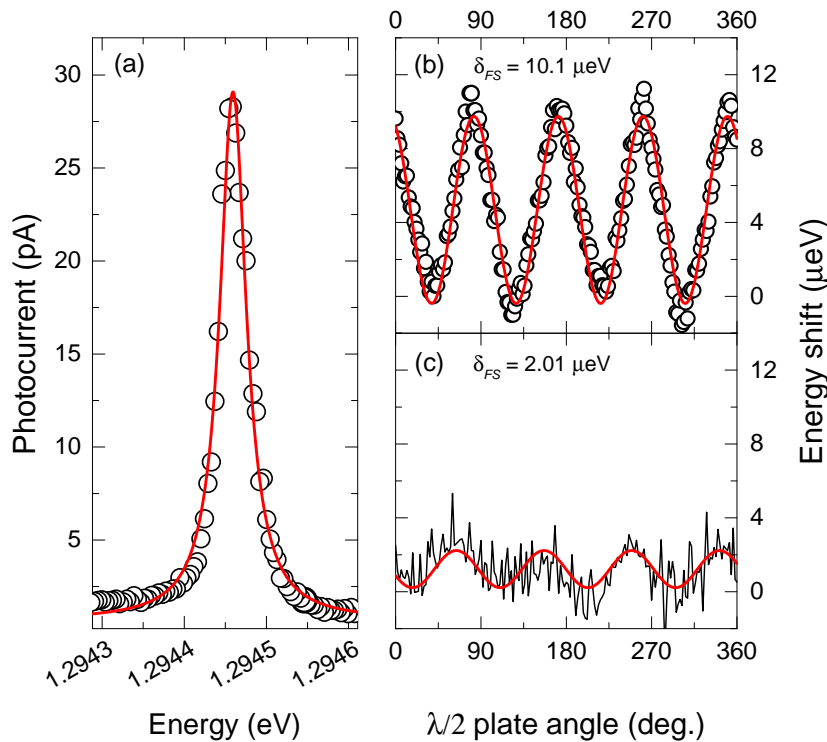
Figure 4.8: (a) Typical high-resolution photocurrent spectrum of the QD
A neutral exciton with a Lorentzian fit (red line) of linewidth
$39.3 \pm 0.3\ \mu eV$. Plot of the neutral exciton energy of QDs with
(b) moderate δ and (c) very small δ (QD A) as a function of
half-wave plate angle. Red lines: Fitting with $\sin^2(\theta)$ function.
The amplitude of the fits yields a fine structure splitting of
$\hbar\delta = 10.1 \pm 0.1\ \mu eV$ and $2.01 \pm 0.2\ \mu eV$ respectively.
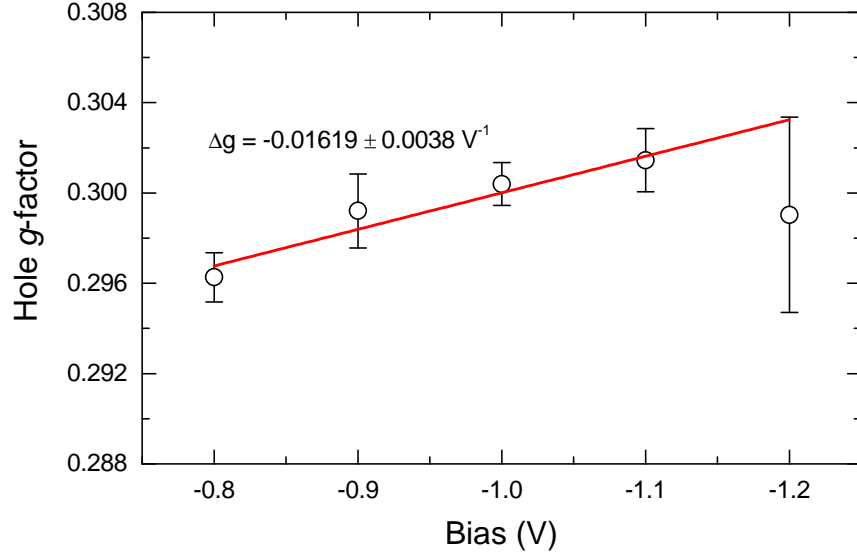
Figure 4.9: Variation of the hole in-plane *g*-factor with applied bias for QD C. The values were extracted from voltage-dependent pump-probe measurements of the hole spin precession as a function of magnetic field.

Rotating the linear polarization angle of the CW laser with a HWP causes the exciton energy to oscillate with an amplitude of $\hbar\delta$ [342]. The physical origin of this is that the linearly polarized laser creates a superposition of the two fine-structure split linear eigenstates. As the polarization rotates, the composition of the superposition changes and accordingly, the energy. The energies of the maxima and minima correspond to the eigenstate energies and as a result the oscillation has an amplitude $\hbar\delta$. Such a measurement is shown for a QD with moderate $\hbar\delta$ $(10.1 \pm 0.1 \, \mu\text{eV})$ (not included in Table 4.1) and very small $\hbar\delta$ $(2.01 \pm 0.20 \, \mu\text{eV})$ (QD A) in Figure 4.8(b) and (c) respectively. This provides a reliable means to measure values of $\hbar\delta$ that are as small as a few μeV, allowing the quantitative study of spin initialisation in the limit of vanishingly small FSS.

4.4.2.1 *Estimation of T_2^* for QD A*

Using the linewidth measurement of Figure 4.8(a) it is possible to estimate the extrinsic pure dephasing time of a hole spin confined within QD A. Subtracting the lifetime-limited linewidth from the measured linewidth leaves a broadening of 25.3 μeV. Assuming that this broadening is dominated by charge noise (in agreement with noise spectroscopy measurements on X^0 [183]), the broadening may be con-

verted to a voltage fluctuation of $\Delta V = 0.0173$ V using the measured Stark shift for QD A. Measurement of the voltage-dependence of the in-plane hole g-factor for a different QD in the same sample (QD C - see Figure 4.9) gives a gradient of -0.01619 V^{-1}. Converting this to a Zeeman energy fluctuation gives $\Delta E_Z = 0.0162$ µeV T^{-1} as a function of appled in-plane magnetic field. Finally, using the relation $T_2^* = 2\hbar/\Delta E_Z$ [256] the extrinsic pure dephasing time may be estimated as $T_2^* = 17.3$ ns at $B_x = 4.7$ T. This agrees well with the value of $T_2^* = 15.4^{+5.5}_{-3.3}$ ns measured by *Godden et al.* for a similar sample at $B_x = 4.7$ T.

4.5   INITIALISATION IN AN OUT-OF-PLANE MAGNETIC FIELD

One of the predictions of the model derived in subsection 4.3.2 is that application of a strong out-of-plane magnetic field will increase the fidelity of spin preparation by inhibiting fine-structure precession of the neutral exciton. Indeed, this approach has previously been used to demonstrate very high fidelities [172] with a free parameter fit of Equation 4.20 showing good agreement with data measured for a single QD with modest FSS. In this section, the predictive power of the model is tested by comparing experimental data with a small magnetic field step of 0.05 T to the predictions of Equation 4.20. Measured values of Γ_e, Γ_h and δ are used rather than a free-parameter fit.

In order to know the variation of ω_z with magnetic field, the exciton g-factor is measured. The energies of the two circularly-polarized exciton states are measured by taking single pulse spectra as a function of magnetic field. The splitting of these states is the Zeeman splitting (see subsection 2.3.2) and relates to the exciton g-factor (g_z^X) by Equation 4.28:

$$E_z^X = \hbar\omega_z = \left| g_z^X \right| \mu_B B_z, \tag{4.28}$$

where μ_B is the Bohr magneton. In Figure 4.10 the measured exciton Zeeman splitting of QD A is plotted (black circles) against magnetic field. A linear fit (red line) allows the magnitude of the g-factor to be found, for this QD a value of $\left| g_z^X \right| = 1.11 \pm 0.02$ is measured which falls within the typical range of InGaAs SAQDs [169, 170]. Thus, using
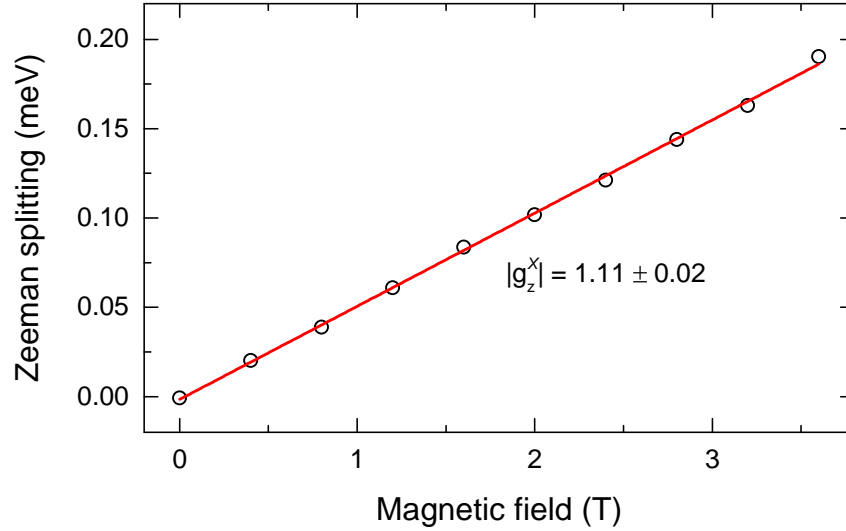
Figure 4.10: Measurement of the exciton Zeeman splitting (black circles) vs. magnetic field for QD A. The red line is a linear fit to the data which allows the magnitude of the g-factor ($|g_z^X|$) to be found from its gradient.

this approach and the methods described in section 4.4 it is possible to determine all the parameters in Equation 4.20 for each QD.

In Figure 4.11 measurements of fidelity (open circles) vs. applied out-of-plane magnetic field are presented for QDs A (red), C (green) and E (blue). The solid lines are plots of Equation 4.20 using the measured parameters of each QD. A small correction (< 0.01) is made to the maximum fidelity value to reflect the noise limit of the PC measurements. It can clearly be seen in Figure 4.11 that the model agrees very well with the measured data, confirming the predictive power of Equation 4.20. For QDs C and E a characteristic Lorentzian dip centred on $B_z = 0$ is observed, corresponding to a reduction in fidelity owing to fine-structure precession. This dip is absent for QD A, a flat line is instead observed owing to its negligible FSS. By $B_z = \pm 2.5$ T all QDs have reached a noise limited fidelity close to unity, illustrating that a strong out-of-plane magnetic field allows for high-fidelity initialisation in QDs with a range of parameters.

However, as discussed in section 4.1, present schemes for coherent control of spin qubits [158, 179, 181, 195] require in-plane spin quantization. Thus, in order to obtain high fidelities that are compatible with coherent control it is necessary to consider varying other
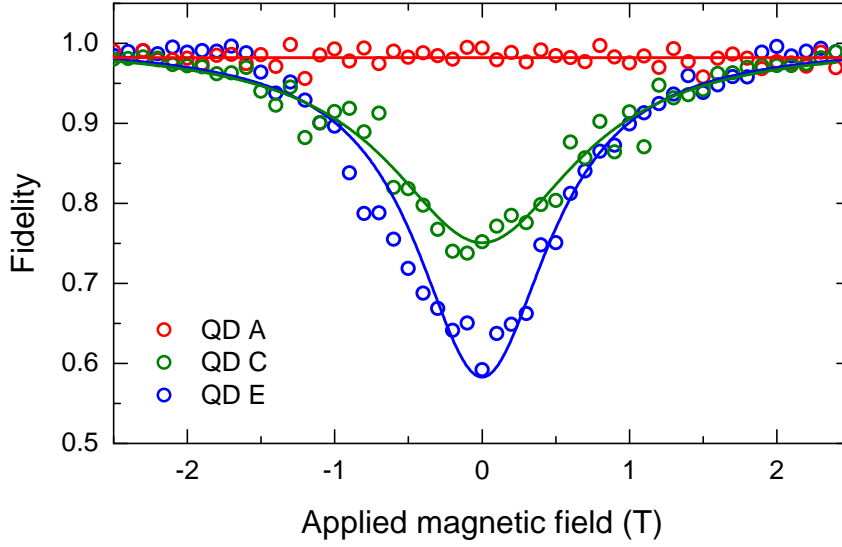
Figure 4.11: A plot of the experimentally measured fidelity (open circles) vs. magnetic field for QDs A (red), C (green) and E (blue). The solid lines represent plots of Equation 4.20 using experimentally measured values of Γ_e, Γ_h, δ and $\left|g_z^X\right|$ for the QD of the corresponding colour.

parameters in order to achieve similar performance without an out-of-plane magnetic field.

4.6 INITIALISATION AT ZERO MAGNETIC FIELD

From inspection of Equation 4.20 it can be seen that if the out-of-plane magnetic field is removed ($\omega_z = 0$) then the remaining strategies to increase $\mathcal{F}$ are either to minimise δ or maximise $(\Gamma_e - \Gamma_h)$. The second approach (fast electron tunnelling) has seen some success at increasing the fidelity [152, 336]; however it has the consequence of reducing the hole lifetime as discussed in the introduction (section 4.1). This is significant as for effective QIP it is desirable to perform as many gate operations as possible within the qubit lifetime (see third DiVincenzo criterion in section 1.2). In this section the variation of fidelity with δ is investigated with the objective of demonstrating high fidelity initialisation that does not compromise the qubit lifetime.
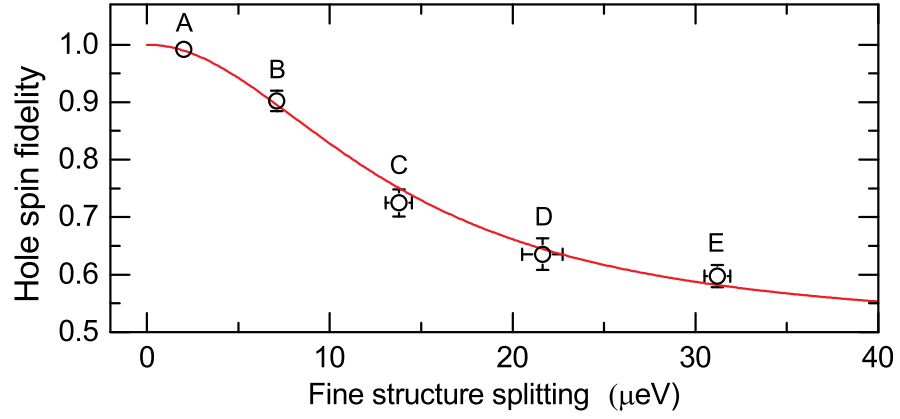
Figure 4.12: Fidelity vs. fine-structure splitting as measured for QDs with different FSS. For all QDs, $\mathcal{F}$ was measured at $\Gamma_e = 0.021\ \mathrm{ps}^{-1}$. The red line is a calculation using Eq. Equation 4.20.

4.6.1 *FSS Dependence of Initialisation Fidelity*

To investigate the variation of $\mathcal{F}$ with δ, the fidelities of the five QDs with different FSS are measured at a constant electron tunnelling rate (Γ_e). This is achieved by measuring the bias-dependence of the tunnelling rates of each QD and setting the bias for each fidelity measurement such that Γ_e is a constant value ($0.021\ \mathrm{ps}^{-1}$). The tunnelling rates and FSS are measured by the methods described in section 4.4. The results of this measurement are shown by the black circles in Figure 4.12 whilst the red line is a plot of Equation 4.20 with $\omega_z = 0$ and $(\Gamma_e - \Gamma_h) = 0.021\ \mathrm{ps}^{-1}$ (as $\Gamma_e \gg \Gamma_h$).

From Figure 4.12 it can be seen that $\mathcal{F}$ falls with δ, fitting with the qualitative expectation that fidelity will fall as the fine-structure precession increases relative to electron tunnelling. For QD A ($\hbar\delta = 2.01 \pm 0.20\ \mu\mathrm{eV}$) a fidelity lower bound of $\mathcal{F} \geq 0.993$ is measured. This value is only limited by the noise present in the co-polarized spectrum and implies an initialisation error rate below the 0.75% threshold required for error correction in a QIP protocol [343].

4.6.2 *High Fidelity Initialisation with Long Qubit Lifetimes*

Owing to the negligible exciton spin precession of QD A, the fidelity is no longer as sensitive to the electron tunnelling rate. This gives the possibility to reduce the diode electric field to maximize the hole life-
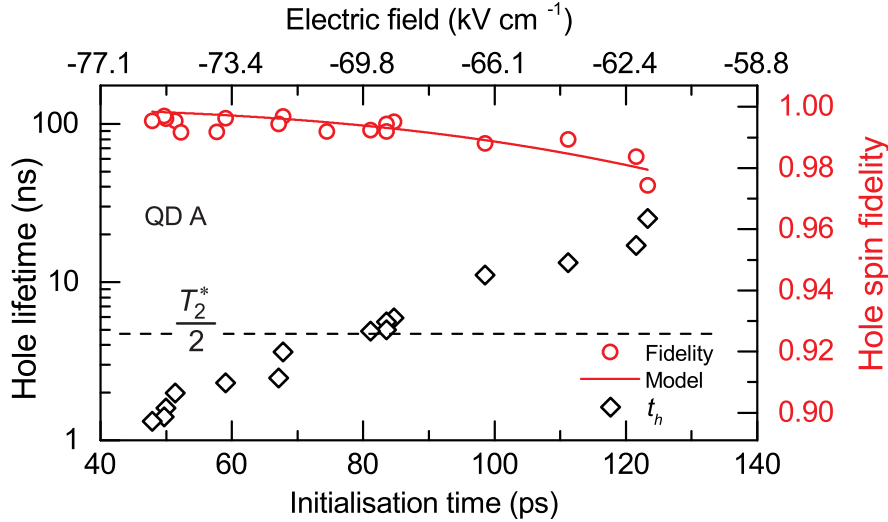
Figure 4.13: Hole lifetime ($1/\Gamma_h$) (diamonds) and fidelity lower bound (red circles) plotted vs. initialisation time ($1/\Gamma_e$) and approximate DC electric field for QD A. Error bars are of the order of the data point size. The model (red line) represents a fit of Equation 4.20 with measured $\hbar\delta = 2.01 \pm 0.20\,\mu\text{eV}$ and fitting parameter $\hbar\chi_E = -0.0219 \pm 0.0007\,\mu\text{eV V}^{-1}\,\text{cm}$ corresponding to a small change in FSS with DC electric field (see Figure 4.14).

time ($T_h = 1/\Gamma_h$) whilst retaining a high initialisation fidelity. Two consequences of reducing the diode bias are a moderate increase in initialisation time ($1/\Gamma_e$) owing to slower electron tunnelling and a small change in FSS [344, 345]. This increase in initialisation time is not significant so long as it remains much smaller than the hole lifetime and comparable to the qubit gate time (~20 ps [179, 181]).

Previous studies on similar samples have shown that the coherence time of the hole spin is limited by the hole tunnelling rate [179] (Γ_h) at typical electric fields. Beyond this, the next limit is the extrinsic pure dephasing time ($T_2^* \simeq 10\,\text{ns}$ [158, 179, 181, 182]) which most likely originates from fluctuations in the electric field acting on the hole g-factor [181–183] (see discussion in subsection 2.4.5). In the limit of negligible extrinsic pure dephasing, or spin-flips, the coherence time is twice the hole lifetime (see discussion in subsection 2.4.1). Thus, a good target is $2T_h > T_2^*$, the point at which pure dephasing rather than hole tunnelling becomes the dominant limitation on the coherence time.

To demonstrate that it is possible both to exceed this target for the lifetime and retain a high initialisation fidelity, Figure 4.13 shows the results of measuring fidelity, initialisation time and hole lifetime for
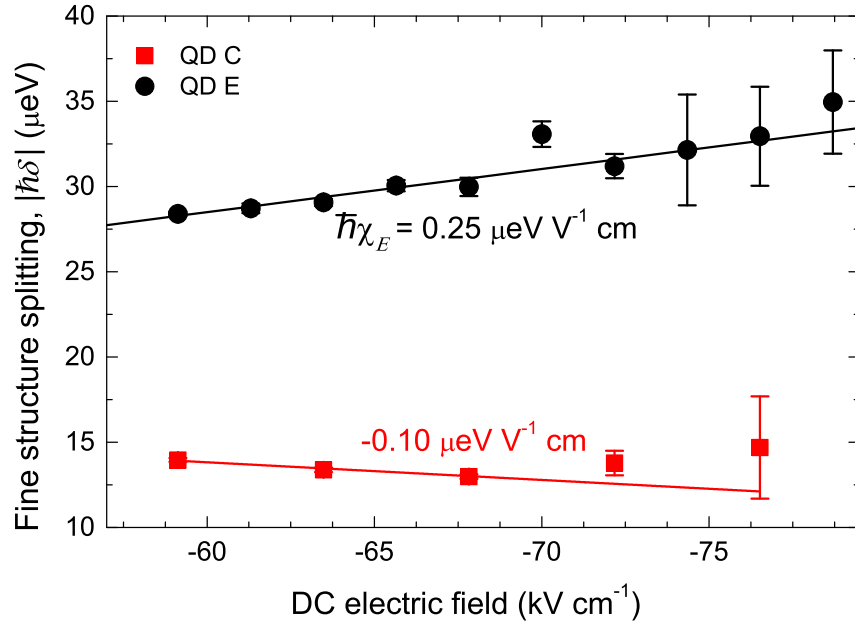
Figure 4.14: Variation of FSS with DC electric field for QDs C and E with different values of δ. The labels show the values of $\hbar\chi_E$ extracted from the linear fits. The opposite signs result from the two QDs being elongated along orthogonal crystal axes whilst the deviation of the red data points from the fit at high DC electric field corresponds to the onset of $\Gamma_e \gg \delta$ and thus the resolution limit for a given QD and DC electric field. This figure is adapted from Ref. [346] and is included with permission.

a range of DC electric fields on the low FSS QD A. At an initialisation time of 83.5 ps, the hole lifetime exceeds 5 ns for the first time and thus the criterion $2T_h > T_2^*$ is satisfied. For electric field strengths satisfying this criterion the measured fidelity lower bounds range from ≥ 0.974 to ≥ 0.995, emphasizing that it is possible to have both high initialisation fidelity and long qubit lifetimes with this scheme. It should be noted that as the electric field is reduced, the photocurrent amplitude for an electron-hole pair also reduces leading to reduced amplitudes of the trion peaks in the fidelity measurement. As the noise level remains approximately constant, this results in a natural roll-off in the highest resolvable fidelity. All of the fidelities measured in Figure 4.13 are noise-limited and thus reported as lower bounds.

To confirm that the fidelities measured fit with the expectations of the model it is first necessary to incorporate the variation of δ with the DC electric field. The full dependence can only be found by numerical simulations and the exact physical origin is still the subject of theoretical study [344, 345]. However, for relatively small variations

in DC field away from the minimum, a linear approximation [162] agrees well with experimental field-dependent time-resolved pump-probe measurements as illustrated in Figure 4.14. As such, δ in Equation 4.20 is substituted according to Equation 4.29:

$$\delta\left(F\right) = \delta\Big|_{F_0} + \chi_E\left[F - F_0\right],\tag{4.29}$$

where F is the DC electric field applied to the diode, $\delta\Big|_{F_0}$ is the FSS measured at electric field F_0 and χ_E is a linear gradient describing the variation of δ with F. The linear fits in Figure 4.14 give $\hbar\chi_E = 0.25 \pm 0.04\,\mu\text{eV V}^{-1}$ cm for QD E and $-0.10 \pm 0.02\,\mu\text{eV V}^{-1}$ cm for QD C. These values are consistent with literature values (0.285 μeV V^{-1} cm [146]) for similar samples. The increased error bars and deviation of the red points from the fit line at higher electric fields corresponds to the onset of $\Gamma_e \gg \delta$ and hence the resolution limit of this measurement. As such, it is not possible to perform the same measurement on QD A. Nor is it possible to accurately measure $\hbar\chi_E$ by the high resolution photocurrent spectroscopy technique as this is reliant on using F to tune the QD into resonance with a fixed wavelength laser.

By inserting Equation 4.29 into the model of Equation 4.20 and taking χ_E as a free fitting parameter (all other parameters are measured), excellent agreement with the data is obtained [see red line in Figure 4.13]. This further supports the conclusion that it is indeed possible to obtain both high fidelities and long lifetimes from a QD exhibiting negligible FSS. From the fit, the value $\hbar\chi_E = -0.0219 \pm 0.0007\,\mu\text{eV V}^{-1}$ cm is found which is smaller than those measured in Figure 4.14 but still physically reasonable. Indeed, from these measurements it appears that the magnitude of $\hbar\chi_E$ decreases for QDs with lower initial FSS. Whilst further studies would be required to draw definitive conclusions, this could indicate that the change in FSS may be related to the electric field modifying the anisotropy of the QD as predicted by some theoretical models [344].

4.7   INCREASING FIDELITY WITH THE OPTICAL STARK EFFECT (OSE)

Due to the importance of low FSS QDs for polarization entangled photon sources [129, 130, 148], deterministic growth of symmetric QDs is a topical area of research [100, 132, 133] but is yet to be demonstrated. As such, in-situ methods for tuning FSS are widely studied, using strain [138, 139], magnetic [140] and laser [141, 142] fields as well as both lateral [144, 145] and vertical [146, 147] DC electric fields. This presents a question - is it possible to use one of these tuning methods to attain performance comparable to QD A for a random QD with non-vanishing FSS?

In order to retain control over the qubit energy and lifetime it is desirable to tune the FSS using a field that is independent from the DC electric field. Thus, in this section a detuned CW laser is used to tune δ by the OSE [141, 142, 164] at a fixed DC electric field.

4.7.1   Tuning FSS by the OSE

In the scheme studied here, the OSE is induced by a linearly polarized CW laser which is positively detuned from the co-polarized $X \rightarrow XX$ (biexciton) transition by Δ_{CW} as illustrated in Figure 4.15. The neutral exciton eigenstates ($X_{H/V}$) are linearly polarized along the in-plane crystal axes and split by $\hbar\delta$ as discussed in subsection 2.2.4. Significantly, this allows the eigenstates to be addressed individually by selecting the laser polarization. Defining X_V as lower in energy, the influence of a positive-detuned V-polarized laser will be to reduce δ by Stark-shifting the X_V state to higher energy. By contrast, an H-polarized laser increases δ by shifting the X_H state to higher energy.

In the case of positive detuning ($\Delta_{CW} > 0$), the change in FSS due to the OSE ($\Delta\omega$) is given by a slightly modified form of Equation 2.5 [164]:

$$\Delta\omega = \frac{s}{2}\left(\Delta_{CW} - \sqrt{\Delta_{CW}^2 + |\Omega|^2}\right), \qquad (4.30)$$

where Ω is the Rabi splitting induced by the CW laser (proportional to the square-root of laser intensity $\sqrt{I}$) and $s = \pm 1$ when the CW laser is H/V polarized. Similar to previous reports [141, 254], a linear
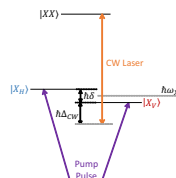
Figure 4.15: Illustration of the OSE scheme using the QD energy levels in the linear basis. The neutral exciton eigenstates $(X_{H/V})$ are split by $\hbar\delta$. The CW laser is V-polarized and positively detuned from the $X_V \to XX$ transition by $\triangle_{CW}$. The pump pulse addresses both exciton levels owing to its circular polarization and FWHM $\gg \hbar\delta$.
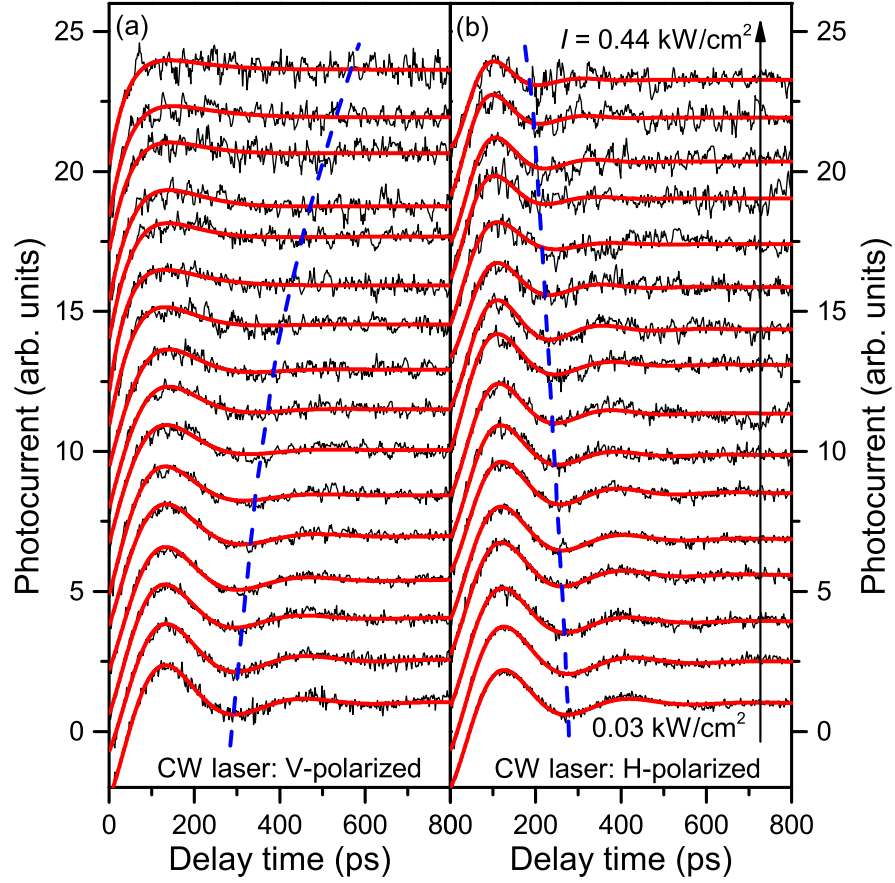
Figure 4.16: Fine structure precession of the exciton spin vs. CW laser intensity (I) measured by time-resolved pump-probe photocurrent on QD C. The CW laser is either (a) V- or (b) H-polarized and positively detuned from the $X \to XX$ transition (see Figure 4.15). $\hbar\Delta_{CW}$ = 76.6 and 63.4 µeV when the CW laser is H/V-polarized respectively. The CW laser intensity ranges from 0.03 to 0.44 kW cm^{-2}. Red lines are fits of an exponentially damped sine function which may be used to extract the value of δ. Blue lines: guides for the eye indicating the change in fine-structure period.

blue-shift of the exciton energy with I that is independent of polarization is observed. This arises due to charge screening from the large number of carriers generated in the surrounding material by the CW laser and results in a linear dependence of Δ_{CW} on I.

In Figure 4.16 the CW laser photon energy is fixed and the FSS of QD C is measured by time-resolved pump-probe spectroscopy as a function of both laser intensity (I) and polarization. It can be seen by eye that for a V-polarized CW laser (Figure 4.16(a)) the fine structure period increases, corresponding to a reduction in FSS. For an H-polarized CW laser (Figure 4.16(b)) the period decreases indicating
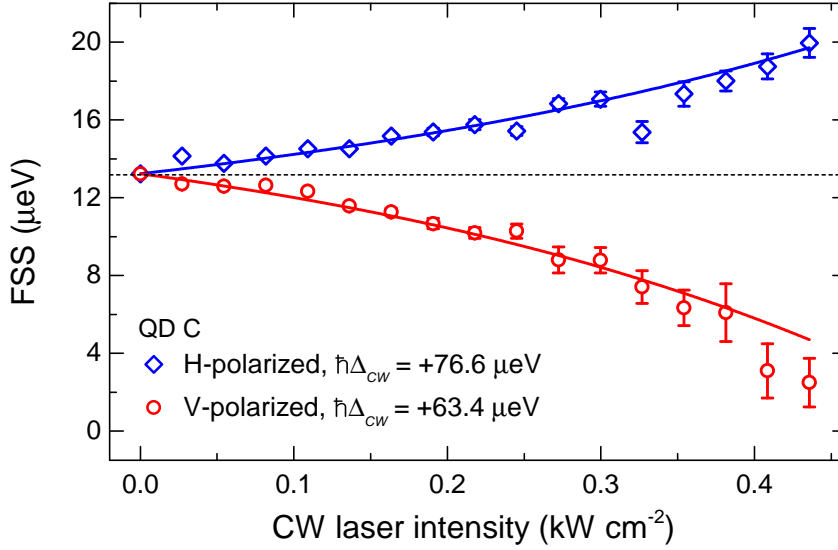
Figure 4.17: FSS vs. CW laser intensity for QD C with initial $\hbar\delta = 13.2\,\mu$eV. The measurement was performed at $E = -60\,$kV cm^{-1} to resolve small δ by maximising the exciton lifetime (see discussion in section 4.4). The blue diamonds (red circles) correspond to an H (V)-polarized CW laser which addresses the high (low) energy exciton eigenstate. The solid lines are fits of Equation 4.30, full details of these fits are contained in appendix A.1.

increased FSS. This is in agreement with the qualitative prediction of Equation 4.30.

The results of plotting the values of δ extracted from the fits in Figure 4.16 against CW laser intensity are shown in Figure 4.17. For a V-polarized CW laser (red circles), δ reduces from its initial value of $\hbar\delta = 13.2 \pm 0.1\,\mu$eV to a minimum of $\hbar\delta = 2.49 \pm 1.25\,\mu$eV at $I = 0.44\,$kW cm^{-2}. Conversely, when the laser is H-polarized (blue diamonds) δ increases, proving that the change in FSS is induced by the OSE. The solid lines show a fit of Equation 4.30 to the data (see appendix A.1 for further details of the fitting parameters and procedure).

4.7.2 *High Fidelity Zero-Field Initialisation for Non-Zero FSS*

To demonstrate that reducing FSS leads to an increase in fidelity, hole spin fidelity was measured as a function of CW laser intensity. The laser is V-polarized and $\hbar\triangle_{CW} = 33.4\,\mu$eV. The result of this measurement is shown in Figure 4.18; for $I = 0.25\,$kW cm^{-2} (FSS $\simeq 8.7\,\mu$eV) a fidelity of $\mathcal{F} = 0.868 \pm 0.036$ is measured, an increase of 0.142 over
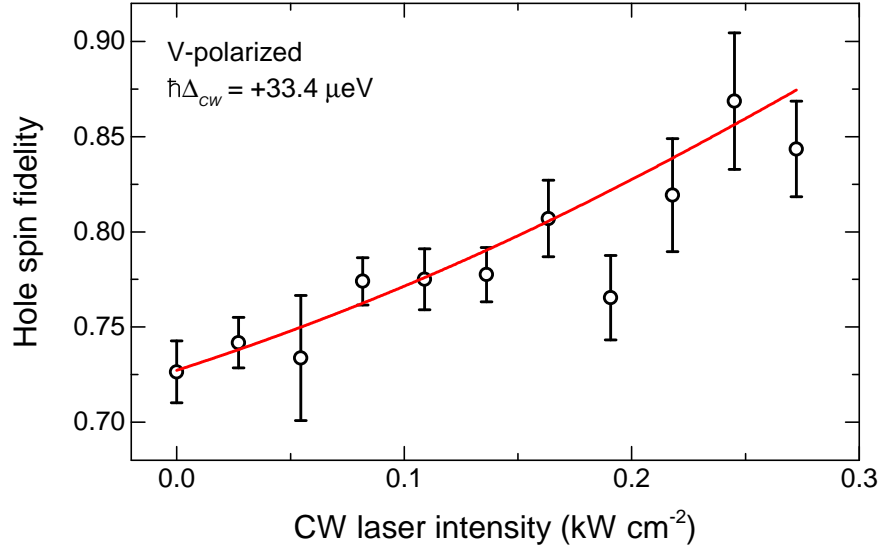
Figure 4.18: Hole spin initialisation fidelity of QD C vs. CW laser intensity for a *V*-polarized CW laser at $E = -72$ kV cm^{-1} to maximize photocurrent detection efficiency. The line is a fit of the model (Equation 4.20) incorporating the variation of δ with CW laser intensity (see appendix A.1 for full details).

that measured with no CW laser. The red line shows a calculation using Equation 4.20 with experimentally derived parameters (see appendix A.1 for details) which again agrees closely with the data. In both experiments, the maximum I is limited by photocurrent fluctuations due to laser power instability. This particularly limits the fidelity measurement as at $I > 0.25$ kW cm^{-2} fluctuations exceed the small (~ 1 pA) co-polarized peak amplitude, limiting the maximum $\mathcal{F}$ that can be measured. However, the agreement with the model and the large optical Stark shift observed in Figure 4.17 indicate that fidelities as high as those measured for QD A could in principle be obtained with this method. It is also significant that the anti-crossing behavior seen with tuning methods such as strain [347] does not occur for the OSE [141] which should enable the FSS to be completely cancelled.

4.8 CONCLUSION & OUTLOOK

The work presented in this chapter demonstrates that a QD with very small FSS (2.01 ± 0.20 µeV) enables fast, on-demand initialisation of a long-lived ($2T_h > T_2^* \sim 10$ ns) hole spin qubit with fidelity $\geq 99.5\%$ at $B = 0$ T, exceeding the threshold required for a fault-tolerant QIP

implementation [343]. Whilst the high fidelities here are measured at zero magnetic field, simulations with small δ show that $\mathcal{F}$ will remain very high even under the presence of a modest in-plane magnetic field [335]. As a result, this initialisation scheme offers performance compatible with coherent control of hole spins [158, 179, 181, 195] where fast gate times ($\sim$20 ps [179, 181]), high gate fidelities (94.5% [181]) and long coherence lifetimes have demonstrated an attractive qubit platform.

Hole lifetimes could be further extended by modulation of the electric field to a very low value between initialisation and readout [348] or engineering the sample structure to decrease hole tunnelling whilst retaining fast electron tunnelling[1]. Devices constructed using a similar *n-i*-Schottky approach have demonstrated hole storage times of $> 100\,\mu s$ [186], illustrating that holes may be stored for far longer than they remain coherent. Combining one of these approaches to extend the hole lifetime with suppression of extrinsic pure dephasing by optical spin echo [188] (or other methods - see subsection 2.4.5) could enable high fidelity initialisation with coherence times in the μs regime. This is significant as error correction codes typically require performing a minimum of 10^4 gate operations within the qubit's coherence lifetime [17]. If the gate time is taken to be $\sim$20 ps [179, 181] then it can be seen that this limit could be comfortably exceeded with the methods discussed. Furthermore, recent works demonstrating remote hole spin entanglement [278] and a spin-photon phase shift [312] have been limited by slow hole spin initialisation using spin pumping (see section 2.7). Owing to the high speeds and fidelities, the scheme presented here could also find application to improve the performance of these protocols.

In addition, section 4.7 demonstrates that the initialisation fidelity for arbitrary QDs with larger FSS can be increased by the OSE, providing additional motivation for FSS tuning [138–142, 144–147] studies that were typically motivated by the generation of entangled photon pairs [129, 130]. Whilst the increase measured here was only modest, this was limited solely by the measurement method rather than the tuning scheme itself. In the device studied here the DC electric field

---

1 Ref. [336] achieves a ratio of Γ_e to Γ_h of 10^3, an order of magnitude greater than the device studied here. However, both tunnelling rates are rather fast with a maximum hole lifetime of 3 ns. Achieving a similar ratio with slower tunnelling rates would be very desirable.

presents an extra tunable parameter that may be used to optimize qubit lifetimes (see Figure 4.13) or to tune two QDs into resonance. This presents a potential route towards fault-tolerant QIP schemes based on multiple long-lived hole spins on a single chip.

Subsequent studies performed by another group have demonstrated tuning the FSS to around $2\,\mu\text{eV}$ using the vertical electric field in a similar device [349]. This approach has the advantage of simplicity as it does not require an additional laser field. However, at the electric field that minimises FSS the hole lifetime is less than 500 ps, illustrating the disadvantage of tuning the FSS using a field that also changes the hole lifetime. A possible future strategy would be to combine electric and strain fields [139] in order to control the lifetime, emission energy and fidelity of the spin qubit without requiring an additional laser. It is important to emphasize that a practical initialisation scheme requires adequate control of all of these parameters in order to satisfy the DiVincenzo criteria (section 1.2), not just high fidelities.

EXCITON-PHONON DYNAMIC VIBRONIC COUPLING

5.1 INTRODUCTION

Solid state qubit implementations are by definition coupled to their host material. One such coupling is the vibronic coupling that arises from the interaction of electrons with quantised vibrations of the host lattice (phonons). In these processes a photon and phonon(s) are absorbed or emitted simultaneously when the electron transitions between two electronic states. A typical signature of these processes is the presence of broad sidebands in spectra. These sidebands have been observed in numerous solid-state materials such as Ti:S [350] and NV centres [37, 38]. Indeed, in NV centers the coupling to the vibrational modes is sufficiently strong that the majority of emission (> 90%) occurs through them [39, 351].

This is not the case in InGaAs QDs where only around 8% of emission occurs from the phonon sideband at cryogenic temperatures [210, 218]. The physical origin of this is that the electron wavefunction is localized on a much larger length scale ($\sim$ 10 nm - determined by the QD size) than in NV centres or Ti:S where the electronic and phonon modes are localized to a similar size. This weak electron-phonon coupling is advantageous for the coherence of both single photon sources [352] and single spins [184].

Despite its relatively low strength, the electron-phonon coupling is responsible for a number of interesting behaviours of InGaAs QDs. One such scenario is the case where a QD is detuned from an optical nanocavity. In this case photon emission can be observed at the cavity energy with the detuning energy accounted for by either the absorption or emission of an LA phonon [86, 208, 216–218]. Similarly, resonant emission from a bare QD may be observed when pumping the phonon sideband [211] or conversely the sideband emission may be monitored when pumping resonantly [353]. A key feature of these processes is that they enable spectral separation of the pump and

the fluorescence whilst only relating to a single exciton transition, unlike above-band excitation. As such, they have interesting applications such as single photon sources [208, 218] and for monitoring the coherent dynamics of single QDs [195, 216, 353].

In all of these experiments the optical driving is relatively weak and hence the QD-laser system is in the weak coupling regime. In this chapter pulsed excitation is used to explore the exciton-phonon coupling in the fundamentally distinct regime of strong QD-laser coupling. This coupling is only strong during the passage of the laser pulse. As the system is driven by ultrafast optical pulses, it is tuned from weak to strong vibronic coupling and back again on picosecond timescales. Thus, the process is termed Dynamic Vibronic Coupling (DVC). A striking feature is that the mechanism is enabled by the electron-phonon coupling contrary to resonant coherent excitation [63, 64, 354, 355] or Adibatic Raman Passage (ARP) [356, 357] where the coupling is a hindrance.

In this chapter, Dynamic Vibronic Coupling (DVC) is explored by a comprehensive series of experiments. The theoretical calculations presented were performed by A. J. Barth, M. Glässl and V. M. Axt at the Institut für Theoretische Physik III, Universität Bayreuth using a path integral approach [358] as employed in their recent theoretical studies [359]. In this chapter, parameters of the model have been carefully matched to those measured experimentally. The theoretical results are included here with permission. The results presented here have been published in various journals: section 5.3 in Physical Review Letters [215], section 5.4 as a Rapid Communication in Physical Review B [360] and section 5.5, section 5.6 and section 5.7 in an invited article in the Journal of the Optical Society of America B [361]. Some of the results in section 5.3 have previously appeared in the PhD thesis of John Quilter [346] with whom I worked alongside on these experiments.

5.2 THEORY

The starting point for DVC is the coupling of excitons to the acoustic phonon bath by the deformation potential [203]. The Hamiltonian for the exciton-phonon interaction is [359]:

$$H_{X-ph} = \sum_{\mathbf{q}} \left(\gamma_{\mathbf{q}} b_{\mathbf{q}}^{\dagger} + \hat{\gamma_{\mathbf{q}}^{*}} b_{\mathbf{q}} \right) |X\rangle \langle X| , \qquad (5.1)$$

where $b_{\mathbf{q}}^{\dagger}$ and $b_{\mathbf{q}}$ are respectively the creation and annihilation operators for an LA phonon with wavevector $\mathbf{q}$ and $\gamma_{\mathbf{q}}$ is the coupling strength of the exciton-phonon interaction. The factors influencing the strength of this coupling are discussed in detail in subsection 5.2.3. In the absence of a laser field this coupling leads to nonexponential pure dephasing of the excitonic dipole [362]. The behaviour of the coupled system becomes more interesting when a strong laser field is applied. The laser pulse has energy $\hbar\omega_L$ (detuned from the exciton energy of $\hbar\omega_X$ by $\hbar\Delta = \hbar(\omega_X - \omega_L)$) and area Θ as defined by:

$$\Theta = \int_{-\infty}^{+\infty} \Omega_R(t)\, \mathrm{d}t , \qquad (5.2)$$

where $\Omega_R(t)$ is the time-dependent Rabi frequency determined by the optical dipole moment and the time-varying electric field amplitude of the pulse. Under these excitation conditions the total Hamiltonian of the system may be written as:

$$H = H_{laser-QD} + H_{ph-QD} \qquad (5.3)$$

where the interaction of the laser and the QD is:

$$H_{laser-QD} = \hbar\omega_X |X\rangle \langle X| + \frac{\hbar\Omega_R(t)}{2} \left[|0\rangle \langle X| e^{i\omega_L t} + |X\rangle \langle 0| e^{-i\omega_L t} \right] , \qquad (5.4)$$

and the contribution of the phonon bath is:

$$H_{ph-QD} = H_{ph} + H_{X-ph} = \sum_{\mathbf{q}} \hbar\omega_{\mathbf{q}} b_{\mathbf{q}}^{\dagger} b_{\mathbf{q}} + \sum_{\mathbf{q}} \left(\gamma_{\mathbf{q}} b_{\mathbf{q}}^{\dagger} + \hat{\gamma_{\mathbf{q}}^{*}} b_{\mathbf{q}} \right) |X\rangle \langle X| . \qquad (5.5)$$

Using the rotating wave approximation, the laser-QD Hamiltonian in the rotating frame becomes time independent:

$$H_{Laser-QD} = H^{RWA} = \frac{\hbar}{2} \begin{pmatrix} 0 & \Omega_R \\ \Omega_R & -2\Delta \end{pmatrix} , \qquad (5.6)$$

and one can thus define the dressed states of the laser-QD system as the corresponding eigenstates. These are given by:

$$|\alpha\rangle = \sin(\theta)|0\rangle + \cos(\theta)|X\rangle \tag{5.7}$$

$$|\beta\rangle = \cos(\theta)|0\rangle - \sin(\theta)|X\rangle, \tag{5.8}$$

where θ is an admixing angle defined by:

$$\tan(2\theta) = -\Omega_R/\Delta, \quad 0 \leq 2\theta \leq \pi. \tag{5.9}$$

The energies of the dressed states are given by:

$$E_\pm = \frac{\hbar}{2}\left(-\Delta \pm \Lambda(t)\right), \tag{5.10}$$

where $\Lambda(t)$ is an effective Rabi frequency defined as:

$$\Lambda(t) = \sqrt{\Omega_R(t)^2 + \Delta^2}. \tag{5.11}$$

The significance of these dressed states is that, in the presence of a driving laser such that $\theta > 0$, both eigenstates of the system contain an excitonic component and may couple to the acoustic phonon bath via the H_{X-ph} term of the Hamiltonian. This enables phonon-mediated relaxation from $|\alpha\rangle$ to $|\beta\rangle$. However, this relaxation is only possible when the states are admixed by the laser ($\theta > 0$), giving rise to the dynamic nature of the vibronic coupling.

In Figure 5.1 the dressed state energies (green lines), admixture angle θ (black line) and occupancy of $|\beta\rangle$ (blue line) are plotted against time during the passage of a $\Theta = 8.5\pi$ pulse with $\hbar\Delta = +1$ meV. The pulse has a temporal FWHM of 16.8 ps and is centred on $t = 0$. The figure illustrates that the dressed state splitting rises and falls in line with the envelope of the laser pulse [363], and that the admixing angle follows it. The transfer of population into $|\beta\rangle$ only occurs whilst the states are admixed, tuning the system from weakly to strongly vibronic and back again in approximately 20 ps.

5.2.1 *Mechanism of Phonon-Assisted Excitation*

The transfer between the dressed states shown in Figure 5.1 can be exploited to achieve ultrafast incoherent excitation and de-excitation
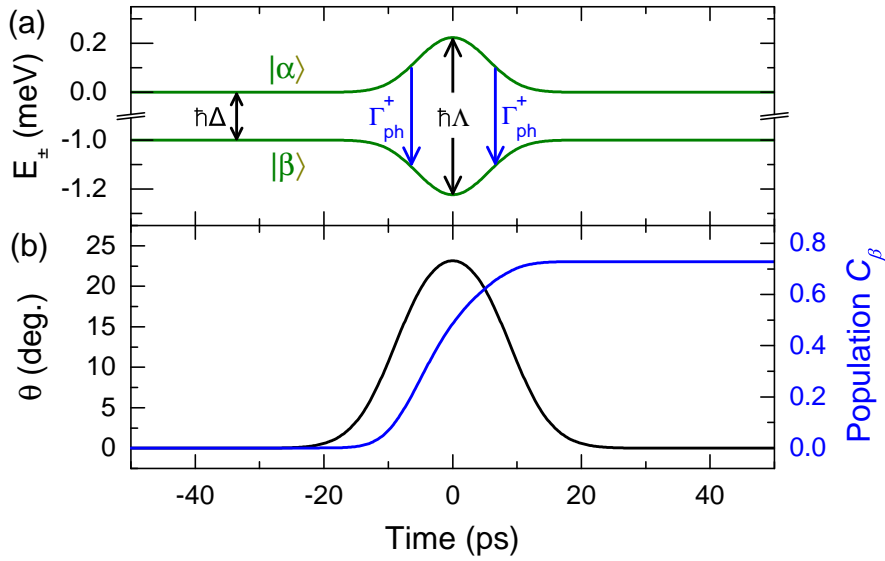
Figure 5.1: Calculation of the dynamics of the dressed states when excited with a 16.8 ps laser pulse centred at $t = 0$ with $\hbar\Delta = +1$ meV and $\Theta = 8.5\ \pi$. (a) Energies ($E_\pm$) of the dressed states (green lines) $|\alpha\rangle$ and $|\beta\rangle$ plotted against time. At $t \to -\infty$, the states are split by the laser detuning $\hbar\Delta$. During the passage of the pulse the states are admixed and the splitting becomes $\hbar\Lambda$ as shown by the shift centred at $t = 0$. This enables relaxation from $|\alpha\rangle$ to $|\beta\rangle$ (blue arrows) by emission of an LA phonon with energy $\hbar\Lambda$. (b) Plot of the admixing angle θ (black line) and the population of the dressed state $|\beta\rangle$ (blue line) against time. θ also follows the envelope of the laser pulse and, as expected, relaxation into $|\beta\rangle$ occurs only when the states are admixed.
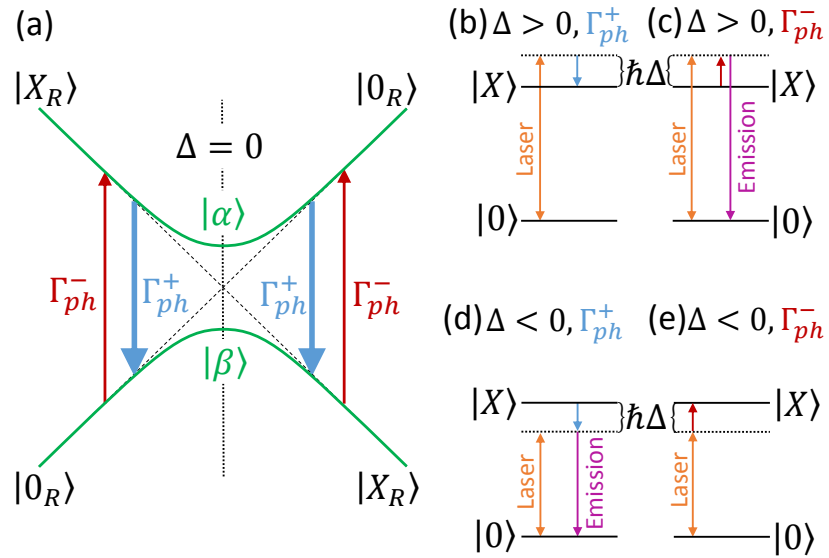
Figure 5.2: (a) Illustration of the energies of the dressed states $|\alpha\rangle$ and $|\beta\rangle$ plotted against detuning Δ at a fixed time. The bare QD states in the frame of the laser are plotted for reference as dotted black lines. At $\Delta = 0$ the states anti-cross with a splitting of $\hbar\Omega_R$. It can be seen that $|\alpha\rangle$ is dominated by the ground state at $\Delta > 0$, leading to phonon-assisted excitation of the exciton. Conversely, $|\alpha\rangle$ is primarily excitonic in character at $\Delta < 0$, and thus phonon-assisted de-excitation of the exciton occurs. The blue arrows illustrate the relaxation process corresponding to the emission of an LA phonon whilst the red arrows show the competing phonon absorption process. (b-e) Phenomenological energy level diagrams of the phonon emission and absorption processes for both positive and negative detunings. For simplicity, the phonon relaxation is incorporated as a virtual state (dotted lines).

of the exciton by detuned laser pulses. Beginning with excitation, in the case of $\Delta > 0$ the higher energy dressed state $|\alpha\rangle$ is dominated by the crystal ground state whilst the lower energy state $|\beta\rangle$ is primarily excitonic in character, as illustrated to the right of Figure 5.2(a). During the passage of the laser pulse, admixing of the states allows relaxation to occur from $|\alpha\rangle$ to $|\beta\rangle$ by emission of an LA phonon (Γ_{ph}^{+} - blue arrows) with energy $\hbar\Lambda$.

For a sufficiently strong pulse, most of the population relaxes into $|\beta\rangle$ and the exciton-dominated nature of $|\beta\rangle$ means that the population of the exciton state after the passage of the pulse is high. The final occupancy also relates to the nature of the adiabatic "undressing" of the states after the passage of the pulse [364]. In the regime considered here, this does not significantly change the occupancy of the states. The potential for a high exciton state population is significant as a basic principle of laser physics is that incoherent excitation of a two-level system can never lead to population inversion [365]. Previous theoretical studies have however predicted that a two-level system coupled to a boson bath could be inverted in the incoherent regime [366] by the interaction between the bath and the dressed states, exactly the scenario presented here. Theoretical calculations for an InGaAs QD [359] indicate that the population of the exciton may significantly exceed the "transparency point" of 0.5, a population inversion. As such, it can be seen that the coupling to the phonon bath causes significant deviations from the isolated atom picture.

In Figure 5.2(b) a phenomenological level diagram of the phonon-assisted excitation process is depicted whilst Figure 5.2(c) illustrates the competing process whereby a phonon is absorbed (Γ_{ph}^{-} - red arrows) and a photon emitted (purple arrow). The latter process is weak at low temperatures ($k_{B}T \ll \hbar\Lambda$), allowing the formation of a significant population inversion. Detailed experimental studies of phonon assisted excitation are performed in section 5.3 whilst the consequences of increasing the temperature are presented in section 5.5.

5.2.2 *Mechanism of Phonon-Assisted De-Excitation*

In the case of $\Delta < 0$ the main difference is that the characteristics of the dressed states are now exchanged. During the passage of the
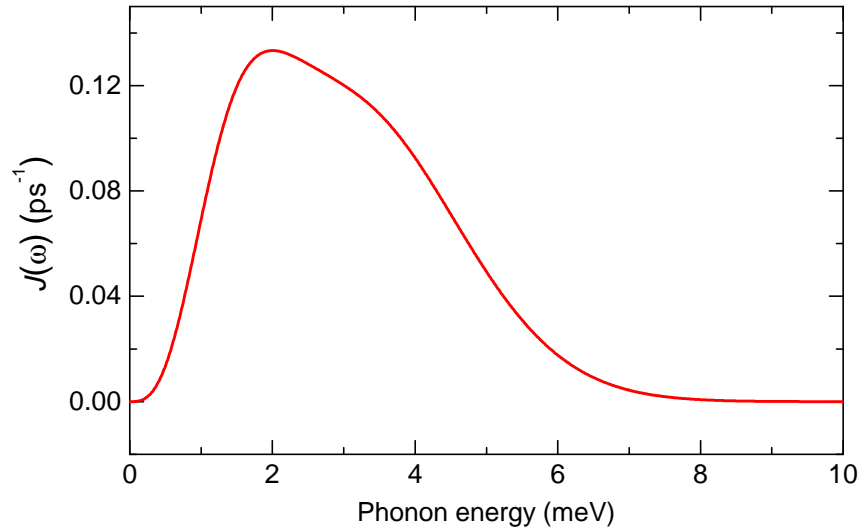
Figure 5.3: Plot of the exciton-phonon interaction strength $J(\omega)$ as determined in subsection 5.3.4. The interaction strength peaks at a cutoff of around 2 meV and rolls off rapidly beyond this.

laser pulse, relaxation by phonon emission again occurs into the $|\beta\rangle$ state. However, as this state is now dominated by the crystal ground state, the effect of the relaxation is instead to de-excite the exciton with most of the population left in the ground state after the passage of the laser pulse. Figure 5.2(d) shows an illustrative schematic of this process with the emission of a photon (purple arrow) accounting for the rest of the energy difference. This emission is stimulated by the laser and hence the process is termed Longitudinal-Acoustic Phonon Stimulated Emission (LAPSE). Figure 5.2(e) again illustrates the competing phonon absorption process. Experimental studies of the LAPSE process are presented in section 5.4.

5.2.3 *Physical Factors Influencing the Efficiency of DVC*

The physical factors that determine the efficiency of phonon-assisted excitation and de-excitation may be considered by analysing the parameters in Equation 5.9. The degree of admixing increases by increasing the driving strength (Ω_R) or decreasing the detuning (Δ) (noting that Δ should exceed the laser linewidth to exclude resonant coherent driving), leading to more efficient relaxation. However, both of

these dependencies are modified by the properties of the phonon bath which are discussed subsequently.

Phonon Form-Factor

The exciton-phonon interaction strength is characterised by the function $J(\omega)$ which increases with ω at first due to the rising phonon density of states, and then rolls-off rapidly beyond a cut-off frequency which is typically around 1-2 meV [64]. The physical origin of this cut-off is the point at which the phonon wavelength is comparable to the spatial FWHM of the carrier wavefunction. As a result, the cut-off frequency depends strongly on the height of the QD and phonon sideband measurements may be used to probe the confinement potential. A plot of $J(\omega)$ derived from fitting data presented in subsection 5.3.4 is shown in Figure 5.3. The form of $J(\omega)$ modifies the detuning dependence of the DVC (see studies of the spectral dependence in subsection 5.3.4 and subsection 5.4.4). It also weakens the exciton-phonon interaction for very strong driving where the effective Rabi frequency Λ exceeds the cut-off frequency [367] (although this regime has not been reached in present experiments).

Phonon Bath Temperature

The processes of interest for DVC both rely on phonon emission rather than phonon absorption, and are therefore highly sensitive to temperature. Increasing the bath temperature increases the phonon occupation leading to a higher probability of phonon emission and thus faster relaxation. However, the probability of phonon absorption generally increases more than that of emission. As illustrated by the red arrows in Figure 5.2(a), phonon absorption (Γ_{ph}^{-}) causes the opposite population transfer between the dressed states to phonon emission (Γ_{ph}^{+} - blue arrows) and results in a lower final occupation of $|\beta\rangle$. As such, DVC processes are generally optimised by low bath temperatures in order to maximise the difference between phonon emission and absorption rates. The influence of temperature on phonon-assisted excitation is studied both experimentally and theoretically in section 5.5.

The Phonon Sideband

It is only by combining all of these influences that the full spectral and power dependence of the DVC emerges. Analytical approximations do not accurately predict these dependencies; hence numerical methods such as path integral calculations [215, 359] or the master equation formalism [368] are employed. The result of such calculations is a broad (few meV) spectral sideband feature that appears at high driving strengths and persists until the Rabi splitting exceeds the cut-off energy for phonon coupling.

5.3   PHONON-ASSISTED EXCITATION

By performing experiments with a positive-detuned driving laser it is possible to investigate the phonon-assisted excitation process described in subsection 5.2.1. The results presented in this section were published in Physical Review Letters [215]

5.3.1   *Experimental Method*

To demonstrate phonon-assisted excitation, two-pulse pump probe experiments were performed with circularly polarized Gaussian pulses with temporal FWHM 16.8 ps. First, the $|0\rangle \rightarrow |X\rangle$ transition was identified by measuring a single pulse PC spectrum with a π-pulse (blue line in Figure 5.4). In two-pulse measurements, a pump pulse detuned by $\hbar\Delta = +0.83$ meV (close to the peak of the spectral distribution - see subsection 5.3.4) is applied and the probe energy was scanned across the $|0\rangle \rightarrow |X\rangle$ and $|X\rangle \rightarrow |2X\rangle$ transitions. The probe pulse area is π and the pump pulse area is 8.46π, the maximum available in this experimental configuration. The delay time between the pump and probe pulses (τ_{delay}) is 10 ps. As illustrated in the energy-level diagram shown in the inset of Figure 5.4, the photon energy of the probe pulse and its polarization relative to the pump selects the transition that is probed. In this situation, the effect of a π-pulse is to exchange the populations of the two levels that are probed, allowing the population created by the pump to be extracted.

The scenario of a co-polarized probe pulse is considered first. In this case, the pump pulse (orange arrow) excites an exciton popu-
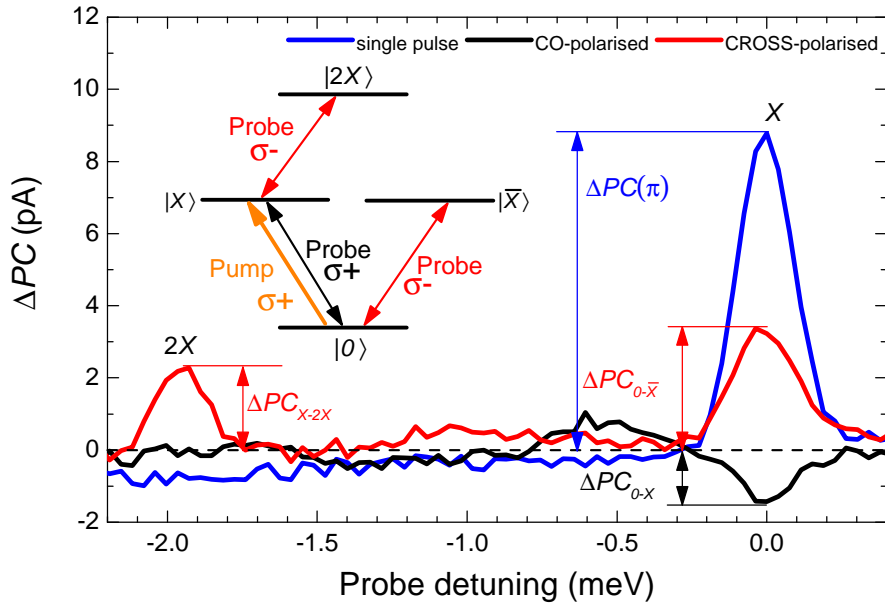
Figure 5.4: Photocurrent signal ΔPC as a function of the probe detuning. A single probe-pulse only spectrum is presented for reference (blue) alongside two pulse spectra where the probe is co-polarized (black) and cross-polarized (red) with the pump. Pump detuning $\Delta = +0.83\,\mathrm{meV}$ and $\tau_{delay} = 10\,\mathrm{ps}$. The peak at a detuning of $-1.96\,\mathrm{meV}$ corresponds to the $|X\rangle \to |2X\rangle$ transition. Inset: energy level diagram for the exciton-biexciton system. Arrows represent transitions induced by the σ^{+} polarized pump pulse tuned to the phonon sideband (orange arrow) and the σ^{+} (σ^{-}) polarized probe pulse tuned either to the exciton or biexciton transition (red arrows). $|X\rangle$ and $|\overline{X}\rangle$ label the orthogonally circularly polarized exciton states whilst $|2X\rangle$ denotes the biexciton state.

lation of C_X (see inset to Figure 5.4). The probe exchanges the $|0\rangle$ population with the $|X\rangle$ population when it is resonant with the neutral exciton transition (black arrow in Figure 5.4 inset), resulting in a change in photocurrent proportional to the population created by the pump: $\Delta PC_{0-X} \propto C_0 - C_X$. ΔPC is the change in the PC signal at the transition energy that is induced by the probe pulse and is measured relative to the background photocurrent measured without a probe. A key signature of population inversion is that ΔPC_{0-X} should be negative. Figure 5.4 shows the result of this measurement (black). The dip at zero detuning clearly demonstrates that a population inversion has been achieved between the $|0\rangle$ and $|X\rangle$ states, in accordance with theoretical predictions.

The red line in Figure 5.4 shows the results obtained for cross-polarized excitation (σ^+ pump, σ^- probe). At $\Delta = 0$, the probe addresses the orthogonally polarized exciton transition $|0\rangle \rightarrow |\overline{X}\rangle$ as shown by the lower red arrow in the inset to Figure 5.4. Thus, in this case $\Delta PC_{0-\overline{X}} \propto C_0 - C_{\overline{X}}$, providing a measure of the occupation of the crystal ground state C_0. The amplitude of the peak at zero detuning falls to less than half the amplitude measured by the single pulse, implying $C_0 < 0.5$ and again confirming a population inversion between $|0\rangle$ and $|X\rangle$. The second peak at a detuning of $-1.96\,\text{meV}$ corresponds to the $|X\rangle \rightarrow |2X\rangle$ transition and provides a third measure of C_X following a similar argument. The absence of a biexciton peak in the co-polarized spectra (black) indicates that population transfer via the phonon-assisted channel is spin preserving. This is expected as the timescale of phonon-assisted relaxation (few picoseconds) [369] is much shorter than exciton spin relaxation (few nanoseconds) [370].

5.3.2   *Extracting the Exciton Population*

Whilst the measurement in Figure 5.4 is sufficient to infer that population inversion has been attained, it is necessary to convert the measured PC into a population of the $|X\rangle$ state in order to make quantitative comparisons with theory. The exciton population created by a pump pulse can be extracted from two-pulse spectra such as Figure 5.4 by analyzing the peak heights of the three transitions: $|0\rangle \rightarrow |X\rangle$, $|0\rangle \rightarrow |\overline{X}\rangle$ and $|X\rangle \rightarrow |2X\rangle$. The PC measured in such an

experiment is determined by the number of electron-hole pairs created by the laser pulses. For the pump-probe measurement, PC can be subdivided into three parts:

$$PC = PC_{\text{R}} + PC_{bg} + \Delta PC. \qquad (5.12)$$

PC_{R} is a reference level induced by the pump pulse, PC_{bg} is a background originating from the diode leakage current and ΔPC is the change in photocurrent induced by the probe pulse. $PC_{\text{R}} + PC_{bg}$ can be evaluated by measuring the photocurrent signal under identical conditions to the pump-probe measurement except for setting the probe frequency far from any of the resonances of the dot or the surrounding material such that $\Delta PC = 0$.

As discussed in subsection 5.3.1, the exciton population created by the pump pulse is proportional to ΔPC. At $t = 0$, the σ^+ polarized pump pulse creates an exciton population C_X (see the orange arrow in Figure 5.4) and thus the occupations of the $(0, X, \bar{X}, 2X)$ states following the pump pulse are

$$\mathbf{C}(0) = (C_0(0), C_X(0), C_{\bar{X}}(0), C_{2X}(0)) = (1 - C_X, C_X, 0, 0). \qquad (5.13)$$

At a time $t < \tau_{\text{delay}}$, before the arrival of the probe pulse, the exciton population decays exponentially due to electron tunnelling and is shelved in the single hole state (see subsection 4.3.2). The radiative decay of the exciton is neglected as the radiative decay time (~ 400 to 800 ps [122, 178]) is much longer than τ_{delay}. The delay time is chosen to maximize the pump-probe signal whilst allowing for complete relaxation between the dressed states. Typically this occurs between 10 and 15 ps, depending on the pulse width and the electron tunnelling time.

To exclude the possibility that a small temporal overlap between the pump and probe may influence the measured exciton population, measurements were performed with a longer delay time (33.6 ps) where the pump and probe are completely separated (for example, Figure 5.7). The result of these measurements agree well with those measured with shorter delay time after correction for the population loss due to electron tunnelling.

The ground-state occupancy is not changed by tunnelling due to the long hole lifetimes of this sample (few ns - see Figure 4.13). The electron tunnelling time at this electric field ($T_1 = 50$ ps) was measured by time-resolved pump-probe as described in subsection 4.4.1. This leads to time-dependent occupations of:

$$\mathbf{C}(t) = (1 - C_X, C_X e^{-t/T_1}, 0, 0). \tag{5.14}$$

At time $t = \tau_{\text{delay}}$, the probe pulse of pulse-area π resonantly excites an optical transition $\alpha \to \beta$ and swaps the populations of the states α and β as discussed in subsection 5.3.1. Here α, β represent $0, X, \bar{X}$ or $2X$ states depending upon the transition addressed. This results in a change in photocurrent due to the probe of:

$$\Delta PC_{0-X} = a(C_0(\tau_{\text{delay}}) - C_X(\tau_{\text{delay}}))$$
$$= a(1 - C_X - C_X e^{-\tau_{\text{delay}}/T_1}), \tag{5.15}$$
$$\Delta PC_{0-\bar{X}} = a(C_0(\tau_{\text{delay}}) - C_{\bar{X}}(\tau_{\text{delay}}))$$
$$= a(1 - C_X), \tag{5.16}$$
$$\Delta PC_{X-2X} = (b - a)(C_X(\tau_{\text{delay}}) - C_{2X}(\tau_{\text{delay}}))$$
$$= (b - a)C_X e^{-\tau_{\text{delay}}/T_1}, \tag{5.17}$$

where a is the photocurrent amplitude corresponding to one exciton, and b is the photocurrent due to one biexciton. $a = \Delta PC(\pi)$ is the amplitude of the photocurrent peak at zero detuning measured with a single π pulse (see blue line in Figure 5.4). $b - a = \Delta PC_{X\text{-}2X}(\pi)e^{\tau_{\text{delay}}/T_1}$ is deduced from a separate pump-probe experiment; an exciton is prepared with a pump pulse of pulse-area π resonant with the $0 - X$ transition and the biexciton is subsequently created by a π probe resonant with the $X - 2X$ transition [371].

The exciton population C_X generated by the pump pulse is then calculated from two-pulse spectra such as Figure 5.4 using equations 5.15 to 5.17, and the experimentally determined parameters a, b, T_1. An interesting consideration is that owing to slow hole tunnelling, ΔPC is unaffected by tunnelling in the cross-polarized probe case (Equation 5.16), simplifying the analysis compared to the other means of extracting the population.
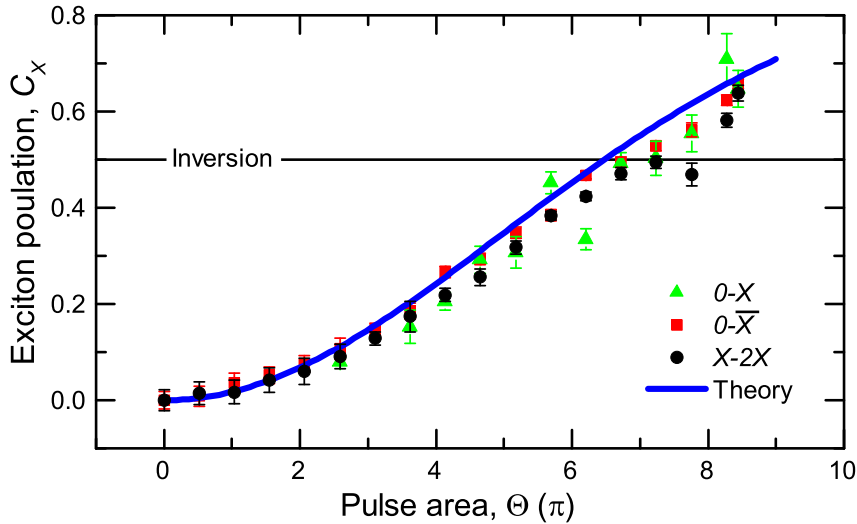
Figure 5.5: The exciton population (C_X) generated by a variable pulse-area (Θ) pump pulse with $\hbar\Delta = +0.83$ meV. C_X is extracted from the exciton and biexciton peaks in two-pulse spectra like Figure 5.4 by using the methods described in subsection 5.3.2. The blue line shows the calculated theoretical C_X from path-integral calculations.

5.3.3 *Pulse Area Dependence: Inversion Threshold*

Using the methods of subsection 5.3.2, Figure 5.5 plots the population of the neutral exciton versus the pulse-area of a $+0.83$ meV detuned pump pulse. The green triangles (red squares) are obtained from an analysis of the co- (cross-) polarized signals at zero detuning, whilst the black cricles derive from the biexciton peak. The three measurements of the exciton population are in close agreement, and pass the transparency point, $C_X = 0.5$, at a pulse-area of $6.5 - 7\pi$. The largest exciton population observed is $C_X = 0.67 \pm 0.06$ for a pump pulse detuned by $+0.83$ meV, limited by the laser power available in the setup. The blue line in Figure 5.5 shows the results of path-integral simulations which quantitatively reproduce the experiments. As such, these measurements present strong evidence for the validity of the theoretical model and also the presence of a population inversion for sufficiently strong driving.
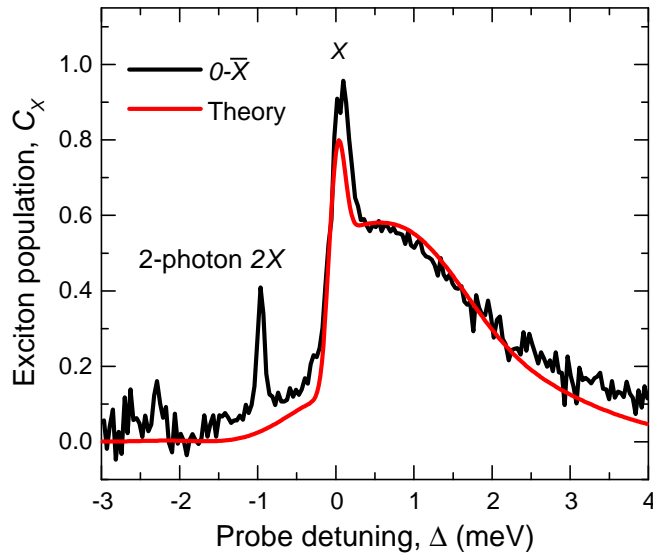
Figure 5.6: Exciton population created by a 7.24π pump as a function of the pump detuning. $\tau_{\text{delay}} = 15$ ps. Red: Calculated C_X. The spectral density of the exciton-phonon interaction $J(\omega)$ shown in Figure 5.3 is calculated by fitting the model incorporating Equation 5.18 to the measured data using the electron and hole confinement lengths $a_{\text{e/h}}$ as fitting parameters (red line). This fit gives $a_{\text{e}} = 4.5$ nm and $a_{\text{h}} = 1.8$ nm. The exciton population was extracted from cross-polarized pump-probe measurements using Equation 5.16.

5.3.4   *Spectral Dependence*

To investigate the dependence of the phonon-assisted population inversion on the pump frequency, a series of two-colour photocurrent spectra were measured for a 7.24π pump pulse as a function of pump detuning with a cross-polarized π-pulse probe. In Figure 5.6 the pump-induced exciton population extracted from these measurements is plotted.

The spectrum has three key features. At $\Delta = 0$ there is a peak corresponding to the zero-phonon $|0\rangle \rightarrow |X\rangle$ transition, the linewidth is that of the excitation pulse. A broad (few meV) sideband feature is observed at positive detuning corresponding to phonon-assisted excitation. The continuous nature of the phonon sideband indicates that any phonon confinement effects are weak. This is expected given the similar lattice properties of the QD and the other sample layers and justifies the assumption of bulk phonon dynamics.

In principle, there can also be a phonon feature at negative detuning due to phonon absorption (see Figure 5.2(e) and discussion in section 5.5). However, this is suppressed by the low phonon occupancy at 4.2 K. The third feature is a narrow peak at a pump detuning of -1 meV, corresponding to the two-photon $|0\rangle \rightarrow |2X\rangle$ biexciton transition [288], indicating that the pump pulse is slightly elliptically polarized [1].

The spectral dependence of the DVC is determined mainly by the phonon spectral density (see subsection 5.2.3): $J(\omega) = \sum_{\mathbf{q}} |\gamma_{\mathbf{q}}|^2\, \delta(\omega - \omega_{\mathbf{q}})$, where $\gamma_{\mathbf{q}}$ is the exciton-phonon coupling. As detailed information on the shape of the QD under study is not known, the simple case of spherically symmetric, parabolic potentials is taken. For bulk LA phonons coupled via the deformation potential $J(\omega)$ then takes the form [358]:

$$J(\omega) = \frac{\omega^3}{4\pi^2 \rho \hbar v_c^5} \left[D_{\mathrm{e}}\, e^{\left(-\omega^2 a_{\mathrm{e}}^2 / 4 v_c^2\right)} - D_{\mathrm{h}}\, e^{\left(-\omega^2 a_{\mathrm{h}}^2 / 4 v_c^2\right)} \right]^2, \qquad (5.18)$$

where ρ is the mass density, v_c the sound velocity and $D_{\mathrm{e/h}}$ denote the deformation potential constants for electrons and holes. These mater-

---

1 By measuring the transition dipole moment the degree of ellipticity can be estimated as around 2%.

ial parameters are taken from the values used for GaAs in Ref. [204], while the electron and hole confinement lengths $a_{e/h}$ are used as fitting parameters. The low frequency asymptote in Equation 5.18 $\sim \omega^3$ is characteristic for bulk acoustic phonons and occurs independent of the material or the dot shape. The second factor contains Gaussian terms originating from the Fourier transforms of the electron and hole probability densities and thus is the influence of the assumption of parabolic confinement potentials. The best fit to experimental data is obtained with $a_e = 4.5$ nm and $a_h = 1.8$ nm, the corresponding spectral density is shown in Figure 5.3.

The red line in Figure 5.6 shows a path-integral calculation (using the spectral density from Figure 5.3) of the exciton population created by the pump pulse. The theoretical calculation shows excellent quantitative agreement with the broadband feature observed at positive detuning. The lineshape of this feature is determined by $J(\omega)$ as previously discussed. Further study may provide a means to extract more information about the deformation potential coupling and electron/hole confinement than previous studies of intensity damping of Rabi rotations [63, 64].

The asymmetry of the spectrum with respect to the sign of $\hbar\Delta$ unambiguously proves that the population created by the off-resonant pump pulse is the result of phonon-assisted relaxation into the lower energy dressed state. Furthermore, this asymmetry emphasizes the importance of a low probability of phonon absorption relative to emission for efficient population transfer by DVC processes (see subsection 5.2.3 and section 5.5 for further discussion).

5.3.5   *Phonon Sideband*

By studying the exciton population created by a strong pump as a function of both detuning ($\hbar\Delta$) and pulse area (Θ) the full dependence of the DVC mechanism is revealed. An experimental measurement using the same method as subsection 5.3.4 is presented in Figure 5.7(a) whilst Figure 5.7(b) presents a theoretical calculation using experimental parameters. On-resonance, the zero-phonon line exhibits intensity-damped Rabi rotations. At positive detuning, there is the phonon-emission sideband that broadens and intensifies for higher
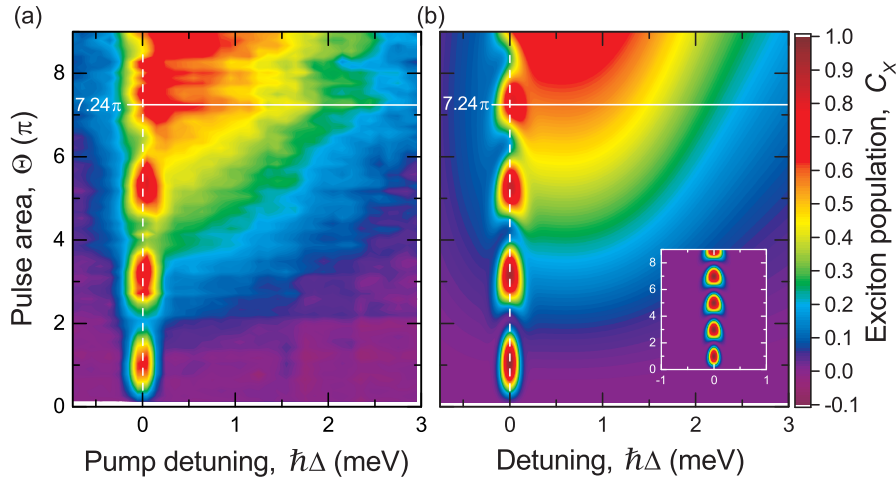
Figure 5.7: (a) Experimentally measured C_X (from $|0\rangle \rightarrow |\bar{X}\rangle$ transition according to Equation 5.16) vs Θ and $\hbar\Delta$ with $\tau_{\text{delay}} = 33.6$ ps. (b) Path-integral results for the same pulse area and detuning range as in (a). The horizontal line is at $\Theta = 7.24\pi$ as shown in Figure 5.6. Inset: calculation with no phonon coupling. All plots use the same colour scale.

pulse areas. The spectrum is again highly asymmetric with the lack of population created at negative detunings indicating the weak probability of phonon absorption. The calculations show excellent quantitative agreement with the experimental data, further confirming the validity of the model. A slight shift of the resonant peaks towards higher energies with increasing pulse area is seen in both experiment and theory; this is a further signature of the exciton-phonon interaction. Finally, the inset to Figure 5.7 shows a theoretical calculation with no phonon coupling. The spectrum is now symmetric with no sidebands, confirming that the sideband observed originates solely from deformation potential coupling of the exciton to the acoustic phonon bath.

5.4 DE-EXCITATION BY LA-PHONON ASSISTED STIMULATED EMISSION

In this section the strong driving laser is instead tuned to negative detuning, creating the conditions to observe Longitudinal-Acoustic Phonon Stimulated Emission (LAPSE) as discussed in subsection 5.2.2. These results were published in Physical Review B [360]. LAPSE differs from conventional stimulated emission as at the low temper-
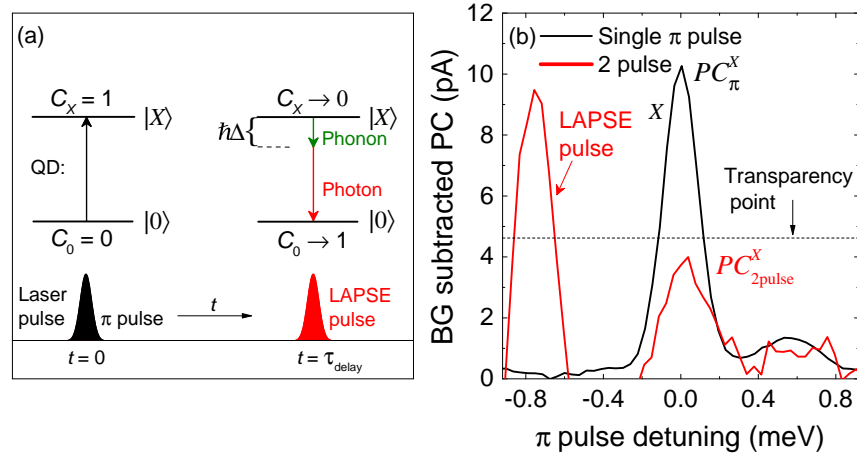
Figure 5.8: (a) Scheme of the two-pulse measurement. The QD is excited to the $|X\rangle$ state by a π-pulse at $t = 0$ and then depopulated by a red-shifted laser pulse (LAPSE pulse) after τ_{delay}. (b) Black: PC spectrum measured only with a π-pulse (FWHM = 0.2 meV, τ_L = 16.8 ps). Red: Two-pulse spectrum measured in the presence of a -0.7 meV detuned LAPSE pulse (FWHM = 0.42 meV, τ_L = 8 ps, $\Theta = 5.25\pi$, $\tau_{\text{delay}} = 7$ ps). PC_π^X and PC_{2pulse}^X denote the amplitude of the exciton peak in the single-pulse and two-pulse spectra, respectively. The background PC has been subtracted from the spectra.

atures considered here, creation of exciton population by the red-detuned pulse is very weak (see discussion in subsection 5.2.2 and Figure 5.6), effectively decoupling emission and absorption. Additionally, as LAPSE can be stimulated by a range of red detunings governed by $J(\omega)$, the energy of the emitted photon can be tuned by the stimulating pulse. As a result, LAPSE could form the basis of tunable single QD lasers and also has potential applications in ultrafast optical switching (see section 5.7) [227–229, 372, 373], semiconductor optical amplifiers [374] and controlling the emission timing of single photon sources [218, 287, 292].

5.4.1 Experimental Method

To investigate LAPSE, a two-colour pump-probe method is again used. However, as LAPSE relates to the depopulation of the exciton state, it is necessary to first populate the exciton. To achieve this, an initial π-pulse resonant with the $|0\rangle \rightarrow |X\rangle$ transition is applied, followed by a strong red-detuned "LAPSE pulse" after a short delay (τ_{delay}).

This is illustrated in Figure 5.8(a). To maximize the efficiency of the de-excitation, the LAPSE pulse should be spectrally broad to cover as many phonon modes as possible. However, the pulse duration τ_L needs to be long enough for complete phonon-assisted relaxation between the dressed states. Guided by theoretical predictions, the spectral FWHM and τ_L of the LAPSE pulse are chosen as 0.42 meV and 8 ps respectively.

The black line in Figure 5.8(b) shows a single pulse PC spectrum measured as a function of the detuning of the π pulse. The peak at zero detuning corresponds to the $|0\rangle \rightarrow |X\rangle$ transition and has amplitude PC_π^X, corresponding to an exciton population of 1. The red line in Figure 5.8(b) shows the PC spectrum measured in the presence of the LAPSE pulse ($\hbar\Delta = -0.7$ meV, $\Theta = 5.25\pi$, $\tau_{\text{delay}} = 7$ ps). The exciton peak is slightly blue-shifted due to the OSE (see Figure 2.10) whilst the peak at $\hbar\Delta = -0.7$ meV is due to the interference between the π pulse and the LAPSE pulse[2].

The reduction of the amplitude of the exciton peak PC_{2pulse}^X relative to PC_π^X directly demonstrates the depopulation of the exciton state by the strong red-detuned pulse. Owing to the relatively fast electron tunnelling of the sample (see initialization times in Figure 4.13), the total population of the ground state and exciton state C_{Total} drops to 0.88 at the arrival of the LAPSE pulse. As a result, the transparency point defined as $C_{\text{Total}}/2$ is shifted to 0.44. In Figure 5.8(b) it can be observed that $PC_{\text{2pulse}}^X < 0.44 PC_\pi^X$, proving that the initially inverted QD is depopulated below the transparency point. This is analogous to the demonstration of population inversion in subsection 5.3.3, further demonstrating that the coupling to the phonon bath enables fundamentally distinct behaviour to conventional incoherent driving.

5.4.2 *Pulse Area Dependence*

In Figure 5.9 the pulse-area dependence of the LAPSE de-excitation process is measured experimentally. The remaining exciton population after the LAPSE pulse is plotted against the pulse area Θ. In

---

2 As there is a temporal overlap between the pulses, they may interfere either constructively or destructively when tuned to the same energy. This modulates the number of background carriers produced by the LAPSE pulse and leads to a peak/dip at the pulse energy.
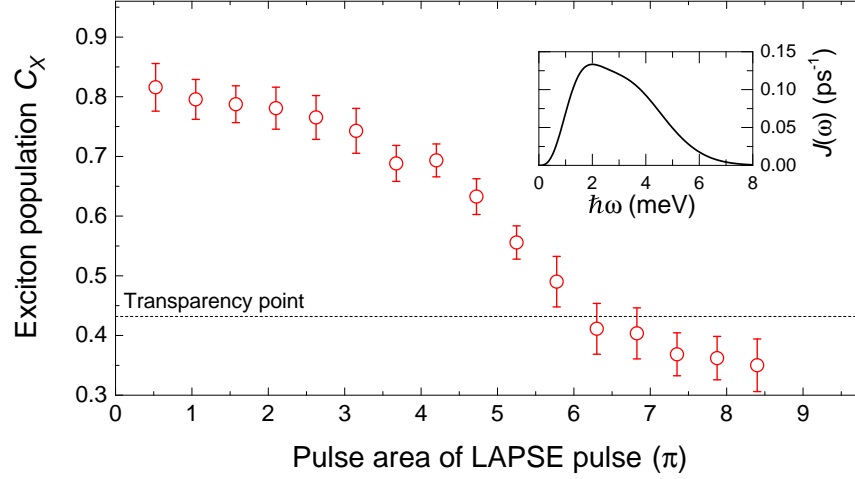
Figure 5.9: Remaining exciton population C_X after the LAPSE pulse versus the pulse area Θ. LAPSE pulse: $\hbar\Delta = -0.7$ meV, FWHM = 0.2 meV, $\tau_L = 16.8$ ps, $\tau_{delay} = 8$ ps. Following similar reasoning to subsection 5.3.2, C_X is calculated using the formula $C_X = e^{-\tau_{delay}/\tau_e} - (1 - PC^X_{2pulse}/PC^X_\pi)$, where τ_e is the electron tunnelling time. Inset: Exciton-phonon coupling spectral density $J(\omega)$ (see subsection 5.3.4).

order to improve the signal to noise ratio, the FWHM of the LAPSE pulse is reduced to 0.2 meV. It can be seen that C_X decreases with the increase of Θ and crosses the transparency point at $\Theta > 6.25\pi$, an equivalent result to the population inversion obtained for excitation in subsection 5.3.3. The minimum C_X measured here is also limited by the total laser power available in this experimental configuration. The efficiency of the LAPSE process strongly depends on the pulse area as the laser detuning and power determine the effective Rabi splitting ($\hbar\Lambda$ - see Equation 5.11) required to be in resonance with the phonon spectral density $J(\omega)$ [375]. The inset to Figure 5.9 shows the calculated exciton-phonon coupling spectral density $J(\omega)$ derived from the measurements of subsection 5.3.4. By inspection of $J(\omega)$ it can be seen that the QD is transformed from a weakly vibronic system into a strongly vibronic one by laser driving when $\hbar\Lambda$ is on the order of a few meV.

5.4.3 Time Dynamics

To investigate the time dynamics of LAPSE, a time-resolved two-colour pump-probe measurement is performed. PC^X_{2pulse}/PC^X_π is measured
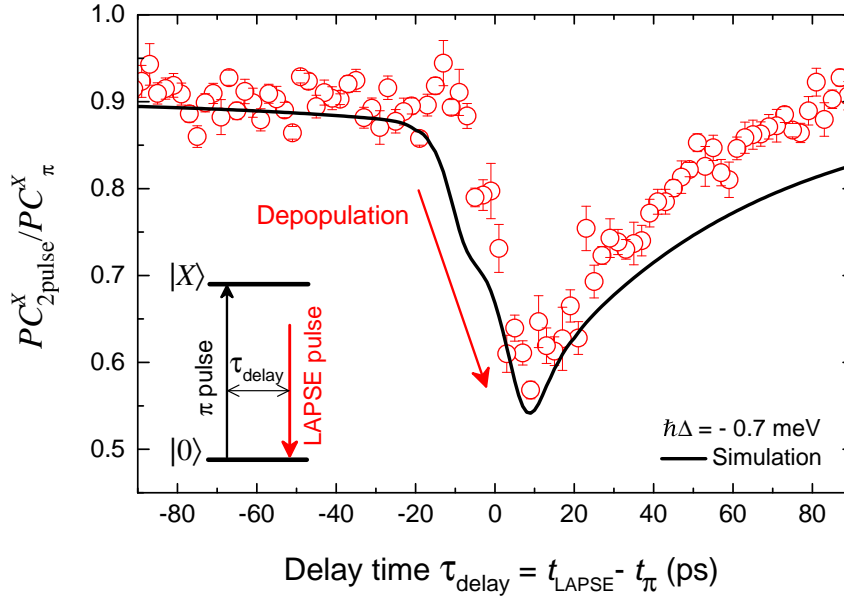
Figure 5.10: Time dynamics of the LAPSE process. Red circles: $PC^X_{2\text{pulse}}/PC^X_\pi$ measured as a function of τ_{delay} using the same pulse configuration as Figure 5.9. $\tau_{\text{delay}} = t_{\text{LAPSE}} - t_\pi$, where t_{LAPSE} and t_π are the arrival times of the LAPSE pulse and the π pulse. The pulse area of the LAPSE pulse is 5.25π. Black line: Numerical simulation. Inset: Excitation scheme.

as a function of the delay (τ_{delay}) between the resonant π-pulse and the LAPSE pulse; this is shown by the red circles in Figure 5.10. At negative delay time, the LAPSE pulse arrives before the π-pulse and therefore there is no exciton population to de-excite. The signal (~ 0.9) is not exactly 1 as the red-shifted LAPSE pulse can also create excitons with very small probability by absorbing phonons as $T > 0$ (see Figure 5.2(e)). When the π-pulse temporally overlaps the LAPSE pulse, $PC^X_{2\text{pulse}}$ decreases to a minimum between $\tau_{\text{delay}} = -10$ and $+10$ ps, indicating that the LAPSE process can be as fast as 20 ps. This is closely linked to the laser pulse duration; in this experiment the temporal FWHM is 16.8 ps. The signal then slowly recovers due to the electron tunnelling before the arrival of the LAPSE pulse, reducing the population that can be de-excited. The electron tunnelling time (55 ps) is again measured using time-resolved pump-probe (see subsection 4.4.1).

As discussed, the depopulation time is determined by the temporal width of the LAPSE pulse and in principle can be further reduced by using shorter laser pulses. However, reducing the pulse duration

too far can reduce the efficiency of the LAPSE process by not allow-
ing enough time for complete phonon-assisted relaxation between the
dressed states [359, 376]. Theoretical studies have found that a pulse
duration of around 10 ps is sufficient for the QD to reach thermal
equilibrium between the two dressed states, opening the possibility
of further reducing the de-excitation time with shorter pulses.

To confirm the LA phonon-assisted relaxation interpretation of these
results, path-integral calculations were performed with electron tun-
nelling incorporated as a Lindblad-type relaxation term. The results
of this calculation (black line in Figure 5.10) show good quantitat-
ive agreement and reproduce all the features observed in the exper-
imental measurement. This further supports the assertion that the
behaviour observed originates from LAPSE relaxation between the
dressed states.

5.4.4   *Spectral Dependence*

A significant difference between the DVC processes studied in this
chapter and resonant coherent excitation is that the phonon bath
provides a broad, continuous resonance as opposed to a single nar-
row line. In the case of LAPSE; this is interesting as it corresponds
to a broad tuning of the stimulated photon. To demonstrate this tun-
ability, the decrease of exciton population (measured as a change in
photocurrent, ΔPC) caused by a strong pulse is measured as a func-
tion of the laser detuning ($\hbar \Delta$). The measurement is performed using
a differential technique, illustrated in Figure 5.11(a),(b) & (c). First a
PC spectrum is taken by scanning the detuning ($\hbar \Delta$) of a strong pulse
($3.15\pi \leq \Theta \leq 7.35\pi$) with a π-pulse resonant with the exciton. This
produces a spectrum with a sideband at negative detuning which cor-
responds to LAPSE, as illustrated in Figure 5.11(a). Next, a second
spectrum is taken without the resonant π-pulse. This results in a
spectrum similar to Figure 5.6 with a positive-detuning sideband cor-
responding to phonon-assisted excitation as shown in Figure 5.11(b).
Subtracting (b) from (a) results in the differential spectrum illustrated
in Figure 5.11(c).

Experimental differential photocurrent spectra measured using this
method are illustrated for co-polarized pulses in Figure 5.11(d) and
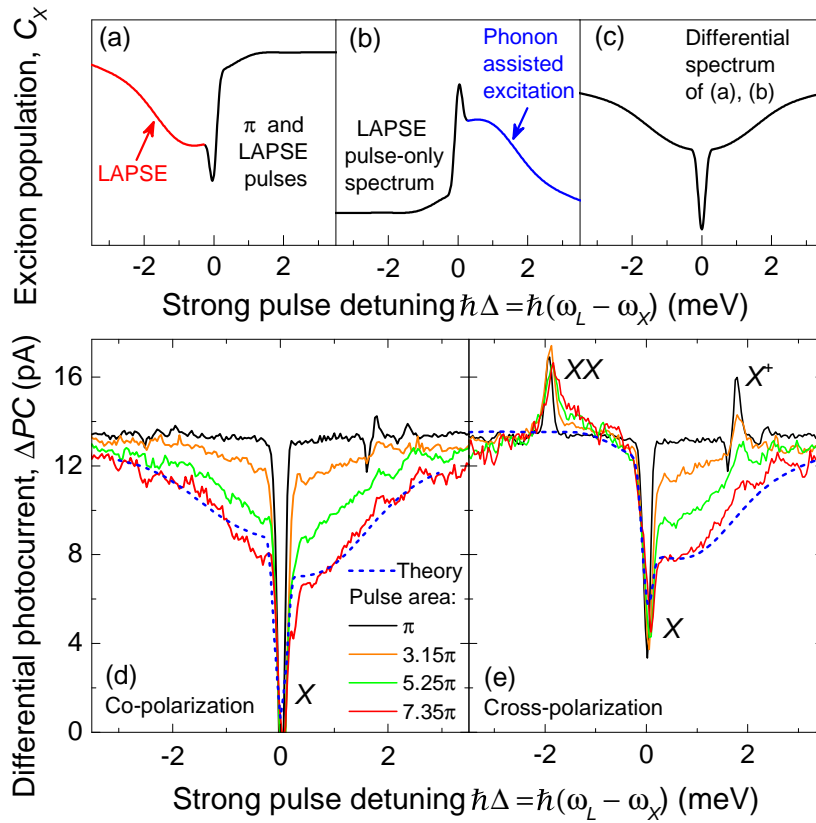
Figure 5.11: (a) - (c): Simulated single-QD spectra illustrating the steps of the differential photocurrent measurement. (a) Exciton occupation as a function of the detuning of the strong pulse which is applied τ_{delay} after a resonant π-pulse, LAPSE occurs at negative detunings (red line); (b) exciton occupation obtained by a single strong pulse, phonon-assisted excitation occurs at positive detunings (blue line); (c) differential spectrum obtained by subtracting the spectrum in (b) from the one in (a). (d), (e): Measured differential PC spectra obtained with strong pulse co/cross-polarized relative to the resonant pulse for different pulse areas. XX: biexciton. X^+: positive trion. $\tau_{delay} = 24$ ps. Blue dashed line: simulated differential measurement for pulse area = 7.35π.
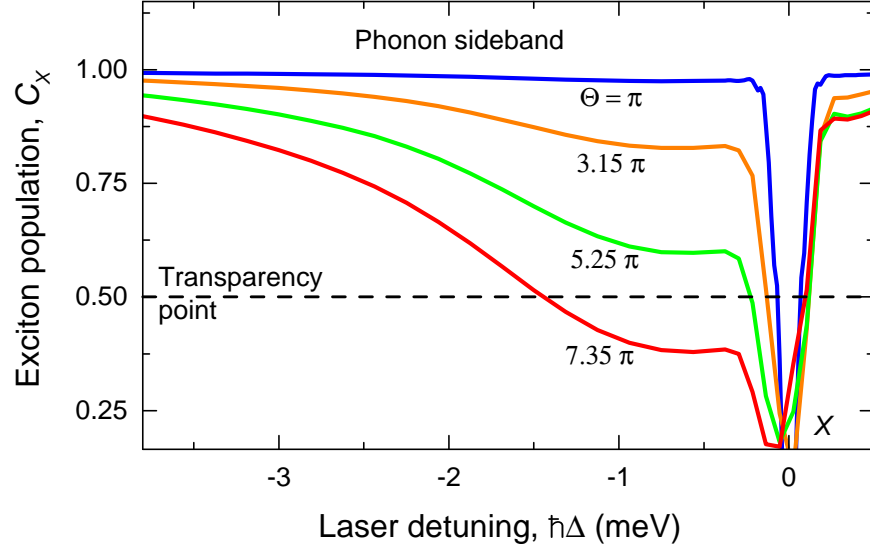
Figure 5.12: Calculated LAPSE sidebands for the same pulse areas as Figure 5.11 without electron tunnelling and the differential method.

for cross-polarized pulses in Figure 5.11(e). The sideband at negative detuning in Figure 5.11(d) demonstrates that LAPSE is effective across a broad tuning range of around 4 meV. Meanwhile, the absence of any sideband to negative detuning in Figure 5.11(e) shows that the strong pulse is unable to depopulate the orthogonal exciton state, illustrating that the DVC mechanism conserves spin. The $|X\rangle \rightarrow |XX\rangle$ transition is also visible with a small phonon sideband in Figure 5.11(e) owing to its cross-polarization with respect to the $|0\rangle \rightarrow |X\rangle$ transition.

The shape of the sidebands observed is primarily determined by $J(\omega)$ as in Figure 5.6. In addition, electron tunnelling between the two pulses also makes a contribution. Evidence of this tunnelling is provided by the $|h^+\rangle \rightarrow |X^+\rangle$ transitions (see subsection 4.3.1) observed at positive detuning in Figure 5.11(d) and (e). The blue dashed line in both figures is the result of a path-integral calculation of the differential spectrum incorporating electron tunnelling for $\Theta = 7.35\pi$. The excellent agreement between theory and experiment confirms the interpretation of the origin of the sidebands. It should be noted that the theoretical calculation only considers the $|0\rangle$ and $|X\rangle$ levels and hence does not reproduce the trion and biexciton features. Repeating the calculations without electron tunnelling or the differential method allows the theoretical change in exciton population to be obtained. The results of these calculations are shown in Figure 5.12 where the

spectral dependence of the de-excited exciton population is clearly visible. A minimum population of $C_X = 0.38$ is observed at around $\hbar\Delta = 0.6$ meV with depopulation to below the transparency point occurring across a broad detuning range of around 1.5 meV. Similarly to Figure 5.5, the maximum population transfer is limited by the strength of the laser driving and would continue to increase for stronger driving.

5.5 TEMPERATURE DEPENDENCE OF DYNAMIC VIBRONIC COUPLING
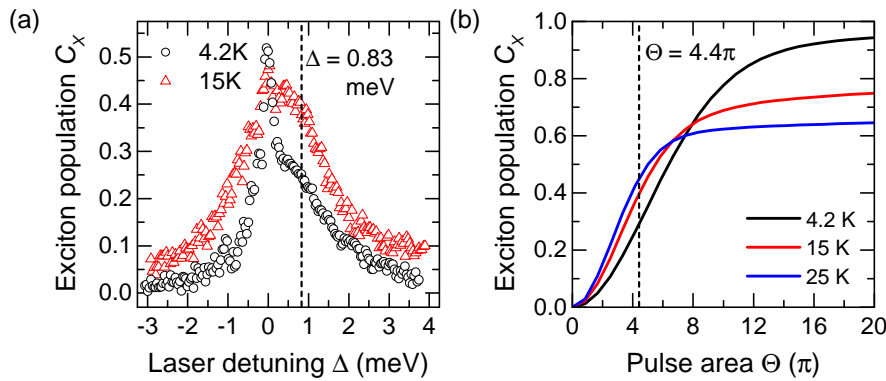
Figure 5.13: (a) Exciton population vs. laser detuning (Δ) at 15 K (red triangles) compared to 4.2 K (black circles) for excitation with pulse area $\Theta = 4.4\,\pi$. The dashed line indicates a detuning of $\hbar\Delta = +0.83$ meV. (b) Calculated variation of the exciton population versus pulse area (Θ) for $T = 4.2$ K (black), $T = 15$ K (red) and $T = 25$ K (blue) for positive detuning of $\hbar\Delta = +0.83$ meV. The dashed line shows $\Theta = 4.4\pi$.

In previous studies DVC processes have mainly been studied at $T = 4.2$ K [215, 368, 376], the temperature of liquid-He. It is interesting to consider the influence of increasing the temperature on the mechanism. Figure 5.13(a) presents phonon sideband measurements similar to Figure 5.6 at $T = 4.2$ K (black circles) and $T = 15$ K (red triangles) whilst Figure 5.13(b) shows calculations of the exciton population as a function of pulse area for different bath temperatures. Increasing the temperature increases the strength of the exciton-phonon interaction, observed for instance by stronger damping and frequency renormalization of excitonic Rabi rotations [64]. As discussed in subsection 5.2.1, this increases the rate of phonon relaxation between the dressed states, and, for relatively weak excitation, increases the result-

ing exciton population as more population relaxes during the pump pulse. This is shown by the higher population observed at positive detuning for $T = 15\,K$ (red triangles) compared to $T = 4.2\,K$ (black circles) in Figure 5.13(a) and also by the steeper initial gradient for higher temperatures observed in the calculations of Figure 5.13(b).

However, this does not illustrate the complete picture. At higher bath temperatures the increased number of phonons increases the probability of the competing process at positive detuning, namely the annihilation of an exciton by absorption of a phonon (see Figure 5.2(c)). This is shown in measurements by the reduced detuning asymmetry of the phonon sidebands at $T = 15\,K$ in Figure 5.13(a). The origin of the negative detuning signal is the creation of exciton population by phonon absorption (see Figure 5.2(e)). As such, the reduced asymmetry in the phonon sidebands can be considered equivalent to the reduced difference between the probability of phonon emission and absorption.

The consequence of this competition is that for driving that is sufficiently strong to allow complete relaxation (i.e. in the plateau region of Figure 5.13(b)), the final occupancy of the exciton state is in fact lower at higher temperatures owing to the thermalisation of the dressed states. This is illustrated by the reduced maximum exciton population attained at higher bath temperatures in Figure 5.13(b). A higher bath temperature will thus lead to a faster rise with pulse area, but a lower maximum population transfer by DVC. As such, increasing the bath temperature may provide a means to enhance DVC processes when the driving is relatively weak, as in Figure 5.13(a).

5.6   COHERENCE OF DYNAMIC VIBRONIC COUPLING

In section 5.3 the DVC creation of a QD exciton by a slightly blue-shifted laser pulse was demonstrated. Since this process involves emission of an LA phonon, in theory it should be incoherent, namely the phase of the exciton is random relative to that of the blue-shifted laser pulse. The exciton coherence time in this case is limited by the phonon relaxation time (few ps [369]). To demonstrate the incoherent nature of the DVC, Ramsey-like interference measurements [340,

377, 378] (see subsection 2.6.3) were performed using an unstabilised interferometer.

The QD is pumped with a blue-detuned pulse with $\hbar\Delta = 1$ meV at $t = 0$. The pulse area (8.4π) is chosen to give an exciton population of $C_X = 0.5$ (note that this is slightly higher than the inversion threshold in section 5.3 due to different laser detunings.) Once the QD has been excited, the state is then probed by a $\pi/2$ pulse resonant with the exciton at $t = \tau_{\text{delay}}$. The relative phase between the pump and probe is proportional to τ_{delay}. If the system is coherent, the probe pulse drives the QD to either $C_X = 0$ or 1 depending on the phase of the exciton with respect to the probe. The degree of coherence can then be determined by measuring the visibility of the Ramsey fringes as a function of τ_{delay}. In the experiment presented here, the relative phase between the pump and probe is unstabilized which may reduce the contrast of the fringes. In addition, the fringe period for $|0\rangle \rightarrow |X\rangle$ Ramsey fringe measurements is determined by the laser frequency, resulting in a fringe spacing of approximately 3 fs for this experiment (see Ref. [340] for experimental measurement). As the delay stage used here has a time resolution of only ~ 1 ps, the fringes are not clearly resolved. However, strong deviations from a flat signal (the incoherent case) are still observed in the case where coherence is present as the under-sampled fringes will still include some points close to the maxima and minima.

Figure 5.14 shows the time-integrated PC signal versus τ_{delay}. The red squares show the results for phonon-sideband pumping with $\hbar\Delta = 1$ meV. A flat line is observed, with no Ramsey-like fringes, indicating that the phase of the exciton is random relative to the probe pulse. By contrast, the black dots show the results measured when the pump pulse is tuned to resonance ($\Delta = 0$) and the pulse area is set to $\pi/2$. In this fully resonant situation, Ramsey-like fringes are observed provided τ_{delay} is shorter than or comparable to the exciton coherence time. The exciton coherence time of ~ 40 ps can be estimated from the dashed line envelope and is limited by the electron tunnelling rate [340]. The slow increase of the average PC signal originates from electron tunnelling between the arrival times of the pump and the probe.
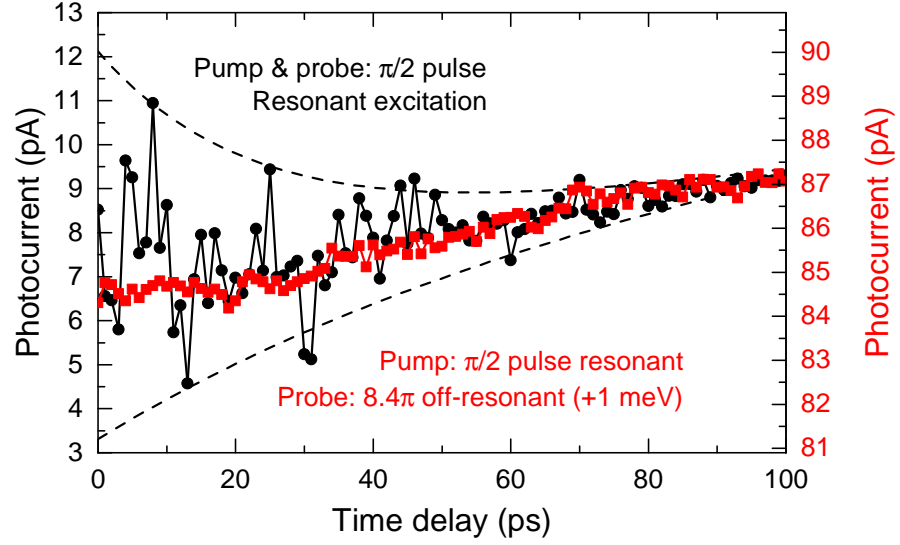
Figure 5.14: Comparison of Ramsey-like fringe data for the exciton when pumping in the phonon sideband (red) and resonant with the exciton (black) at $T = 4.2$ K. In both cases the second $\pi/2$-pulse is resonant with the exciton. The pulse area (Θ) of the +1 meV detuned pump pulse is set to be 8.4π to generate $C_X = 0.5$. The dashed lines are a guide to the eye.

5.6.1 *Discussion*

The incoherent nature of the DVC is clearly demonstrated by the absence of the fluctuations in the PC signal in the red data compared with that in the black data. This result is consistent with that reported by Weiler et al. [211] showing that the coherence properties of an emitted photon created via continuous pumping of the phonon sideband is much worse than resonant CW excitation. However, Bounouar et al. [376] demonstrate that the photons generated by quasi-resonantly pumping the biexciton state using pulsed excitation show similar coherence properties to those measured in the resonant two-photon scheme.

A possible interpretation of the seeming discrepancy between these results can be obtained by considering these experiments on the Bloch sphere as shown in Figure 5.15. As these experiments can involve either the $|0\rangle \rightarrow |X\rangle$ or $|0\rangle \rightarrow |2X\rangle$ transitions a general notation of $|g\rangle$ for the ground state and $|e\rangle$ for the excited state is used with C_e being the population of the excited state after the passage of the laser pulse. In the case where $C_e = 0.5$ (Figure 5.15(a)) a resonant $\frac{\pi}{2}$-pulse
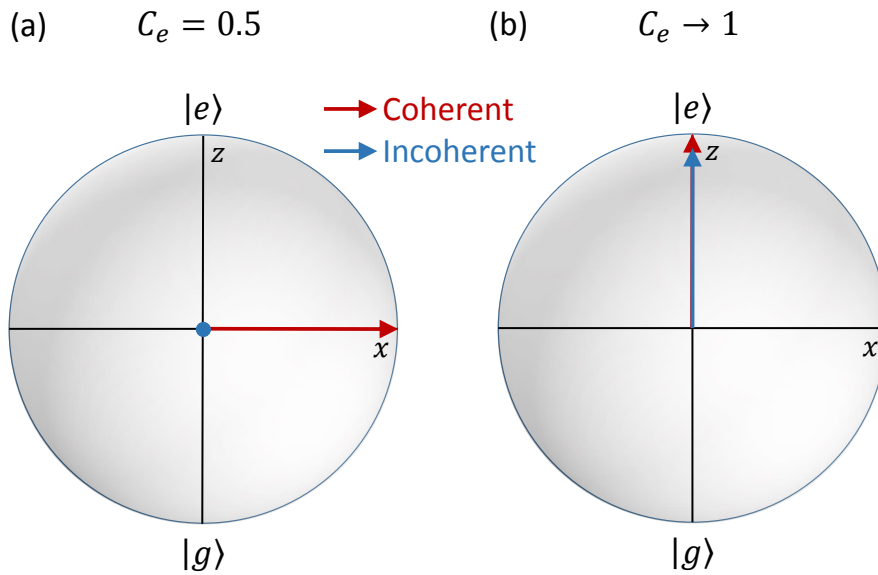
Figure 5.15: Illustrations of the final Bloch vector for coherent (red) and incoherent (blue) excitation to an excited state population of (a) 0.5 and (b) ~ 1.

coherently rotates the Bloch vector along the surface of the sphere to the equatorial plane (red arrow).

By contrast, an incoherent process produces a mixed state and can be visualised as the vector moving only along the z-axis, in this case to the origin of the sphere (blue point). Hence at $C_e = 0.5$ (the configuration in Figure 5.14) the difference between the Bloch vectors of the incoherent and coherent processes is maximised. This interpretation also illustrates why no fringes are observed for incoherent excitation in Figure 5.14; the Bloch vector has a length of zero hence the second $\frac{\pi}{2}$-pulse does not change the state.

In the photon coherence measurement of Bounouar et al. [376], the system is pumped to a biexciton population of $C_e = 0.95 \pm 0.02$, close to the thermalisation limit. Comparing this to a resonant π-pulse in Figure 5.15(b), it can be seen that the final Bloch vectors are now very close as an ideal π-pulse should also only have a z component. These results illustrate the incoherent nature of the DVC whilst illustrating that this need not be a significant problem for systems where a large excited population is desired.

It should be noticed that the fact that the DVC process is incoherent does not imply that the exciton spin is random. The results shown

in Figure 5.11 clearly indicate that the spin of the exciton is strongly correlated with the polarization of the excitation laser. It can thus be concluded that DVC is incoherent, but spin-preserving.

5.7   ULTRAFAST NON-RESONANT OPTICAL SWITCHING

A combination of the LA-phonon-assisted excitation and de-excitation processes allows the creation and destruction of an exciton within picosecond time scales, enabling ultrafast incoherent optical switching with a single QD that is much faster than the exciton radiative lifetime (∼ns) [122, 215]. To demonstrate this, a two-colour pump-probe experiment is performed with a blue-shifted (excitation) and red-shifted (de-excitation) pulse with the same pulse area. The pulses are equally detuned ($\hbar\Delta = \pm 0.7$ meV) from the exciton. At negative delay times, the excitation pulse creates some exciton population; this corresponds to the background PC level. At $\tau_{\text{delay}} < 0$, the de-excitation pulse arrives before the excitation pulse; thus the dot is empty and the pulse has no effect. When the two pulses overlap, the PC signal decreases to a minimum within 20 ps, as shown in Figure 5.16. This occurs due to erasure of the exciton created by the excitation pulse by the de-excitation pulse. The PC signal then slowly recovers due to the electron tunnelling out from the QD before the de-excitation pulse arrives in a manner similar to Figure 5.10.

In Figure 5.16(b) the calculated exciton population is shown for similar parameters to Figure 5.16(a). The calculation again incorporates the electron tunnelling in the PC experiment by incorporating it as an Lindblad-type relaxation term. The phase between the two pulses is assumed to be random and the result presented is the average of multiple repetitions of the simulation. This model well reproduces the de-excitation of the exciton and the subsequent recovery of the signal. The increase in PC signal at approximately $t = -10$ ps can be attributed to weak phonon-assisted excitation of the biexciton arising from the imperfect circular polarisation of the pulses. The oscillation of the exciton population at ∼5 ps is not clearly visible in the measured data in Figure 5.16(a) due to the limited time resolution of the experiment.
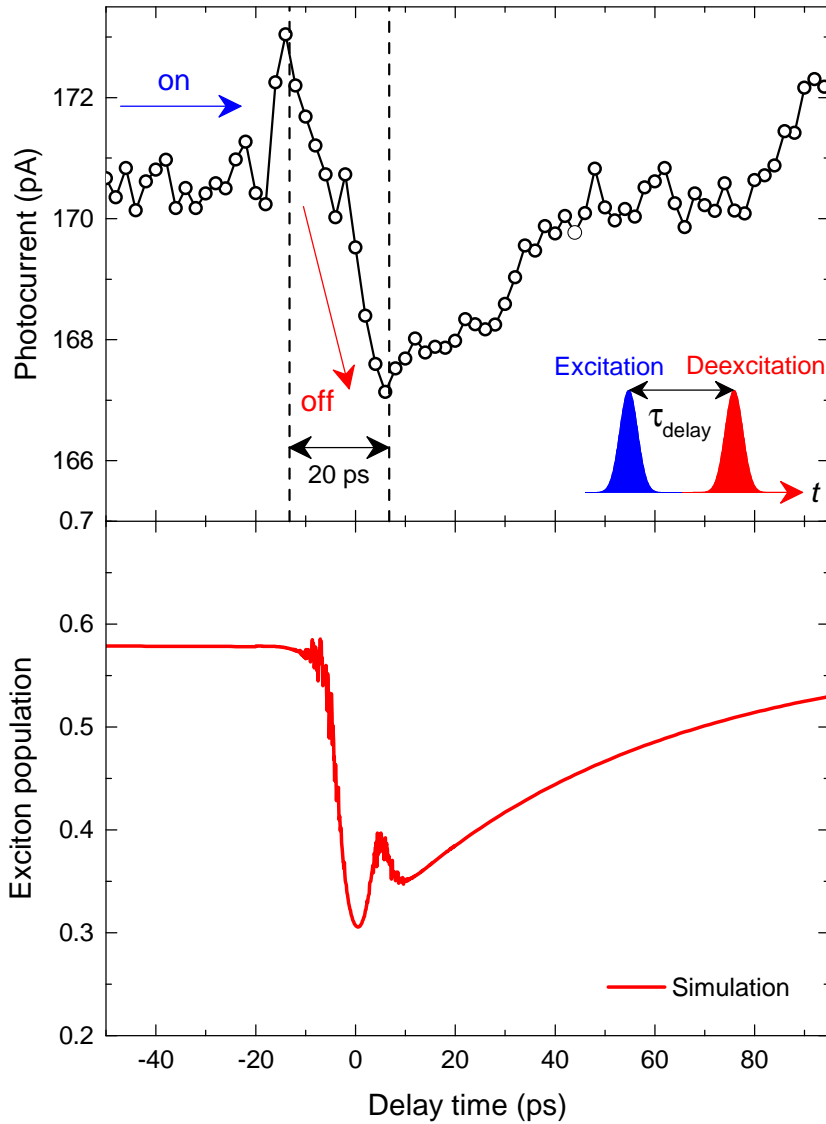
Figure 5.16: (a) PC signal measured with positively and negatively detuned control pulses as a function of the delay time $\tau_{\text{delay}} = t_{\text{OFF}} - t_{\text{ON}}$, where t_{OFF} and t_{ON} are the arrival time of the deexcitation and excitation pulses, respectively. $\hbar\Delta = \pm 0.7$ meV. $\Theta = 5.25\pi$. FWHM= 0.42 meV. Pulse duration = 8 ps. Inset: Pulse sequence. (b) Exciton population detected in the two-colour pump-probe measurement calculated using similar parameters to Figure 5.16(a): $\hbar\Delta = \pm 0.7$ meV, $\Theta = 5.25\pi$, Pulse duration = 10 ps. The phase between the two pulses is assumed to be random.

The ~ 20 ps excitation/de-excitation time observed in Figure 5.16(a) is determined by the laser pulse duration. The ultimate limit is set by the phonon thermalisation time ($\sim$ few ps [369]). In contrast to optical switching schemes employing resonant coherent excitation [372], the DVC-based scheme is robust against the fluctuation of laser power and detuning [359]. Furthermore, the incoherent nature of the phonon-assisted relaxation process determines that no phase locking is needed, in contrast to fully coherent excitation schemes. It is worth noting that the experimentally available laser power again limits the strength of the effect and that higher (lower) "on" ("off") populations would be observed for stronger driving.

5.8 CONCLUSION & OUTLOOK

The results presented in this chapter have demonstrated that the mechanism of DVC allows ultrafast (~ 20 ps) population and depopulation of a single QD exciton. The DVC process has been experimentally found to be incoherent but spin-preserving. The results presented here demonstrate that the DVC enables a QD exciton to be excited or de-excited across the transparency point, a fundamentally different behaviour to the case of an isolated two-level system. The spectral dependence of the DVC was shown to originate primarily in the phonon spectral density $J(\omega)$ with DVC processes effective over several meV of detuning up to the cut-off energy governed by the QD size. In addition, it was shown that the DVC mechanism is highly sensitive to temperature with increased temperatures resulting in higher efficiencies for weak driving but a lower population transfer in the limit of strong driving. Finally, picosecond incoherent all-optical switching of a single QD was demonstrated by combining the effects of phonon-assisted excitation and de-excitation. Similar results to those attained in section 5.3 have also subsequently been published by other groups for the exciton [368] and the two-photon $|0\rangle \rightarrow |XX\rangle$ transition [368, 376].

In terms of applications, phonon assisted excitation offers potential for a driving both single-photon [208] and entangled pair [376] sources where spectral filtering would enable simple separation of the excitation and emission. The demonstration of a population in-

version combined with the fast relaxation time is an interesting result that could aid development of quasi-resonantly pumped single QD lasers. Furthermore, whilst the population that can be created is limited by the available laser power, theoretical studies show that the presence of an optical cavity can enhance the driving strength experienced by the phonon bath significantly [379, 380]. Indeed, chapter 6 presents some initial results on the exciton-phonon coupling in the presence of a Photonic Crystal Cavity (PCC).

Turning to LAPSE, the depopulation time ($\sim$20 ps) is determined by the laser pulse width, making it possible to reset a QD exciton much faster than waiting for radiative recombination or tunnelling to occur. Due to the spectral width of the phonon sideband, LAPSE can occur in a tuning range of a few meV and could form the basis of tunable single QD lasers. This fast stimulated emission process could also find applications in semiconductor optical amplifiers [374] and precisely controlling the emission time of a single photon source in cavities [218, 287, 292].

The results of section 5.7 show that a combination of the excitation and de-excitation DVC processes could potentially be used for ultra-fast optical switching [227–229, 372, 373] with incoherent detuned pulses. The switching contrast could be improved significantly by increasing the effective driving strength; addition of an optical microcavity would again be a possible route towards this.

Finally, knowledge of phonon interactions in the strong QD-phonon coupling regime is an essential requirement for a full understanding of the behaviour of optically driven QDs, particularly in the case of QDs coupled to optical microcavities, where driving strengths are further enhanced. Indeed, various recent studies have shown new physical phenomena that arise from this coupling [381–385]. Furthermore, the physics of phonon coupling is also of interest for other solid-state qubit implementations. For example, it has been predicted that the strong phonon coupling in NV centres could enable a bright single photon source with a > 100 nm tuning range [218].

CAVITY INFLUENCES IN PULSED DRIVING OF SINGLE QDS

6.1 INTRODUCTION

Quantum dots weakly coupled to optical microcavities are a widely studied system. The Purcell enhancement [231] of the spontaneous emission that occurs when the QD is resonant with the cavity [233–235] has been widely exploited in the development of brighter and more indistinguishable single photon sources [225, 226]. Furthermore, the cavity has been used to enhance weaker emission channels such as LA phonon-assisted emission [86, 208, 216, 218] or two-photon transitions [293]. However, almost all of these experiments have been performed with relatively weak CW laser driving.

By comparison, the strong-driving regime of cQED has seen relatively little study. The recent demonstration of a near-optimal single photon source based on a strongly-driven weak-coupled QD-cavity system [226] provides motivation to develop a complete understanding of the physics of the system. For example, theoretical studies have shown that careful choice of parameters in a cQED system may allow phonon interactions to be tailored to potentially quench phonon-induced pure dephasing [386]. In addition, theoretical work also shows that the driving strength experienced by a QD weakly coupled to a microcavity can be strongly enhanced [379, 380]. This enables more efficient driving of the QD, potentially leading to efficient interactions between single photons and spins and also increasing the strength of the DVC processes discussed in chapter 5 [379, 380].

In this chapter initial results are presented concerning the influence of an optical microcavity on the QD when it is driven with strong resonant or quasi-resonant pulses. In particular, it is demonstrated that, in agreement with theoretical predictions, the cavity strongly modulates the effective driving strength experienced by the QD for both resonant coherent and quasi-resonant LA phonon-assisted driving.

6.2 THEORY

When a resonant laser is applied to an optical microcavity, the effect of the cavity is to concentrate the electric field into a smaller region, focused on the centre of the cavity. If a QD is present at the centre of the cavity, this results in a QD-cavity coupling with strength g defined by:

$$g = \frac{1}{\hbar}\sqrt{\frac{\hbar\omega}{2V_m}}\mu,\tag{6.1}$$

where μ is the dipole moment of the QD and V_m is the mode volume of the cavity (see Equation 2.10).

In the weak QD-cavity coupling limit, the effective drive strength (defined here as a pulse area Θ_{eff}) experienced by a resonantly driven QD in a cavity is given by Equation 6.2 [380]:

$$\Theta_{eff} = \frac{g\Theta_c}{\sqrt{\kappa^2 + \Delta_{Lc}^2}},\tag{6.2}$$

where Θ_c is the cavity driving strength (pulse area), $\kappa = \frac{\Delta\omega}{2}$ is the cavity loss rate and Δ_{Lc} is the laser-cavity detuning.

The cavity confines the pump light, causing a build-up of the pump field. The strength of the field that builds up is determined by the cavity Q-factor. Hence, the cavity driving strength is linked to the drive strength in the absence of a cavity (Θ) by $\Theta_c = Q\Theta$. This allows the driving strength experienced by a QD coupled to a cavity to be defined as an enhancement factor (F_{drive}):

$$F_{drive} = \frac{gQ}{\sqrt{\kappa^2 + \Delta_{LC}^2}}.\tag{6.3}$$

Taking the case of $\Delta_{Lc} = 0$, this means that the driving strength experienced by the QD is enhanced if $\kappa/g < Q$. The enhancement may be increased either by reducing the mode volume or increasing the Q-factor.
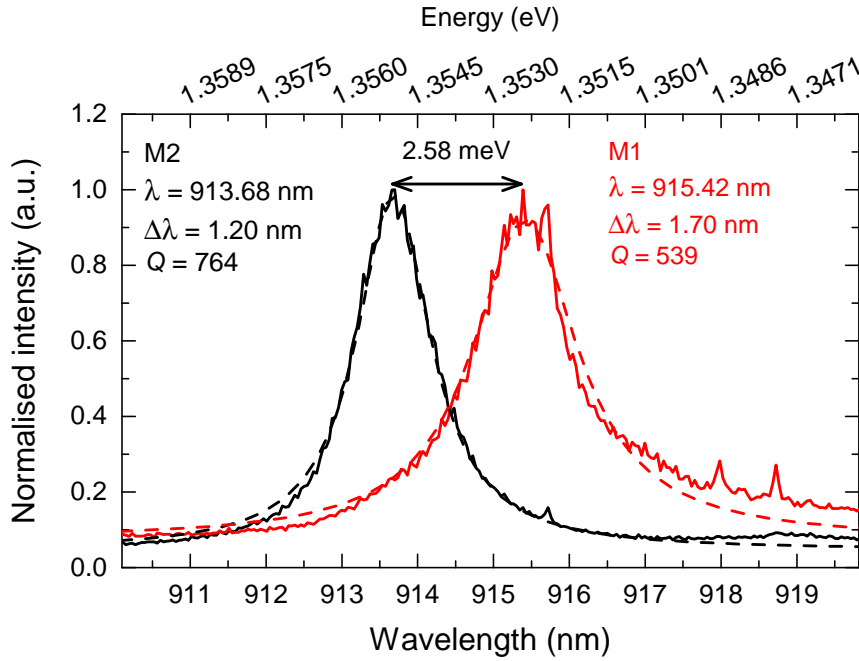
Figure 6.1: High power µPL spectra of the cavity under study. The excitation linear polarization is rotated by 90° between the two (black / red) spectra. Lorentzian fits to the two cavity modes (dashed lines) allow the Q-factors of the two modes to be evaluated. Weak, narrow emission corresponding to single QD lines is observed at around 918 nm and 919 nm as this is sufficiently spectrally separated from the cavity modes.

6.3 OPTICAL CHARACTERISATION

For the experiments presented in this chapter, the sample described in subsection 3.4.2 is used. In order to initially characterise the sample, µPL measurements were performed using above band-gap excitation focused on the cavity centre. This allows for fast and simple identification of all the QD lines present and the modes of the cavity by observing the ensemble emission of the sample.

6.3.1 Cavity Modes

By exciting the sample with high laser power (far beyond the level at which QD emission saturates), the cavity modes may be observed in µPL spectra. The polarization of these modes may also be determined by repeating the spectra at different linear polarization angles. In Figure 6.1 two orthogonally-polarized spectra are presented for the cavity chosen for further study. One cavity mode is observed in
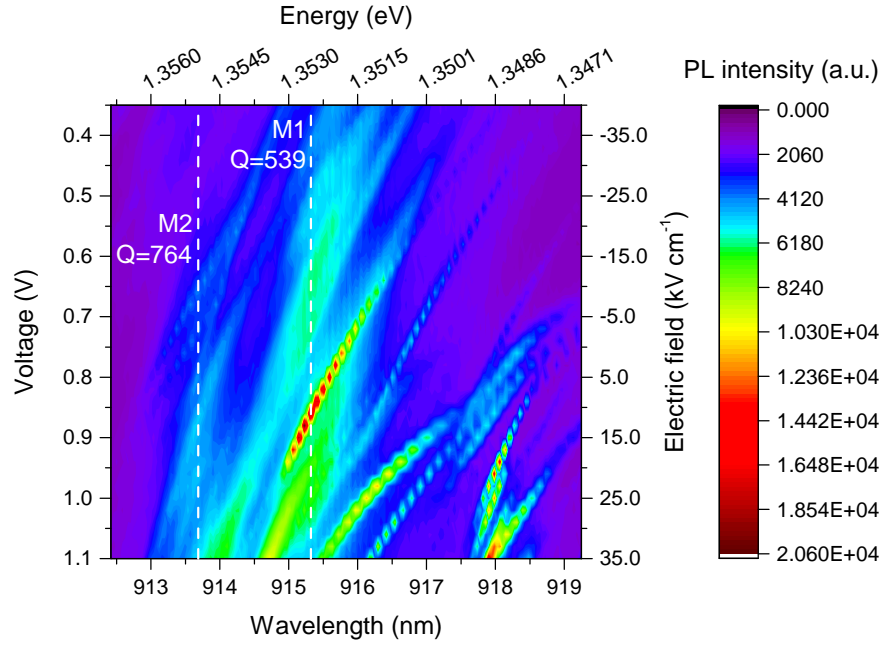
Figure 6.2: Bias dependent low excitation power μPL spectra of the cavity under study. The excitation is oriented at 45° to the cavity modes.

each spectrum, indicating that the modes are orthogonally-polarized as would be expected for these structures [328]. The small spectral splitting between the modes originates in a small modification of the cavity air hole pattern (see subsection 3.4.2) [329].

By fitting Lorentzian profiles to each mode (dashed lines), the Q-factors may be evaluated as 539 and 764 for the M1 and M2 modes respectively. These Q-factors are relatively low compared to theoretical calculations of $Q \approx 30,000$ [328] although these calculations do not account for the waveguide coupling. It is likely that the low experimental Q-factors originate from absorption from the Be doping present in the sample (see subsection 3.4.2), disorder introduced by fabrication errors and coupling to the waveguides. However, the small mode volume of the H1 cavity structure ($V_m = 0.39(\lambda/n)^3$ [245]) means that a strong enhancement of the QD driving strength can still be expected for a cavity coupled QD.

6.3.2 *Purcell Enhancement*

Reducing the excitation laser power to below the QD saturation level allows the lines corresponding to individual QD transitions to be re-

solved. If a QD is coupled to a cavity, Purcell enhancement of the spontaneous emission rate will cause a strong increase in μPL intensity when the transition is resonant with the cavity. To demonstrate this, Figure 6.2 presents the result of taking many μPL spectra as the QD energies are tuned by the QCSE. At an applied bias of around −0.86 V, a sharp increase in intensity of one transition is observed at the wavelength of the M1 cavity mode. This result demonstrates that this transition is weakly coupled to the M1 mode of the cavity. Observation of the biexciton cascade in other measurements (see subsection 6.4.2) reveals that this transition is the neutral exciton of a QD that will be referred to as QD A in subsequent sections.

6.4 PULSED RESONANT DRIVING

In order to study the coupled cavity-QD system in more detail, pulsed resonant excitation was used. By using the cross-polarized excitation-collection method described in subsection 3.6.2, it is possible to employ resonant excitation whilst collecting the resonant emission of the QD. The excitation and collection polarizations are both oriented at 45° to the cavity modes (which are in turn aligned with the sample crystal axes - see subsection 3.4.2) to allow both cavity modes to be studied.

6.4.1 *Resonance Fluorescence*

By setting the sample bias such that the QD is resonant with the cavity, bright Resonance Fluorescence (RF) is observed as shown by the red line in Figure 6.3. To confirm that the emission originates from the QD as opposed to scattered laser light, the experiment is repeated with the QD red-detuned by several laser linewidths. This case is shown by the black line in Figure 6.3; the absence of any significant intensity at the QD position confirms that the peak in the red spectrum originates from RF of the QD. Comparison of the amplitudes at the QD wavelength reveals a signal to noise ratio of 40:1. The QD linewidth measured here is limited by the spectral resolution of the spectrometer whilst the laser linewidth is around 3 times larger.
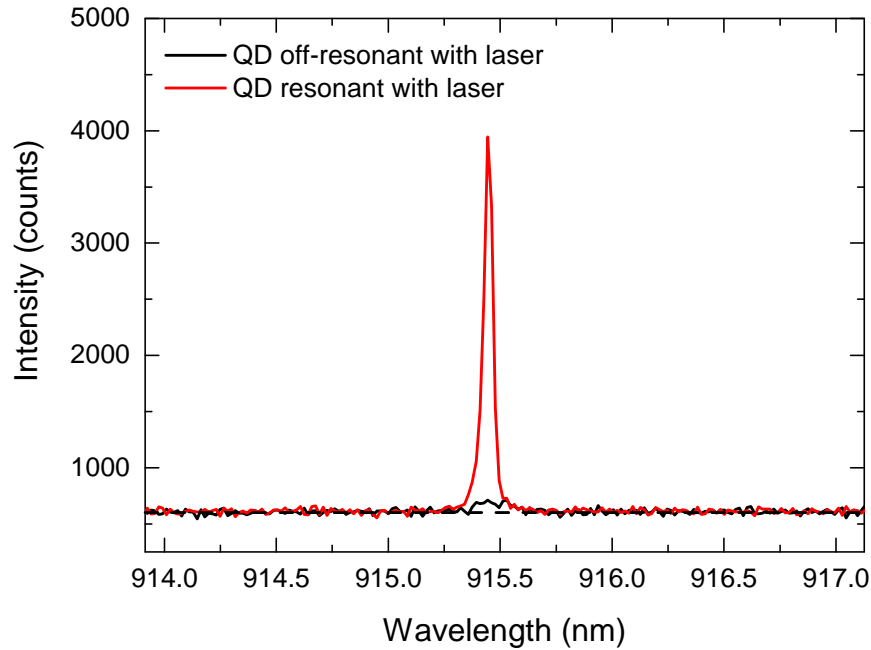
Figure 6.3: Low power pulsed RF spectrum of the QD when resonant with the cavity (red line). The signal is almost completely suppressed when the QD is red-detuned from the laser (black line). The exposure time was 5 s for each spectrum.

6.4.2 *Phonon-Assisted Identification of QD Transitions*

To confirm that the peak observed in Figure 6.3 is a neutral exciton, measurements were made to observe the biexciton transition of the QD. If the laser is red-detuned from the $|0\rangle \rightarrow |X\rangle$ transition, phonon-assisted excitation of the two-photon $|0\rangle \rightarrow |XX\rangle$ transition becomes the dominant excitation mechanism [359, 376]. Once the QD is excited to the $|XX\rangle$ state, it may decay either by radiative cascade via the $|X\rangle$ state (see subsection 2.2.5) or through spontaneous two-photon emission. The spectral signature of the biexciton cascade is a pair of peaks separated by the biexciton binding energy ($\hbar\Delta_{XX}$) whilst two-photon emission is observed as a single peak detuned from the exciton by half the biexciton binding energy.

Figure 6.4 presents the results of performing such a measurement on the sample studied in this chapter. The laser is red-detuned by -0.65 meV from the transition identified in Figure 6.3 which is resonant with the M1 mode of the cavity. Three peaks are observed in the differential RF spectrum: one at -3.40 meV corresponding to the $|XX\rangle \rightarrow |X\rangle$ transition, one at -1.70 meV corresponding to $|XX\rangle \rightarrow$
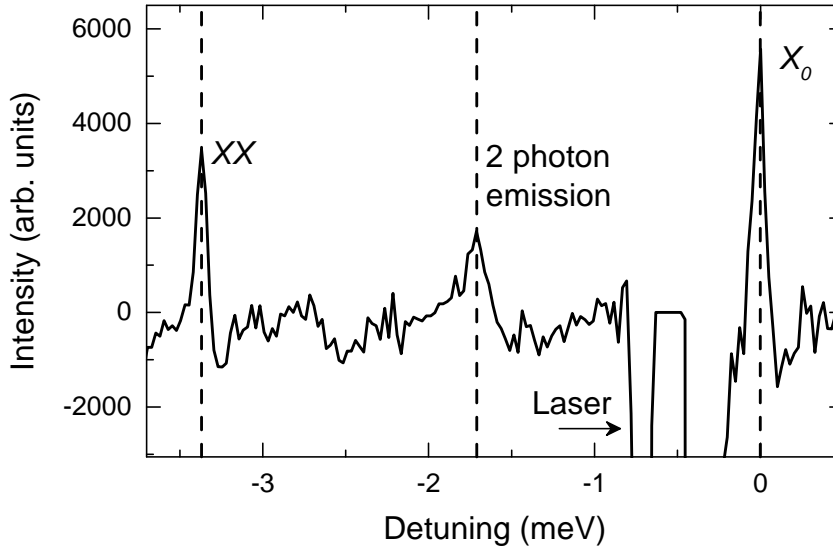
Figure 6.4: Differential RF spectrum of QD A under strong red-detuned excitation. Under these excitation conditions, phonon-assisted excitation of the two-photon biexciton transition dominates. Three peaks are observed, the XX (-3.40 meV) and X_0 peaks (0 meV) corresponding to decay via radiative cascade and a peak corresponding to two-photon emission (-1.70 meV).

$|0\rangle$ spontaneous two-photon emission and one at 0 meV corresponding to $|X\rangle \rightarrow |0\rangle$. As a result, the transition identified in Figure 6.3 is confirmed as being the neutral exciton of QD A with the biexciton having a binding energy of $\hbar\Delta_{XX} = -3.40$ meV.

The two-photon peak is around half as bright as the biexciton peak. However, as the dipole moment of the $|XX\rangle \rightarrow |0\rangle$ transition is much weaker [288]; this indicates that the broad cavity mode is likely enhancing the two photon emission decay channel [293] despite not being resonant with it. The greater exciton peak intensity when compared to the biexciton can be attributed to creation of exciton population through phonon absorption (see illustration in Figure 5.2). This arises due to the relatively small red-detuning from the exciton and the non-zero temperature. By increasing the red-detuning and shifting the cavity to be resonant with the two-photon transition, it would be possible to increase the amount of two-photon emission. This could have potential applications as a source of highly entangled photon pairs (see discussion in subsection 2.7.2).
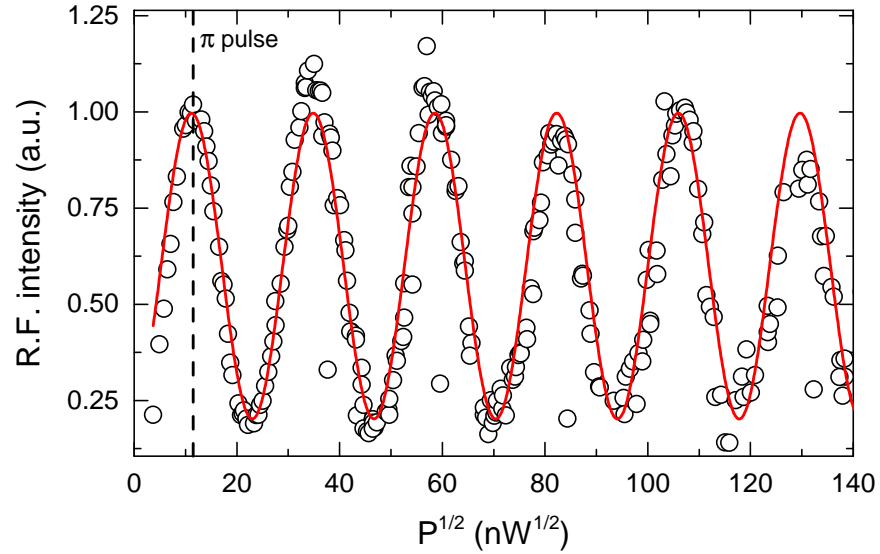
Figure 6.5: Rabi rotation of the neutral exciton of QD A when resonant with the M1 cavity mode. The intensity is obtained by fitting the QD peak amplitude of a series of RF spectra measured at different laser powers (*P*). The red line is a damped sine fit to the data.

6.4.3   *Rabi Rotation in a Cavity*

By performing power-dependent RF measurements with both the laser and the QD tuned to the cavity resonance, it is possible to observe a coherent Rabi rotation of the exciton population (see subsection 2.6.2). This is illustrated in figure Figure 6.5. A rotation of 12π is clearly visible with the observation of additional periods prevented by the scattered laser becoming so strong it can no longer be effectively suppressed. Improving the coupling efficiency of the system would allow this limit to be overcome, potentially allowing driving strengths to reach the point where theoretical studies have predicted that the rotations may "revive" owing to the non-monotonic power dependence of the phonon coupling [367].

It is interesting to note that the EID mediated damping of the Rabi rotation appears to be much weaker in this measurement compared to similar measurements on the photocurrent sample (see Figure 2.18). Further study is required to determine the physical reason for this but it is worth noting that the phonon coupling strength has been theoretically predicted to be influenced by the QD size [387], asymmetry [386] and material composition [386].
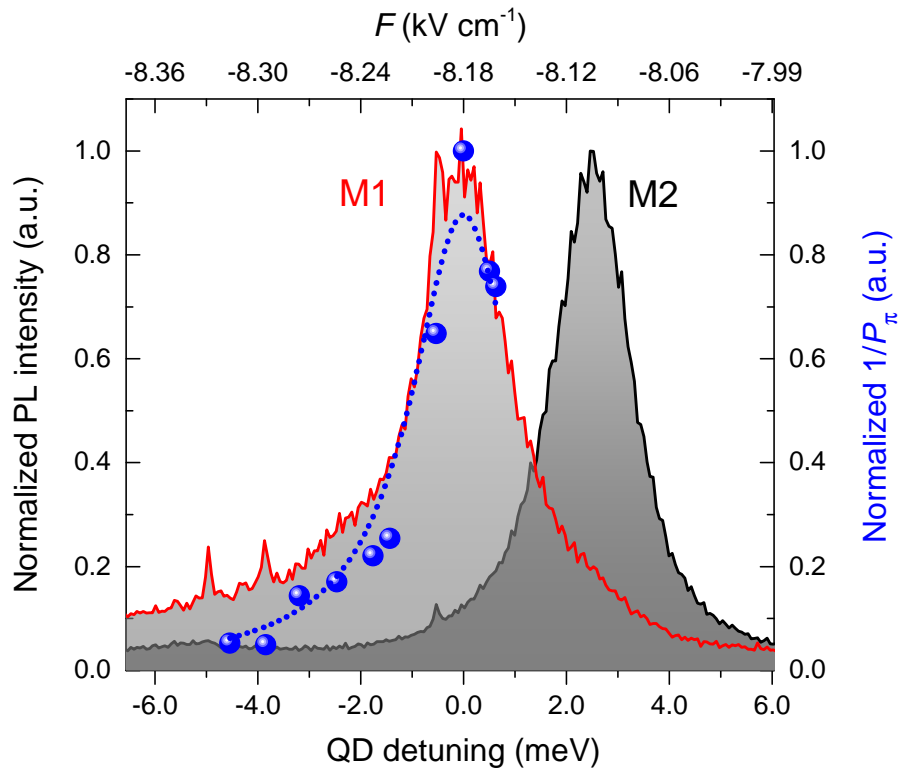
Figure 6.6: Plot of the inverse of the π-power of a resonant Rabi rotation vs. the detuning of the QD from the cavity mode M1. The blue dashed line is a fit of Equation 6.2 using the measured cavity linewidth. The shaded grey spectra are normalized plots of the cavity modes from Figure 6.1.

To investigate the influence of the cavity on the driving strength experienced by the QD, a series of resonant Rabi rotation measurements were performed. The QD-cavity detuning is varied by QCSE tuning of the QD energy and the change in the π-power (P_π) measured. The results of this measurement are presented in Figure 6.6. The blue data points correspond to a normalized $1/P_\pi$. The grey shaded spectra are normalized plots of the cavity modes from Figure 6.1.

It can clearly be seen in Figure 6.6 that the π-power follows closely the profile of the M1 cavity mode. The power required for a π-pulse when the cavity is resonant with the QD is a factor of 20 smaller than the far-detuned cases. The dashed blue line represents a fit of Equation 6.2 using the measured cavity linewidth, indicating that the detuning dependence of the driving strength agrees with the theoretically expected trend. This behaviour is analogous to the Purcell effect where the spontaneous emission rate of a QD is enhanced on resonance with a cavity and suppressed when the cavity is far detuned [233–235]. The electric field strength changes slightly during this measurement due to the QCSE tuning; this is shown on the top axis. The change in field is very small and thus the influence of changing oscillator strength with electric field can be discounted.

6.4.4   *Exciton Lifetime in a Cavity*

As discussed in subsection 2.5.2, if a QD is weakly coupled to a resonant cavity, Purcell enhancement of the spontaneous emission rate is expected. This results in a reduction of the lifetime of the QD state, in this case the neutral exciton. To confirm that this occurs in the sample measured here, a time-resolved pump-probe experiment is performed. The principle of the measurement is similar to that described in subsection 4.4.1; the time delay between a pair of resonant π-pulses is scanned and the RF intensity is monitored. When the two pulses arrive simultaneously at $t = 0$, they add to produce a $\sim 2\pi$ rotation of the Bloch vector. As a result, the exciton population is close to zero and the RF signal is very small. As the delay time is increased, more population has the chance to undergo radiative recombination before the arrival of the second pulse, causing the signal to increase. As the pulse separation exceeds the exciton lifetime (T_1), the pulses
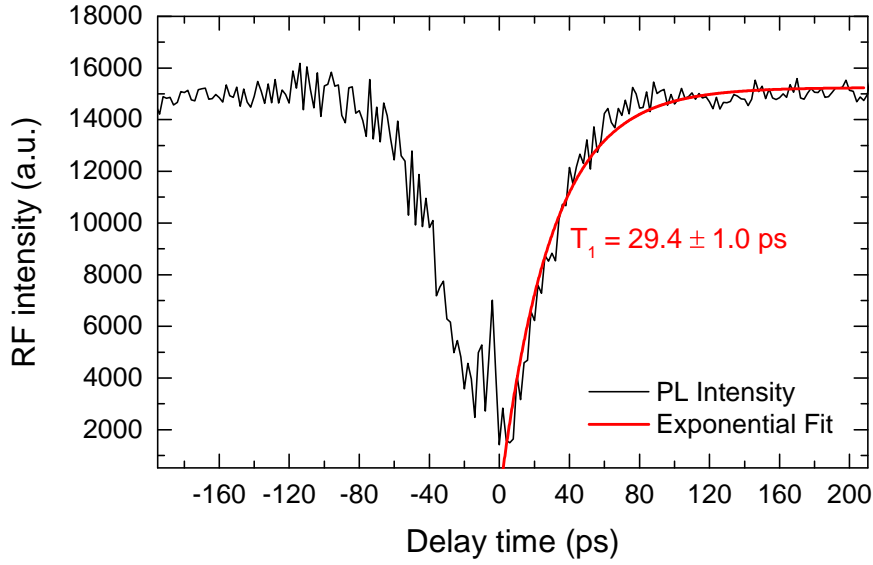
Figure 6.7: Time-resolved pump-probe RF measurement of the exciton life-time of QD A when resonant with the M1 cavity mode. The delay time between two π-pulses is scanned and the change in RF intensity monitored. The pump and probe pulses have temporal FWHMs of 20.0 ps and 11.2 ps respectively. Positive delay times correspond to the probe arriving after the pump.

act as two independent π-pulses and the RF signal reaches a corresponding maximum level.

Figure 6.7 shows the result of performing this measurement on QD A when it is resonant with the M1 cavity mode. Fitting an exponential decay to the RF signal at positive delay time (red line) gives a value of $T_1 = 29.4 \pm 1.0$ ps. This value is not deconvoluted from the duration of the excitation pulses and as such may be a moderate over-estimate. Interpreting this value as the exciton radiative lifetime and taking a conservative literature average for the exciton lifetime in bulk of 600 ps [122, 178] gives a Purcell factor of $F_P = 20.4$. Using the measured Q-factor (539) of the M1 mode and calculated mode volume ($0.39(\lambda/n)^3$ [245] and substituting into Equation 2.14 gives a theoretical $F_P = 105$. The discrepancy between these two values is reasonable as Equation 2.14 assumes that the QD is at the centre of the cavity mode; this is unlikely owing to the stochastic positioning of QDs in this sample.

6.4.5   *Discussion: Cavity Enhancement of Driving Strength*

Based on the results of Figure 6.6, it is reasonable to suggest that
the resonant cavity enhances the driving strength experienced by the
neutral exciton of QD A. However, as the driving strength is governed
by Equation 6.2, for sufficiently large laser-cavity detunings the driv-
ing strength is reduced compared to the bare QD case. This is equi-
valent to the Purcell suppression of the exciton lifetime observed for
large detunings [233–235]. As such, comparison of the resonant and
far-detuned cases is not sufficient to demonstrate enhancement. It is
also clearly not possible to measure the driving strength experienced
in the absence of the cavity for the same QD.

  As shown by Equation 6.3, the resonant enhancement factor is de-
termined by Q, g and κ. Q and κ are known from the measurement
of the Q-factor in Figure 6.1. It is only possible to directly measure g
in the strong coupling regime (see Ref. [388] for example) so to calcu-
late the enhancement factor here, a literature value of g must be used.
Measurement of the vacuum Rabi splitting of an H1 cavity in the
strong-coupling regime resulted in a value of $g = 76\,\mu eV$ [388]. A the-
oretical maximum of $200\,\mu eV$ was calculated [388] with the difference
accounted for by displacement of the QD from the cavity mode.

  In subsection 6.4.4, the Purcell factor was found to be a factor
of 5.15 less than the theoretical maximum. Applying the same scal-
ing to the literature value for the theoretical maximum of g gives
$g = 38.9\,\mu eV$ for the coupling strength between QD A and the M1
cavity mode. Substituting this into Equation 6.3 gives an estimated en-
hancement factor of $F_{drive} = 16.7$ for the parameters of the M1 mode.
As the parameters used in this calculation have been chosen to be
quite conservative, this is a reasonable estimate.

  Figure 6.8 presents a comparison of Rabi rotations between QD A
and a dot (QD C) located outside of the Photonic Crystal (PhC). Note
that the π-power measured here for QD A is lower than in Figure 6.5
due to better optimisation of the sample position and laser focus. For
QD A (black squares), when resonant with the M1 cavity mode a π-
power (P_π) of 13.4 nW is measured. For QD C (red circles), a π-power
of 162 nW is measured. Taking the ratio of these two values gives an
enhancement factor of 12.1. Of course, QD A and QD C are different
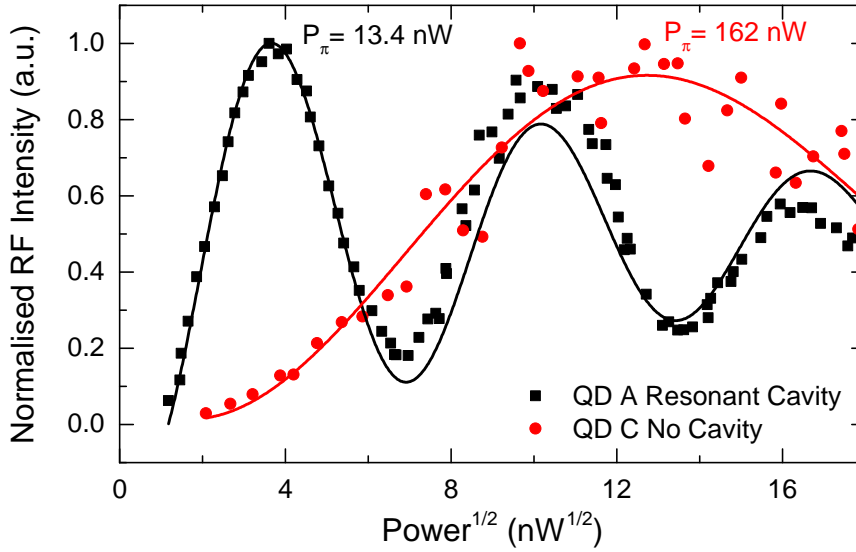
Figure 6.8: Comparison of the Rabi rotations of QD A (black squares) when coupled to the M1 cavity mode and QD C (red circles) which is outside of the PhC. The solid lines represent damped sinusoidal fits to the data from which the π-powers (P_π) are extracted.

dots in different regions of the sample and as such may well have different oscillator strengths. However, the extracted enhancement factor of 12.1 is reasonably close to the previously calculated estimate of 16.7, supporting the hypothesis that the cavity significantly enhances the driving strength experienced by the QD. Repeating the π-power comparison with multiple QDs that are outside the cavity would give further confirmation of this.

As a result of this analysis, a tentative conclusion that the QD driving strength is enhanced by around 1 order of magnitude can be reached. Further study will allow this to be confirmed with greater certainty.

6.5 LA-PHONON INFLUENCES

By detuning the laser from the QD exciton transition, similar phenomena to those observed in chapter 5 can be expected. However, the presence of a cavity introduces a new variable to the system in that the cavity can either enhance the driving strength when resonant with the laser as in subsection 6.4.3 or reduce the exciton lifetime via Purcell enhancement. In this section initial studies of the influence
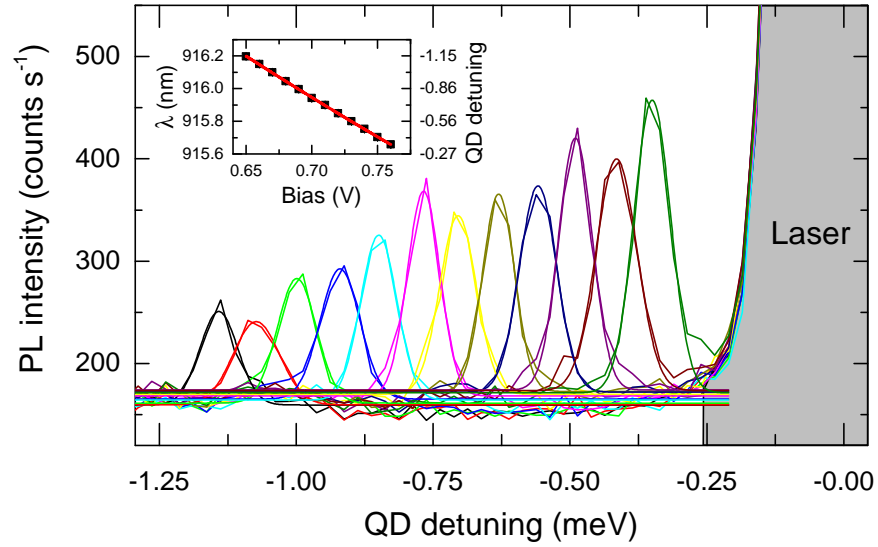
Figure 6.9: Spectra of the neutral exciton emission of QD A under strong pulsed driving of the cavity mode M1 which is tuned to the LA phonon sideband. The coloured lines represent spectra taken at different applied biases whilst the grey shaded region is scattered light from the pump laser. *Inset:* Exciton peak wavelength (extracted from fits to the main figure) plotted against applied bias. The red line is a quadratic fit of the data.

of the cavity are presented, focusing on the case where the laser and cavity are resonant with the LA phonon sideband of the QD.

6.5.1 *Tunable Emission of a QD Under LA-Phonon Pumping*

To demonstrate LA phonon excitation in such a system, the first scenario investigated is the case where the laser is resonant with the cavity whilst the QD is blue-detuned by around 1 meV. A clear narrow emission is observed at the QD exciton energy when the cavity is strongly pumped by the laser. Varying the bias applied to the sample Stark shifts the exciton peak as would be expected. This is shown in Figure 6.9 where the different coloured spectra represent different values of the diode bias. The emission intensity rolls off with increasing QD-cavity detuning due to the phonon form factor $J(\omega)$ (see Figure 5.3). As a result, the amplitude of these peaks map out $J(\omega)$. Repeating this measurement with higher detuning resolution would give an indication to the form of $J(\omega)$ for this QD. Plotting the peak wavelengths as in the inset to Figure 6.9 shows the energy shift

of the QCSE which is approximately linear as the sample bias is close to the flat-band condition in this measurement.

It is interesting to note how this experiment differs from experiments with above-band excitation such as Figure 6.2. Firstly, discounting the scattered laser light, emission is observed only from one peak, corresponding to the neutral exciton of QD A. This contrasts markedly from above-band excitation where emission is seen from various states of multiple QDs. Secondly, whilst the quadratic and linear coefficients of the observed QCSE are very similar, the offset is different. This can be attributed to a DC Stark shift owing to the introduction of extra charges into the device under above-band excitation. As studies have shown that this charging leads to charge-noise dephasing [183, 197], this result indicates that the charge environment under LA phonon excitation may be more favourable for the coherence of the exciton.

The potential for reduced charge noise combined with the single-line emission, simple spectral separation of the pump laser and the broad (∼ 1 meV) tuning of the emission offers a number of attractive features for a single photon source. Further study, in particular of the coherence properties of the emitted photons, would be of interest. It is worth noting that studies with a bare QD have measured photon coherence properties very close to those measured under resonant excitation for strong phonon pumping [376] (see discussion in subsection 5.6.1).

6.5.2 *Cavity Influences in Phonon-Assisted Excitation*

To demonstrate that the cavity also modulates the effective driving strength of LA phonon-assisted excitation, measurements are made on a second QD where the laser power and detuning are varied. This QD is referred to as QD B and is detuned from the M1 cavity mode by −4.47 meV. As the detuning is relatively large, the QD is excited by the LA phonon assisted mechanism discussed in chapter 5. The results of this measurement are illustrated in Figure 6.10 with the normalized emission intensity of QD B plotted against the square root of the laser power and the laser detuning with respect to the M1 cavity mode. On resonance with QD B, intermittent RF is observed. Blinking
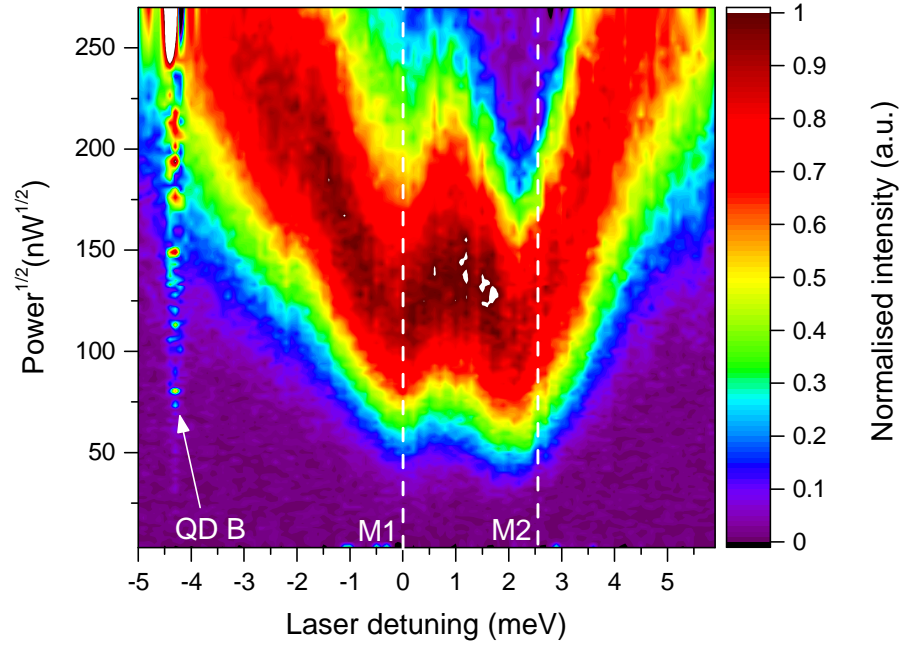
Figure 6.10: Normalised photo-luminescence intensity of QD B plotted against the square root of laser power and the laser detuning with respect to the M1 cavity mode. Intermittent RF is observed from QD B at a detuning of $-4.47\,\mathrm{meV}$.

of RF has previously been observed [389, 390] and potentially originates in competition between the bright and dark exciton states [169, 389].

The intensity of the QD emission exhibits a characteristic W-shape with the strongest emission at the lowest powers occuring close to both the M1 & M2 cavity modes. This gives a clear indication that the two cavity modes act to enhance the effective driving strength experienced by the phonon bath.

The splitting of the two modes appears smaller in this measurement, possibly due to the influence of the phonon form-factor $J(\omega)$ (see subsection 5.2.3). Detuning cross-sections of the data are shown in Figure 6.11 for the power minimas close to the cavity modes (blue and green points) and for larger detunings further from the cavity modes (red and black points). This further illustrates that the LA phonon assisted excitation is most efficient when resonant with the cavity.

The fact that the emission intensity reaches a peak and then declines when driving close to the cavity resonances (see Figure 6.11) is potentially evidence of the non-monotonic power dependence of the
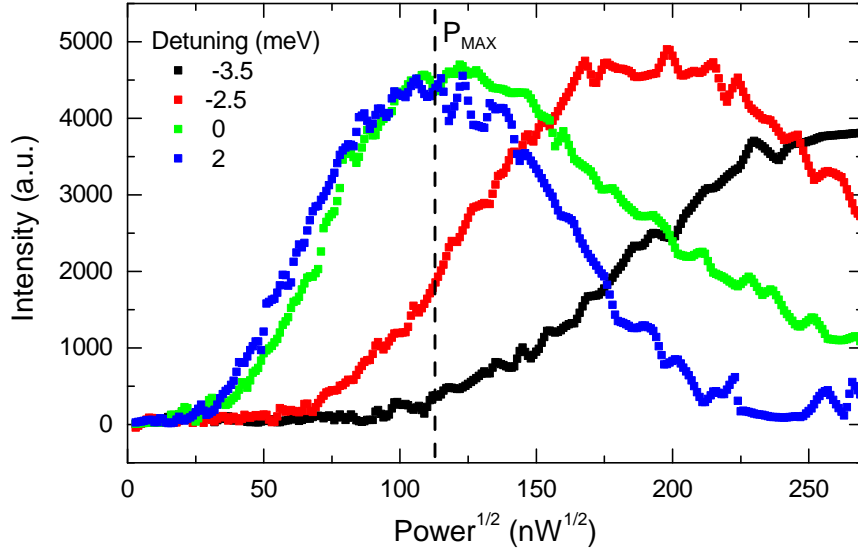
Figure 6.11: Plots of QD emission intensity against excitation laser power for a range of different laser detunings from the M1 cavity mode. The data is extracted from Figure 6.10.

exciton-phonon coupling [367]. If this interpretation is correct, the exciton population is reaching the thermalisation limit and then declining as the instantaneous Rabi frequency $\Lambda(t)$ exceeds the cut-off for LA phonon coupling defined by $J(\omega)$. This is significant as previous experiments (see subsection 5.3.3 for example) have been unable to reach the maximum exciton population due to insufficient driving strength. Although further study is required to give a complete interpretation, the decline of the QD emission at strong driving may indicate that the phonon coupling becomes weaker and can even be quenched. As discussed in subsection 6.4.3, this regime has been theoretically predicted [367] but is yet to be observed experimentally.

It is also interesting to note that the detunings between the cavity mode and the QD are very large here, almost 7 meV for M2. This is significantly beyond the detunings at which any significant interaction is seen in the absence of a cavity (see Figure 5.6). However, this is in agreement with theoretical predictions that the enhanced driving strength in a cavity could lead to significant population transfer at large detunings [379]. Single photon emission attributed to LA phonon excitation has also been observed for similar detunings with a QD in a PCC [208]. This indicates that the field enhancement provided by a cavity can significantly extend the detuning range over which DVC processes are effective.
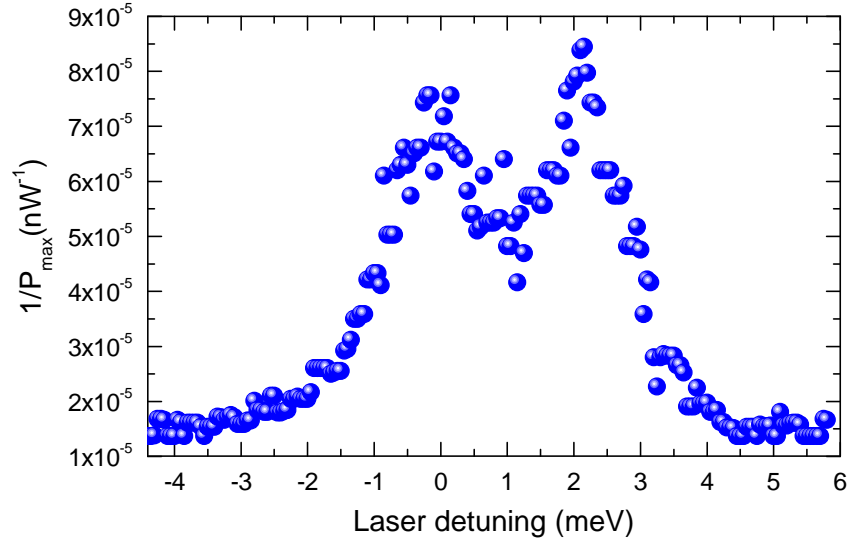
Figure 6.12: Plot of the inverse of the laser power at which QD emission is strongest in Figure 6.10 ($1/P_{max}$) against the detuning of the laser with respect to the M1 cavity mode.

By plotting $1/P_{max}$ (where P_{max} is the laser power at which the QD emission is strongest) as a function of laser detuning, Figure 6.12 is obtained. This figure is analogous to Figure 6.6 but for quasi-resonant LA phonon driving as opposed to resonant coherent driving. Figure 6.12 reproduces the double mode structure of the cavity observed in Figure 6.1 with peaks (corresponding to the most efficient driving) close to the two cavity modes. The laser power required to reach maximum emission intensity is around a factor of 6 smaller when the laser is resonant with a cavity mode. Unlike the resonant case, the spectral dependence is also influenced by $J(\omega)$, the form of which is unknown for this QD. As such, these results give a strong indication that the cavity enhances the driving strength experienced by the phonon bath but require further study.

6.6   CONCLUSION & OUTLOOK

The results presented in this chapter demonstrate that a Photonic Crystal Cavity (PCC) modulates the driving strength experienced by a single QD both for resonant coherent and quasi-resonant LA phonon driving. This modulation is analogous to the Purcell enhancement and suppression of the spontaneous emission rate that has previously

been observed. An estimated enhancement factor of 16.7 is calculated for resonant coherent driving despite the relatively low Q-factor of the cavity. The strong calculated enhancement despite the low cavity Q-factor is attributed to the small mode volume of the H1 cavity design used in the sample. Comparison of the π-power of the QD resonant with the cavity with another QD outside the cavity gives an experimentally estimated enhancement factor of 12.1, in reasonable agreement with the calculation. In future work it would be possible to further increase the enhancement factor by increasing the cavity Q-factor. This could be achieved by optimisation of the fabrication process along with replacing the Beryllium p-type doping used in the sample with Carbon to reduce absorption losses. Using an experimentally demonstrated literature value of $Q = 7200$ for an H1 cavity [388] and keeping $g = 38.9\,\mu eV$ (just below the onset of strong coupling) increases the enhancement predicted by Equation 6.3 by two orders of magnitude.

In recent studies of a QD weakly coupled to a micropillar cavity [391], Giesz et al. demonstrated a π Rabi rotation with a very weak excitation pulse (mean photon number 3.8). Whilst the pulse energies used in this chapter are significantly larger owing to large scattering losses at the sample surface, the smaller mode volume of the PCC means that it has the potential to operate with lower photon numbers than the micropillar, particularly if efforts are made to increase the Q-factor as previously discussed. This, combined with the planar architecture of the PCC shows strong potential for on-chip interactions between single photons and spins where scattering losses could be overcome either by including an on-chip single photon source or by injecting light through a waveguide.

In addition, the demonstration of similar behaviour for LA phonon assisted excitation shows the potential to reach maximum efficiency for the DVC processes discussed in chapter 5 without needing impractically large laser powers. In particular, this enhancement would greatly increase the contrast ratio of the non-resonant optical switch demonstrated in section 5.7. The tunable, single line emission demonstrated in Figure 6.9 shows the potential of this scheme to be employed as a tunable quasi-resonantly pumped single photon source. In addition, strong LA phonon assisted excitation was observed at large ($\sim 7\,meV$) detunings

It is also of note that the non-monotonic power dependence of the LA phonon assisted excitation observed in Figure 6.10 hints that the cavity system may enter the theoretically predicted [367] but experimentally unexplored regime where the phonon coupling weakens with increased driving strength. Finally, the cavity enhancement of LA phonon driving could also allow the exciton population to be driven to a stationary population inversion by a CW laser [379]. This would be very interesting both from a physics perspective and for the potential application of a tunable, quasi-resonantly pumped single QD laser.

Part III

CONCLUSIONS & OUTLOOK

In this part of the thesis the results presented are summarised and conclusions drawn with a view to future advances in the field. Some suggestions for future experiments building on the work presented in this thesis are also outlined.

7

CONCLUSION AND OUTLOOK

7.1 CONCLUSION

In this thesis the results of experimental investigations of the dynamics of single InGaAs SAQDs driven with picosecond laser pulses have been presented. Three main conclusions can be drawn:

1. Picosecond excitation of a SAQD exhibiting vanishingly small fine-structure can enable on-demand, fast and high-fidelity initialization of a single hole spin by exciton ionization. Compared to previous work, this high fidelity does not compromise the lifetime of the spin, allowing the full coherence lifetime of the hole spin qubit to be exploited. In addition, it was demonstrated that the initialisation fidelity can also be increased in the common case of SAQDs with non-zero fine structure by applying a detuned CW laser to reduce the FSS by the OSE.

2. Strong pulsed driving of the LA phonon sideband of a single InGaAs SAQD tunes the system from weakly to strongly vibronic on the timescale of the laser pulse duration, a process which is termed Dynamic Vibronic Coupling (DVC). This can enable both incoherent excitation and de-excitation of exciton population conditional upon the sign of the laser detuning. Significantly, the exciton population may cross the transparency point of 0.5 from both above and below, signifying that the presence of the phonon bath enables the realisation of a population inversion. This is contrary to the case of incoherent excitation of an ideal two-level system where the transparency point cannot be crossed. Study of the spectral properties reveals that the interaction is significant over detunings of several meV with the shape offering new insight into the form factor of the exciton-phonon interaction. The process was experimentally found to be incoherent and it was shown that the influence of temperature is to accelerate the phonon-assisted relaxation process whilst re-

ducing the maximum population transfer. Finally, it was shown that combining phonon-assisted excitation and de-excitation can realise an ultrafast switch operating on picosecond timescales with non-resonant excitation.

3. The addition of a Photonic Crystal Cavity (PCC) modulates the driving strength experienced by a single QD. This modulation was demonstrated to be effective for both resonant coherent driving and quasi-resonant incoherent LA phonon excitation. An estimated enhancement factor of 16.7 is calculated for resonant driving which is in reasonable agreement with a factor of 12.1 obtained by comparison with a QD outside the cavity. Significant enhancement is obtained despite the relatively low Q-factor of the cavity owing to the very small mode volume of the H1 Photonic Crystal Cavity (PCC) design. Purcell enhancement of the exciton spontaneous emission rate is also observed through reduction of the radiative lifetime by a Purcell factor of 20.4. High contrast pulsed resonance fluorescence of a single exciton was measured as was tunable emission of the same transition under quasi-resonant cavity-enhanced LA phonon excitation. In addition, the same LA phonon excitation mechanism was used to excite the biexciton and observe both the radiative cascade and two-photon emission.

7.2 FUTURE WORK

In this section a number of possible future directions of research building upon the results presented in this thesis are outlined.

7.2.1 *LA Phonon Processes in Weak-Coupled cQED*

The results presented in chapter 6 show resonant coherent and LA phonon assisted excitation (see section 5.3) of a weakly coupled QD-cavity system. As the parameter space of this experiment is very large, there are many potential directions to explore. For example, further studies of the resonant Rabi rotation as a function of the cavity-QD detuning may provide some insight into the weak intensity damping of the Rabi rotation observed in Figure 6.5, potentially

leading to regimes where phonon scattering may be enhanced or suppressed. Further studies of the system under high driving strengths combined with theoretical input could help explain the observed non-monotonic power dependence of the phonon sideband observed in Figure 6.10 and potentially the observation of the theoretically predicted revival of the Rabi rotation signal at high driving strengths [367]. Cavity enhancement of LA phonon processes demonstrated in section 6.5 could also enable a large increase in the switching contrast of the quasi-resonant optical switch demonstrated in section 5.7.

There is also significant motivation to study the coherence properties of the emitted photons under LA phonon excitation, particularly as a function of the drive strength. This would further the understanding of the coherence of DVC processes (see section 5.6) whilst also illustrating the suitability of such an excitation scheme for single and entangled photon sources. The influence of the QD-cavity and QD-laser detunings is also likely to have a strong influence on the emission properties of the system by changing the dominant influence of the cavity between enhancing the drive strength and Purcell reduction of the exciton lifetime. Furthermore, it would be possible to exploit both cavity modes of the non-degenerate H1 cavity studied in chapter 6 to obtain both Purcell enhancement and enhanced driving simultaneously.

Finally, the cavity enhanced driving strength presents the possibility that the driving strength of a CW laser tuned to the LA phonon sideband could be sufficiently enhanced to generate a stationary excitonic population inversion [379]. This contrasts strongly with the case of continuous resonant driving where Rabi oscillations of the population are observed (see subsection 2.6.2). The generation of a stationary population inversion combined with the presence of a cavity could realise the conditions required for an optically-pumped single QD laser. Recent studies with microwave photons have demonstrated a double QD maser with phonon-assisted transitions as the dominant gain mechanism [392].

7.2.2   *On-Chip Cavity-Enhanced Single & Entangled Photon Sources*

The sample and experimental configuration described in chapter 6 also has considerable potential as a source of both single and entangled pairs of photons. Recent studies involving pulsed driving of a micropillar cavity have demonstrated very high quality single photon sources [226]. However, the small mode volume of the H1 PCC offers the potential to improve this performance further still by increasing the Purcell factor, reducing the susceptibility to dephasing during the exciton lifetime. Additionally, the waveguides present in the sample mean that the single photon emission could efficiently be routed in an on-chip device with the added benefit that the pump laser is orthogonal to the fluorescence, suppressing the coupling of the pump to the waveguide for low background single photon emission.

High quality entangled pair emission should also be possible in such a sample by exploiting the biexciton radiative cascade (see subsection 2.2.5). Tuning the cavity mode to the two-photon transition could enhance both excitation and emission through this channel, potentially leading to highly entangled pairs of photons independent of the QD FSS (see discussion of entangled pair sources in subsection 2.7.2). The sample presented here could also be used to study a proposed scheme for tunable generation of highly indistinguishable single photons by stimulated two-photon emission [287].

7.2.3   *Fast Initialisation of a Hole Spin Coupled to an Optical Microcavity*

A number of studies have observed the coupling of single carriers to optical microcavities [317, 393]. Optimisation of the wafer structure of the H1 cavity sample (see subsection 3.4.2) to maximise electron tunnelling[1] could allow the fast, high fidelity hole spin initialisation scheme demonstrated in chapter 4 to be applied to a cavity-QD system. As noted in section 2.7, a number of interesting recent studies involving charged QDs have been limited by slow spin initialization [278, 312]. The long coherence lifetimes of single carriers compared to excitons could open numerous new possibilities for cQED with QDs, particularly when combined with rapid initialization. In addi-

---

[1] For example, removal of the upper AlGaAs barrier.

tion, the mode structure of the H1 PCC used in chapter 6 presents two orthogonally-polarized near-degenerate modes, exactly the structure that has been proposed for demonstration of fast, high-fidelity cavity enhanced initialisation and manipulation of a single spin qubit [318].

7.2.4 *Single Photon - Spin Interactions*

The low mode volume of the H1 PCC makes it an ideal platform for efficient light-matter interactions, particularly if improvements to the doping and fabrication processes can be made to increase the Q-factor. As discussed in section 6.6, the H1 PCC forms an ideal platform to attempt to study photon-spin interactions at the single photon level. The recent observation of a π Rabi rotation for an incident laser pulse with a mean photon number of 3.8 in a micropillar cavity demonstrates the potential of such an approach. The greatly reduced mode volume of the H1 PCC compared to the micropillar (see Table 2.1) should enable a further enhancement of this interaction. The coupling of an external laser source to a photonic crystal is much lossier than coupling to a micropillar; however this could potentially be overcome by using the waveguides and grating couplers on the current sample or by directing the emission from a waveguide-coupled single photon source to the cavity. Efficient conversion between photonic and spin qubits on a chip could play a crucial role in future QIP implementations.

Part IV

APPENDIX

A

SUPPLEMENTARY MATERIALS

This appendix contains extra details of models and parameters relating to the experimental work detailed in Part ii.

A.1 MODEL OF FIDELITY VS. OPTICAL STARK SHIFT

The increased hole spin fidelity attained by reducing the FSS by the OSE (see Figure 4.18 in section 4.7) can be well described by incorporating the OSE into the model derived in subsection 4.3.2. The FSS in the presence of a CW laser positively detuned from the $X \rightarrow XX$ transition (see Figure 4.15 in section 4.7) is given by:

$$\delta(I) = \delta|_{I=0} + \Delta\omega, \tag{A.1}$$

where I is the CW laser intensity and $\Delta\omega$ is the change of the FSS induced by OSE [164]. $\Delta\omega$ is in turn defined by:

$$\Delta\omega = \frac{s}{2}\left(\Delta_{CW} - \sqrt{\Delta_{CW}^2 + |\Omega|^2}\right), \tag{A.2}$$

where Δ_{CW} is the detuning of the CW laser, $s = \pm 1$ when the CW laser is H/V polarized and $\Omega = \sqrt{aI}/\hbar$ is the Rabi splitting induced by the CW laser. a is a fitting parameter proportional to the optical dipole moment of the $X \rightarrow XX$ transition.

In the literature [141, 254] and the experiments of section 4.7 a linear blue-shift of the $0 \rightarrow X_{H/V}$ transitions with laser intensity is observed when the CW laser is applied. This effect is independent of laser polarization and thus the shift is attributed to charge screening from the large number of carriers generated in the surrounding material by the CW laser. This interpretation is in agreement with previous studies [141, 254]. A similar blue shift is expected for the $X \rightarrow XX$ transition; hence Δ_{CW} is dependent on the incident CW laser intensity (I) according to:

Pol.	$\hbar\delta\|_{I=0}(\mu\text{eV})$	s	$a\ (\frac{\text{meV}^2\,\mu\text{m}^2}{\text{W}})$	$\hbar\triangle_{CW}\|_{I=0}\ (\mu\text{eV})$	$k\ (\frac{\text{eV}\,\mu\text{m}^2}{\text{W}})$
H	13.2	$+1$	275	76.6	8.4
V	13.2	-1	275	63.4	8.4

Table A.1: Parameters used in the fits of FSS vs. CW laser power shown in Figure 4.17. $\hbar\delta\|_{I=0}$ and $\hbar\triangle_{CW}\|_{I=0}$ are measured values whilst a and k are fitted to the data.

Pol.	$\hbar\delta\|_{I=0}(\mu\text{eV})$	s	$a\ (\frac{\text{meV}^2\,\mu\text{m}^2}{\text{W}})$	$\hbar\triangle_{CW}\|_{I=0}\ (\mu\text{eV})$	$k\ (\frac{\text{eV}\,\mu\text{m}^2}{\text{W}})$	$\Gamma_X - \Gamma_h(\text{ps}^{-1})$
V	13.2	-1	275	33.4	3.5	0.021

Table A.2: Parameters used in the fit of the measurement of hole spin fidelity vs. CW laser power (Figure 4.18).

$$\Delta_{CW}\left(I\right) = \Delta_{CW}\big|_{I=0} - kI/\hbar, \tag{A.3}$$

where k is a fitting parameter. Figure 4.17 in section 4.7 shows δ vs. the CW laser intensity measured at $E = 60\ \text{kV cm}^{-1}$ and the fits according to Equation A.1. The parameters used in these fits are shown in Table A.1.

Knowing how the FSS depends on the CW laser intensity, it is now possible to consider how the fidelity of the hole spin initialization varies with the intensity of the CW laser. To demonstrate the increase of the hole spin fidelity by reducing the FSS using OSE, the hole spin fidelity is measured as a function of the CW laser intensity (see Figure 4.18 in section 4.7). This data can be well reproduced by substituting Equation A.1 into Equation 4.20 as derived in subsection 4.3.2:

$$F = 1 - \frac{1}{2}\left[\frac{\left(\delta\big|_{I=0} + \Delta\omega\right)^2}{\left(\delta\big|_{I=0} + \Delta\omega\right)^2 + \left(\Gamma_e - \Gamma_h\right)^2}\right], \tag{A.4}$$

where Γ_e and Γ_h are the electron and hole tunnelling rates. The parameters used to fit Equation A.4 to the data in Figure 4.18 are shown in Table A.2. The paramater a is determined from the fit to the measurement of δ vs. CW laser intensity measured at $E = 60\ \text{kV cm}^{-1}$(see Figure 4.17) whilst k is a fitting parameter owing to the different electric field value. $\Gamma_e - \Gamma_h$ is determined from time-resolved pump-probe spectroscopy [340] as discussed in subsection 4.4.1.

[1] P. Dirac. *The principles of quantum mechanics*. International series of monographs on physics. The Clarendon Press, 1930 (cit. on p. 3).

[2] W. Hermanns and A. Einstein. *Einstein and the Poet: In Search of the Cosmic Man*. Branden Press, 1983 (cit. on p. 3).

[3] A. Einstein, B. Podolsky, and N. Rosen. 'Can Quantum-Mechanical Description of Physical Reality Be Considered Complete?' *Physical Review* 47 (May 1935), pp. 777–780. DOI: 10.1103/PhysRev.47.777 (cit. on p. 3).

[4] E. Schrödinger. 'Discussion of Probability Relations between Separated Systems.' *Proceedings of the Cambridge Philosophical Society* 31 (1935), p. 555. DOI: 10.1017/S0305004100013554 (cit. on p. 3).

[5] B. Schumacher. 'Quantum coding.' *Phys. Rev. A* 51 (4 Apr. 1995), pp. 2738–2747. DOI: 10.1103/PhysRevA.51.2738 (cit. on p. 4).

[6] S. Wiesner. 'Conjugate Coding.' *SIGACT News* 15.1 (Jan. 1983), pp. 78–88. DOI: 10.1145/1008908.1008920 (cit. on p. 4).

[7] R. P. Feynman, F. L. Vernon, and R. W. Hellwarth. 'Geometrical Representation of the Schrödinger Equation for Solving Maser Problems.' *Journal of Applied Physics* 28.1 (1957), pp. 49–52. DOI: 10.1063/1.1722572 (cit. on p. 4).

[8] J. S. Bell et al. 'On the Einstein-Podolsky-Rosen paradox.' *Physics* 1.3 (1964), pp. 195–200 (cit. on p. 5).

[9] R. P. Feynman. 'Simulating physics with computers.' English. *International Journal of Theoretical Physics* 21.6-7 (1982), pp. 467–488. DOI: 10.1007/BF02650179 (cit. on p. 5).

[10] B. P. Lanyon, C. Hempel, D. Nigg, M. Müller, R. Gerritsma, F. Zähringer, P. Schindler, J. T. Barreiro, M. Rambach, G. Kirchmair, M. Hennrich, P. Zoller, R. Blatt, and C. F. Roos. 'Universal Digital Quantum Simulation with Trapped Ions.' *Science*

334.6052 (2011), pp. 57–61. DOI: 10.1126/science.1208001 (cit. on p. 5).

[11]   I. M. Georgescu, S. Ashhab, and F. Nori. 'Quantum simulation.' *Rev. Mod. Phys.* 86 (1 Mar. 2014), pp. 153–185. DOI: 10.1103/RevModPhys.86.153 (cit. on p. 6).

[12]   E. Bernstein and U. Vazirani. 'Quantum complexity theory.' In: *in Proc. 25th Annual ACM Symposium on Theory of Computing, ACM*. 1993, pp. 11–20 (cit. on p. 6).

[13]   P. W. Shor. 'Polynomial-Time Algorithms for Prime Factorization and Discrete Logarithms on a Quantum Computer.' *SIAM Review* 41.2 (1999), pp. 303–332. DOI: 10.1137/S0036144598347011 (cit. on p. 6).

[14]   L. K. Grover. 'A fast quantum mechanical algorithm for database search.' *eprint arXiv:quant-ph/9605043* (May 1996) (cit. on p. 6).

[15]   A. M. Childs, R. Cleve, E. Deotto, E. Farhi, S. Gutmann, and D. A. Spielman. 'Exponential Algorithmic Speedup by a Quantum Walk.' In: *Proceedings of the Thirty-fifth Annual ACM Symposium on Theory of Computing*. STOC '03. San Diego, CA, USA: ACM, 2003, pp. 59–68. DOI: 10.1145/780542.780552 (cit. on p. 6).

[16]   E. Martin-Lopez, A. Laing, T. Lawson, R. Alvarez, X.-Q. Zhou, and J. L. O'Brien. 'Experimental realization of Shor's quantum factoring algorithm using qubit recycling.' *Nat Photon* 6.11 (Nov. 2012), pp. 773–776. DOI: 10.1038/nphoton.2012.259 (cit. on p. 6).

[17]   D. P. DiVincenzo. 'The Physical Implementation of Quantum Computation.' *Fortschritte der Physik* 48.9-11 (2000), pp. 771–783. DOI: 10.1002/1521-3978(200009)48:9/11<771::AID-PROP771>3.0.CO;2-E (cit. on pp. 7, 93, 121).

[18]   A. Barenco, C. H. Bennett, R. Cleve, D. P. DiVincenzo, N. Margolus, P. Shor, T. Sleator, J. A. Smolin, and H. Weinfurter. 'Elementary gates for quantum computation.' *Phys. Rev. A* 52 (5 Nov. 1995), pp. 3457–3467. DOI: 10.1103/PhysRevA.52.3457 (cit. on p. 7).

[19] J. L. O'Brien, A. Furusawa, and J. Vuckovic. 'Photonic quantum technologies.' *Nat Photon* 3.12 (Dec. 2009), pp. 687–695. DOI: 10.1038/nphoton.2009.229 (cit. on p. 8).

[20] E. Knill, R. Laflamme, and G. J. Milburn. 'A scheme for efficient quantum computation with linear optics.' *Nature* 409.6816 (Jan. 2001), pp. 46–52. DOI: 10.1038/35051009 (cit. on p. 8).

[21] A. Politi, M. J. Cryan, J. G. Rarity, S. Yu, and J. L. O'Brien. 'Silica-on-Silicon Waveguide Quantum Circuits.' *Science* 320.5876 (2008), pp. 646–649. DOI: 10.1126/science.1155441 (cit. on p. 9).

[22] R. Grimm, M. Weidemüller, and Y. B. Ovchinnikov. 'Optical Dipole Traps for Neutral Atoms.' In: ed. by B. Bederson and H. Walther. Vol. 42. Advances In Atomic, Molecular, and Optical Physics. Academic Press, 2000, pp. 95–170. DOI: 10.1016/S1049-250X(08)60186-X (cit. on p. 9).

[23] M. Saffman, T. G. Walker, and K. Mølmer. 'Quantum information with Rydberg atoms.' *Rev. Mod. Phys.* 82 (3 Aug. 2010), pp. 2313–2363. DOI: 10.1103/RevModPhys.82.2313 (cit. on p. 9).

[24] D. Leibfried, R. Blatt, C. Monroe, and D. Wineland. 'Quantum dynamics of single trapped ions.' *Rev. Mod. Phys.* 75 (1 Mar. 2003), pp. 281–324. DOI: 10.1103/RevModPhys.75.281 (cit. on p. 9).

[25] J. I. Cirac and P. Zoller. 'Quantum Computations with Cold Trapped Ions.' *Phys. Rev. Lett.* 74 (20 May 1995), pp. 4091–4094. DOI: 10.1103/PhysRevLett.74.4091 (cit. on pp. 9, 10).

[26] J. Dalibard and C. Cohen-Tannoudji. 'Dressed-atom approach to atomic motion in laser light: the dipole force revisited.' *J. Opt. Soc. Am. B* 2.11 (Nov. 1985), pp. 1707–1720. DOI: 10.1364/JOSAB.2.001707 (cit. on p. 9).

[27] P. Domokos, J. M. Raimond, M. Brune, and S. Haroche. 'Simple cavity-QED two-bit universal quantum logic gate: The principle and expected performances.' *Phys. Rev. A* 52 (5 Nov. 1995), pp. 3554–3559. DOI: 10.1103/PhysRevA.52.3554 (cit. on p. 10).

[28] S. Chu, J. E. Bjorkholm, A. Ashkin, and A. Cable. 'Experimental Observation of Optically Trapped Atoms.' *Phys. Rev. Lett.* 57 (3 July 1986), pp. 314–317. DOI: 10.1103/PhysRevLett.57.314 (cit. on p. 10).

[29] L. Deslauriers, S. Olmschenk, D. Stick, W. K. Hensinger, J. Sterk, and C. Monroe. 'Scaling and Suppression of Anomalous Heating in Ion Traps.' *Phys. Rev. Lett.* 97 (10 Sept. 2006), p. 103007. DOI: 10.1103/PhysRevLett.97.103007 (cit. on p. 10).

[30] J. Labaziewicz, Y. Ge, P. Antohi, D. Leibrandt, K. R. Brown, and I. L. Chuang. 'Suppression of Heating Rates in Cryogenic Surface-Electrode Ion Traps.' *Phys. Rev. Lett.* 100 (1 Jan. 2008), p. 013001. DOI: 10.1103/PhysRevLett.100.013001 (cit. on p. 10).

[31] F. Jelezko, I. Popa, A. Gruber, C. Tietz, J. Wrachtrup, A. Nizovtsev, and S. Kilin. 'Single spin states in a defect center resolved by optical spectroscopy.' *Applied Physics Letters* 81.12 (2002), pp. 2160–2162. DOI: 10.1063/1.1507838 (cit. on p. 10).

[32] F. Jelezko, T. Gaebel, I. Popa, A. Gruber, and J. Wrachtrup. 'Observation of Coherent Oscillations in a Single Electron Spin.' *Phys. Rev. Lett.* 92 (7 Feb. 2004), p. 076401. DOI: 10.1103/PhysRevLett.92.076401 (cit. on p. 10).

[33] B. E. Kane. 'A silicon-based nuclear spin quantum computer.' *Nature* 393.6681 (May 1998), pp. 133–137. DOI: 10.1038/30156 (cit. on p. 10).

[34] K. Saeedi, S. Simmons, J. Z. Salvail, P. Dluhy, H. Riemann, N. V. Abrosimov, P. Becker, H.-J. Pohl, J. J. L. Morton, and M. L. W. Thewalt. 'Room-Temperature Quantum Bit Storage Exceeding 39 Minutes Using Ionized Donors in Silicon-28.' *Science* 342.6160 (2013), pp. 830–833. DOI: 10.1126/science.1239584 (cit. on pp. 10, 39).

[35] F. Jelezko, T. Gaebel, I. Popa, M. Domhan, A. Gruber, and J. Wrachtrup. 'Observation of Coherent Oscillation of a Single Nuclear Spin and Realization of a Two-Qubit Conditional Quantum Gate.' *Phys. Rev. Lett.* 93 (13 Sept. 2004), p. 130501. DOI: 10.1103/PhysRevLett.93.130501 (cit. on p. 10).

[36] K. M. Itoh and H. Watanabe. 'Isotope engineering of silicon and diamond for quantum computing and sensing applications.' *MRS Communications* 4 (04 2014), pp. 143–157. DOI: 10.1557/mrc.2014.32 (cit. on pp. 10, 39).

[37] G. Davies and M. F. Hamer. 'Optical Studies of the 1.945 eV Vibronic Band in Diamond.' *Proceedings of the Royal Society of London A: Mathematical, Physical and Engineering Sciences* 348.1653 (1976), pp. 285–298. DOI: 10.1098/rspa.1976.0039 (cit. on pp. 10, 123).

[38] G. Davies. 'The Jahn-Teller effect and vibronic coupling at deep levels in diamond.' *Reports on Progress in Physics* 44 (July 1981), pp. 787–830. DOI: 10.1088/0034-4885/44/7/003 (cit. on pp. 10, 123).

[39] F. Jelezko, C. Tietz, A. Gruber, I. Popa, A. Nizovtsev, S. Kilin, and J. Wrachtrup. 'Spectroscopy of Single N-V Centers in Diamond.' *Single Molecules* 2.4 (2001), pp. 255–260. DOI: 10.1002/1438-5171(200112)2:4<255::AID-SIMO255>3.0.CO;2-D (cit. on pp. 10, 12, 123).

[40] J. C. Lee, D. O. Bracher, S. Cui, K. Ohno, C. A. McLellan, X. Zhang, P. Andrich, B. Alemán, K. J. Russell, A. P. Magyar, I. Aharonovich, A. Bleszynski Jayich, D. Awschalom, and E. L. Hu. 'Deterministic coupling of delta-doped nitrogen vacancy centers to a nanobeam photonic crystal cavity.' *Applied Physics Letters* 105.26, 261101 (2014), pp. -. DOI: 10.1063/1.4904909 (cit. on p. 10).

[41] Y. Chu, N. de Leon, B. Shields, B. Hausmann, R. Evans, E. Togan, M. J. Burek, M. Markham, A. Stacey, A. Zibrov, A. Yacoby, D. Twitchen, M. Loncar, H. Park, P. Maletinsky, and M. Lukin. 'Coherent Optical Transitions in Implanted Nitrogen Vacancy Centers.' *Nano Letters* 14.4 (2014), pp. 1982–1986. DOI: 10.1021/nl404836p (cit. on p. 10).

[42] L. M. K. Vandersypen and I. L. Chuang. 'NMR techniques for quantum control and computation.' *Rev. Mod. Phys.* 76 (4 Jan. 2005), pp. 1037–1069. DOI: 10.1103/RevModPhys.76.1037 (cit. on p. 11).

[43]   N. C. Menicucci and C. M. Caves. 'Local Realistic Model for the Dynamics of Bulk-Ensemble NMR Information Processing.' *Phys. Rev. Lett.* 88 (16 Apr. 2002), p. 167901. DOI: `10.1103/PhysRevLett.88.167901` (cit. on p. 11).

[44]   W. S. Warren. 'The Usefulness of NMR Quantum Computing.' *Science* 277.5332 (1997), pp. 1688–1690. DOI: `10.1126/science.277.5332.1688` (cit. on p. 11).

[45]   B. Josephson. 'Possible new effects in superconductive tunnelling.' *Physics Letters* 1.7 (1962), pp. 251–253. DOI: `10.1016/0031-9163(62)91369-0` (cit. on p. 11).

[46]   P. W. Anderson and J. M. Rowell. 'Probable Observation of the Josephson Superconducting Tunneling Effect.' *Phys. Rev. Lett.* 10 (6 Mar. 1963), pp. 230–232. DOI: `10.1103/PhysRevLett.10.230` (cit. on p. 11).

[47]   Y. Nakamura, Y. A. Pashkin, and J. S. Tsai. 'Coherent control of macroscopic quantum states in a single-Cooper-pair box.' *Nature* 398.6730 (Apr. 1999), pp. 786–788. DOI: `10.1038/19718` (cit. on p. 11).

[48]   J. M. Martinis, S. Nam, J. Aumentado, and C. Urbina. 'Rabi Oscillations in a Large Josephson-Junction Qubit.' *Phys. Rev. Lett.* 89 (11 Aug. 2002), p. 117901. DOI: `10.1103/PhysRevLett.89.117901` (cit. on pp. 11, 12).

[49]   I. Chiorescu, Y. Nakamura, C. J. P. M. Harmans, and J. E. Mooij. 'Coherent Quantum Dynamics of a Superconducting Flux Qubit.' *Science* 299.5614 (2003), pp. 1869–1871. DOI: `10.1126/science.1081045` (cit. on p. 11).

[50]   J. A. Schreier, A. A. Houck, J. Koch, D. I. Schuster, B. R. Johnson, J. M. Chow, J. M. Gambetta, J. Majer, L. Frunzio, M. H. Devoret, S. M. Girvin, and R. J. Schoelkopf. 'Suppressing charge noise decoherence in superconducting charge qubits.' *Phys. Rev. B* 77 (18 May 2008), p. 180502. DOI: `10.1103/PhysRevB.77.180502` (cit. on p. 11).

[51]   C. Rigetti, J. M. Gambetta, S. Poletto, B. L. T. Plourde, J. M. Chow, A. D. Córcoles, J. A. Smolin, S. T. Merkel, J. R. Rozen, G. A. Keefe, M. B. Rothwell, M. B. Ketchen, and M. Steffen. 'Superconducting qubit in a waveguide cavity with a coher-

ence time approaching 0.1 ms.' *Phys. Rev. B* 86 (10 Sept. 2012), p. 100506. DOI: 10.1103/PhysRevB.86.100506 (cit. on p. 12).

[52] M. H. Devoret and R. J. Schoelkopf. 'Superconducting Circuits for Quantum Information: An Outlook.' *Science* 339.6124 (2013), pp. 1169–1174. DOI: 10.1126/science.1231930 (cit. on p. 12).

[53] S. Fafard, H. C. Liu, Z. R. Wasilewski, J. P. McCaffrey, M. Spanner, S. Raymond, C. N. Allen, K. Hinzer, J. Lapointe, C. Struby, M. Gao, P. Hawrylak, C. Gould, A. Sachrajda, and P. Zawadzki. 'Quantum dot devices.' In: vol. 4078. 2000, pp. 100–114. DOI: 10.1117/12.392130 (cit. on p. 12).

[54] A. Zrenner, L. V. Butov, M. Hagn, G. Abstreiter, G. Böhm, and G. Weimann. 'Quantum dots formed by interface fluctuations in AlAs/GaAs coupled quantum well structures.' *Phys. Rev. Lett.* 72 (21 May 1994), pp. 3382–3385. DOI: 10.1103/PhysRevLett.72.3382 (cit. on p. 12).

[55] N. Akopian, G. Patriarche, L. Liu, J.-C. Harmand, and V. Zwiller. 'Crystal Phase Quantum Dots.' *Nano Letters* 10.4 (2010), pp. 1198–1201. DOI: 10.1021/nl903534n (cit. on p. 12).

[56] G. H. Carey, A. L. Abdelhady, Z. Ning, S. M. Thon, O. M. Bakr, and E. H. Sargent. 'Colloidal Quantum Dot Solar Cells.' *Chemical Reviews* 115.23 (2015), pp. 12732–12763. DOI: 10.1021/acs.chemrev.5b00063 (cit. on p. 12).

[57] R. Hanson, L. P. Kouwenhoven, J. R. Petta, S. Tarucha, and L. M. K. Vandersypen. 'Spins in few-electron quantum dots.' *Rev. Mod. Phys.* 79 (4 Oct. 2007), pp. 1217–1265. DOI: 10.1103/RevModPhys.79.1217 (cit. on p. 12).

[58] S. Nadj-Perge, S. M. Frolov, E. P. A. M. Bakkers, and L. P. Kouwenhoven. 'Spin-orbit qubit in a semiconductor nanowire.' *Nature* 468.7327 (Dec. 2010), pp. 1084–1087. DOI: 10.1038/nature09682 (cit. on p. 12).

[59] W. Heller, U. Bockelmann, and G. Abstreiter. 'Electric-field effects on excitons in quantum dots.' *Phys. Rev. B* 57 (11 Mar. 1998), pp. 6270–6273. DOI: 10.1103/PhysRevB.57.6270 (cit. on p. 12).

[60]   A. Zrenner, E. Beham, S. Stufler, F. Findeis, M. Bichler, and G. Abstreiter. 'Coherent properties of a two-level system based on a quantum-dot photodiode.' *Nature* 418.6898 (Aug. 2002), pp. 612–614. DOI: `10.1038/nature00912` (cit. on pp. 12, 51, 81).

[61]   T. Yoshie, A. Scherer, J. Hendrickson, G. Khitrova, H. M. Gibbs, G. Rupper, C. Ell, O. B. Shchekin, and D. G. Deppe. 'Vacuum Rabi splitting with a single quantum dot in a photonic crystal nanocavity.' *Nature* 432.7014 (Nov. 2004), pp. 200–203. DOI: `10.1038/nature03119` (cit. on pp. 12, 19).

[62]   T. Lund-Hansen, S. Stobbe, B. Julsgaard, H. Thyrrestrup, T. Sünner, M. Kamp, A. Forchel, and P. Lodahl. 'Experimental Realization of Highly Efficient Broadband Coupling of Single Quantum Dots to a Photonic Crystal Waveguide.' *Phys. Rev. Lett.* 101 (11 Sept. 2008), p. 113903. DOI: `10.1103/PhysRevLett.101.113903` (cit. on pp. 12, 44).

[63]   A. J. Ramsay, A. V. Gopal, E. M. Gauger, A. Nazir, B. W. Lovett, A. M. Fox, and M. S. Skolnick. 'Damping of Exciton Rabi Rotations by Acoustic Phonons in Optically Excited InGaAs/GaAs Quantum Dots.' *Phys. Rev. Lett.* 104 (1 Jan. 2010), p. 017402. DOI: `10.1103/PhysRevLett.104.017402` (cit. on pp. 12, 38, 41, 50, 51, 87, 124, 140).

[64]   A. J. Ramsay, T. M. Godden, S. J. Boyle, E. M. Gauger, A. Nazir, B. W. Lovett, A. M. Fox, and M. S. Skolnick. 'Phonon-Induced Rabi-Frequency Renormalization of Optically Driven Single InGaAs/GaAs Quantum Dots.' *Phys. Rev. Lett.* 105 (17 Oct. 2010), p. 177402. DOI: `10.1103/PhysRevLett.105.177402` (cit. on pp. 12, 38, 41, 50, 51, 87, 124, 131, 140, 149).

[65]   B. Urbaszek, E. J. McGhee, M. Krüger, R. J. Warburton, K. Karrai, T. Amand, B. D. Gerardot, P. M. Petroff, and J. M. Garcia. 'Temperature-dependent linewidth of charged excitons in semiconductor quantum dots: Strongly broadened ground state transitions due to acoustic phonon scattering.' *Phys. Rev. B* 69 (3 Jan. 2004), p. 035304. DOI: `10.1103/PhysRevB.69.035304` (cit. on p. 12).

[66]   E. A. Chekhovich, M. N. Makhonin, A. I. Tartakovskii, A. Yacoby, H. Bluhm, K. C. Nowack, and L. M. K. Vandersypen. 'Nu-

clear spin effects in semiconductor quantum dots.' *Nat Mater*
12.6 (June 2013), pp. 494–504. DOI: 10.1038/nmat3652 (cit. on
pp. 13, 39).

[67] W. B. Gao, P. Fallahi, E. Togan, J. Miguel-Sanchez, and A.
Imamoglu. 'Observation of entanglement between a quantum
dot spin and a single photon.' *Nature* 491.7424 (Nov. 2012),
pp. 426–430. DOI: 10.1038/nature11573 (cit. on pp. 13, 55, 93).

[68] K. De Greve, L. Yu, P. L. McMahon, J. S. Pelc, C. M. Natara-
jan, N. Y. Kim, E. Abe, S. Maier, C. Schneider, M. Kamp,
S. Hofling, R. H. Hadfield, A. Forchel, M. M. Fejer, and
Y. Yamamoto. 'Quantum-dot spin-photon entanglement via
frequency downconversion to telecom wavelength.' *Nature*
491.7424 (Nov. 2012), pp. 421–425. DOI: 10.1038/nature11577
(cit. on pp. 13, 55, 93).

[69] J. R. Schaibley, A. P. Burgers, G. A. McCracken, L.-M. Duan,
P. R. Berman, D. G. Steel, A. S. Bracker, D. Gammon, and L. J.
Sham. 'Demonstration of Quantum Entanglement between a
Single Electron Spin Confined to an InAs Quantum Dot and
a Photon.' *Phys. Rev. Lett.* 110 (16 Apr. 2013), p. 167401. DOI:
10.1103/PhysRevLett.110.167401 (cit. on pp. 13, 55).

[70] H. M. Meyer, R. Stockill, M. Steiner, C. Le Gall, C. Matthiesen,
E. Clarke, A. Ludwig, J. Reichel, M. Atatüre, and M. Köhl. 'Di-
rect Photonic Coupling of a Semiconductor Quantum Dot and
a Trapped Ion.' *Phys. Rev. Lett.* 114 (12 Mar. 2015), p. 123001.
DOI: 10.1103/PhysRevLett.114.123001 (cit. on p. 13).

[71] Y. Kubo, C. Grezes, A. Dewes, T. Umeda, J. Isoya, H. Sumiya,
N. Morishita, H. Abe, S. Onoda, T. Ohshima, V. Jacques, A.
Dréau, J.-F. Roch, I. Diniz, A. Auffeves, D. Vion, D. Esteve, and
P. Bertet. 'Hybrid Quantum Circuit with a Superconducting
Qubit Coupled to a Spin Ensemble.' *Phys. Rev. Lett.* 107 (22
Nov. 2011), p. 220501. DOI: 10.1103/PhysRevLett.107.220501
(cit. on p. 13).

[72] M. Reed, J. Randall, and R. Aggarwal. 'Observation of discrete
electronic states in a zero-dimensional semiconductor nanos-
tructure.' *Physical Review Letters* 60.6 (1988), pp. 535–537. DOI:
10.1103/PhysRevLett.60.535 (cit. on p. 18).

[73]   A. Ekimov and A. Onushchenko. 'Quantum size effect in three-dimensional microscopic semiconductor crystals.' *Journal of Experimental and Theoretical Physics Letters* 34 (1981), p. 345 (cit. on p. 18).

[74]   C. Matthiesen, A. N. Vamivakas, and M. Atatüre. 'Subnatural Linewidth Single Photons from a Quantum Dot.' *Phys. Rev. Lett.* 108 (9 Feb. 2012), p. 093602. DOI: `10.1103/PhysRevLett.108.093602` (cit. on p. 18).

[75]   D. Leonard, M. Krishnamurthy, C. M. Reaves, S. P. Denbaars, and P. M. Petroff. 'Direct formation of quantum-sized dots from uniform coherent islands of InGaAs on GaAs surfaces.' *Applied Physics Letters* 63.23 (1993), p. 3203. DOI: `10.1063/1.110199` (cit. on p. 18).

[76]   D. Leonard, M. Krishnamurthy, S. Fafard, J. L. Merz, and P. M. Petroff. 'Molecular beam epitaxy growth of quantum dots from strained coherent uniform islands of InGaAs on GaAs.' *Journal of Vacuum Science Technology B: Microelectronics and Nanometer Structures* 12.2 (Mar. 1994), pp. 1063–1066. DOI: `10.1116/1.587088` (cit. on p. 18).

[77]   D. Leonard, S. Fafard, K. Pond, Y. H. Zhang, J. L. Merz, and P. M. Petroff. 'Structural and optical properties of self-assembled InGaAs quantum dots.' *Journal of Vacuum Science Technology B: Microelectronics and Nanometer Structures* 12.4 (July 1994), pp. 2516–2520. DOI: `10.1116/1.587794` (cit. on p. 18).

[78]   J. M. Moison, F. Houzay, F. Barthe, L. Leprince, E. André, and O. Vatel. 'Self-organized growth of regular nanometer-scale InAs dots on GaAs.' *Applied Physics Letters* 64.2 (1994), pp. 196–198. DOI: `http://dx.doi.org/10.1063/1.111502` (cit. on pp. 18, 19, 23).

[79]   P. Petroff. 'Single Quantum Dots: Fundamentals, Applications and New Concepts.' In: ed. by P. Michler. Topics in Applied Physics 2. Springer, 2004. Chap. Epitaxial Growth and Electronic Structure of Self-Assembled Quantum Dots, pp. 1–24 (cit. on pp. 18, 20, 24, 26).

[80] P. Michler. *Single semiconductor quantum dots:* DE: Springer Verlag, June 2009, pp. – (cit. on p. 18).

[81] I. N. Stranski and L. Krastanov. *Abhandlungen der Mathematisch-Naturwissenschaftlichen Klasse IIb. Akademie der Wissenschaften Wien* 146 (1938), pp. 797–810 (cit. on p. 19).

[82] E. Bauer. 'Phänomenologische Theorie der Kristallabscheidung an Oberflächen. I.' *Zeitschrift fur Kristallographie* 110 (Jan. 1958), pp. 372–394. DOI: 10.1524/zkri.1958.110.1-6.372 (cit. on p. 19).

[83] S. Franchi, G. Trevisi, L. Seravalli, and P. Frigeri. 'Quantum dot nanostructures and molecular beam epitaxy.' *Progress in Crystal Growth and Characterization of Materials* 47.23 (2003). Vapour Growth of Bulk Crystals and Epitaxy: Part I, pp. 166–195. DOI: 10.1016/j.pcrysgrow.2005.01.002 (cit. on p. 19).

[84] M. Grundmann, O. Stier, and D. Bimberg. 'InAs/GaAs pyramidal quantum dots: Strain distribution, optical phonons, and electronic structure.' *Phys. Rev. B* 52 (16 Oct. 1995), pp. 11969–11981. DOI: 10.1103/PhysRevB.52.11969 (cit. on pp. 19, 23).

[85] J. M. Garcia, G. Medeiros-Ribeiro, K. Schmidt, T. Ngo, J. L. Feng, A. Lorke, J. Kotthaus, and P. M. Petroff. 'Intermixing and shape changes during the formation of InAs self-assembled quantum dots.' *Applied Physics Letters* 71.14 (1997), pp. 2014–2016. DOI: 10.1063/1.119772 (cit. on p. 19).

[86] K. Hennessy, A. Badolato, M. Winger, D. Gerace, M. Atature, S. Gulde, S. Falt, E. L. Hu, and A. Imamoglu. 'Quantum nature of a strongly coupled single quantum dot-cavity system.' *Nature* 445.7130 (Feb. 2007), pp. 896–899. DOI: 10.1038/nature05586 (cit. on pp. 20, 41, 42, 123, 159).

[87] M. Winger, A. Badolato, K. J. Hennessy, E. L. Hu, and A. İmamoğlu. 'Quantum Dot Spectroscopy Using Cavity Quantum Electrodynamics.' *Phys. Rev. Lett.* 101 (22 Nov. 2008), p. 226808. DOI: 10.1103/PhysRevLett.101.226808 (cit. on p. 20).

[88] A. Kaganskiy, M. Gschrey, A. Schlehahn, R. Schmidt, J.-H. Schulze, T. Heindel, A. Strittmatter, S. Rodt, and S. Reitzenstein. 'Advanced in-situ electron-beam lithography for deter-

ministic nanophotonic device processing.' *Review of Scientific Instruments* 86.7, 073903 (2015). DOI: 10.1063/1.4926995 (cit. on p. 20).

[89] K. H. Lee, A. M. Green, R. A. Taylor, D. N. Sharp, J. Scrimgeour, O. M. Roche, J. H. Na, A. F. Jarjour, A. J. Turberfield, F. S. F. Brossard, D. A. Williams, and G. A. D. Briggs. 'Registration of single quantum dots using cryogenic laser photolithography.' *Applied Physics Letters* 88.19, 193106 (2006), p. 193106. DOI: 10.1063/1.2202193 (cit. on p. 20).

[90] S. M. Thon, M. T. Rakher, H. Kim, J. Gudat, W. T. M. Irvine, P. M. Petroff, and D. Bouwmeester. 'Strong coupling through optical positioning of a quantum dot in a photonic crystal cavity.' *Applied Physics Letters* 94.11, 111115 (2009), p. 111115. DOI: 10.1063/1.3103885 (cit. on pp. 20, 48).

[91] N. Walsey. 'Nano-photonics in III-V semiconductors for integrated quantum optical circuits.' PhD thesis. University of Sheffield, 2012 (cit. on p. 20).

[92] A. Dousse, L. Lanco, J. Suffczyński, E. Semenova, A. Miard, A. Lemaître, I. Sagnes, C. Roblin, J. Bloch, and P. Senellart. 'Controlled Light-Matter Coupling for a Single Quantum Dot Embedded in a Pillar Microcavity Using Far-Field Optical Lithography.' *Phys. Rev. Lett.* 101 (26 Dec. 2008), p. 267404. DOI: 10.1103/PhysRevLett.101.267404 (cit. on p. 20).

[93] H. Lee, J. A. Johnson, J. S. Speck, and Petroff. 'Controlled ordering and positioning of InAs self-assembled quantum dots.' *Journal of Vacuum Science & Technology B* 18 (2000), p. 2193 (cit. on p. 20).

[94] H. Lee, J. A. Johnson, M. Y. He, J. S. Speck, and P. M. Petroff. 'Strain-engineered self-assembled semiconductor quantum dot lattices.' *Applied Physics Letters* 78.1 (2001), pp. 105–107. DOI: 10.1063/1.1336554 (cit. on p. 20).

[95] J.-Y. Marzin, J.-M. Gérard, A. Izraël, D. Barrier, and G. Bastard. 'Photoluminescence of Single InAs Quantum Dots Obtained by Self-Organized Growth on GaAs.' *Phys. Rev. Lett.* 73 (5 Aug. 1994), pp. 716–719. DOI: 10.1103/PhysRevLett.73.716 (cit. on p. 20).

[96]   T. Ishikawa, S. Kohmoto, S. Nishikawa, T. Nishimura, and K. Asakawa. 'Site control of InAs quantum dots on GaAs surfaces patterned by in situ electron-beam lithography.' *Journal of Vacuum Science & Technology B: Microelectronics and Nanometer Structures* 18.6 (2000), pp. 2635–2639. DOI: 10.1116/1.1322039 (cit. on p. 20).

[97]   A. Strittmatter, A. Holzbecher, A. Schliwa, J.-H. Schulze, D. Quandt, T. D. Germann, A. Dreismann, O. Hitzemann, E. Stock, I. A. Ostapenko, S. Rodt, W. Unrau, U. W. Pohl, A. Hoffmann, D. Bimberg, and V. Haisler. 'Site-controlled quantum dot growth on buried oxide stressor layers.' *physica status solidi (a)* 209.12 (2012), pp. 2411–2420. DOI: 10.1002/pssa.201228407 (cit. on p. 20).

[98]   M. H. Baier, S. Watanabe, E. Pelucchi, and E. Kapon. 'High uniformity of site-controlled pyramidal quantum dots grown on prepatterned substrates.' *Applied Physics Letters* 84.11 (2004), pp. 1943–1945. DOI: 10.1063/1.1682677 (cit. on p. 21).

[99]   A. Mohan, P. Gallo, M. Felici, B. Dwir, A. Rudra, J. Faist, and E. Kapon. 'Record-Low Inhomogeneous Broadening of Site-Controlled Quantum Dots for Nanophotonics.' *Small* 6.12 (2010), pp. 1268–1272. DOI: 10.1002/smll.201000341 (cit. on p. 21).

[100]   G. Juska, V. Dimastrodonato, L. O. Mereni, A. Gocalinska, and E. Pelucchi. 'Towards quantum-dot arrays of entangled photon emitters.' *Nature Photonics* (2013), pp. -. DOI: 10.1038/nphoton.2013.128 (cit. on pp. 21, 27, 116).

[101]   Y. Watanabe, H. Hibino, S. Bhunia, K. Tateno, and T. Sekiguchi. 'Site-controlled InP nanowires grown on patterned Si substrates.' *Physica E: Low-dimensional Systems and Nanostructures* 24.1-2 (2004). <ce:title>Proceedings of the International Symposium on Functional Semiconductor Nanostructures 2003</ce:title>, pp. 133–137. DOI: 10.1016/j.physe.2004.04.002 (cit. on p. 21).

[102]   B. Bauer, A. Rudolph, M. Soda, A. F. i Morral, J. Zweck, D. Schuh, and E. Reiger. 'Position controlled self-catalyzed growth of GaAs nanowires by molecular beam epitaxy.' *Nan-*

otechnology 21.43 (2010), p. 435601. DOI: `10.1088/0957-4484/21/43/435601` (cit. on p. 21).

[103]   A. L. Roest, M. A. Verheijen, O. Wunnicke, S. Serafin, H. Wondergem, and E. P. A. M. Bakkers. 'Position-controlled epitaxial III-V nanowires on silicon.' *Nanotechnology* 17.11 (2006), S271. DOI: `10.1088/0957-4484/17/11/S07` (cit. on p. 21).

[104]   S. G. Ghalamestani, S. Johansson, B. M. Borg, E. Lind, K. A. Dick, and L.-E. Wernersson. 'Uniform and position-controlled InAs nanowires on 2" Si substrates for transistor applications.' *Nanotechnology* 23.1 (2012), p. 015302. DOI: `10.1088/0957-4484/23/1/015302` (cit. on p. 21).

[105]   M. T. Björk, A. Fuhrer, A. E. Hansen, M. W. Larsson, L. E. Fröberg, and L. Samuelson. 'Tunable effective g-factor in InAs nanowire quantum dots.' *Phys. Rev. B* 72 (20 Nov. 2005), p. 201307. DOI: `10.1103/PhysRevB.72.201307` (cit. on p. 21).

[106]   C. Fasth, A. Fuhrer, L. Samuelson, V. N. Golovach, and D. Loss. 'Direct Measurement of the Spin-Orbit Interaction in a Two-Electron InAs Nanowire Quantum Dot.' *Phys. Rev. Lett.* 98 (26 June 2007), p. 266801. DOI: `10.1103/PhysRevLett.98.266801` (cit. on p. 21).

[107]   M. N. Makhonin, A. P. Foster, A. B. Krysa, P. W. Fry, D. G. Davies, T. Grange, T. Walther, M. S. Skolnick, and L. R. Wilson. 'Homogeneous Array of Nanowire-Embedded Quantum Light Emitters.' *Nano Letters* 13.3 (2013), pp. 861–865. DOI: `10.1021/nl303075q` (cit. on p. 21).

[108]   A. Fox. *Optical Properties of Solids*. Oxford master series in condensed matter physics. Oxford University Press, 2001 (cit. on p. 21).

[109]   E. A. Chekhovich, M. M. Glazov, A. B. Krysa, M. Hopkinson, P. Senellart, A. Lemaitre, M. S. Skolnick, and A. I. Tartakovskii. 'Element-sensitive measurement of the hole-nuclear spin interaction in quantum dots.' *Nat Phys* 9.2 (Feb. 2013), pp. 74–78. DOI: `10.1038/nphys2514` (cit. on pp. 21, 42).

[110]   J. Berezovsky. 'Optical Control and Detection of Spin Coherence in Semiconductor Nanostructures.' In: University of Cal-

ifornia, Santa Barbara, 2007. Chap. Background, pp. 11–44 (cit. on p. 22).

[111]   M. Dyakonov. 'Spin Physics in Semiconductors.' In: Springer Series in Solid-State Sciences. Springer, 2008. Chap. Basics of Semiconductor and Spin Physics, pp. 1–28 (cit. on p. 22).

[112]   S. Economou and T. Reinecke. 'Optical Generation and Control of Quantum Coherence in Semiconductor Nanostructures.' In: ed. by G. Slavcheva and P. Roussignol. NanoScience and Technology. Springer Berlin Heidelberg, 2010. Chap. Optically Induced Spin Rotations in Quantum Dots, pp. 63–84 (cit. on p. 23).

[113]   P. Hawrylak and M. Korkusinski. 'Single Quantum Dots: Fundamentals, Applications and New Concepts.' In: ed. by P. Michler. Topics in Applied Physics. Springer, 2004. Chap. Electronic Properties of Self-Assembled Quantum Dots, pp. 25–91 (cit. on pp. 23, 25).

[114]   F. Rossi. 'Semiconductor Macroatoms: Basics Physics and Quantum-Device Applications.' In: Imperial College Press, 2005. Chap. Fundamentals of Zero-Dimensional Nanostructures, pp. 1–41 (cit. on p. 23).

[115]   M. A. Cusack, P. R. Briddon, and M. Jaros. 'Electronic structure of InAs/GaAs self-assembled quantum dots.' *Phys. Rev. B* 54 (4 July 1996), R2300–R2303. DOI: 10.1103/PhysRevB.54.R2300 (cit. on p. 23).

[116]   G. Bester, A. Zunger, X. Wu, and D. Vanderbilt. 'Effects of linear and nonlinear piezoelectricity on the electronic properties of InAs/GaAs quantum dots.' *Phys. Rev. B* 74 (8 Aug. 2006), p. 081305. DOI: 10.1103/PhysRevB.74.081305 (cit. on p. 23).

[117]   W. Que. 'Excitons in quantum dots with parabolic confinement.' *Phys. Rev. B* 45 (19 May 1992), pp. 11036–11041. DOI: 10.1103/PhysRevB.45.11036 (cit. on p. 23).

[118]   A. Wojs, P. Hawrylak, S. Fafard, and L. Jacak. 'Electronic structure and magneto-optics of self-assembled quantum dots.' *Phys. Rev. B* 54 (8 Aug. 1996), pp. 5604–5608. DOI: 10.1103/PhysRevB.54.5604 (cit. on p. 23).

[119]   S. Tarucha, D. G. Austing, T. Honda, R. J. van der Hage, and L. P. Kouwenhoven. 'Shell Filling and Spin Effects in a Few Electron Quantum Dot.' *Phys. Rev. Lett.* 77 (17 Oct. 1996), pp. 3613–3616. DOI: 10.1103/PhysRevLett.77.3613 (cit. on p. 23).

[120]   W. Porod and D. K. Ferry. 'Modification of the virtual-crystal approximation for ternary III-V compounds.' *Phys. Rev. B* 27 (4 Feb. 1983), pp. 2587–2589. DOI: 10.1103/PhysRevB.27.2587 (cit. on p. 24).

[121]   P. Hawrylak, G. A. Narvaez, M. Bayer, and A. Forchel. 'Excitonic Absorption in a Quantum Dot.' *Phys. Rev. Lett.* 85 (2 July 2000), pp. 389–392. DOI: 10.1103/PhysRevLett.85.389 (cit. on p. 25).

[122]   P. A. Dalgarno, J. M. Smith, J. McFarlane, B. D. Gerardot, K. Karrai, A. Badolato, P. M. Petroff, and R. J. Warburton. 'Coulomb interactions in single charged self-assembled quantum dots: Radiative lifetime and recombination energy.' *Phys. Rev. B* 77 (24 June 2008), p. 245311. DOI: 10.1103/PhysRevB.77.245311 (cit. on pp. 25, 38, 81, 96, 135, 154, 169).

[123]   Y. H. Huo, B. J. Witek, S. Kumar, J. R. Cardenas, J. X. Zhang, N. Akopian, R. Singh, E. Zallo, R. Grifone, D. Kriegner, R. Trotta, F. Ding, J. Stangl, V. Zwiller, G. Bester, A. Rastelli, and O. G. Schmidt. 'A light-hole exciton in a quantum dot.' *Nat Phys* 10.1 (Jan. 2014), pp. 46–51. DOI: 10.1038/nphys2799 (cit. on p. 25).

[124]   T. Belhadj, T. Amand, A. Kunold, C.-M. Simon, T. Kuroda, M. Abbarchi, T. Mano, K. Sakoda, S. Kunz, X. Marie, and B. Urbaszek. 'Impact of heavy hole-light hole coupling on optical selection rules in GaAs quantum dots.' *Applied Physics Letters* 97.5, 051111 (2010). DOI: http://dx.doi.org/10.1063/1.3473824 (cit. on p. 25).

[125]   R. Feynman, R. Leighton, and M. Sands. 'The Feynman Lectures on Physics.' In: vol. 3. The Feynman Lectures on Physics 18. Addison-Wesley, 1963. Chap. Angular Momentum (cit. on p. 25).

[126]   D. Gammon, E. S. Snow, B. V. Shanabrook, D. S. Katzer, and D. Park. 'Fine Structure Splitting in the Optical Spectra of Single

GaAs Quantum Dots.' *Physical Review Letters* 76.16 (Apr. 1996), pp. 3005–3008. DOI: `10.1103/PhysRevLett.76.3005` (cit. on pp. 26, 93).

[127]   A. J. Ramsay, S. J. Boyle, R. S. Kolodka, J. B. B. Oliveira, J. Skiba-Szymanska, H. Y. Liu, M. Hopkinson, A. M. Fox, and M. S. Skolnick. 'Fast Optical Preparation, Control, and Readout of a Single Quantum Dot Spin.' *Phys. Rev. Lett.* 100 (19 May 2008), p. 197401. DOI: `10.1103/PhysRevLett.100.197401` (cit. on pp. 26, 29, 93).

[128]   R. Seguin, A. Schliwa, S. Rodt, K. Pötschke, U. W. Pohl, and D. Bimberg. 'Size-Dependent Fine-Structure Splitting in Self-Organized InAs/GaAs Quantum Dots.' *Phys. Rev. Lett.* 95 (25 Dec. 2005), p. 257402. DOI: `10.1103/PhysRevLett.95.257402` (cit. on pp. 27, 93).

[129]   R. M. Stevenson, R. J. Young, P. Atkinson, K. Cooper, D. a. Ritchie, and a. J. Shields. 'A semiconductor source of triggered entangled photon pairs.' *Nature* 439.7073 (Jan. 2006), pp. 179–82. DOI: `10.1038/nature04446` (cit. on pp. 27, 28, 34, 56, 116, 121).

[130]   N. Akopian, N. H. Lindner, E. Poem, Y. Berlatzky, J. Avron, D. Gershoni, B. D. Gerardot, and P. M. Petroff. 'Entangled photon pairs from semiconductor quantum dots.' *Physical Review Letters* 96.13 (2006), p. 130501. DOI: `10.1103/PhysRevLett.96.130501` (cit. on pp. 27, 28, 56, 57, 116, 121).

[131]   A. J. Brash, L. M. P. P. Martins, F. Liu, J. H. Quilter, A. J. Ramsay, M. S. Skolnick, and A. M. Fox. 'High-fidelity initialization of long-lived quantum dot hole spin qubits by reduced fine-structure splitting.' *Phys. Rev. B* 92 (12 Sept. 2015), p. 121301. DOI: `10.1103/PhysRevB.92.121301` (cit. on pp. 27, 94).

[132]   J. Treu, C. Schneider, A. Huggenberger, T. Braun, S. Reitzenstein, S. Höfling, and M. Kamp. 'Substrate orientation dependent fine structure splitting of symmetric In(Ga)As/GaAs quantum dots.' *Applied Physics Letters* 101.2, 022102 (2012), pp. - . DOI: `http://dx.doi.org/10.1063/1.4733664` (cit. on pp. 27, 116).

[133] Y. H. Huo, A. Rastelli, and O. G. Schmidt. 'Ultra-small excitonic fine structure splitting in highly symmetric quantum dots on GaAs (001) substrate.' *Applied Physics Letters* 102.15, 152105 (2013), pp. -. DOI: http://dx.doi.org/10.1063/1.4802088 (cit. on pp. 27, 116).

[134] A. I. Tartakovskii, M. N. Makhonin, I. R. Sellers, J. Cahill, A. D. Andreev, D. M. Whittaker, J.-P. R. Wells, A. M. Fox, D. J. Mowbray, M. S. Skolnick, K. M. Groom, M. J. Steer, H. Y. Liu, and M. Hopkinson. 'Effect of thermal annealing and strain engineering on the fine structure of quantum dot excitons.' *Phys. Rev. B* 70 (19 Nov. 2004), p. 193303. DOI: 10.1103/PhysRevB.70.193303 (cit. on p. 27).

[135] W. Langbein, P. Borri, U. Woggon, V. Stavarache, D. Reuter, and A. D. Wieck. 'Control of fine-structure splitting and biexciton binding in In$_x$Ga$_{1-x}$As quantum dots by annealing.' *Phys. Rev. B* 69 (16 Apr. 2004), p. 161301. DOI: 10.1103/PhysRevB.69.161301 (cit. on p. 27).

[136] R. J. Young, R. M. Stevenson, A. J. Shields, P. Atkinson, K. Cooper, D. A. Ritchie, K. M. Groom, A. I. Tartakovskii, and M. S. Skolnick. 'Inversion of exciton level splitting in quantum dots.' *Phys. Rev. B* 72 (11 Sept. 2005), p. 113305. DOI: 10.1103/PhysRevB.72.113305 (cit. on p. 27).

[137] D. J. P. Ellis, R. M. Stevenson, R. J. Young, A. J. Shields, P. Atkinson, and D. A. Ritchie. 'Control of fine-structure splitting of individual InAs quantum dots by rapid thermal annealing.' *Applied Physics Letters* 90.1, 011907 (2007). DOI: http://dx.doi.org/10.1063/1.2430489 (cit. on p. 27).

[138] S. Seidl, M. Kroner, A. Högele, K. Karrai, R. J. Warburton, A. Badolato, and P. M. Petroff. 'Effect of uniaxial stress on excitons in a self-assembled quantum dot.' *Applied Physics Letters* 88.20, 203113 (2006), pp. -. DOI: http://dx.doi.org/10.1063/1.2204843 (cit. on pp. 27, 116, 121).

[139] R. Trotta, E. Zallo, C. Ortix, P. Atkinson, J. D. Plumhof, J. van den Brink, A. Rastelli, and O. G. Schmidt. 'Universal Recovery of the Energy-Level Degeneracy of Bright Excitons in InGaAs Quantum Dots without a Structure Symmetry.' *Phys. Rev. Lett.*

109 (14 Oct. 2012), p. 147401. DOI: `10.1103/PhysRevLett.109.147401` (cit. on pp. 27, 57, 116, 121, 122).

[140] R. M. Stevenson, R. J. Young, P. See, D. G. Gevaux, K. Cooper, P. Atkinson, I. Farrer, D. A. Ritchie, and A. J. Shields. 'Magnetic-field-induced reduction of the exciton polarization splitting in InAs quantum dots.' *Phys. Rev. B* 73 (3 Jan. 2006), p. 033306. DOI: `10.1103/PhysRevB.73.033306` (cit. on pp. 27, 116, 121).

[141] G. Jundt, L. Robledo, A. Högele, S. Fält, and A. Imamoglu. 'Observation of Dressed Excitonic States in a Single Quantum Dot.' *Phys. Rev. Lett.* 100 (17 Apr. 2008), p. 177401. DOI: `10.1103/PhysRevLett.100.177401` (cit. on pp. 27, 33, 49, 94, 116, 120, 121, 189).

[142] A. Muller, W. Fang, J. Lawall, and G. S. Solomon. 'Creating Polarization-Entangled Photon Pairs from a Semiconductor Quantum Dot Using the Optical Stark Effect.' *Phys. Rev. Lett.* 103 (21 Nov. 2009), p. 217402. DOI: `10.1103/PhysRevLett.103.217402` (cit. on pp. 27, 33, 57, 94, 116, 121).

[143] K. Kowalik, O. Krebs, A. Lemaître, S. Laurent, P. Senellart, P. Voisin, and J. A. Gaj. 'Influence of an in-plane electric field on exciton fine structure in InAs-GaAs self-assembled quantum dots.' *Applied Physics Letters* 86.4, 041907 (2005). DOI: `http://dx.doi.org/10.1063/1.1855409` (cit. on pp. 27, 31).

[144] K. Kowalik, O. Krebs, A. Lemaitre, B. Eble, A. Kudelski, P. Voisin, S. Seidl, and J. A. Gaj. 'Monitoring electrically driven cancellation of exciton fine structure in a semiconductor quantum dot by optical orientation.' *Applied Physics Letters* 91.18, 183104 (2007), pp. -. DOI: `http://dx.doi.org/10.1063/1.2805025` (cit. on pp. 27, 31, 116, 121).

[145] B. D. Gerardot, S. Seidl, P. A. Dalgarno, R. J. Warburton, D. Granados, J. M. Garcia, K. Kowalik, O. Krebs, K. Karrai, A. Badolato, and P. M. Petroff. 'Manipulating exciton fine structure in quantum dots with a lateral electric field.' *Applied Physics Letters* 90.4, 041101 (2007), pp. -. DOI: `http://dx.doi.org/10.1063/1.2431758` (cit. on pp. 27, 31, 116, 121).

[146] A. J. Bennett, M. A. Pooley, R. M. Stevenson, M. B. Ward, R. B. Patel, A. B. de la Giroday, N. Skold, I. Farrer, C. A. Nicoll, D. A.

Ritchie, and A. J. Shields. 'Electric-field-induced coherent coupling of the exciton states in a single quantum dot.' *Nat Phys* 6.12 (Dec. 2010), pp. 947–950. DOI: 10.1038/nphys1780 (cit. on pp. 27, 115, 116, 121).

[147] M. Ghali, K. Ohtani, Y. Ohno, and H. Ohno. 'Generation and control of polarization-entangled photons from GaAs island quantum dots by an electric field.' *Nat Commun* 3 (Feb. 2012), pp. 661–. DOI: 10.1038/ncomms1657 (cit. on pp. 27, 116, 121).

[148] O. Benson, C. Santori, M. Pelton, and Y. Yamamoto. 'Regulated and Entangled Photons from a Single Quantum Dot.' *Phys. Rev. Lett.* 84 (11 Mar. 2000), pp. 2513–2516. DOI: 10.1103/PhysRevLett.84.2513 (cit. on pp. 28, 56, 57, 116).

[149] M. Kroutvar, Y. Ducommun, D. Heiss, M. Bichler, D. Schuh, G. Abstreiter, and J. J. Finley. 'Optically programmable electron spin memory using semiconductor quantum dots.' *Nature* 432.7013 (Nov. 2004), pp. 81–84. DOI: 10.1038/nature03008 (cit. on pp. 29, 38, 93).

[150] R. J. Young, S. J. Dewhurst, R. M. Stevenson, P. Atkinson, A. J. Bennett, M. B. Ward, K. Cooper, D. A. Ritchie, and A. J. Shields. 'Single electron-spin memory with a semiconductor quantum dot.' *New Journal of Physics* 9.10 (2007), p. 365. DOI: 10.1088/1367-2630/9/10/365 (cit. on pp. 29, 93).

[151] D. Heiss, V. Jovanov, M. Bichler, G. Abstreiter, and J. J. Finley. 'Charge and spin readout scheme for single self-assembled quantum dots.' *Phys. Rev. B* 77 (23 June 2008), p. 235442. DOI: 10.1103/PhysRevB.77.235442 (cit. on pp. 29, 93).

[152] K. Müller, A. Bechtold, C. Ruppert, C. Hautmann, J. S. Wildmann, T. Kaldewey, M. Bichler, H. J. Krenner, G. Abstreiter, M. Betz, and J. J. Finley. 'High-fidelity optical preparation and coherent Larmor precession of a single hole in an (In,Ga)As quantum dot molecule.' *Phys. Rev. B* 85 (24 June 2012), p. 241306. DOI: 10.1103/PhysRevB.85.241306 (cit. on pp. 29, 93, 94, 111).

[153] R. J. Warburton, C. Schaflein, D. Haft, F. Bickel, A. Lorke, K. Karrai, J. M. Garcia, W. Schoenfeld, and P. M. Petroff. 'Optical emission from a charge-tunable quantum ring.' *Nature*

405.6789 (June 2000), pp. 926–929. DOI: 10.1038/35016030 (cit. on pp. 29, 31).

[154]   M. Baier, F. Findeis, A. Zrenner, M. Bichler, and G. Abstreiter. 'Optical spectroscopy of charged excitons in single quantum dot photodiodes.' *Phys. Rev. B* 64 (19 Oct. 2001), p. 195326. DOI: 10.1103/PhysRevB.64.195326 (cit. on pp. 29, 31, 83).

[155]   D. V. Regelman, E. Dekel, D. Gershoni, E. Ehrenfreund, A. J. Williamson, J. Shumway, A. Zunger, W. V. Schoenfeld, and P. M. Petroff. 'Optical spectroscopy of single quantum dots at tunable positive, neutral, and negative charge states.' *Phys. Rev. B* 64 (16 Sept. 2001), p. 165301. DOI: 10.1103/PhysRevB.64.165301 (cit. on pp. 29, 31).

[156]   M. Atatüre, J. Dreiser, A. Badolato, A. Högele, K. Karrai, and A. Imamoglu. 'Quantum-Dot Spin-State Preparation with Near-Unity Fidelity.' *Science* 312.5773 (2006), pp. 551–553. DOI: 10.1126/science.1126074 (cit. on pp. 29, 36, 93).

[157]   X. Xu, Y. Wu, B. Sun, Q. Huang, J. Cheng, D. G. Steel, A. S. Bracker, D. Gammon, C. Emary, and L. J. Sham. 'Fast Spin State Initialization in a Singly Charged InAs-GaAs Quantum Dot by Optical Cooling.' *Phys. Rev. Lett.* 99 (9 Aug. 2007), p. 097401. DOI: 10.1103/PhysRevLett.99.097401 (cit. on pp. 29, 93).

[158]   D. Brunner, B. D. Gerardot, P. A. Dalgarno, G. Wüst, K. Karrai, N. G. Stoltz, P. M. Petroff, and R. J. Warburton. 'A Coherent Single-Hole Spin in a Semiconductor.' *Science* 325.5936 (2009), pp. 70–72. DOI: 10.1126/science.1173684 (cit. on pp. 29, 38, 93, 94, 110, 113, 121).

[159]   S. Cortez, O. Krebs, S. Laurent, M. Senes, X. Marie, P. Voisin, R. Ferreira, G. Bastard, J.-M. Gérard, and T. Amand. 'Optically Driven Spin Memory in n-Doped InAs-GaAs Quantum Dots.' *Phys. Rev. Lett.* 89 (20 Oct. 2002), p. 207401. DOI: 10.1103/PhysRevLett.89.207401 (cit. on p. 29).

[160]   A. B. Henriques, A. Schwan, S. Varwig, A. D. B. Maia, A. A. Quivy, D. R. Yakovlev, and M. Bayer. 'Spin coherence generation in negatively charged self-assembled (In,Ga)As quantum dots by pumping excited trion states.' *Phys. Rev. B* 86 (11 Sept.

2012), p. 115333. DOI: 10.1103/PhysRevB.86.115333 (cit. on p. 29).

[161]   P. W. Fry, I. E. Itskevich, D. J. Mowbray, M. S. Skolnick, J. J. Finley, J. A. Barker, E. P. O'Reilly, L. R. Wilson, I. A. Larkin, P. A. Maksym, M. Hopkinson, M. Al-Khafaji, J. P. R. David, A. G. Cullis, G. Hill, and J. C. Clark. 'Inverted Electron-Hole Alignment in InAs-GaAs Self-Assembled Quantum Dots.' *Phys. Rev. Lett.* 84 (4 Jan. 2000), pp. 733–736. DOI: 10.1103/PhysRevLett.84.733 (cit. on pp. 30, 31).

[162]   J. J. Finley, M. Sabathil, P. Vogl, G. Abstreiter, R. Oulton, A. I. Tartakovskii, D. J. Mowbray, M. S. Skolnick, S. L. Liew, A. G. Cullis, and M. Hopkinson. 'Quantum-confined Stark shifts of charged exciton complexes in quantum dots.' *Phys. Rev. B* 70 (20 Nov. 2004), p. 201308. DOI: 10.1103/PhysRevB.70.201308 (cit. on pp. 30, 31, 115).

[163]   P. W. Fry, I. E. Itskevich, S. R. Parnell, J. J. Finley, L. R. Wilson, K. L. Schumacher, D. J. Mowbray, M. S. Skolnick, M. Al-Khafaji, A. G. Cullis, M. Hopkinson, J. C. Clark, and G. Hill. 'Photocurrent spectroscopy of InAs/GaAs self-assembled quantum dots.' *Phys. Rev. B* 62 (24 Dec. 2000), pp. 16784–16791. DOI: 10.1103/PhysRevB.62.16784 (cit. on pp. 31, 81, 106).

[164]   T. Unold, K. Mueller, C. Lienau, T. Elsaesser, and A. D. Wieck. 'Optical Stark Effect in a Quantum Dot: Ultrafast Control of Single Exciton Polarizations.' *Phys. Rev. Lett.* 92 (15 Apr. 2004), p. 157401. DOI: 10.1103/PhysRevLett.92.157401 (cit. on pp. 32, 52, 94, 116, 189).

[165]   S. N. Walck and T. L. Reinecke. 'Exciton diamagnetic shift in semiconductor nanostructures.' *Phys. Rev. B* 57 (15 Apr. 1998), pp. 9088–9096. DOI: 10.1103/PhysRevB.57.9088 (cit. on p. 34).

[166]   M. Bayer, S. N. Walck, T. L. Reinecke, and A. Forchel. 'Exciton binding energies and diamagnetic shifts in semiconductor quantum wires and quantum dots.' *Phys. Rev. B* 57 (11 Mar. 1998), pp. 6584–6591. DOI: 10.1103/PhysRevB.57.6584 (cit. on p. 34).

[167]   M. Bayer, A. Kuther, A. Forchel, A. Gorbunov, V. B. Timofeev, F. Schäfer, J. P. Reithmaier, T. L. Reinecke, and S. N. Walck.

'Electron and Hole *g* Factors and Exchange Interaction from Studies of the Exciton Fine Structure in $In_{0.60}Ga_{0.40}As$ Quantum Dots.' *Phys. Rev. Lett.* 82 (8 Feb. 1999), pp. 1748–1751. DOI: 10.1103/PhysRevLett.82.1748 (cit. on p. 34).

[168] A. Kuther, M. Bayer, A. Forchel, A. Gorbunov, V. B. Timofeev, F. Schäfer, and J. P. Reithmaier. 'Zeeman splitting of excitons and biexcitons in single $In_{0.60}Ga_{0.40}As$/GaAs self-assembled quantum dots.' *Phys. Rev. B* 58 (12 Sept. 1998), R7508–R7511. DOI: 10.1103/PhysRevB.58.R7508 (cit. on p. 34).

[169] M. Bayer, G. Ortner, O. Stern, A. Kuther, A. A. Gorbunov, A. Forchel, P. Hawrylak, S. Fafard, K. Hinzer, T. L. Reinecke, S. N. Walck, J. P. Reithmaier, F. Klopf, and F. Schäfer. 'Fine structure of neutral and charged excitons in self-assembled In(Ga)As/(Al)GaAs quantum dots.' *Phys. Rev. B* 65 (19 May 2002), p. 195315. DOI: 10.1103/PhysRevB.65.195315 (cit. on pp. 34, 36, 93, 109, 174).

[170] T. Nakaoka, T. Saito, J. Tatebayashi, and Y. Arakawa. 'Size, shape, and strain dependence of the *g* factor in self-assembled In(Ga)As quantum dots.' *Phys. Rev. B* 70 (23 Dec. 2004), p. 235337. DOI: 10.1103/PhysRevB.70.235337 (cit. on pp. 34, 109).

[171] A. Schwan, B.-M. Meiners, A. Greilich, D. R. Yakovlev, M. Bayer, A. D. B. Maia, A. A. Quivy, and A. B. Henriques. 'Anisotropy of electron and hole g-factors in (In,Ga)As quantum dots.' *Applied Physics Letters* 99.22, 221914 (2011). DOI: http://dx.doi.org/10.1063/1.3665634 (cit. on pp. 34, 36, 37).

[172] T. M. Godden, S. J. Boyle, A. J. Ramsay, A. M. Fox, and M. S. Skolnick. 'Fast high fidelity hole spin initialization in a single InGaAs quantum dot.' *Applied Physics Letters* 97.6, 061113 (2010), pp. -. DOI: http://dx.doi.org/10.1063/1.3476353 (cit. on pp. 34, 93, 94, 97, 109).

[173] A. Delteil, W.-b. Gao, P. Fallahi, J. Miguel-Sanchez, and A. Imamoğlu. 'Observation of Quantum Jumps of a Single Quantum Dot Spin Using Submicrosecond Single-Shot Optical

Readout.' *Phys. Rev. Lett.* 112 (11 Mar. 2014), p. 116802. DOI: 10.1103/PhysRevLett.112.116802 (cit. on p. 36).

[174]   M. Kroner, K. M. Weiss, B. Biedermann, S. Seidl, A. W. Holleitner, A. Badolato, P. M. Petroff, P. Öhberg, R. J. Warburton, and K. Karrai. 'Resonant two-color high-resolution spectroscopy of a negatively charged exciton in a self-assembled quantum dot.' *Phys. Rev. B* 78 (7 Aug. 2008), p. 075429. DOI: 10.1103/PhysRevB.78.075429 (cit. on p. 36).

[175]   S. Takahashi, R. S. Deacon, A. Oiwa, K. Shibata, K. Hirakawa, and S. Tarucha. 'Electrically tunable three-dimensional *g*-factor anisotropy in single InAs self-assembled quantum dots.' *Phys. Rev. B* 87 (16 Apr. 2013), p. 161302. DOI: 10.1103/PhysRevB.87.161302 (cit. on p. 36).

[176]   R. Zielke, F. Maier, and D. Loss. 'Anisotropic *g* factor in InAs self-assembled quantum dots.' *Phys. Rev. B* 89 (11 Mar. 2014), p. 115438. DOI: 10.1103/PhysRevB.89.115438 (cit. on p. 36).

[177]   A. Ramsay. 'A review of the coherent optical control of the exciton and spin states of semiconductor quantum dots.' *Semiconductor Science and Technology* 25.10 (Oct. 2010), p. 103001. DOI: 10.1088/0268-1242/25/10/103001 (cit. on pp. 37, 52).

[178]   W. Langbein, P. Borri, U. Woggon, V. Stavarache, D. Reuter, and A. D. Wieck. 'Radiatively limited dephasing in InAs quantum dots.' *Phys. Rev. B* 70 (3 July 2004), p. 033301. DOI: 10.1103/PhysRevB.70.033301 (cit. on pp. 38, 81, 96, 135, 169).

[179]   T. M. Godden, J. H. Quilter, A. J. Ramsay, Y. Wu, P. Brereton, S. J. Boyle, I. J. Luxmoore, J. Puebla-Nunez, A. M. Fox, and M. S. Skolnick. 'Coherent Optical Control of the Spin of a Single Hole in an InAs/GaAs Quantum Dot.' *Phys. Rev. Lett.* 108 (1 Jan. 2012), p. 017402. DOI: 10.1103/PhysRevLett.108.017402 (cit. on pp. 38, 51, 53, 54, 93, 94, 110, 113, 121).

[180]   J. R. Petta, A. C. Johnson, J. M. Taylor, E. A. Laird, A. Yacoby, M. D. Lukin, C. M. Marcus, M. P. Hanson, and A. C. Gossard. 'Coherent Manipulation of Coupled Electron Spins in Semiconductor Quantum Dots.' *Science* 309.5744 (2005), pp. 2180–2184. DOI: 10.1126/science.1116955 (cit. on p. 38).

[181] K. De Greve, P. L. McMahon, D. Press, T. D. Ladd, D. Bisping, C. Schneider, M. Kamp, L. Worschech, S. Hofling, A. Forchel, and Y. Yamamoto. 'Ultrafast coherent control and suppressed nuclear feedback of a single quantum dot hole qubit.' *Nat Phys* 7.11 (Nov. 2011), pp. 872–878. DOI: 10.1038/nphys2078 (cit. on pp. 38, 40–42, 51, 53, 93, 94, 110, 113, 121).

[182] A. Greilich, S. G. Carter, D. Kim, A. S. Bracker, and D. Gammon. 'Optical control of one and two hole spins in interacting quantum dots.' *Nat Photon* 5.11 (Nov. 2011), pp. 702–708. DOI: 10.1038/nphoton.2011.237 (cit. on pp. 38, 40–42, 53, 55, 93, 94, 113).

[183] A. V. Kuhlmann, J. Houel, A. Ludwig, L. Greuter, D. Reuter, A. D. Wieck, M. Poggio, and R. J. Warburton. 'Charge noise and spin noise in a semiconductor quantum device.' *Nat Phys* 9.9 (Sept. 2013), pp. 570–575. DOI: 10.1038/nphys2688 (cit. on pp. 38–42, 108, 113, 173).

[184] P. Borri, W. Langbein, S. Schneider, U. Woggon, R. L. Sellin, D. Ouyang, and D. Bimberg. 'Ultralong Dephasing Time in InGaAs Quantum Dots.' *Phys. Rev. Lett.* 87 (15 Sept. 2001), p. 157401. DOI: 10.1103/PhysRevLett.87.157401 (cit. on pp. 38, 123).

[185] M. Bayer and A. Forchel. 'Temperature dependence of the exciton homogeneous linewidth in $In_{0.60}Ga_{0.40}As/GaAs$ self-assembled quantum dots.' *Phys. Rev. B* 65 (4 Jan. 2002), p. 041308. DOI: 10.1103/PhysRevB.65.041308 (cit. on pp. 38, 41).

[186] D. Heiss, S. Schaeck, H. Huebl, M. Bichler, G. Abstreiter, J. J. Finley, D. V. Bulaev, and D. Loss. 'Observation of extremely slow hole spin relaxation in self-assembled quantum dots.' *Phys. Rev. B* 76 (24 Dec. 2007), p. 241306. DOI: 10.1103/PhysRevB.76.241306 (cit. on pp. 38, 99, 100, 121).

[187] A. Greilich, D. R. Yakovlev, A. Shabaev, A. L. Efros, I. A. Yugova, R. Oulton, V. Stavarache, D. Reuter, A. Wieck, and M. Bayer. 'Mode Locking of Electron Spin Coherences in Singly Charged Quantum Dots.' *Science* 313.5785 (2006), pp. 341–345. DOI: 10.1126/science.1128215 (cit. on p. 38).

[188]   D. Press, K. De Greve, P. L. McMahon, T. D. Ladd, B. Friess, C. Schneider, M. Kamp, S. Hofling, A. Forchel, and Y. Yamamoto. 'Ultrafast optical spin echo in a single quantum dot.' *Nat Photon* 4.6 (June 2010), pp. 367–370. DOI: 10.1038/nphoton.2010. 83 (cit. on pp. 38, 40, 41, 121).

[189]   I. A. Merkulov, A. L. Efros, and M. Rosen. 'Electron spin relaxation by nuclei in semiconductor quantum dots.' *Phys. Rev. B* 65 (20 Apr. 2002), p. 205309. DOI: 10.1103/PhysRevB.65. 205309 (cit. on p. 39).

[190]   A. Abragam. *The Principles of Nuclear Magnetism*. International series of monographs on physics. Clarendon Press, 1961 (cit. on p. 39).

[191]   F. Meier and B. Zakharchenya. *Optical Orientation*. Modern Problems in Condensed Matter Sciences. Elsevier Science, 1984 (cit. on p. 39).

[192]   C. W. Lai, P. Maletinsky, A. Badolato, and A. Imamoglu. 'Knight-Field-Enabled Nuclear Spin Polarization in Single Quantum Dots.' *Phys. Rev. Lett.* 96 (16 Apr. 2006), p. 167403. DOI: 10.1103/PhysRevLett.96.167403 (cit. on p. 39).

[193]   R. N. E. Malein, T. S. Santana, J. M. Zajac, A. C. Dada, E. M. Gauger, P. M. Petroff, J. Y. Lim, J. D. Song, and B. D. Gerardot. 'Screening nuclear field fluctuations in quantum dots for indistinguishable photon generation.' *ArXiv e-prints* (Sept. 2015) (cit. on pp. 39, 40).

[194]   R. Stockill, C. Le Gall, C. Matthiesen, L. Huthmacher, E. Clarke, M. Hugues, and M. Atature. 'Intrinsic limit to electron spin coherence in InGaAs quantum dots featuring strain-induced nuclear dispersion.' *ArXiv e-prints* (Dec. 2015) (cit. on p. 39).

[195]   J. Hansom, C. H. H. Schulte, C. Le Gall, C. Matthiesen, E. Clarke, M. Hugues, J. M. Taylor, and M. Atature. 'Environment-assisted quantum control of a solid-state spin via coherent dark states.' *Nat Phys* 10.10 (Oct. 2014), pp. 725–730. DOI: 10.1038/nphys3077 (cit. on pp. 40, 54, 94, 110, 121, 124).

[196] A. V. Kuhlmann, J. H. Prechtel, J. Houel, A. Ludwig, D. Reuter, A. D. Wieck, and R. J. Warburton. 'Transform-limited single photons from a single quantum dot.' *Nat Commun* 6 (Sept. 2015), pp. –. DOI: 10.1038/ncomms9204 (cit. on pp. 40, 56).

[197] J. Houel, A. V. Kuhlmann, L. Greuter, F. Xue, M. Poggio, B. D. Gerardot, P. A. Dalgarno, A. Badolato, P. M. Petroff, A. Ludwig, D. Reuter, A. D. Wieck, and R. J. Warburton. 'Probing Single-Charge Fluctuations at a GaAs/AlAs Interface Using Laser Spectroscopy on a Nearby InGaAs Quantum Dot.' *Phys. Rev. Lett.* 108 (10 Mar. 2012), p. 107401. DOI: 10.1103/PhysRevLett.108.107401 (cit. on pp. 40, 42, 106, 173).

[198] A. Högele, S. Seidl, M. Kroner, K. Karrai, R. J. Warburton, B. D. Gerardot, and P. M. Petroff. 'Voltage-Controlled Optics of a Quantum Dot.' *Phys. Rev. Lett.* 93 (21 Nov. 2004), p. 217401. DOI: 10.1103/PhysRevLett.93.217401 (cit. on p. 40).

[199] A. J. Bennett, M. A. Pooley, Y. Cao, N. Sköld, I. Farrer, D. A. Ritchie, and A. J. Shields. 'Voltage tunability of single-spin states in a quantum dot.' *Nat Commun* 4 (Feb. 2013), pp. 1522–. DOI: 10.1038/ncomms2519 (cit. on pp. 40, 54).

[200] V. Jovanov, T. Eissfeller, S. Kapfinger, E. C. Clark, F. Klotz, M. Bichler, J. G. Keizer, P. M. Koenraad, G. Abstreiter, and J. J. Finley. 'Observation and explanation of strong electrically tunable exciton g factors in composition engineered In(Ga)As quantum dots.' *Phys. Rev. B* 83 (16 Apr. 2011), p. 161303. DOI: 10.1103/PhysRevB.83.161303 (cit. on p. 40).

[201] J. Pingenot, C. E. Pryor, and M. E. Flatté. 'Electric-field manipulation of the Landé g tensor of a hole in an In$_{0.5}$Ga$_{0.5}$As/GaAs self-assembled quantum dot.' *Phys. Rev. B* 84 (19 Nov. 2011), p. 195403. DOI: 10.1103/PhysRevB.84.195403 (cit. on p. 40).

[202] J. H. Prechtel, F. Maier, J. Houel, A. V. Kuhlmann, A. Ludwig, A. D. Wieck, D. Loss, and R. J. Warburton. 'Electrically tunable hole g factor of an optically active quantum dot for fast spin rotations.' *Phys. Rev. B* 91 (16 Apr. 2015), p. 165304. DOI: 10.1103/PhysRevB.91.165304 (cit. on p. 40).

[203] B. Krummheuer, V. M. Axt, and T. Kuhn. 'Theory of pure de-phasing and the resulting absorption line shape in semiconductor quantum dots.' *Phys. Rev. B* 65 (19 May 2002), p. 195313. DOI: 10.1103/PhysRevB.65.195313 (cit. on pp. 40, 124).

[204] B. Krummheuer, V. M. Axt, T. Kuhn, I. D'Amico, and F. Rossi. 'Pure dephasing and phonon dynamics in GaAs- and GaN-based quantum dot structures: Interplay between material parameters and geometry.' *Phys. Rev. B* 71 (23 June 2005), p. 235329. DOI: 10.1103/PhysRevB.71.235329 (cit. on pp. 40, 41, 140).

[205] E. Stock, M.-R. Dachner, T. Warming, A. Schliwa, A. Lochmann, A. Hoffmann, A. I. Toropov, A. K. Bakarov, I. A. Derebezov, M. Richter, V. A. Haisler, A. Knorr, and D. Bimberg. 'Acoustic and optical phonon scattering in a single In(Ga)As quantum dot.' *Phys. Rev. B* 83 (4 Jan. 2011), p. 041304. DOI: 10.1103/PhysRevB.83.041304 (cit. on pp. 40, 41).

[206] T. Flissikowski, A. Hundt, M. Lowisch, M. Rabe, and F. Henneberger. 'Photon Beats from a Single Semiconductor Quantum Dot.' *Phys. Rev. Lett.* 86 (14 Apr. 2001), pp. 3172–3175. DOI: 10.1103/PhysRevLett.86.3172 (cit. on p. 40).

[207] H. Kumano, H. Kobayashi, S. Ekuni, Y. Hayashi, M. Jo, H. Sasakura, S. Adachi, S. Muto, and I. Suemune. 'Excitonic spin-state preservation mediated by optical-phonon resonant excitation in a single quantum dot.' *Phys. Rev. B* 78 (8 Aug. 2008), p. 081306. DOI: 10.1103/PhysRevB.78.081306 (cit. on p. 40).

[208] K. H. Madsen, S. Ates, J. Liu, A. Javadi, S. M. Albrecht, I. Yeo, S. Stobbe, and P. Lodahl. 'Efficient out-coupling of high-purity single photons from a coherent quantum dot in a photonic-crystal cavity.' *Phys. Rev. B* 90 (15 Oct. 2014), p. 155303. DOI: 10.1103/PhysRevB.90.155303 (cit. on pp. 40–42, 123, 124, 156, 159, 175).

[209] E. A. Muljarov and R. Zimmermann. 'Exciton Dephasing in Quantum Dots due to LO-Phonon Coupling: An Exactly Solvable Model.' *Phys. Rev. Lett.* 98 (18 May 2007), p. 187401. DOI: 10.1103/PhysRevLett.98.187401 (cit. on p. 41).

[210] I. Favero, G. Cassabois, R. Ferreira, D. Darson, C. Voisin, J. Tignon, C. Delalande, G. Bastard, P. Roussignol, and J. M. Gérard. 'Acoustic phonon sidebands in the emission line of single InAs/GaAs quantum dots.' *Phys. Rev. B* 68 (23 Dec. 2003), p. 233301. DOI: 10.1103/PhysRevB.68.233301 (cit. on pp. 41, 123).

[211] S. Weiler, A. Ulhaq, S. M. Ulrich, D. Richter, M. Jetter, P. Michler, C. Roy, and S. Hughes. 'Phonon-assisted incoherent excitation of a quantum dot and its emission properties.' *Phys. Rev. B* 86 (24 Dec. 2012), p. 241304. DOI: 10.1103/PhysRevB.86.241304 (cit. on pp. 41, 123, 152).

[212] G. Ortner, D. R. Yakovlev, M. Bayer, S. Rudin, T. L. Reinecke, S. Fafard, Z. Wasilewski, and A. Forchel. 'Temperature dependence of the zero-phonon linewidth in InAs/GaAs quantum dots.' *Phys. Rev. B* 70 (20 Nov. 2004), p. 201301. DOI: 10.1103/PhysRevB.70.201301 (cit. on p. 41).

[213] M. Kroner, K. M. Weiss, S. Seidl, R. J. Warburton, A. Badolato, P. M. Petroff, and K. Karrai. 'Temperature dependent high resolution resonant spectroscopy on a charged quantum dot.' *physica status solidi (b)* 246.4 (2009), pp. 795–798. DOI: 10.1002/pssb.200880610 (cit. on p. 41).

[214] G. Ortner, M. Schwab, M. Bayer, R. Pässler, S. Fafard, Z. Wasilewski, P. Hawrylak, and A. Forchel. 'Temperature dependence of the excitonic band gap in $In_xGa_{1-x}As$/GaAs self-assembled quantum dots.' *Phys. Rev. B* 72 (8 Aug. 2005), p. 085328. DOI: 10.1103/PhysRevB.72.085328 (cit. on p. 41).

[215] J. H. Quilter, A. J. Brash, F. Liu, M. Glässl, A. M. Barth, V. M. Axt, A. J. Ramsay, M. S. Skolnick, and A. M. Fox. 'Phonon-Assisted Population Inversion of a Single InGaAs/GaAs Quantum Dot by Pulsed Laser Excitation.' *Phys. Rev. Lett.* 114 (13 Mar. 2015), p. 137401. DOI: 10.1103/PhysRevLett.114.137401 (cit. on pp. 41, 124, 132, 149, 154).

[216] S. M. Ates, S. Ulrich, A. Ulhaq, S. Reitzenstein, A. Loffler, S. Hofling, F. A., and P. Michler. 'Non-resonant dot-cavity coupling and its potential for resonant single-quantum-dot spec-

troscopy.' *Nat Photon* 3.12 (Dec. 2009), pp. 724–728. DOI: `10 . 1038/nphoton.2009.215` (cit. on pp. 41, 42, 123, 124, 159).

[217] D. Press, S. Götzinger, S. Reitzenstein, C. Hofmann, A. Löffler, M. Kamp, A. Forchel, and Y. Yamamoto. 'Photon Antibunching from a Single Quantum-Dot-Microcavity System in the Strong Coupling Regime.' *Phys. Rev. Lett.* 98 (11 Mar. 2007), p. 117402. DOI: `10 . 1103 / PhysRevLett . 98 . 117402` (cit. on pp. 41, 123).

[218] S. L. Portalupi, G. Hornecker, V. Giesz, T. Grange, A. Lemaître, J. Demory, I. Sagnes, N. D. Lanzillotti-Kimura, L. Lanco, A. Auffèves, and P. Senellart. 'Bright Phonon-Tuned Single-Photon Source.' *Nano Letters* 15.10 (2015), pp. 6290–6294. DOI: `10 . 1021 / acs . nanolett . 5b00876` (cit. on pp. 41, 42, 57, 123, 124, 142, 157, 159).

[219] E. L. Hahn. 'Spin Echoes.' *Phys. Rev.* 80 (4 Nov. 1950), pp. 580–594. DOI: `10.1103/PhysRev.80.580` (cit. on p. 41).

[220] E. A. Chekhovich, M. N. Makhonin, K. V. Kavokin, A. B. Krysa, M. S. Skolnick, and A. I. Tartakovskii. 'Pumping of Nuclear Spins by Optical Excitation of Spin-Forbidden Transitions in a Quantum Dot.' *Phys. Rev. Lett.* 104 (6 Feb. 2010), p. 066804. DOI: `10.1103/PhysRevLett.104.066804` (cit. on p. 42).

[221] E. Chekhovich, M. Hopkinson, M. Skolnick, and A. Tartakovskii. 'Suppression of nuclear spin bath fluctuations in self-assembled quantum dots induced by inhomogeneous strain.' *Nat Commun* 6 (Feb. 2015), pp. –. DOI: `10 . 1038 / ncomms7348` (cit. on p. 42).

[222] J. Houel, J. H. Prechtel, A. V. Kuhlmann, D. Brunner, C. E. Kuklewicz, B. D. Gerardot, N. G. Stoltz, P. M. Petroff, and R. J. Warburton. 'High Resolution Coherent Population Trapping on a Single Hole Spin in a Semiconductor Quantum Dot.' *Phys. Rev. Lett.* 112 (10 Mar. 2014), p. 107401. DOI: `10.1103/PhysRevLett. 112.107401` (cit. on p. 42).

[223] A. J. Ramsay. 'Passive stabilization of a hole spin qubit using the optical Stark effect.' *Phys. Rev. B* 93 (7 Feb. 2016), p. 075303. DOI: `10.1103/PhysRevB.93.075303` (cit. on p. 42).

[224] S. Haroche. 'Nobel Lecture: Controlling photons in a box and exploring the quantum to classical boundary.' *Rev. Mod. Phys.* 85 (3 July 2013), pp. 1083–1102. DOI: 10.1103/RevModPhys.85.1083 (cit. on p. 42).

[225] X. Ding, Y. He, Z.-C. Duan, N. Gregersen, M.-C. Chen, S. Unsleber, S. Maier, C. Schneider, M. Kamp, S. Höfling, C.-Y. Lu, and J.-W. Pan. 'On-Demand Single Photons with High Extraction Efficiency and Near-Unity Indistinguishability from a Resonantly Driven Quantum Dot in a Micropillar.' *Phys. Rev. Lett.* 116 (2 Jan. 2016), p. 020401. DOI: 10.1103/PhysRevLett.116.020401 (cit. on pp. 42, 56, 159).

[226] N. Somaschi, V. Giesz, L. De Santis, J. C. Loredo, M. P. Almeida, G. Hornecker, L. Portalupi, T. Grange, C. Antón, J. Demory, C. Gómez, I. Sagnes, N. D. Lanzillotti-Kimura, A. Lemaítre, A. Auffeves, A. G. White, L. Lanco, and P. Senellart. 'Near-optimal single-photon sources in the solid state.' *Nat Photon* 10.5 (May 2016), pp. 340–345. DOI: 10.1038/nphoton.2016.23 (cit. on pp. 42, 48, 56, 57, 159, 184).

[227] R. Bose, D. Sridharan, H. Kim, G. S. Solomon, and E. Waks. 'Low-Photon-Number Optical Switching with a Single Quantum Dot Coupled to a Photonic Crystal Cavity.' *Phys. Rev. Lett.* 108 (22 May 2012), p. 227402. DOI: 10.1103/PhysRevLett.108.227402 (cit. on pp. 42, 59, 142, 157).

[228] D. Englund, A. Majumdar, M. Bajcsy, A. Faraon, P. Petroff, and J. Vučković. 'Ultrafast Photon-Photon Interaction in a Strongly Coupled Quantum Dot-Cavity System.' *Phys. Rev. Lett.* 108 (9 Mar. 2012), p. 093604. DOI: 10.1103/PhysRevLett.108.093604 (cit. on pp. 42, 59, 142, 157).

[229] T. Volz, A. Reinhard, M. Winger, A. Badolato, K. J. Hennessy, E. L. Hu, and A. Imamoglu. 'Ultrafast all-optical switching by single photons.' *Nat Photon* 6.9 (Sept. 2012), pp. 605–609. DOI: 10.1038/nphoton.2012.181 (cit. on pp. 42, 59, 142, 157).

[230] H. J. Kimble. 'Strong interactions of single atoms and photons in cavity QED.' *Physica Scripta* 1998.T76 (1998), p. 127. DOI: 10.1238/Physica.Topical.076a00127 (cit. on p. 43).

[231] E. M. Purcell. 'Proceedings of the American Physical Society.' *Phys. Rev.* 69 (11-12 June 1946), p. 681. DOI: `10.1103/PhysRev.69.674.2` (cit. on pp. 43, 44, 159).

[232] R. Coccioli, M. Boroditsky, K. W. Kim, Y. Rahmat-Samii, and E. Yablonovitch. 'Smallest possible electromagnetic mode volume in a dielectric cavity.' *Optoelectronics, IEE Proceedings -* 145.6 (1998), pp. 391–397. DOI: `10.1049/ip-opt:19982468` (cit. on p. 43).

[233] P. Lodahl, A. Floris van Driel, I. S. Nikolaev, A. Irman, K. Overgaag, D. Vanmaekelbergh, and W. L. Vos. 'Controlling the dynamics of spontaneous emission from quantum dots by photonic crystals.' *Nature* 430.7000 (Aug. 2004), pp. 654–657. DOI: `10.1038/nature02772` (cit. on pp. 44, 159, 168, 170).

[234] D. Englund, D. Fattal, E. Waks, G. Solomon, B. Zhang, T. Nakaoka, Y. Arakawa, Y. Yamamoto, and J. Vučković. 'Controlling the Spontaneous Emission Rate of Single Quantum Dots in a Two-Dimensional Photonic Crystal.' *Phys. Rev. Lett.* 95 (1 July 2005), p. 013904. DOI: `10.1103/PhysRevLett.95.013904` (cit. on pp. 44, 159, 168, 170).

[235] A. Kress, F. Hofbauer, N. Reinelt, M. Kaniber, H. J. Krenner, R. Meyer, G. Böhm, and J. J. Finley. 'Manipulation of the spontaneous emission dynamics of quantum dots in two-dimensional photonic crystals.' *Phys. Rev. B* 71 (24 June 2005), p. 241304. DOI: `10.1103/PhysRevB.71.241304` (cit. on pp. 44, 159, 168, 170).

[236] A. Dousse, J. Suffczynski, A. Beveratos, O. Krebs, A. Lemaitre, I. Sagnes, J. Bloch, P. Voisin, and P. Senellart. 'Ultrabright source of entangled photon pairs.' *Nature* 466.7303 (July 2010), pp. 217–220. DOI: `10.1038/nature09148` (cit. on pp. 44, 58).

[237] T. B. Norris, J.-K. Rhee, C.-Y. Sung, Y. Arakawa, M. Nishioka, and C. Weisbuch. 'Time-resolved vacuum Rabi oscillations in a semiconductor quantum microcavity.' *Phys. Rev. B* 50 (19 Nov. 1994), pp. 14663–14666. DOI: `10.1103/PhysRevB.50.14663` (cit. on p. 45).

[238] S. He, C. Wang, Q.-H. Chen, X.-Z. Ren, T. Liu, and K.-L. Wang. 'First-order corrections to the rotating-wave approximation in

the Jaynes-Cummings model.' *Phys. Rev. A* 86 (3 Sept. 2012), p. 033837. DOI: 10.1103/PhysRevA.86.033837 (cit. on p. 45).

[239]   J. Casanova, G. Romero, I. Lizuain, J. J. Garcia-Ripoll, and E. Solano. 'Deep Strong Coupling Regime of the Jaynes-Cummings Model.' *Phys. Rev. Lett.* 105 (26 Dec. 2010), p. 263603. DOI: 10.1103/PhysRevLett.105.263603 (cit. on p. 45).

[240]   T. Niemczyk, F. Deppe, H. Huebl, E. P. Menzel, F. Hocke, M. J. Schwarz, J. J. Garcia-Ripoll, D. Zueco, T. Hummer, E. Solano, A. Marx, and R. Gross. 'Circuit quantum electrodynamics in the ultrastrong-coupling regime.' *Nat Phys* 6.10 (Oct. 2010), pp. 772–776. DOI: 10.1038/nphys1730 (cit. on p. 45).

[241]   G. Scalari, C. Maissen, D. Turčinková, D. Hagenmüller, S. De Liberato, C. Ciuti, C. Reichl, D. Schuh, W. Wegscheider, M. Beck, and J. Faist. 'Ultrastrong Coupling of the Cyclotron Transition of a 2D Electron Gas to a THz Metamaterial.' *Science* 335.6074 (2012), pp. 1323–1326. DOI: 10.1126/science.1216022 (cit. on p. 45).

[242]   Y. Todorov, A. M. Andrews, R. Colombelli, S. De Liberato, C. Ciuti, P. Klang, G. Strasser, and C. Sirtori. 'Ultrastrong Light-Matter Coupling Regime with Polariton Dots.' *Phys. Rev. Lett.* 105 (19 Nov. 2010), p. 196402. DOI: 10.1103/PhysRevLett.105.196402 (cit. on p. 45).

[243]   E. Yablonovitch. 'Inhibited Spontaneous Emission in Solid-State Physics and Electronics.' *Phys. Rev. Lett.* 58 (20 May 1987), pp. 2059–2062. DOI: 10.1103/PhysRevLett.58.2059 (cit. on p. 45).

[244]   S. John. 'Strong localization of photons in certain disordered dielectric superlattices.' *Phys. Rev. Lett.* 58 (23 June 1987), pp. 2486–2489. DOI: 10.1103/PhysRevLett.58.2486 (cit. on p. 45).

[245]   M. Shirane, S. Kono, J. Ushida, S. Ohkouchi, N. Ikeda, Y. Sugimoto, and A. Tomita. 'Mode identification of high-quality-factor single-defect nanocavities in quantum dot-embedded photonic crystals.' *Journal of Applied Physics* 101.7, 073107

(2007). DOI: http://dx.doi.org/10.1063/1.2714644 (cit. on pp. 48, 77, 162, 169).

[246] A. Reinhard, T. Volz, M. Winger, A. Badolato, K. J. Hennessy, E. L. Hu, and A. Imamoglu. 'Strongly correlated photons on a chip.' *Nat Photon* 6.2 (Feb. 2012), pp. 93–96. DOI: 10.1038/nphoton.2011.321 (cit. on p. 48).

[247] R. Ohta, Y. Ota, M. Nomura, N. Kumagai, S. Ishida, S. Iwamoto, and Y. Arakawa. 'Strong coupling between a photonic crystal nanobeam cavity and a single quantum dot.' *Applied Physics Letters* 98.17, 173104 (2011), p. 173104. DOI: 10.1063/1.3579535 (cit. on p. 48).

[248] E. Peter, P. Senellart, D. Martrou, A. Lemaitre, J. Hours, J. M. Gérard, and J. Bloch. 'Exciton-Photon Strong-Coupling Regime for a Single Quantum Dot Embedded in a Microcavity.' *Phys. Rev. Lett.* 95 (6 Aug. 2005), p. 067401. DOI: 10.1103/PhysRevLett.95.067401 (cit. on p. 48).

[249] J. P. Reithmaier, G. Sek, A. Loffler, C. Hofmann, S. Kuhn, S. Reitzenstein, L. V. Keldysh, V. D. Kulakovskii, T. L. Reinecke, and A. Forchel. 'Strong coupling in a single quantum dot-semiconductor microcavity system.' *Nature* 432.7014 (Nov. 2004), pp. 197–200. DOI: 10.1038/nature02969 (cit. on p. 48).

[250] F. Faisal. *Theory of Multiphoton Processes*. Physics of Atoms and Molecules. Springer, 1987 (cit. on p. 48).

[251] S. H. Autler and C. H. Townes. 'Stark Effect in Rapidly Varying Fields.' *Phys. Rev.* 100 (2 Oct. 1955), pp. 703–722. DOI: 10.1103/PhysRev.100.703 (cit. on p. 49).

[252] B. R. Mollow. 'Power Spectrum of Light Scattered by Two-Level Systems.' *Phys. Rev.* 188 (5 Dec. 1969), pp. 1969–1975. DOI: 10.1103/PhysRev.188.1969 (cit. on p. 49).

[253] B. D. Gerardot, D. Brunner, P. A. Dalgarno, K. Karrai, A. Badolato, P. M. Petroff, and R. J. Warburton. 'Dressed excitonic states and quantum interference in a three-level quantum dot ladder system.' *New Journal of Physics* 11.1 (2009), p. 013028. DOI: 10.1088/1367-2630/11/1/013028 (cit. on p. 49).

[254] X. Xu, B. Sun, P. R. Berman, D. G. Steel, A. S. Bracker, D. Gammon, and L. J. Sham. 'Coherent Optical Spectroscopy of a Strongly Driven Quantum Dot.' *Science* 317.5840 (Aug. 2007), pp. 929–32. DOI: 10.1126/science.1142979 (cit. on pp. 49, 116, 189).

[255] E. B. Flagg, A. Muller, J. W. Robertson, S. Founta, D. G. Deppe, M. Xiao, W. Ma, G. J. Salamo, and C. K. Shih. 'Resonantly driven coherent oscillations in a solid-state quantum emitter.' *Nat Phys* 5.3 (Mar. 2009), pp. 203–207. DOI: 10.1038/nphys1184 (cit. on pp. 49, 50).

[256] M. Fox. *Quantum Optics: An Introduction*. Oxford Master Series in Physics. OUP Oxford, 2006 (cit. on pp. 50, 109).

[257] T. H. Stievater, X. Li, D. G. Steel, D. Gammon, D. S. Katzer, D. Park, C. Piermarocchi, and L. J. Sham. 'Rabi Oscillations of Excitons in Single Quantum Dots.' *Phys. Rev. Lett.* 87 (13 Sept. 2001), p. 133603. DOI: 10.1103/PhysRevLett.87.133603 (cit. on p. 51).

[258] L. Besombes, J. J. Baumberg, and J. Motohisa. 'Coherent Spectroscopy of Optically Gated Charged Single InGaAs Quantum Dots.' *Phys. Rev. Lett.* 90 (25 June 2003), p. 257402. DOI: 10.1103/PhysRevLett.90.257402 (cit. on p. 51).

[259] Q. Q. Wang, A. Muller, P. Bianucci, E. Rossi, Q. K. Xue, T. Takagahara, C. Piermarocchi, A. H. MacDonald, and C. K. Shih. 'Decoherence processes during optical manipulation of excitonic qubits in semiconductor quantum dots.' *Phys. Rev. B* 72 (3 July 2005), p. 035306. DOI: 10.1103/PhysRevB.72.035306 (cit. on p. 51).

[260] B. Patton, U. Woggon, and W. Langbein. 'Coherent Control and Polarization Readout of Individual Excitonic States.' *Phys. Rev. Lett.* 95 (26 Dec. 2005), p. 266401. DOI: 10.1103/PhysRevLett.95.266401 (cit. on p. 51).

[261] A. J. Ramsay, R. S. Kolodka, F. Bello, P. W. Fry, W. K. Ng, A. Tahraoui, H. Y. Liu, M. Hopkinson, D. M. Whittaker, A. M. Fox, and M. S. Skolnick. 'Coherent response of a quantum dot exciton driven by a rectangular spectrum optical pulse.' *Phys.*

Rev. B 75 (11 Mar. 2007), p. 113302. DOI: `10.1103/PhysRevB.75.113302` (cit. on p. 51).

[262]   H. Takagi, T. Nakaoka, K. Watanabe, N. Kumagai, and Y. Arakawa. 'Coherently driven semiconductor quantum dot at a telecommunication wavelength.' *Opt. Express* 16.18 (Sept. 2008), pp. 13949–13954. DOI: `10.1364/OE.16.013949` (cit. on p. 51).

[263]   R. Melet, V. Voliotis, A. Enderlin, D. Roditchev, X. L. Wang, T. Guillet, and R. Grousson. 'Resonant excitonic emission of a single quantum dot in the Rabi regime.' *Phys. Rev. B* 78 (7 Aug. 2008), p. 073301. DOI: `10.1103/PhysRevB.78.073301` (cit. on p. 51).

[264]   A. A. Freschi and J. Frejlich. 'Adjustable phase control in stabilized interferometry.' *Opt. Lett.* 20.6 (Mar. 1995), pp. 635–637. DOI: `10.1364/OL.20.000635` (cit. on p. 51).

[265]   T. Okada, K. Komori, K. Goshima, S. Yamauchi, I. Morohashi, T. Sugaya, M. Ogura, and N. Tsurumachi. 'Development of high resolution Michelson interferometer for stable phase-locked ultrashort pulse pair generation.' *Review of Scientific Instruments* 79.10, 103101 (2008), p. 103101. DOI: `10.1063/1.2993980` (cit. on p. 51).

[266]   D. Press, T. D. Ladd, B. Zhang, and Y. Yamamoto. 'Complete quantum control of a single quantum dot spin using ultrafast optical pulses.' *Nature* 456.7219 (Nov. 2008), pp. 218–221. DOI: `10.1038/nature07530` (cit. on pp. 51, 52).

[267]   M. H. Mikkelsen, J. Berezovsky, N. G. Stoltz, L. a. Coldren, and D. D. Awschalom. 'Optically detected coherent spin dynamics of a single electron in a quantum dot.' *Nature Physics* 3.11 (Oct. 2007), pp. 770–773. DOI: `10.1038/nphys736` (cit. on p. 53).

[268]   J. Berezovsky, M. H. Mikkelsen, N. G. Stoltz, L. A. Coldren, and D. D. Awschalom. 'Picosecond Coherent Optical Manipulation of a Single Electron Spin in a Quantum Dot.' *Science* 320.5874 (2008), pp. 349–352. DOI: `10.1126/science.1154798` (cit. on p. 53).

[269] M. Mikkelsen, J. Berezovsky, and D. Awschalom. 'Ultrafast optical manipulation of single electron spins in quantum dots.' *Solid State Communications* 149.35-36 (Sept. 2009), pp. 1451–1457. DOI: 10.1016/j.ssc.2009.04.038 (cit. on p. 53).

[270] S. E. Economou and T. L. Reinecke. 'Theory of Fast Optical Spin Rotation in a Quantum Dot Based on Geometric Phases and Trapped States.' *Phys. Rev. Lett.* 99 (21 Nov. 2007), p. 217401. DOI: 10.1103/PhysRevLett.99.217401 (cit. on pp. 53, 54).

[271] J. Pingenot, C. E. Pryor, and M. E. Flatté. 'Method for full Bloch sphere control of a localized spin via a single electrical gate.' *Applied Physics Letters* 92.22, 222502 (2008). DOI: http://dx.doi.org/10.1063/1.2937305 (cit. on p. 54).

[272] M. Kroner, K. M. Weiss, B. Biedermann, S. Seidl, S. Manus, A. W. Holleitner, A. Badolato, P. M. Petroff, B. D. Gerardot, R. J. Warburton, and K. Karrai. 'Optical Detection of Single-Electron Spin Resonance in a Quantum Dot.' *Phys. Rev. Lett.* 100 (15 Apr. 2008), p. 156803. DOI: 10.1103/PhysRevLett.100.156803 (cit. on p. 55).

[273] I. Schwartz, E. R. Schmidgall, L. Gantz, D. Cogan, E. Bordo, Y. Don, M. Zielinski, and D. Gershoni. 'Deterministic Writing and Control of the Dark Exciton Spin Using Single Short Optical Pulses.' *Phys. Rev. X* 5 (1 Jan. 2015), p. 011009. DOI: 10.1103/PhysRevX.5.011009 (cit. on p. 55).

[274] D. Kim, S. G. Carter, A. Greilich, A. S. Bracker, and D. Gammon. 'Ultrafast optical control of entanglement between two quantum-dot spins.' *Nat Phys* 7.3 (Mar. 2011), pp. 223–229. DOI: 10.1038/nphys1863 (cit. on p. 55).

[275] K. M. Weiss, J. M. Elzerman, Y. L. Delley, J. Miguel-Sanchez, and A. Imamoğlu. 'Coherent Two-Electron Spin Qubits in an Optically Active Pair of Coupled InGaAs Quantum Dots.' *Phys. Rev. Lett.* 109 (10 Sept. 2012), p. 107401. DOI: 10.1103/PhysRevLett.109.107401 (cit. on p. 55).

[276] Y. Benny, S. Khatsevich, Y. Kodriano, E. Poem, R. Presman, D. Galushko, P. M. Petroff, and D. Gershoni. 'Coherent Optical Writing and Reading of the Exciton Spin State in Single Quan-

tum Dots.' *Phys. Rev. Lett.* 106 (4 Jan. 2011), p. 040504. DOI: `10.1103/PhysRevLett.106.040504` (cit. on p. 55).

[277] W. Gao, P. Fallahi, E. Togan, A. Delteil, Y. Chin, J. Miguel-Sanchez, and A. Imamoğlu. 'Quantum teleportation from a propagating photon to a solid-state spin qubit.' *Nat Commun* 4 (Nov. 2013), pp. –. DOI: `10.1038/ncomms3744` (cit. on p. 55).

[278] A. Delteil, Z. Sun, W.-b. Gao, E. Togan, S. Faelt, and A. Imamoğlu. 'Generation of heralded entanglement between distant hole spins.' *Nat Phys* 12.3 (Mar. 2016), pp. 218–223. DOI: `10.1038/ncomms3744` (cit. on pp. 55, 121, 184).

[279] D. Hucul, I. V. Inlek, G. Vittorini, C. Crocker, S. Debnath, S. M. Clark, and C. Monroe. 'Modular entanglement of atomic qubits using photons and phonons.' *Nat Phys* 11.1 (Jan. 2015), pp. 37–42. DOI: `10.1038/nphys3150` (cit. on p. 56).

[280] H. Bernien, B. Hensen, W. Pfaff, G. Koolstra, M. S. Blok, L. Robledo, T. H. Taminiau, M. Markham, D. J. Twitchen, L. Childress, and R. Hanson. 'Heralded entanglement between solid-state qubits separated by three metres.' *Nature* 497.7447 (May 2013), pp. 86–90. DOI: `10.1038/nature12016` (cit. on p. 56).

[281] P. L. McMahon and K. de Greve. 'Engineering the Atom-Photon Interaction: Controlling Fundamental Processes with Photons, Atoms and Solids.' In: ed. by A. Predojević and M. Mitchell. Nano-Optics and Nanophotonics. Springer International Publishing, 2015. Chap. Towards Quantum Repeaters with Solid-State Qubits: Spin-Photon Entanglement Generation using Self-Assembled Quantum Dots, pp. 363–402 (cit. on p. 56).

[282] P. Michler, A. Kiraz, C. Becher, W. V. Schoenfeld, P. M. Petroff, L. Zhang, E. Hu, and A. Imamoglu. 'A Quantum Dot Single-Photon Turnstile Device.' *Science* 290.5500 (2000), pp. 2282–2285. DOI: `10.1126/science.290.5500.2282` (cit. on p. 56).

[283] C. Santori, D. Fattal, J. Vuckovic, G. S. Solomon, and Y. Yamamoto. 'Indistinguishable photons from a single-photon device.' *Nature* 419.6907 (Oct. 2002), pp. 594–597. DOI: `10.1038/nature01086` (cit. on p. 56).

[284] Y.-M. He, Y. He, Y.-J. Wei, D. Wu, M. Atature, C. Schneider, S. Hofling, M. Kamp, C.-Y. Lu, and J.-W. Pan. 'On-demand semiconductor single-photon source with near-unity indistinguishability.' *Nat Nano* 8.3 (Mar. 2013), pp. 213–217. DOI: 10.1038/nnano.2012.262 (cit. on p. 56).

[285] E. B. Flagg, A. Muller, S. V. Polyakov, A. Ling, A. Migdall, and G. S. Solomon. 'Interference of Single Photons from Two Separate Semiconductor Quantum Dots.' *Phys. Rev. Lett.* 104 (13 Apr. 2010), p. 137401. DOI: 10.1103/PhysRevLett.104.137401 (cit. on p. 56).

[286] C. Santori, D. Fattal, J. Vuckovic, G. S. Solomon, and Y. Yamamoto. 'Single-photon generation with InAs quantum dots.' *New Journal of Physics* 6.1 (2004), p. 89. DOI: 10.1088/1367-2630/6/1/089 (cit. on p. 56).

[287] D. Heinze, D. Breddermann, A. Zrenner, and S. Schumacher. 'A quantum dot single-photon source with on-the-fly all-optical polarization control and timed emission.' *Nat Commun* 6 (Oct. 2015), pp. –. DOI: 10.1038/ncomms9473 (cit. on pp. 57, 142, 157, 184).

[288] S. Stufler, P. Machnikowski, P. Ester, M. Bichler, V. M. Axt, T. Kuhn, and A. Zrenner. 'Two-photon Rabi oscillations in a single $In_xGa_{1-x}As/GaAs$ quantum dot.' *Phys. Rev. B* 73 (12 Mar. 2006), p. 125304. DOI: 10.1103/PhysRevB.73.125304 (cit. on pp. 58, 139, 165).

[289] M. Muller, S. Bounouar, K. D. Jons, M. Glassl, and P. Michler. 'On-demand generation of indistinguishable polarization-entangled photon pairs.' *Nat Photon* 8.3 (Mar. 2014), pp. 224–228. DOI: 10.1038/nphoton.2013.377 (cit. on p. 58).

[290] S. Schumacher, J. Förstner, A. Zrenner, M. Florian, C. Gies, P. Gartner, and F. Jahnke. 'Cavity-assisted emission of polarization-entangled photons from biexcitons in quantum dots with fine-structure splitting.' *Opt. Express* 20.5 (Feb. 2012), pp. 5335–5342. DOI: 10.1364/OE.20.005335 (cit. on p. 58).

[291] E. del Valle. 'Distilling one, two and entangled pairs of photons from a quantum dot with cavity QED effects and spec-

tral filtering.' *New Journal of Physics* 15.2 (2013), p. 025019. DOI: `10.1088/1367-2630/15/2/025019` (cit. on p. 58).

[292]   C. S. Muñoz, F. P. Laussy, C. Tejedor, and E. del Valle. 'Enhanced two-photon emission from a dressed biexciton.' *New Journal of Physics* 17.12 (2015), p. 123021. DOI: `10.1088/1367-2630/17/12/123021` (cit. on pp. 58, 142, 157).

[293]   Y. Ota, S. Iwamoto, N. Kumagai, and Y. Arakawa. 'Spontaneous Two-Photon Emission from a Single Quantum Dot.' *Phys. Rev. Lett.* 107 (23 Nov. 2011), p. 233602. DOI: `10.1103/PhysRevLett.107.233602` (cit. on pp. 58, 159, 165).

[294]   H. J. Briegel and R. Raussendorf. 'Persistent Entanglement in Arrays of Interacting Particles.' *Phys. Rev. Lett.* 86 (5 Jan. 2001), pp. 910–913. DOI: `10.1103/PhysRevLett.86.910` (cit. on p. 58).

[295]   N. H. Lindner and T. Rudolph. 'Proposal for Pulsed On-Demand Sources of Photonic Cluster State Strings.' *Phys. Rev. Lett.* 103 (11 Sept. 2009), p. 113602. DOI: `10.1103/PhysRevLett.103.113602` (cit. on pp. 58, 59).

[296]   N. Kiesel, C. Schmid, U. Weber, G. Tóth, O. Gühne, R. Ursin, and H. Weinfurter. 'Experimental Analysis of a Four-Qubit Photon Cluster State.' *Phys. Rev. Lett.* 95 (21 Nov. 2005), p. 210502. DOI: `10.1103/PhysRevLett.95.210502` (cit. on p. 58).

[297]   P. Walther, K. J. Resch, T. Rudolph, E. Schenck, H. Weinfurter, V. Vedral, M. Aspelmeyer, and A. Zeilinger. 'Experimental one-way quantum computing.' *Nature* 434.7030 (Mar. 2005), pp. 169–176. DOI: `10.1038/nature03347` (cit. on p. 58).

[298]   C.-Y. Lu, X.-Q. Zhou, O. Guhne, W.-B. Gao, J. Zhang, Z.-S. Yuan, A. Goebel, T. Yang, and J.-W. Pan. 'Experimental entanglement of six photons in graph states.' *Nat Phys* 3.2 (Feb. 2007), pp. 91–95. DOI: `10.1038/nphys507` (cit. on p. 59).

[299]   S. E. Economou, N. Lindner, and T. Rudolph. 'Optically Generated 2-Dimensional Photonic Cluster State from Coupled Quantum Dots.' *Phys. Rev. Lett.* 105 (9 Aug. 2010), p. 093601. DOI: `10.1103/PhysRevLett.105.093601` (cit. on p. 59).

[300]   I. Schwartz, D. Cogan, E. R. Shchmidgall, Y. Don, L. Gantz, O. Kenneth, N. H. Lindner, and D. Gershoni. 'Quantum Dots - Deterinistic Source for Long Strings of Entangled Photons and Photonic Cluster States.' In: *Solid State Quantum Photonics 2016*. 2016 (cit. on p. 59).

[301]   C. S. Munoz, E. del Valle, A. G. Tudela, K. Muller, S. Lichtman-necker, M. Kaniber, C. Tejedor, J. J. Finley, and F. P. Laussy. 'Emitters of N-photon bundles.' *Nat Photon* 8.7 (July 2014), pp. 550–555. DOI: 10.1038/nphoton.2014.114 (cit. on p. 59).

[302]   E. Waks and J. Vuckovic. 'Dipole Induced Transparency in Drop-Filter Cavity-Waveguide Systems.' *Phys. Rev. Lett.* 96 (15 Apr. 2006), p. 153601. DOI: 10.1103/PhysRevLett.96.153601 (cit. on p. 59).

[303]   D. Englund, A. Faraon, I. Fushman, N. Stoltz, P. Petroff, and J. Vuckovic. 'Controlling cavity reflectivity with a single quantum dot.' *Nature* 450.7171 (Dec. 2007), pp. 857–861. DOI: 10.1038/nature06234 (cit. on p. 59).

[304]   A. Javadi, I. Sollner, M. Arcari, S. L. Hansen, L. Midolo, S. Mah-moodian, G. Kirsanske, T. Pregnolato, E. H. Lee, J. D. Song, S. Stobbe, and P. Lodahl. 'Single-photon non-linear optics with a quantum dot in a waveguide.' *Nat Commun* 6 (Oct. 2015), pp. –. DOI: 10.1038/ncomms9655 (cit. on p. 59).

[305]   A. Majumdar, N. Manquest, A. Faraon, and J. Vučković. 'Theory of electro-optic modulation via a quantum dot coupled to a nano-resonator.' *Opt. Express* 18.5 (Mar. 2010), pp. 3974–3984. DOI: 10.1364/OE.18.003974 (cit. on p. 60).

[306]   D. Englund, A. Faraon, A. Majumdar, N. Stoltz, P. Petroff, and J. Vuckovic. 'An optical modulator based on a single strongly coupled quantum dot - cavity system in a p-i-n junction.' *Opt. Express* 17.21 (Oct. 2009), pp. 18651–18658. DOI: 10.1364/OE.17.018651 (cit. on p. 60).

[307]   A. Faraon, A. Majumdar, H. Kim, P. Petroff, and J. Vučković. 'Fast Electrical Control of a Quantum Dot Strongly Coupled to a Photonic-Crystal Cavity.' *Phys. Rev. Lett.* 104 (4 Jan. 2010), p. 047402. DOI: 10.1103/PhysRevLett.104.047402 (cit. on p. 60).

[308] H. Kim, R. Bose, T. C. Shen, G. S. Solomon, and E. Waks. 'A quantum logic gate between a solid-state quantum bit and a photon.' *Nat Photon* 7.5 (May 2013), pp. 373–377. DOI: 10.1038/nphoton.2013.48 (cit. on p. 60).

[309] M. Atature, J. Dreiser, A. Badolato, and A. Imamoglu. 'Observation of Faraday rotation from a single confined spin.' *Nat Phys* 3.2 (Feb. 2007), pp. 101–106. DOI: 10.1038/nphys521 (cit. on p. 60).

[310] C. Arnold, J. Demory, V. Loo, A. Lemaître, I. Sagnes, M. Glazov, O. Krebs, P. Voisin, P. Senellart, and L. Lanco. 'Macroscopic rotation of photon polarization induced by a single spin.' *Nat Commun* 6 (Feb. 2015), pp. –. DOI: 10.1038/ncomms7236 (cit. on p. 60).

[311] P. Androvitsaneas, A. B. Young, C. Schneider, S. Maier, M. Kamp, S. Höfling, S. Knauer, E. Harbord, C.-Y. Hu, J. G. Rarity, and R. Oulton. 'A charged quantum dot micropillar system for deterministic light matter interactions.' *ArXiv e-prints* (Nov. 2015) (cit. on p. 60).

[312] S. Sun, H. Kim, G. S. Solomon, and E. Waks. 'A quantum phase switch between a single solid-state spin and a photon.' *Nat Nano* 11.6 (Feb. 2016), pp. 539–544. DOI: 10.1038/nnano.2015.334 (cit. on pp. 60, 61, 121, 184).

[313] J. Cho and H.-W. Lee. 'Generation of Atomic Cluster States through the Cavity Input-Output Process.' *Phys. Rev. Lett.* 95 (16 Oct. 2005), p. 160501. DOI: 10.1103/PhysRevLett.95.160501 (cit. on p. 61).

[314] S. Ritter, C. Nolleke, C. Hahn, A. Reiserer, A. Neuzner, M. Uphoff, M. Mucke, E. Figueroa, J. Bochmann, and G. Rempe. 'An elementary quantum network of single atoms in optical cavities.' *Nature* 484.7393 (Apr. 2012), pp. 195–200. DOI: 10.1038/nature11023 (cit. on p. 61).

[315] J. Volz, R. Gehr, G. Dubois, J. Esteve, and J. Reichel. 'Measurement of the internal state of a single atom without energy exchange.' *Nature* 475.7355 (July 2011), pp. 210–213. DOI: 10.1038/nature10225 (cit. on p. 61).

[316] A. Reiserer, S. Ritter, and G. Rempe. 'Nondestructive Detection of an Optical Photon.' *Science* 342.6164 (2013), pp. 1349–1351. DOI: `10.1126/science.1246164` (cit. on p. 61).

[317] S. G. Carter, T. M. Sweeney, M. Kim, C. S. Kim, D. Solenov, S. E. Economou, T. L. Reinecke, L. Yang, A. S. Bracker, and D. Gammon. 'Quantum control of a spin qubit coupled to a photonic crystal cavity.' *Nat Photon* 7.4 (Apr. 2013), pp. 329–334. DOI: `10.1038/nphoton.2013.41` (cit. on pp. 61, 184).

[318] A. Majumdar, P. Kaer, M. Bajcsy, E. D. Kim, K. G. Lagoudakis, A. Rundquist, and J. Vučković. 'Proposed Coupling of an Electron Spin in a Semiconductor Quantum Dot to a Nanosize Optical Cavity.' *Phys. Rev. Lett.* 111 (2 July 2013), p. 027402. DOI: `10.1103/PhysRevLett.111.027402` (cit. on pp. 61, 185).

[319] R. Bose, T. Cai, K. R. Choudhury, G. S. Solomon, and E. Waks. 'All-optical coherent control of vacuum Rabi oscillations.' *Nat Photon* 8.11 (Nov. 2014), pp. 858–864. DOI: `10.1038/nphoton.2014.224` (cit. on p. 61).

[320] *Coherent Mira 900 Data Sheet*. Coherent Inc. 5100 Patrick Henry Drive, Santa Clara, CA, 95054, 2002 (cit. on p. 65).

[321] *Coherent Verdi G-Series Family Data Sheet*. Rev. D. Coherent Inc. 5100 Patrick Henry Drive, Santa Clara, CA, 95054, 2013 (cit. on p. 65).

[322] T. Brabec, C. Spielmann, P. F. Curley, and F. Krausz. 'Kerr lens mode locking.' *Opt. Lett.* 17.18 (Sept. 1992), pp. 1292–1294. DOI: `10.1364/OL.17.001292` (cit. on p. 66).

[323] *Toptica Tunable Diode Lasers*. Toptica. TOPTICA Photonics AG, Lochhamer Schlag 19, 82166 Graefelfing (Munich), Germany, 2009 (cit. on p. 66).

[324] A. M. Weiner. 'Femtosecond pulse shaping using spatial light modulators.' *Review of Scientific Instruments* 71.5 (2000), pp. 1929–1960. DOI: `http://dx.doi.org/10.1063/1.1150614` (cit. on p. 69).

[325] A. M. Weiner. 'Ultrafast optical pulse shaping: A tutorial review.' *Optics Communications* 284.15 (2011). Special Issue on Optical Pulse Shaping, Arbitrary Waveform Generation, and

Pulse Characterization, pp. 3669–3692. DOI: http://dx.doi.
org/10.1016/j.optcom.2011.03.084 (cit. on p. 69).

[326]   P. Drexler and P. Fiala. 'Recent Progress in Optical Fiber Research.' In: ed. by M. Yasin. InTech, 2012. Chap. Optical Fiber Birefringence Effects – Sources, Utilization and Methods of Suppression, pp. 127–150. DOI: 10.5772/27517 (cit. on p. 72).

[327]   A. J. Bennett, R. B. Patel, J. Skiba-Szymanska, C. A. Nicoll, I. Farrer, D. A. Ritchie, and A. J. Shields. 'Giant Stark effect in the emission of single semiconductor quantum dots.' *Applied Physics Letters* 97.3, 031104 (2010). DOI: http://dx.doi.org/10.1063/1.3460912 (cit. on p. 76).

[328]   R. J. Coles, N. Prtljaga, B. Royall, I. J. Luxmoore, A. M. Fox, and M. S. Skolnick. 'Waveguide-coupled photonic crystal cavity for quantum dot spin readout.' *Opt. Express* 22.3 (Feb. 2014), pp. 2376–2385. DOI: 10.1364/OE.22.002376 (cit. on pp. 78, 162).

[329]   C. Bentham, I. E. Itskevich, R. J. Coles, B. Royall, E. Clarke, J. O'Hara, N. Prtljaga, A. M. Fox, M. S. Skolnick, and L. R. Wilson. 'On-chip electrically controlled routing of photons from a single quantum dot.' *Applied Physics Letters* 106.22, 221101 (2015). DOI: http://dx.doi.org/10.1063/1.4922041 (cit. on pp. 78, 162).

[330]   *Model 6485 Picoammeter User Manual*. Rev. A. Keithley Instruments. 2001 (cit. on p. 84).

[331]   N. Prtljaga, R. J. Coles, J. O'Hara, B. Royall, E. Clarke, A. M. Fox, and M. S. Skolnick. 'Monolithic integration of a quantum emitter with a compact on-chip beam-splitter.' *Applied Physics Letters* 104.23, 231107 (2014), pp. -. DOI: http://dx.doi.org/10.1063/1.4883374 (cit. on p. 93).

[332]   J. Preskill. 'Reliable quantum computers.' *Proceedings of the Royal Society A: Mathematical, Physical and Engineering Sciences* 454.1969 (Jan. 1998), pp. 385–410. DOI: 10.1098/rspa.1998.0167 (cit. on p. 93).

[333]   D. Kim, S. E. Economou, S. C. Badescu, M. Scheibner, A. S. Bracker, M. Bashkansky, T. L. Reinecke, and D. Gammon. 'Optical Spin Initialization and Nondestructive Measurement in

a Quantum Dot Molecule.' *Phys. Rev. Lett.* 101 (23 Dec. 2008), p. 236804. DOI: 10.1103/PhysRevLett.101.236804 (cit. on p. 93).

[334] X. Xu, B. Sun, P. R. Berman, D. G. Steel, A. S. Bracker, D. Gammon, and L. J. Sham. 'Coherent population trapping of an electron spin in a single negatively charged quantum dot.' *Nat Phys* 4.9 (Sept. 2008), pp. 692–695. DOI: 10.1038/nphys1054 (cit. on p. 93).

[335] T. M. Godden, J. H. Quilter, A. J. Ramsay, Y. Wu, P. Brereton, I. J. Luxmoore, J. Puebla, A. M. Fox, and M. S. Skolnick. 'Fast preparation of a single-hole spin in an InAs/GaAs quantum dot in a Voigt-geometry magnetic field.' *Phys. Rev. B* 85 (15 Apr. 2012), p. 155310. DOI: 10.1103/PhysRevB.85.155310 (cit. on pp. 93, 121).

[336] J. D. Mar, J. J. Baumberg, X. Xu, A. C. Irvine, and D. A. Williams. 'Ultrafast high-fidelity initialization of a quantum-dot spin qubit without magnetic fields.' *Phys. Rev. B* 90 (24 Dec. 2014), p. 241303. DOI: 10.1103/PhysRevB.90.241303 (cit. on pp. 94, 111, 121).

[337] A. F. A. Khatab, A. J. Ramsay, S. J. Boyle, A. M. Fox, and M. S. Skolnick. 'Inversion recovery measurements of exciton fine-structure beats in a single quantum dot.' *Journal of Physics: Conference Series* 245.1 (2010), p. 012010. DOI: 10.1088/1742-6596/245/1/012010 (cit. on pp. 96, 104).

[338] R. Jozsa. 'Fidelity for Mixed Quantum States.' *Journal of Modern Optics* 41 (Dec. 1994), pp. 2315–2323. DOI: 10.1080/09500349414552171 (cit. on p. 97).

[339] T. M. Godden. 'Coherent optical control of the spin of a single hole in a quantum dot.' PhD thesis. University of Sheffield, Mar. 2012 (cit. on pp. 97, 103).

[340] R. S. Kolodka, A. J. Ramsay, J. Skiba-Szymanska, P. W. Fry, H. Y. Liu, A. M. Fox, and M. S. Skolnick. 'Inversion recovery of single quantum-dot exciton based qubit.' *Phys. Rev. B* 75 (19 May 2007), p. 193306. DOI: 10.1103/PhysRevB.75.193306 (cit. on pp. 104, 150, 151, 190).

[341]   S. Stufler, P. Ester, A. Zrenner, and M. Bichler. 'Power broadening of the exciton linewidth in a single InGaAs/GaAs quantum dot.' *Applied Physics Letters* 85.18 (2004), pp. 4202–4204. DOI: http://dx.doi.org/10.1063/1.1815373 (cit. on p. 106).

[342]   P. Ester, S. Stufler, S. Michaelis de Vasconcellos, M. Bichler, and A. Zrenner. 'High resolution photocurrent-spectroscopy of a single quantum dot.' *Physica Status Solidi (c)* 3.11 (2006), pp. 3722–3725. DOI: 10.1002/pssc.200671572 (cit. on pp. 106, 108).

[343]   R. Raussendorf and J. Harrington. 'Fault-Tolerant Quantum Computation with High Threshold in Two Dimensions.' *Phys. Rev. Lett.* 98 (19 May 2007), p. 190504. DOI: 10.1103/PhysRevLett.98.190504 (cit. on pp. 112, 121).

[344]   E. Kadantsev and P. Hawrylak. 'Theory of exciton fine structure in semiconductor quantum dots: Quantum dot anisotropy and lateral electric field.' *Phys. Rev. B* 81 (4 Jan. 2010), p. 045311. DOI: 10.1103/PhysRevB.81.045311 (cit. on pp. 113–115).

[345]   G. W. Bryant, N. Malkova, and J. Sims. 'Mechanism for controlling the exciton fine structure in quantum dots using electric fields: Manipulation of exciton orientation and exchange splitting at the atomic scale.' *Phys. Rev. B* 88 (16 Oct. 2013), p. 161301. DOI: 10.1103/PhysRevB.88.161301 (cit. on pp. 113, 114).

[346]   J. H. Quilter. 'Coherent spectroscopy of single quantum dots.' PhD thesis. University of Sheffield, Dec. 2014 (cit. on pp. 114, 124).

[347]   J. D. Plumhof, V. Křapek, F. Ding, K. D. Jöns, R. Hafenbrak, P. Klenovský, A. Herklotz, K. Dörr, P. Michler, A. Rastelli, and O. G. Schmidt. 'Strain-induced anticrossing of bright exciton levels in single self-assembled GaAs/Al$_x$Ga$_{1-x}$As and In$_x$Ga$_{1-x}$As/GaAs quantum dots.' *Phys. Rev. B* 83 (12 Mar. 2011), p. 121302. DOI: 10.1103/PhysRevB.83.121302 (cit. on p. 120).

[348]   J. H. Quilter, R. J. Coles, A. J. Ramsay, A. M. Fox, and M. S. Skolnick. 'Enhanced photocurrent readout for a quantum dot qubit by bias modulation.' *Applied Physics Letters* 102.18,

181108 (2013), pp. -. DOI: http://dx.doi.org/10.1063/1.4804373 (cit. on p. 121).

[349] J. D. Mar, J. J. Baumberg, X. L. Xu, A. C. Irvine, and D. A. Williams. 'Electrical control of quantum-dot fine-structure splitting for high-fidelity hole spin initialization.' *Phys. Rev. B* 93 (4 Jan. 2016), p. 045316. DOI: 10.1103/PhysRevB.93.045316 (cit. on p. 122).

[350] J. Klein and J. D. Kafka. 'The Ti:Sapphire laser: The flexible research tool.' *Nat Photon* 4.5 (May 2010), pp. 289–289. DOI: 10.1038/nphoton.2010.108 (cit. on p. 123).

[351] R. Schirhagl, K. Chang, M. Loretz, and C. L. Degen. 'Nitrogen-Vacancy Centers in Diamond: Nanoscale Sensors for Physics and Biology.' *Annual Review of Physical Chemistry* 65.1 (2014), pp. 83–105. DOI: 10.1146/annurev-physchem-040513-103659 (cit. on p. 123).

[352] P. Lodahl, S. Mahmoodian, and S. Stobbe. 'Interfacing single photons and single quantum dots with photonic nanostructures.' *Rev. Mod. Phys.* 87 (2 May 2015), pp. 347–400. DOI: 10.1103/RevModPhys.87.347 (cit. on p. 123).

[353] J. Hansom, C. H. H. Schulte, C. Matthiesen, M. J. Stanley, and M. Atatüre. 'Frequency stabilization of the zero-phonon line of a quantum dot via phonon-assisted active feedback.' *Applied Physics Letters* 105.17, 172107 (2014). DOI: http://dx.doi.org/10.1063/1.4901045 (cit. on pp. 123, 124).

[354] A. J. Ramsay, T. M. Godden, S. J. Boyle, E. M. Gauger, A. Nazir, B. W. Lovett, A. V. Gopal, A. M. Fox, and M. S. Skolnick. 'Effect of detuning on the phonon induced dephasing of optically driven InGaAs/GaAs quantum dots.' *Journal of Applied Physics* 109.10, 102415 (2011). DOI: http://dx.doi.org/10.1063/1.3577963 (cit. on p. 124).

[355] L. Monniello, C. Tonin, R. Hostein, A. Lemaitre, A. Martinez, V. Voliotis, and R. Grousson. 'Excitation-Induced Dephasing in a Resonantly Driven InAs/GaAs Quantum Dot.' *Phys. Rev. Lett.* 111 (2 July 2013), p. 026403. DOI: 10.1103/PhysRevLett.111.026403 (cit. on p. 124).

[356] Y.-J. Wei, Y.-M. He, M.-C. Chen, Y.-N. Hu, Y. He, D. Wu, C. Schneider, M. Kamp, S. Hofling, C.-Y. Lu, and J.-W. Pan. 'Deterministic and Robust Generation of Single Photons from a Single Quantum Dot with 99.5% Indistinguishability Using Adiabatic Rapid Passage.' *Nano Lett.* 14.11 (Nov. 2014), pp. 6515–6519. DOI: 10.1021/nl503081n (cit. on p. 124).

[357] R. Mathew, E. Dilcher, A. Gamouras, A. Ramachandran, H. Y. S. Yang, S. Freisem, D. Deppe, and K. C. Hall. 'Subpicosecond adiabatic rapid passage on a single semiconductor quantum dot: Phonon-mediated dephasing in the strong-driving regime.' *Phys. Rev. B* 90 (3 July 2014), p. 035316. DOI: 10.1103/PhysRevB.90.035316 (cit. on p. 124).

[358] A. Vagov, M. D. Croitoru, M. Glässl, V. M. Axt, and T. Kuhn. 'Real-time path integrals for quantum dots: Quantum dissipative dynamics with superohmic environment coupling.' *Phys. Rev. B* 83 (9 Mar. 2011), p. 094303. DOI: 10.1103/PhysRevB.83.094303 (cit. on pp. 124, 139).

[359] M. Glässl, A. M. Barth, and V. M. Axt. 'Proposed Robust and High-Fidelity Preparation of Excitons and Biexcitons in Semiconductor Quantum Dots Making Active Use of Phonons.' *Phys. Rev. Lett.* 110 (14 Apr. 2013), p. 147401. DOI: 10.1103/PhysRevLett.110.147401 (cit. on pp. 124, 129, 132, 146, 156, 164).

[360] F. Liu, L. M. P. Martins, A. J. Brash, A. M. Barth, J. H. Quilter, V. M. Axt, M. S. Skolnick, and A. M. Fox. 'Ultrafast depopulation of a quantum dot by LA-phonon-assisted stimulated emission.' *Phys. Rev. B* 93 (16 Apr. 2016), p. 161407. DOI: 10.1103/PhysRevB.93.161407 (cit. on pp. 124, 141).

[361] A. J. Brash, L. M. P. P. Martins, A. M. Barth, F. Liu, J. H. Quilter, M. Glässl, V. M. Axt, A. J. Ramsay, M. S. Skolnick, and A. M. Fox. 'Dynamic vibronic coupling in InGaAs quantum dots [Invited].' *J. Opt. Soc. Am. B* 33.7 (July 2016), pp. C115–C122. DOI: 10.1364/JOSAB.33.00C115 (cit. on p. 124).

[362] P. Borri, W. Langbein, U. Woggon, V. Stavarache, D. Reuter, and A. D. Wieck. 'Exciton dephasing via phonon interactions in InAs quantum dots: Dependence on quantum confinement.'

Phys. Rev. B 71 (11 Mar. 2005), p. 115328. DOI: `10.1103/PhysRevB.71.115328` (cit. on p. 125).

[363] S. J. Boyle, A. J. Ramsay, A. M. Fox, M. S. Skolnick, A. P. Heberle, and M. Hopkinson. 'Beating of Exciton-Dressed States in a Single Semiconductor InGaAs/GaAs Quantum Dot.' *Phys. Rev. Lett.* 102 (20 May 2009), p. 207401. DOI: `10.1103/PhysRevLett.102.207401` (cit. on p. 126).

[364] A. M. Barth, S. Lüker, A. Vagov, D. E. Reiter, T. Kuhn, and V. M. Axt. 'Fast and selective phonon-assisted state preparation of a quantum dot by adiabatic undressing.' *ArXiv e-prints* (Jan. 2016) (cit. on p. 129).

[365] A. Siegman. *Lasers.* University Science Books, 1986 (cit. on p. 129).

[366] A. J. Leggett, S. Chakravarty, A. T. Dorsey, M. P. A. Fisher, A. Garg, and W. Zwerger. 'Dynamics of the dissipative two-state system.' *Rev. Mod. Phys.* 59 (1 Jan. 1987), pp. 1–85. DOI: `10.1103/RevModPhys.59.1` (cit. on p. 129).

[367] A. Vagov, M. D. Croitoru, V. M. Axt, T. Kuhn, and F. M. Peeters. 'Nonmonotonic Field Dependence of Damping and Reappearance of Rabi Oscillations in Quantum Dots.' *Phys. Rev. Lett.* 98 (22 June 2007), p. 227403. DOI: `10.1103/PhysRevLett.98.227403` (cit. on pp. 131, 166, 175, 178, 183).

[368] P.-L. Ardelt, L. Hanschke, K. A. Fischer, K. Müller, A. Kleinkauf, M. Koller, A. Bechtold, T. Simmet, J. Wierzbowski, H. Riedl, G. Abstreiter, and J. J. Finley. 'Dissipative preparation of the exciton and biexciton in self-assembled quantum dots on picosecond time scales.' *Phys. Rev. B* 90 (24 Dec. 2014), p. 241404. DOI: `10.1103/PhysRevB.90.241404` (cit. on pp. 132, 149, 156).

[369] D. P. S. McCutcheon and A. Nazir. 'Quantum dot Rabi rotations beyond the weak exciton phonon coupling regime.' *New Journal of Physics* 12.11 (2010), p. 113042. DOI: `10.1088/1367-2630/12/11/113042` (cit. on pp. 134, 150, 156).

[370] K. Roszak, V. M. Axt, T. Kuhn, and P. Machnikowski. 'Exciton spin decay in quantum dots to bright and dark states.' *Phys.*

Rev. B 76 (19 Nov. 2007), p. 195324. DOI: `10.1103/PhysRevB.76.195324` (cit. on p. 134).

[371]   S. J. Boyle, A. J. Ramsay, F. Bello, H. Y. Liu, M. Hopkinson, A. M. Fox, and M. S. Skolnick. 'Two-qubit conditional quantum-logic operation in a single self-assembled quantum dot.' *Phys. Rev. B* 78 (7 Aug. 2008), p. 075301. DOI: `10.1103/PhysRevB.78.075301` (cit. on p. 136).

[372]   A. P. Heberle, J. J. Baumberg, and K. Köhler. 'Ultrafast Coherent Control and Destruction of Excitons in Quantum Wells.' *Phys. Rev. Lett.* 75 (13 Sept. 1995), pp. 2598–2601. DOI: `10.1103/PhysRevLett.75.2598` (cit. on pp. 142, 156, 157).

[373]   N. H. Bonadeo, J. Erland, D. Gammon, D. Park, D. S. Katzer, and D. G. Steel. 'Coherent Optical Control of the Quantum State of a Single Quantum Dot.' *Science* 282.5393 (1998), pp. 1473–1476. DOI: `10.1126/science.282.5393.1473` (cit. on pp. 142, 157).

[374]   A. Capua, O. Karni, G. Eisenstein, V. Sichkovskyi, V. Ivanov, and J. P. Reithmaier. 'Coherent control in a semiconductor optical amplifier operating at room temperature.' *Nat Commun* 5 (Sept. 2014), pp. –. DOI: `10.1038/ncomms6025` (cit. on pp. 142, 157).

[375]   A. Nazir. 'Photon statistics from a resonantly driven quantum dot.' *Phys. Rev. B* 78 (15 Oct. 2008), p. 153309. DOI: `10.1103/PhysRevB.78.153309` (cit. on p. 144).

[376]   S. Bounouar, M. Müller, A. M. Barth, M. Glässl, V. M. Axt, and P. Michler. 'Phonon-assisted robust and deterministic two-photon biexciton preparation in a quantum dot.' *Phys. Rev. B* 91 (16 Apr. 2015), p. 161302. DOI: `10.1103/PhysRevB.91.161302` (cit. on pp. 146, 149, 152, 153, 156, 164, 173).

[377]   H. Kamada, H. Gotoh, J. Temmyo, T. Takagahara, and H. Ando. 'Exciton Rabi Oscillation in a Single Quantum Dot.' *Phys. Rev. Lett.* 87 (24 Nov. 2001), p. 246401. DOI: `10.1103/PhysRevLett.87.246401` (cit. on p. 150).

[378]   S. Stufler, P. Ester, A. Zrenner, and M. Bichler. 'Quantum optical properties of a single $In_xGa_{1-x}As$-GaAs quantum dot two-

level system.' *Phys. Rev. B* 72 (12 Sept. 2005), p. 121301. DOI: 10.1103/PhysRevB.72.121301 (cit. on p. 151).

[379] S. Hughes and H. J. Carmichael. 'Phonon-mediated population inversion in a semiconductor quantum-dot cavity system.' *New Journal of Physics* 15.5 (2013), p. 053039. DOI: 10.1088/1367-2630/15/5/053039 (cit. on pp. 157, 159, 175, 178, 183).

[380] R. Manson, K. Roy-Choudhury, and S. Hughes. 'Polaron master equation theory of pulse-driven phonon-assisted population inversion and single-photon emission from quantum-dot excitons.' *Phys. Rev. B* 93 (15 Apr. 2016), p. 155423. DOI: 10.1103/PhysRevB.93.155423 (cit. on pp. 157, 159, 160).

[381] D. P. S. McCutcheon and A. Nazir. 'Model of the Optical Emission of a Driven Semiconductor Quantum Dot: Phonon-Enhanced Coherent Scattering and Off-Resonant Sideband Narrowing.' *Phys. Rev. Lett.* 110 (21 May 2013), p. 217401. DOI: 10.1103/PhysRevLett.110.217401 (cit. on p. 157).

[382] Y.-J. Wei, Y. He, Y.-M. He, C.-Y. Lu, J.-W. Pan, C. Schneider, M. Kamp, S. Höfling, D. P. S. McCutcheon, and A. Nazir. 'Temperature-Dependent Mollow Triplet Spectra from a Single Quantum Dot: Rabi Frequency Renormalization and Sideband Linewidth Insensitivity.' *Phys. Rev. Lett.* 113 (9 Aug. 2014), p. 097401. DOI: 10.1103/PhysRevLett.113.097401 (cit. on p. 157).

[383] K. Müller, K. A. Fischer, A. Rundquist, C. Dory, K. G. Lagoudakis, T. Sarmiento, Y. A. Kelaita, V. Borish, and J. Vučković. 'Ultrafast Polariton-Phonon Dynamics of Strongly Coupled Quantum Dot-Nanocavity Systems.' *Phys. Rev. X* 5 (3 July 2015), p. 031006. DOI: 10.1103/PhysRevX.5.031006 (cit. on p. 157).

[384] F. Hargart, M. Müller, K. Roy-Choudhury, S. L. Portalupi, C. Schneider, S. Höfling, M. Kamp, S. Hughes, and P. Michler. 'Cavity-enhanced simultaneous dressing of quantum dot exciton and biexciton states.' *Phys. Rev. B* 93 (11 Mar. 2016), p. 115308. DOI: 10.1103/PhysRevB.93.115308 (cit. on p. 157).

[385] J. Iles-Smith and A. Nazir. 'Quantum correlations of light and matter through environmental transitions.' *Optica* 3.2 (Feb.

2016), pp. 207–211. DOI: 10.1364/OPTICA.3.000207 (cit. on p. 157).

[386]   A. Nysteen, P. Kaer, and J. Mork. 'Proposed Quenching of Phonon-Induced Processes in Photoexcited Quantum Dots due to Electron-Hole Asymmetries.' *Phys. Rev. Lett.* 110 (8 Feb. 2013), p. 087401. DOI: 10.1103/PhysRevLett.110.087401 (cit. on pp. 159, 166).

[387]   M. Glässl, M. D. Croitoru, A. Vagov, V. M. Axt, and T. Kuhn. 'Influence of the pulse shape and the dot size on the decay and reappearance of Rabi rotations in laser driven quantum dots.' *Phys. Rev. B* 84 (12 Sept. 2011), p. 125304. DOI: 10.1103/PhysRevB.84.125304 (cit. on p. 166).

[388]   Y. Ota, M. Shirane, M. Nomura, N. Kumagai, S. Ishida, S. Iwamoto, S. Yorozu, and Y. Arakawa. 'Vacuum Rabi splitting with a single quantum dot embedded in a H1 photonic crystal nanocavity.' *Applied Physics Letters* 94.3, 033102 (2009). DOI: http://dx.doi.org/10.1063/1.3073859 (cit. on pp. 170, 177).

[389]   A. Ulhaq, W. S., S. Ulrich, R. Roszbach, M. Jetter, and M. P. 'Cascaded single-photon emission from the Mollow triplet sidebands of a quantum dot.' *Nat Photon* 6.4 (Apr. 2012), pp. 238–242. DOI: 10.1038/nphoton.2012.23 (cit. on p. 174).

[390]   C. Matthiesen, M. J. Stanley, M. Hugues, E. Clarke, and M. Atatüre. 'Full counting statistics of quantum dot resonance fluorescence.' *Scientific Reports* 4 (May 2014), pp. 4911– (cit. on p. 174).

[391]   V. Giesz, N. Somaschi, G. Hornecker, T. Grange, B. Reznychenko, L. De Santis, J. Demory, C. Gomez, I. Sagnes, A. Lemaitre, O. Krebs, N. D. Lanzillotti-Kimura, L. Lanco, A. Auffeves, and P. Senellart. 'Coherent control of a solid-state quantum bit with few-photon pulses.' *ArXiv e-prints* (Dec. 2015) (cit. on p. 177).

[392]   M. J. Gullans, Y.-Y. Liu, J. Stehlik, J. R. Petta, and J. M. Taylor. 'Phonon-Assisted Gain in a Semiconductor Double Quantum Dot Maser.' *Phys. Rev. Lett.* 114 (19 May 2015), p. 196802. DOI: 10.1103/PhysRevLett.114.196802 (cit. on p. 183).

[393] D. Pinotsi, P. Fallahi, J. Miguel-Sanchez, and A. Imamoglu. 'Resonant Spectroscopy on Charge Tunable Quantum Dots in Photonic Crystal Structures.' *IEEE Journal of Quantum Electronics* 47.11 (Nov. 2011), pp. 1371–1374. DOI: 10.1109/JQE.2011.2164898 (cit. on p. 184).